SAPIENZA
UNIVERSITÀ DI ROMA

SCUOLA DI INGEGNERIA AEROSPAZIALE

DOTTORATO DI RICERCA IN INGEGNERIA AEROSPAZIALE
XXIV CICLO

THE DETERMINATION OF THE ROTATIONAL STATE OF CELESTIAL BODIES

Rachele Meriggiola

Advisor:

Prof. Luciano Iess

ANNO ACCADEMICO 2011-2012

Acknowledgments

I am first and foremost grateful to my principal advisor Prof. Luciano Iess for introducing me to this opportunity, for his guidance, encouragement, and to be a continue source of inspiration. It is clear that none of this work would have been possible without him. I am especially thankful to Giuseppe Mitri for all the invaluable assistance and the support, especially for the geophysics part, thanks indeed. I owe my thanks also to Prof. Jonathan I. Lunine for his helpful feedback and suggestions, all the while continually expressing an active interesting on the progress of this work. I am grateful to all the past and present members of the Radio Science Laboratory, Alessandro Ardito, Gabriele Rapino, Paolo Racioppa, Mauro Di Benedetto, Stefano Finocchiaro, Manuela Marabucci, Francesco Barbaglio, Marco Ducci and Antonio Genova for supporting and assisting me in the last years and for their insight, intellect and friendliness. I want to thank deeply also Alessandra Palli for all the work done and the purely insane hours of fun spent together.

I am also tremendously grateful to my closest friends, Sandro, Raffaele, Paolo, EmA, Eleonora, Joseph and Hanzo, who supported and sustained me with their advices, wisdom and constant presence, in spite of the distance.

Finally, last but first in my heart, I want to thank my beloved parents and the love of my life for all the support, the unconditional love, the infinite patience and the invaluable advices. Andrea, you always gave my world meaning and helped me to keep on track in the good and in the hard times. Mom, Dad, none of what I have done it would be possible without you. I dedicate to you this work.

Table of Contents

III. OBSERVING THE PLANETARY ROTATION: APPLIED TECHNIQUES 35

List of Tables

List of Figures

Acronyms

BIDR	Basic Image Data Records
DEC	Declination
DEM	Digital Elevation Model
EM	Extended Mission
EMEJ2000	Earth Mean Equator at J2000 epoch reference frame
EXT	Extended rotational model
HGA	High Gain Antenna
HRIC	High spatial Resolution Imaging Channel
IAU	IAU rotational model
ICRF	International Celestial Reference Frame
IERF	Instantaneous Equator of date Reference Frame
LGA	Low Gain Antenna
MMO	Mercury Magnetospheric Orbiter
MOI	Polar Moment Of Inertia
MORE	Mercury Orbiter Radio-science Experiment
MORF	Mean Orbital plane Reference Frame
MPO	Mercury Planetary Orbiter
NSR	Not Synchronous Rotation
PM	Prime Mission
P+E	Prime and Extended Mission
RA	Right Ascension
RES	Rotation Experiment Simulator
RF	Reference Frame
RSDS	Rotational State Determination Software
ROI	Region of Interest
SAR	Synthetic Aperture Radar
SIFT	Scale Invariant Feature Transform
SURF	Speeded Up Robust Feature
TERF	True Equator of date Reference Frame

Introduction

The knowledge of the rotational state of planets and satellites is crucial to gather information on their interior structure and long term geophysical processes. Evolution models of the orbital dynamics of celestial bodies use the obliquity and the eccentricity as a constraint. When the quadrupole gravity field is known, the obliquity may provide also the moment of inertia, one of the most important quantities to infer the body's density profile. The spin rate and physical librations indicate the degree of internal differentiation, as well as information on the possible orbital resonances (Murray and Dermott, 1999). Finally, the occupancy of a Cassini state (Yseboodt and Margot, 2006) allows to trace back the orbital evolution of a satellite system.

Given the value of the geophysical inferences, it is not surprising that the determination of the rotational state is a primary goal for several deep-space missions. For many bodies, the rotational state has not been determined by direct observations from ground or space. For solar system satellites, the rotational models prescribed by the IAU assume the occupancy of a zero-obliquity Cassini state, where the orbit normal and the Laplace pole are determined from astronomical observations. The only solar system bodies for which the rotational state is known with excellent accuracy are the Earth and the Moon. Thanks to long lived landers and rovers or radar observations, also the rotation Mars, Mercury and Venus are known with good accuracy.

The main goal of the present work is the application of radar or optical imaging techniques to the determination of the rotational state of Titan and Mercury. In order to attain this goal, current rotational models were reviewed and modified, and a numerical estimator of the rotational parameters was developed. Although the code can be used to estimate the rotational state of a generic solar system body, it has been applied to the determination of the rotational state of Titan, using SAR images from the Cassini mission and to the simulation of the rotation experiment of the mission BepiColombo to Mercury.

A rotational motion of a body is described by a set of parameters which provide the location of the spin pole and the longitude of the prime meridian. A rotational model needs to take into account many effects: precession and nutation, length of day variations, Chandler's wobble and free core nutations, librations, interaction of the solid body with its atmosphere, tidal interactions. An introduction to planetary rotations is presented in Chapter I.

Given the limited experimental accuracies, available rotational models take into account only a part of these effects. For this reason a review of the rotational models is reported on Chapter II. The current IAU models were modified, including the libration terms, and a new model, the Extended Rotational Model (EXT), was developed in order to include polar motion and other effects. Analytical formulations both for the IAU and EXT models have been provided.

The rotational state can be estimated using different techniques, such as radio-tracking data or optical and radar observables. The rotational parameters can be estimated as a part of a global orbit determination fit or by a dedicated estimation process. All the available techniques used for the determination of the rotational state are reviewed in the Chapter III.

The core of this work is reported in Chapter IV, where the imaging from orbit technique and its application to the estimate of the rotational parameters is presented. Georeferenced images of the same area, taken at different times, are compared by pattern matching algorithms in order to determine the registration error. Different pattern matching procedures can be applied, as such as cross-correlation, mutual information technique, and SIFT/SURF algorithms. The mismatching is mainly due to errors in the rotational model, with smaller contributions from the spacecraft ephemerides and attitude, camera or radar calibration, and image processing. The image correlation is followed by a weighted least-squares fit to update the rotational model and minimize the mismatch between the features. Chapter IV reports on feature and cross-over classification, guidelines for the optimization of the data processing, applied pattern matching algorithms and the analytical formulation for the estimate algorithm. The analytical formulation of the partial derivatives of the optical observables with respect to the rotational parameters is reported on the Annex A and B.

A dedicated software code (RSDS - Rotational State Determination Software) was written in order to carry out the estimate of the rotational parameters. The RSDS estimator accepts misregistration vectors as inputs and produces an estimate of the selected rotational parameters. The code fits the misregistration vectors against the IAU or EXT models.

A complete description of the software and the performed simulations are reported in Chapter V. The application of RSDS to Cassini and BepiColombo rotation experiments is reported in Chapter VII and VIII.

Titan and the NASA/ESA/ASI Cassini mission to the Saturn system have been the first application of the technique and the code. In this case multiple RADAR observations were used for the experiment. Since the rotation experiment is intimately connected to the geophysics of Titan, the current interior models of the satellite, its surface morphology and atmospheric models are reported in the thesis (Chapter VI) along with the main characteristics of the Cassini spacecraft and the RADAR system.

The results of the Cassini Rotation Experiment are presented on Chapter VII. After an erroneous estimate of a non-synchronous rotation (Lorentz et al, 2008), no rotational model is available at the moment for Titan. This work is also meant to fill this gap and provide a rotational model by means of data from Cassini's extended mission.

SAR images from 2004 to 2009 were processed and correlated to provide the misregistration vectors. New estimates for the spin axis direction, the obliquity and the spin rate were obtained for both the prime and extended mission data, providing relevant information on the internal structure of the body and constraints for the evolution models of the orbit and the interior. A new rotational model for Titan is also provided, including also the precession terms. An obliquity of 0.31° was estimated, suggesting the presence of a differentiated interior and a decoupling between the outer icy shell and the rocky core, such as caused by the presence of a global subsurface ocean. Titan is found in a rotational state compatible with the occupancy of a Cassini state 1, even if a weak deviation can still be observed. This small inconsistency has been attributed to short period effects not included in the model. A spin rate of 22.5769 °/day has been estimated, confirming the 1:1 resonance with the orbital period. Slight deviations from the synchronous rotation are still observed, likely due to atmospheric seasonal variations acting on the icy shell, suggesting one more time a core – shell decoupling (Karatekin et al., 2008). The analysis is part of a complex picture of Titan's geodesy, whose determination requires very long observation periods.

The application of the imaging from orbit technique to the BepiColombo Rotation Experiment has been reported in Chapter VII. BepiColombo is an ESA/JAXA mission to Mercury. The spacecraft will be launched on 2015 and it will be inserted into the final polar orbit around Mercury at the end of 2021. As part of the outstanding scientific payload used for the exploration of one of the less known planets of the Solar System, the Mercury Orbiter Radioscience Experiment (MORE) will determine the rotational state with the goals of an accuracy 1 arcsec for the obliquity and the amplitude of the physical librations in longitude. In order to simulate the operative conditions and to perform the data processing, a complex simulation of the experiment has been designed and implemented by the MORE team. A stand-alone application has been realized and the RSDS was updated for a successful integration into the overal system. I report on preliminary simulations in Chapter VIII.

The final assessment for the used technique, the implemented software and the reported results show the accuracy, the stability and the reliability of the proposed procedure for the determination of the rotational state.

To Mom and Dad
To Andrea

Chapter I

Planetary Rotation

The rotational motion of a body of the solar system depends on several factors. Fundamentals of the precession, nutation, polar motion and libration theory are here reported in order to allow a full understanding of the rotational models (Chapter II). A formulation of the polar moment of inertia of a body as a function of the obliquity and the amplitude of physical librations in longitude is presented, in order to show the geophysical implications of an estimation of the rotational state.

The rotation is one of the most important elements used to describe the motion of a celestial body. The rotation periods of most objects orbiting the Sun vary between five hours and a week. Mercury and Venus rotations have almost certainly been slowed by solar tides, and form exceptions with period of 59 and 243 days respectively. Six of the nine planets rotate in a prograde sense with obliquities of 30° or less. Venus rotates in a retrograde direction with an obliquity of 177°; the rotation axes of Uranus and Pluto are tilted nearly perpendicular to the ecliptic plane. Most planetary satellites show a synchronous rotation as a result of planet-induced tides.

The oblateness of a planet is tied to the rotation, which introduces a centrifugal pseudo-force which causes the planet to bulge out at the equator and to flatten at the poles. A perfect fluid planet would be shaped as an oblate spheroid. Polar flattening is greatest for planets characterized by a low density and rapid rotation.

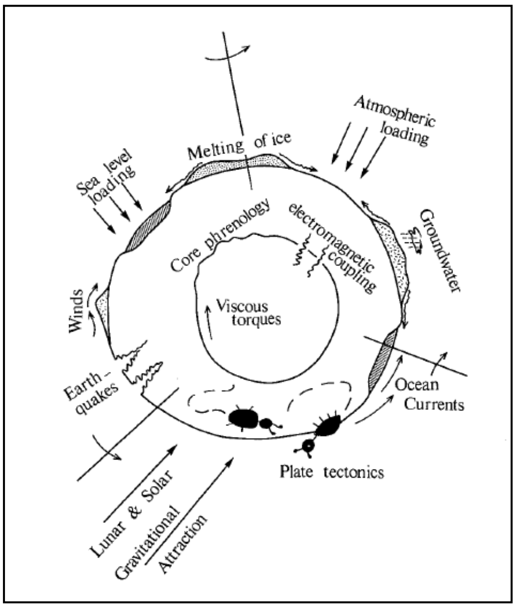

Figure 1 - Forces acting on the Earth's rotation

1. Earth's rotation

The rotation period of the Earth relative to the fixed stars is named *stellar day* and is equal to 23h 56m 4.098 903 691 s of mean solar time (UT1). The rotation period relative to the precessing or moving mean vernal equinox, named the *sidereal day*, is equal to 23h 56m 4.090 530 832 88s of mean solar time (UT1). Thus the sidereal day is shorter than the stellar day by about 8.4 ms. Both the stellar day and the sidereal day are shorter than the mean solar day by about 3 minutes 56 seconds.

The permanent monitoring of the Earth's rotation requires the use of Very Long Baseline Interferometry (VLBI) coordinated with the Global Positioning System (GPS), Satellite laser ranging, and other satellite techniques (see Chapter 3 for details). This provides the absolute reference for the determination of universal time, precession, and nutation.

Over millions of years, the rotation is significantly slowed by gravitational interactions with the Moon; both rotational energy and angular momentum are being slowly transferred to the Moon. However some large scale seismic events can speed up the rotation by affecting the Earth's moment of inertia. Also the post-glacial rebound, ongoing since the last Ice age, is changing the distribution of the Earth's mass thus affecting the moment of inertia and the rotation period. The spin rate is mainly determined by precession, nutation and polar motion effects. A representation of all these effects is reported on Figure 1.

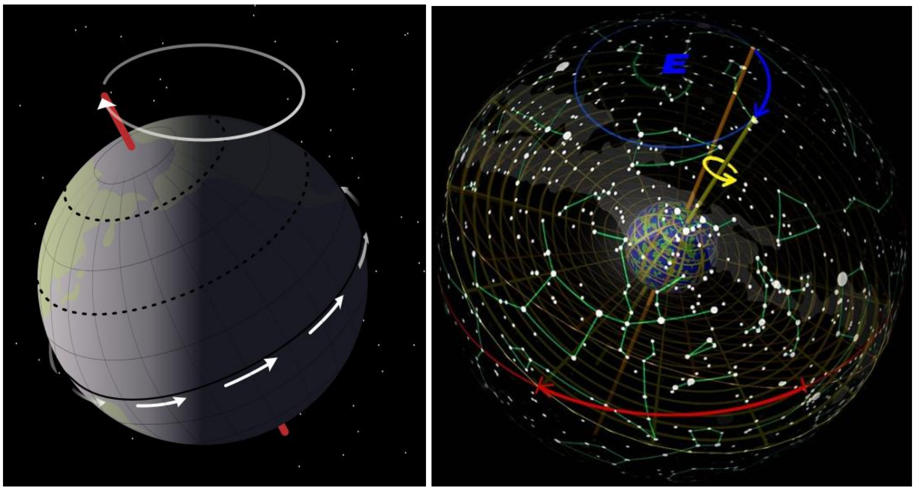

Figure 2 – A physical representation of the precession

1.1. Precession

Precession is a change in the orientation of the spin axis of a rotating body. For the Earth (and for all the solar system bodies) the *general precession* is formed by two distinct contributes, respectively the axial and the orbital plane precession. A physical representation of the precession is reported on Figure 2.

Axial precession

Also called *equator precession* or *precession of the equinoxes*, the axial precession is a gravity-induced, long-period and continuous change in the orientation of the spin axis. For the Earth the precession period is equal to ~ 26,000 years, with a precession rate equal to 12 arcsec per century and a decrease in the obliquity of ~ 47 arcsec per century. For the Earth the motion of the equator is due to the torque of the Sun and the Moon (lunisolar precession) and in minor part (about 500 times smaller) of the other planets, on the equatorial bulge.

In general the precession constant can be computed as:

$$\frac{d\psi}{dt} = \frac{3}{2}\frac{GM_p}{a^3(1-e^2)^{3/2}}\frac{C-A}{C}\frac{\cos\epsilon}{\omega} \tag{1.1}$$

where a and e are respectively the semimajor axis and the eccentricity of the orbit for the perturbing body, M_p the perturbing mass, A and C the principal moments of inertia of the perturbed body; it is evident the correlation with the obliquity ϵ and the spin rate ω of the perturbed body.

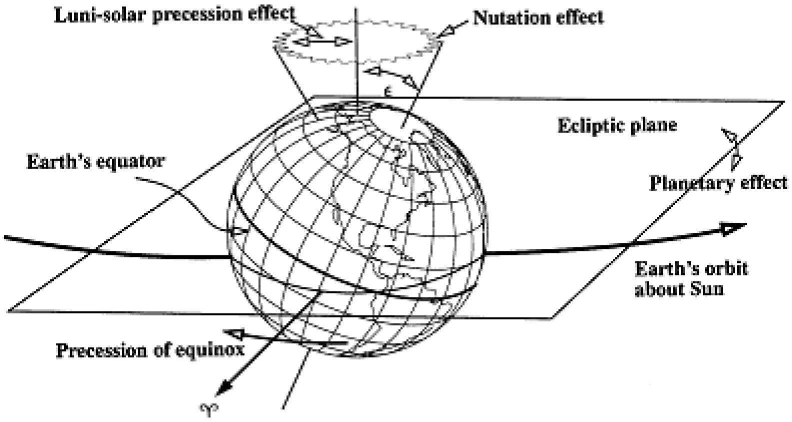

Figure 3 – Precession and nutation effects for the Earth

Orbital Precession
Also called in a misleading way *planetary precession*, is the retrograde motion of the orbital plane around the Laplace plane (see 1.4) due to the small angle between the gravitational force of the other planets on the Earth and the ecliptic, causing the plane of the ecliptic to shift slightly relative to inertial space.

1.2. Nutation

The nutation is a short-period oscillation of the rotation axis with respect to a space-fixed coordinate system. For the Earth the nutation terms have a maximum amplitude of 9 arcsec and a variety of periods up to 18.6 years (Seidelmann, 2005). This short-period rotational motion includes effects of both forced motion and free motion. The *forced motion* is due to the torque produced by the gravitational attraction of the Moon (and to a lesser extent that of the Sun and planets) on the equatorial bulge of the Earth. The *free motion* is determined only from observations and may be excited by internal processes. The non-rigidity of the Earth causes a difference between the computed and the observed coefficients of the forced periodic terms. The principal difference occurs in the coefficient of the 18.6 year nutation term, known as the constant of nutation.

1.3. Polar motion

For a celestial body the spin motion is represented by a diurnal rotation around a reference axis, the normal to the true equator. This axis is not fixed into the inertial reference frame, but it moves over short and long time scales due to the nutation and precession.

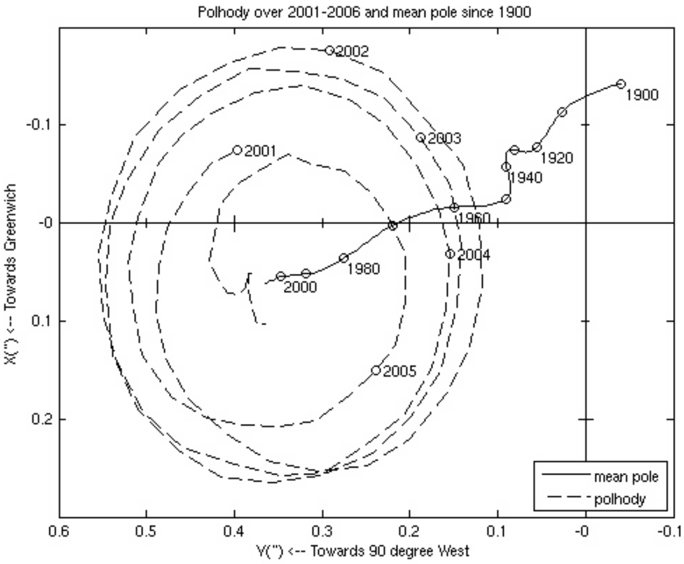

Figure 4 - Polar motion over 2001 - 2006 and mean pole since 1900 (JPL – NASA)

In addition, for some bodies as the Earth and Mars the reference axis does not coincide with the figure axis, but moves slowly in a quasi-circular path around it (Figure 4). This motion is known as *polar motion*. For the Earth the maximum amplitude of the polar motion is ~ 0.3 arcsec (9 m displacement on the surface) with two principal periods of about 365 and 428 days. The motion is affected by unpredictable geophysical forces and is determined from VLBI and laser ranging observations (see Chapter III).

The amplitude of this motion, also called *Chandler's wobble*, varies on a time scale of years, reaching its largest size in 1910 and fluctuating noticeably from one decade to another (Seidelmann, 2005). Changes in the mass distribution or angular momentum of the Earth's outer core, atmosphere, oceans, or seismic activity can affect the motion. Gross (2000) recently found that during 1985.0-1996.0 two thirds of the 'wobble' was caused by fluctuating pressure on the sea bottom due to temperature and salinity changes and wind-driven changes in the circulation of the oceans. The remaining third is due to atmospheric fluctuations.

2. Cassini state

Cassini state is defined as an evolved rotational state where the spin axis, orbit normal, and normal to the Laplace plane are coplanar while the obliquity remains constant (Yseboodt and Margot, 2006). The Laplace plane is defined as the plane about which a planet's orbit precesses with constant inclination to the equatorial and ecliptic planes.

In this configuration the normal to the orbital plane precesses at a uniform rate about the Laplace pole. For nearly circular orbits this configuration can be described by the following condition (Ward, 1975):

$$[v+(u-v)\cos\varepsilon]\sin\varepsilon=\sin(i-\varepsilon) \tag{1.2}$$

where i is the inclination of the orbit plane respect to the invariable plane, and ε is the obliquity, defined as the angle between the rotation axis and the normal to the orbital plane. The parameters u and v are related to the moments of inertia of the body, and the relative rates of orbital motion and orbital precession:

$$\left.\begin{aligned} u &= \frac{3}{2}\,p\,\frac{J_2+2C_{22}}{c} \\ v &= \frac{3}{2}\,p\,\frac{C_{22}}{c} \end{aligned}\right\} \tag{1.3}$$

where p is the ratio between the mean motion (n) and the precession rate of the orbital plane and Ω is the longitude of the ascending node of the orbit:

$$p=\frac{n}{d\Omega/dt} \tag{1.4}$$

Being the Cassini State a state of minimum energy, it is verified for some bodies as the Moon and Mercury, and it is a crucial point to be verified into the determination of rotational state for a body.

3. Libirations

Librations are short-period oscillations of the rotational motion due to the interaction between the gravitational forces and the geometry of the orbit.

Librations in longitude

Librations in longitude are due to the eccentricity of the satellite orbit. A satellite in a 1:1 resonance is orbiting to the central body at the same rate as its body is rotating around its axis. If the orbit is circular the planet-satellite line and the long axis of the satellite are aligned (excluding tidal effects). But nevertheless if the orbit is eccentric (Figure 5, A), the satellite is advancing fastest at the pericenter, and a small angle (*libration angle*) is formed between the long axis and the planet-satellite line. The libration motion is the variation over time of this angle.

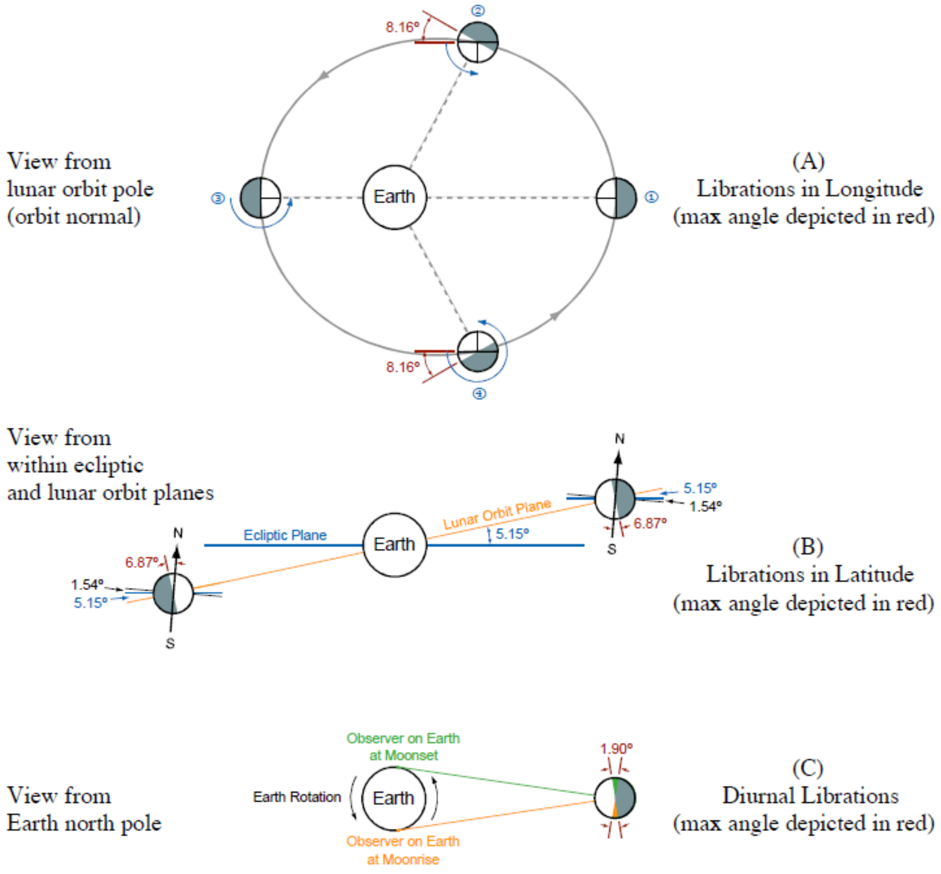

Figure 5 - the different typologies of librations (JPL - D-32296)

Librations in latitude

The physical librations in latitude depending on a North-South oscillation due to the obliquity of the body (Figure 5 - B). Its origin is analogous to the librations in longitude.

Diurnal libration

Diurnal libration is a small daily oscillation due to the Earth's rotation, which carries an observer first to one side and then to the other side of the straight line joining Earth's and the Moon's centers, allowing the observer to look first around one side of the Moon and then around the other—because the observer is on the surface of the Earth, not at its center.

Analytical formulation for the physical librations in longitude

Considering for a satellite in a 1:1 resonance only the averaged equation of motion (drag term included), librations are damped to zero. If the short-period terms are included and the full equation of motion is analyzed, the satellite shows short-period librations about the equilibrium configuration

(Murray and Dermott,1999). The equation of motion for a satellite that orbits around a central body, expressed in function of librations angle γ, is:

$$C\ddot{\gamma} - \frac{3}{2}(B-A)n^2\left(\frac{a}{r}\right)^3 \sin(4e\sin nt - 2\gamma) = 0 \tag{1.5}$$

where *A*<*B*<*C* are the moments of inertia and *n* is the mean motion. The coordinate axes of the reference frame are assumed as aligned with the principal moment of inertia. Thus, considering small deviations from equilibrium and introducing some approximations, equation 1.5 can be reduced to:

$$\ddot{\gamma} = -{\omega_0}^2\gamma + 2e{\omega_0}^2 \sin nt \tag{1.6}$$

where:

$$\omega_0 = n\sqrt{3\frac{(B-A)}{C}H(p,e)} \tag{1.7}$$

is the *libration frequency*. For a synchronous satellite (*p*=1) H*(p,e)* is given by:

$$H(1,e) = 1 - \frac{5}{2}e^2 + \frac{13}{16}e^4 \tag{1.8}$$

The solution for γ is found substituting $\gamma = \gamma_0 \sin(nt)$ into the equation:

$$\gamma = -\frac{2\omega_0^2 e}{n^2 - \omega_0^2}\sin(nt) \tag{1.9}$$

Then the amplitude γ_0 of the forced librations can be expressed in function of the polar moment of inertia C_s:

$$\gamma_0 = \frac{2\omega_0^2 e}{n^2 - \omega_0^2} \cong 6e\left(\frac{B-A}{C}\right) \tag{1.10}$$

Following (Soler, 1984) it is possible to express *B* – *A* in function of the gravity coefficients:

$$B - A = 4C_{22}MR^2 \tag{1.11}$$

So the normalized polar Moment of Inertia (MoI) *c* can be expressed as it follows:

$$c \cong 24e\,\frac{C_{22}}{\gamma_0} \tag{1.12}$$

The equation 1.12 relates the quadrupole gravity field with the amplitude of the libration in longitude and the polar MoI.

4. Rotational state and polar moment of inertia

The polar Moment of Inertia (MoI) of a celestial body is a fundamental quantity to be measured because it provides constraints on the interior structure, specifying the level of the internal differentiation. MoI is generally inferred from gravity field data (see 2.1), but it can be also derived from the rotational parameters by specific assumptions. The correlation between the rotational parameters and the MoI will be presented in the next sections.

4.1. MoI and the gravity field

Assuming the hydrostatic equilibrium for a target body it is possible to infer the polar MoI from the gravity field coefficients using the secular Love number, by the well known Radau-Darwin equation:

$$c \equiv \frac{C}{MR^2} = \frac{2}{3}\left(1 - \frac{2}{5}\sqrt{\frac{4-k_s}{1+k_s}}\right) \tag{1.13}$$

where k_s is the *secular Love number*, expressed as a function of the harmonic coefficient C_{22}:

$$k_s = 4\,\frac{C_{22}}{q_r} \tag{1.14}$$

and q_r the *rotational parameter*, defined as the ratio between the product between the squared spin rate and the cubic radius, and the gravitational parameter of the body:

$$q_r = \frac{\omega^2 R^3}{GM} \tag{1.15}$$

The Radau-Darwin equation holds exactly for uniform density fluids and it is a reasonably good approximation for radially stratified bodies (Nakiboglu, 1982).

4.2. MoI and the obliquity

The obliquity of a body may be used to place constraints on the internal structure. Polar moment of inertia can be directly computed from the measured gravity coefficients assuming the body in a hydrostatic equilibrium, an assumption valid for most but not for all the bodies of the Solar System. The polar MoI can also be directly estimated from the obliquity assuming the occupancy of the Cassini State (Bills and Nimmo, 2008). In this case, the relation between the MoI and the obliquity can be expressed as:

$$c = \frac{3p}{2}\left(\frac{\left(C_{22} + \left(J_2 + C_{22}\right)\cos\varepsilon\right)\sin\varepsilon}{\sin\left[i - \varepsilon\right]}\right) \tag{1.16}$$

where c is the dimensionless MoI, i the orbit inclination and ε the obliquity. In the Figure 6 is reported the c computed by the equation 1.16 applied to the Titan case.

4.3. MoI of differentiated bodies

The measurement of γ is sufficient to estimate the polar moment of inertia c. Since librations are measured respect to the surface, the derived measure of c may refer to the entire body, in the case of an homogeneous body; for a core-shell structure (as for icy satellites), may be instead referred only to the shell, assuming a core-shell decoupling.

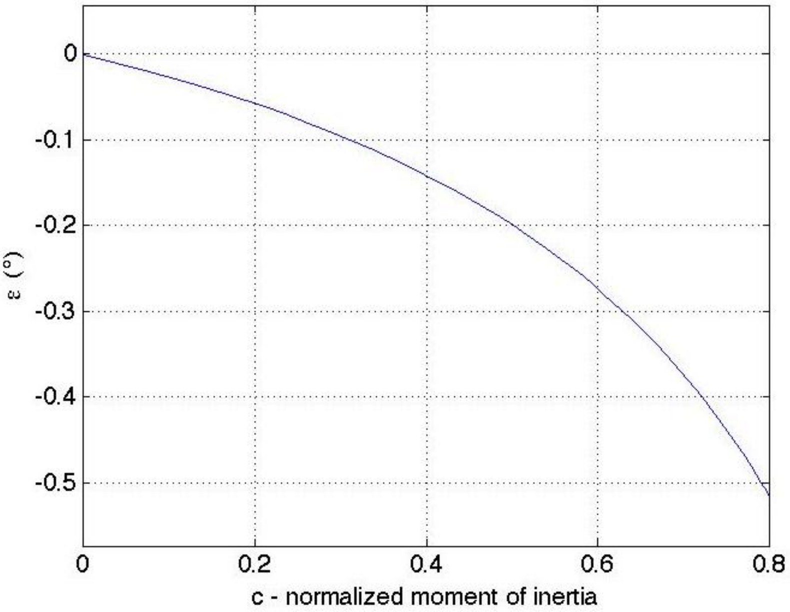

Figure 6 - obliquity in function of MoI applied to Titan (Bills and Nimmo, 2008)

This implies that the determination of the librations amplitude is crucial in order to derive relevant information on the interior structure and its differentiation, because the radius of the core and the thickness of the shell can be derived from these measurements (Peale et al., 2002; Margot et al., 2007).

In the presence of a partially or fully differentiated interior structure it is necessary to investigate the coupling between the core and the shell on both long and short time periods. The shell cannot be considered fully decoupled from the interior because of the existence of viscous, pressure and gravitational torques (e.g. Peale et al., 2002, VanHoolst et al., 2009). As regarding viscous effects, following (Peale et al., 2002) a time constant for small viscosities is defined in order to define the coupling:

$$\tau = \frac{R_o}{\sqrt{\nu\,\omega}} \tag{1.17}$$

where ν is the kinematic viscosity, ω the spin rate and the radius of the mantle. If t << 1 the decoupling can be assumed for the short period.

MOI from obliquity

Considering that there is a specific relation between gravity field coefficients for the entire body and the shell (Bills and Nimmo, 2008):

$$\begin{bmatrix} \delta J_2 \\ \delta C_{22} \end{bmatrix} = \frac{3}{5}\left(\frac{1-z^5}{1-z^3}\right)\begin{bmatrix} J_2 \\ C_{22} \end{bmatrix} \tag{1.18}$$

it is possible for a differentiated structure to calculate the dimensionless polar MOI directly in function of the thickness of the shell, of the obliquity and of the gravity field coefficients providing useful information on the interior:

$$c_{sh} = \frac{3}{2}p\left[\frac{3}{5}\left(\frac{1-z^5}{1-z^3}\right)\frac{(C_{22}+(J_2+C_{22})\cos\varepsilon)\sin\varepsilon}{\sin(i-\varepsilon)}\right] \tag{1.19}$$

MoI from Librations

It is possible to infer the polar MoI of the shell directly from the amplitude of the physical librations in longitude. Also the thickness of the shell itself can be inferred by the following assumptions:

- the core is assumed as fully decoupled from the shell, in order to neglect interaction effects and viscoelastic effects;
- the core and shell are assumed as axially symmetric in order to not contribute to *B-A* term.

In this case the moment of inertia of an ellipsoidal shell of mass δM can be calculated as (Bills and Nimmo, 2008):

$$C_{sh} = \frac{2}{5}\delta MR^2\left(\frac{1-z^3}{1-z^5}\right) \tag{1.20}$$

where z is the correction factor due to the thickness of the shell (h):

$$z = 1 - \frac{h}{R} \tag{1.21}$$

The mass δM of the shell can be expressed by a geometrical approximation as:

$$\delta M = \frac{4}{3}\pi\rho_{sh}R^3\left[1-z^3\right] \tag{1.22}$$

ρ_{sh} is the density of the shell.
It is then possible to relate the MoI of the shell (C_{sh}) to the eccentricity and the libration amplitude:

$$C_{sh} = 24e\frac{C_{22}}{\gamma_0}MR^2 \tag{1.23}$$

The dimensionless polar MoI is then expressed as:

$$c_{sh} = \frac{C_{sh}}{\delta M{R_{sh}}^2} = 24e\frac{C_{22}}{\gamma_0}\frac{M}{\delta M} \tag{1.24}$$

The definition of the c_{sh} can be used to relate the amplitude of the physical librations in longitude to the thickness of the shell:

$$\frac{C_{sh}}{MR^2} = \frac{2}{5}\frac{\rho_{sh}}{\overline{\rho}}\left[1-z^5\right] \tag{1.25}$$

substituting the equations 1.21 and 1.22 into the 1.25, the final expression for h with respect to the libration amplitude γ_0 can be derived:

$$h = R\left[1-\left(1-60\frac{C_{22}}{\gamma_0}\frac{\overline{\rho}}{\rho_{sh}}\right)^{1/5}\right] \tag{1.26}$$

it is possible, for a differentiated body where the quadrupole gravity is known, to correlate the thickness of the outer shell to the amplitude of the librations. If the librations are known, *h* can be directly inferred. For the Titan case the *h* trend with respect to the amplitude of the physical librations in longitude is reported in the Figure 7.

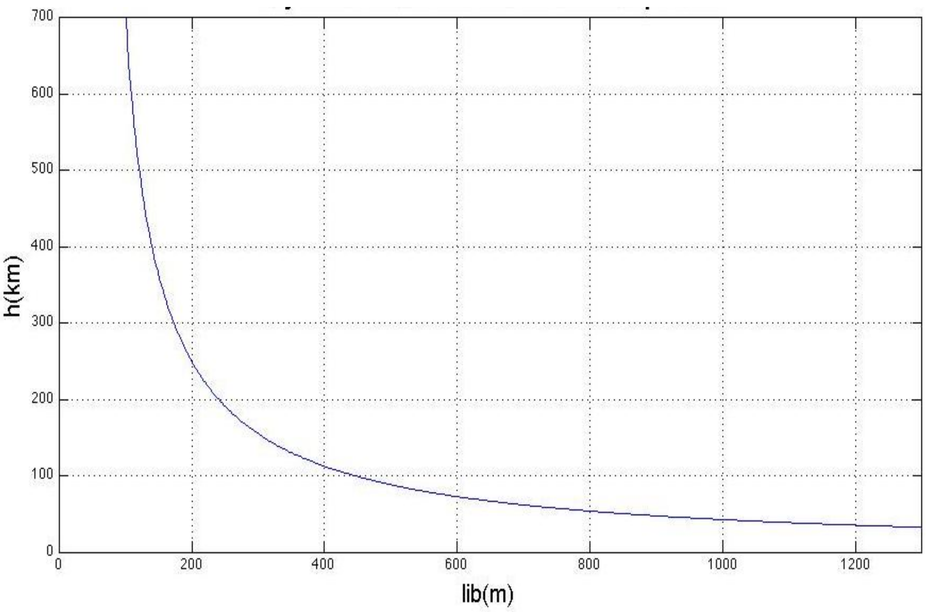

Figure 7 – thickness of the outer shell (h) vs. amplitude of physical librations in longitude computed for Titan case

Chapter II

Rotational Models

The rotational models describe the motion of a celestial body including precession, nutation, libration and (if available) polar motion effects. Any refinement of the model will directly affect the level of accuracy of the georeferencing. For example, the determination of the position of a lander on Mars or the Moon requires a refined rotational model including the polar motion or the libration terms. For the purpose of this work a review of the current rotational models is required, being the determination of the rotational state based on the applied model. The selection of the model depends on the target body, the required accuracy and the scientific goals.

1. Inertial to body-fixed coordinate transformation

The reference frame transformation from a body-fixed vector $\boldsymbol{R}$ to a space-fixed vector $\boldsymbol{r}$ can be computed as:

$$\boldsymbol{R} = M\boldsymbol{r} \qquad (2.0)$$

where M is called the *rotation* or *transformation matrix*. M is representing the transformation from an inertial to a body-fixed reference frame and it depends on the model used to represent the rotation of the body. For convenience we will define as *direct* a transformation from inertial to body-fixed coordinates (IAU model) and as *inverse* a transformation from body-fixed to inertial coordinates (Extended model). Direct transformations are generally applied for georeferencing or data analysis, while inverse transformations are often applied for orbit determination purposes. In this chapter the following models will be presented:

- □ The **IAU model** – the standard model provided by IAU and used to describe the rotation of the celestial bodies. The model is widely adopted for ephemerides kernels, and by orbital determination software. The IAU model takes into account only precession, nutation (not for all bodies) and libration (only for the Moon) effects.

- ☐ The **Extended model** – a new model appositely developed. It is a synthesis and an extension of some models developed for Mars or the Moon. The model includes the polar motion, libration (for the Moon), precession and nutation effects.
- ☐ The **Libration models** – expansion of IAU models including libration effects for other bodies than the Moon.

The reported models stand for all the celestial bodies of the Solar System, presenting slight differences in the formulation for the Moon and some satellites.

1.1. Used reference frames

Specifying the used reference frames is fundamental in order to define the rotation matrices. Used reference frames are reported in Section 2 and 3 in order to present all the occurred coordinate transformations. In particular, the used reference frames are:

Body-Fixed Reference Frames

- True Equator Reference Frame (TERF)
- Instantaneous Equator Reference Frame (IERF)

Space Fixed Reference Frames

- Mean Orbital plane Reference Frame (MORF)
- Earth Mean Equator at J2000 epoch (EMEJ2000)
- International Celestial Reference Frame (ICRF)

Table 1 - Prime Meridian definition for the planets of the Solar System

Planet	Prime Meridian
Mercury	the crater Hun Kal
Venus	the central peak in the crater Ariadne
Earth	Greenwich
Mars	the crater Airy-0
Pluto	the mean sub-Charon meridian

2. Body-fixed reference frames

Body –fixed reference frames are by definition tied to the celestial object. Following IAU definition, for rocky planets, satellites, and asteroids the reference frame is tied to a pre-defined element of the surface (Table 1). For Jupiter, Saturn, Uranus and Neptune it is instead referred to the rotation of their magnetic fields (System III) (Seidelmann et al., 2006).

2.1. True equator of date (TERF)

The *True Equator of Date Reference Frame* (TERF) is the reference frame tied to the surface of the target body. The position of the pole is estimated taking into account precession and nutation effects, but not the polar motion. The XY reference plane is the true equator of date, while the X direction is individuated by the intersection between the prime meridian and the true equator plane. Z axis is orthogonal to the reference plane while Y axis forms with X and Z a right handed coordinate system.

2.2. Instantaneous equator of date (IERF)

The body-centered *Instantaneous Equator-of-Date Reference Frame* (IERF) is the reference frame which expresses the instantaneous position of the body. It is different from TERF because of the polar motion effects (Chandler Wobble, free core nutation), taken into account into the definition of the equator and of X axis. Z axis is orthogonal to the reference plane while Y axis forms with X and Z a right-handed coordinate system.

3. Space – fixed reference frames

Space-fixed reference frames, also called inertial frames, are tied to predefined orbital elements, assumed as not changing along time.

3.1. Mean Orbital plane (MORF)

The *Mean Orbital plane Reference Frame* (MORF) is used to express the inertial coordinates referred to the orbital elements of the target body. The reference plane is the mean orbital plane of the body, and the X direction is the intersection between the mean orbital plane and the Earth Mean Equator at the reference epoch J2000.0. Z axis is the normal to the mean orbital plane while Y axis forms with X and Z a right-handed coordinate system.

3.2. Earth Mean Equator at J2000 epoch (EMEJ2000)

The *Earth Mean Equator at J2000 epoch Reference Frame* (EMEJ2000) is the reference frame commonly used into navigation and data analysis to express the inertial coordinates of a target body (a planet, a satellite, an asteroid). The reference frame is centered into the barycenter of the body (or of the system, in the case of a satellite). The XY reference plane is the Earth Mean Equator at J2000.0 epoch, while X axis direction is the intersection between the Earth mean orbital plane and the Earth mean Equator (EME) at J2000.0 epoch (parallel to the J2000.0 vernal equinox of the Earth). Z axis is orthogonal to the reference plane while Y axis forms with X and Z a right-handed coordinate system.

3.3. International Celestial Reference Frame (ICRF)

The International Celestial Reference Frame (ICRF) is the inertial reference frame centered at the solar system barycenter and defined by the measured positions of 212 extragalactic sources. ICRF is the standard reference frame used to define the positions of the planets (including the Earth) and other astronomical objects.

4. IAU model

The IAU model expresses the transformation from inertial coordinates expressed in the EMEJ2000 reference frame to body-fixed coordinates expressed in the TERF. Therefore the model does not take into account any polar motion effect, and only the pole precession and nutation are included. IAU model is widely adopted for both navigation and data analysis purposes and it is applicable to every body of the solar system (Seidelmann et al., 2006).

4.1. Rotation angles

For each planetary body the north pole is assumed as that pole of rotation that lies on the north side of the invariable plane of the solar system (Seidelmann et al., 2006). The direction of the north pole is specified by the value of its right ascension α_0 and declination δ_0, while the ephemeris position of the prime meridian is expressed by the value of the angle W. α_0 and δ_0 are ICRF equatorial coordinates at epoch J2000.0, while W is estimated as the angle measured easterly along the body true equator between the node Q and the point B (see Fig.1).

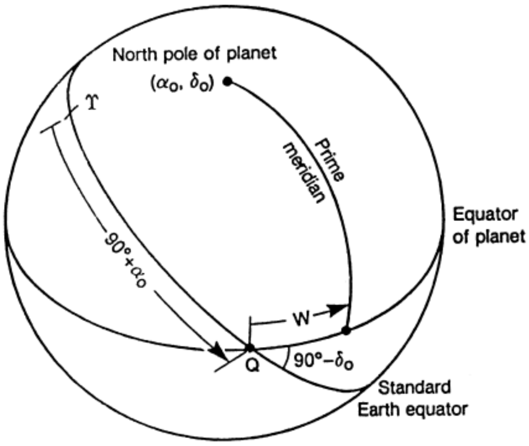

Figure 1 - IAU Rotational model (Seidelmann et al., 2006)

Q is the $\alpha_0 + 90°$ intersection point between the body true equator and the ICRF equator, while B is the intersection point between the prime meridian and the body's equator (Figure 1).

$\dot{W}_0$, also called ω, is the *spin rate*, expressed in units of degrees per day. If W increases with time, the planet has a direct rotation, otherwise, the rotation is said to be *retrograde*. These angles can be expressed as a linear combination of precession and nutation terms. Precession is represented by the first term of the trigonometric series, while the nutation effects are expressed by the $n \geq 2$ terms, as it can be observed in the equation 2.1:

$$\begin{cases} \alpha = \alpha_0 + \dot{\alpha}_0 t + \sum_{i=1}^{n} [S_i^{\alpha} \sin A_i^{\alpha} + C_i^{\alpha} \cos A_i^{\alpha}] \\ \delta = \delta_0 + \dot{\delta}_0 t + \sum_{i=1}^{n} [S_i^{\delta} \sin A_i^{\delta} + C_i^{\delta} \cos A_i^{\delta}] \\ W = W_0 + \dot{W}_0 d + Q t^2 + \sum_{i=1}^{n} [S_i^{W} \sin A_i^{W} + C_i^{W} \cos A_i^{W}] \end{cases} \quad (2.1)$$

where the arguments A_i of the trigonometric series are:

$$\begin{aligned} A_i^{\alpha} &= \gamma_i^{\alpha} + \omega_{IAU,i}^{\alpha} t + \beta_{IAU,i}^{\alpha} t^2 \\ A_i^{\delta} &= \gamma_i^{\delta} + \omega_{IAU,i}^{\delta} t + \beta_{IAU,i}^{\delta} t^2 \\ A_i^{W} &= \gamma_i^{W} + \omega_{IAU,i}^{W} t + \beta_{IAU,i}^{W} t^2 \end{aligned} \quad (2.2)$$

where:

t	Time (Julian centuries - 36525 days)
D	Time (Julian days)
α_0	Center of precession (RA)
δ_0	Center of precession (DEC)
W_0	Prime Meridian at J2000 Epoch
$\dot{\alpha}_0$	time drift of the precession center (RA)
$\dot{\delta}_0$	time drift of the precession center (DEC)
$\dot{W}_0$	Spin Rate (= ω)
C_i^α, S_i^α	Amplitude of the precession - nutation terms (RA)
C_i^δ, S_i^δ	Amplitude of the precession - nutation terms (DEC)
C_i^W, S_i^W	Amplitude of the precession - nutation terms (W)
A_i^α, A_i^δ, A_i^W	Arguments of the precession - nutation terms

All the *0* parameters are meant to be referred to the J2000 reference epoch. For the numerical values of the parameters see (Seidelmann et al., 2006).

4.2. From EMEJ2000 to True Equator of date

The coordinate transformation from a vector $\boldsymbol{r}_{\mathrm{EME}}$, expressed in EMEJ2000 coordinates, to a vector $\boldsymbol{R}_{\mathrm{TE}}$, expressed in TERF coordinates, is performed by a 3-1-3 rotation (eq. 2.3):

$$\mathbf{R}_{TE} = R_z(w)R_x(d)R_z(a)\mathbf{r}_{EME} = M_{IAU}\mathbf{r}_{EME} \tag{2.3}$$

Where M_{IAU} is the transformation matrix for the IAU model and the a, d, w angles are the Euler angles, related to the pole right ascension (α), declination (δ) and to the prime meridian (W) by the eq. 2.4:

$$\begin{cases} a = \dfrac{\pi}{2} + \alpha \\ d = \dfrac{\pi}{2} - \delta \\ w = W \end{cases} \tag{2.4}$$

The formulation of the rotation matrices is reported on eq. 2.5.

$$\begin{cases} \Re_z(w) = \begin{bmatrix} \cos(w) & \sin(w) & 0 \\ -\sin(w) & \cos(w) & 0 \\ 0 & 0 & 1 \end{bmatrix} \\ \Re_x(d) = \begin{bmatrix} 1 & 0 & 0 \\ 0 & \cos(d) & \sin(d) \\ 0 & -\sin(d) & \cos(d) \end{bmatrix} \\ \Re_z(a) = \begin{bmatrix} \cos(a) & \sin(a) & 0 \\ -\sin(a) & \cos(a) & 0 \\ 0 & 0 & 1 \end{bmatrix} \end{cases} \tag{2.5}$$

Following the previous formulation it is possible to express the position vector $\boldsymbol{R}$ in function of the rotational parameters. This will be crucial on the estimate process, where the partial derivatives of $\boldsymbol{R}$ (and consequently M_{IAU}) with respect to the p rotational parameters have to be calculated. The analytical expressions for the derivatives of $\mathrm{M}_{\mathrm{IAU}}$ with respect to each p parameter have been developed and are reported in the Annex A.

5. EXT: the extended model

The *Extended model* (EXT) is a synthesis of current rotation models developed for Mars and the Moon extended to all solar system bodies. Unlike the IAU, the Extended model is used to transform the body-fixed coordinates of a point to the correspondent inertial EMEJ2000 coordinates (*inverse transformation*). This is due to historical reasons, since the models used for reference were initially developed for the radiotracking of the landers on Mars surface (Folkner et al., 1997). In this case the body-fixed position was known with an accuracy of meters or less and the orbit determination process was used to estimate the rotational parameters.

5.1. Coordinate transformation

Passing from TERF to EMEJ2000 coordinates includes three different transformations:

1. from TERF to IERF: polar motion effects are included
2. from IERF to MORF: BF to Inertial transformation
3. from MORF to EMEJ2000: a standard RF is adopted

The correspondent transformation matrices are three: the first from True Equator to the Instantaneous Equator of date (M_1), the second from IERF to the inertial MORF (M_2), and the third from the Mean Orbital plane RF to EMEJ2000 (M_3), as expressed in the eq. 2.6.

$$\boldsymbol{r}_{EME} = M_3 M_2 M_1 \boldsymbol{R}_{TE} = M_{EXT} \boldsymbol{R}_{TE} \tag{2.6}$$

M_{EXT} is the total transformation matrix. Similarly to the IAU case, the derivatives of M_{EXT} with respect to the rotational parameters have been analytically developed and they are reported in the Annex B.

5.2. From TERF to MORF

Since the TERF does not take into account the polar motion effects due to the seasonal redistributions of mass and Chandler wobble, the first transformation to realize is the coordinate transformation to IERF. In the case the polar motion effects were unknown, the TERF to IERF transformation can be neglected assuming IERF = TERF.

For the Earth not considering the polar motion implies an error on the surface varying from 5 to 20 meters. Apart from the Earth, this effect is currently known and determined only for Mars. The polar motion (see Chapter I) can be expressed by a nearly circular motion and a time drift, described by two angles, x_p and y_p. Their analytical expression is:

$$\begin{cases} x_p = \sum_{n=1}^{N} \left[C_{x,n} \cos(2\pi f_n t) + S_{x,n} \sin(2\pi f_n t) \right] + C_{CW,x} \cos(2\pi f_{CW} t) + S_{CW,x} \sin(2\pi f_{CW} t) \\ y_p = \sum_{n=1}^{N} \left[C_{y,n} \cos(2\pi f_n t) + S_{y,n} \sin(2\pi f_n t) \right] + C_{CW,y} \cos(2\pi f_{CW} t) + S_{CW,y} \sin(2\pi f_{CW} t) \end{cases} \tag{ 2.7}$$

where the *n* sinusoidal terms are representing the free core nutations and the CW terms the Chandler's Wobble effects. Consequently the transformation from a vector $\boldsymbol{R}_{TE}$(TERF coordinates) to a vector $\boldsymbol{R}_{IE}$ (IERF coordinates) is a 1-2 rotation:

$$\boldsymbol{R}_{IE} = \Re_y(x_p)\Re_x(y_p)\, \boldsymbol{R}_{TE} = M_1 \boldsymbol{R}_{TE} \tag{2.8}$$

the Y-axis rotation matrix $\Re_y(x_p)$can be written as:

$$\Re_y(x_p) = \begin{bmatrix} \cos(x_p) & 0 & -\sin(x_p) \\ 0 & 1 & 0 \\ \sin(x_p) & 0 & \cos(x_p) \end{bmatrix} \tag{2.9}$$

while the X-axis rotation matrix $\Re_x(y_p)$ is expressed as:

$$\Re_x(y_p) = \begin{bmatrix} 1 & 0 & 0 \\ 0 & \cos(y_p) & \sin(y_p) \\ 0 & -\sin(y_p) & \cos(y_p) \end{bmatrix} \tag{2.10}$$

5.3. From IERF to MORF

The position of a point on the surface, expressed in a body–fixed reference frame (IERF), has to be expressed in inertial coordinates using a space-fixed reference frame. In this case it is physically meaningful to use as reference plane for the inertial reference frame the *mean orbital plane* of the body (MORF). In this transformation the length of day variations and the precession and nutation effects are taken into account. The transformation from IERF to MORF is provided by a 3-1-3 rotation, using the angles:

$\boldsymbol{\phi}$ - position of the instantaneous X_{IE} axis with respect to the ascending node of the Instantaneous Equator (Figure 2). Please notice that irregular changes in ϕ describe the length of day (LOD) variations;

$\boldsymbol{I}$ - inclination of the mean orbital plane with respect to the instantaneous equator of date (obliquity of the body with the opposite sign) (Figure 3);

$\boldsymbol{\psi}$ - longitude (with respect to the mean orbital plane) of the intersection point between the body instantaneous equator plane and the mean orbital plane (Figure 4). The ascending node of instantaneous equator with respect to the mean orbital plane is taken as point of intersection.

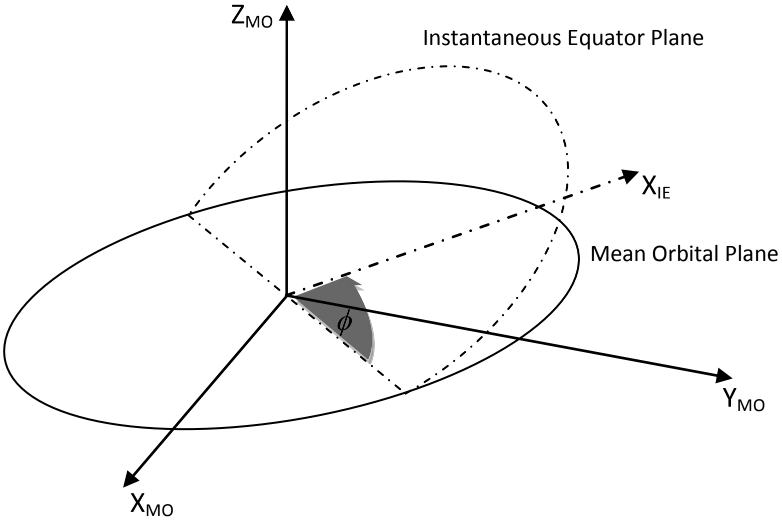

Figure 2 - ϕ angle between the intersection instantaneous equator/mean orbital plane and the X axis of IERF

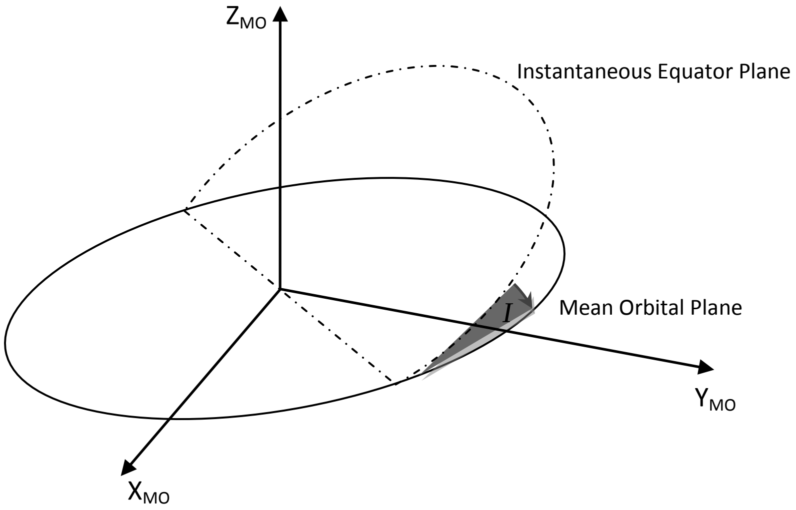

Figure 3 - inclination angle I between the instantaneous equator and the mean orbital plane

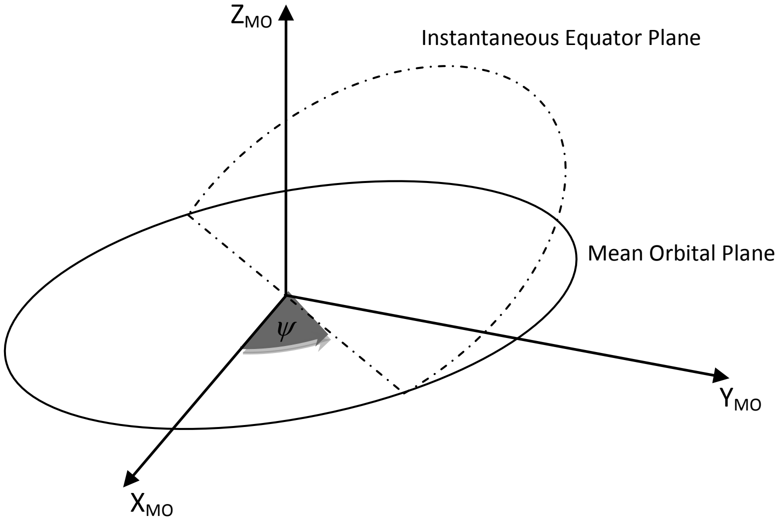

Figure 4 - Longitude of the intersection point between the IERF reference plane and the MORF reference plane

I and ψ describe the precession rates (secular variations) and the nutation motion (periodic variations), while ϕ describes the diurnal sidereal rotation and length of day variations:

$$\left.\begin{aligned}
\phi(t) &= \phi_0 + \dot{\phi_0} t + \sum_{n=1}^{N} \left[C_{\phi,n} \cos\left(\omega_{\phi,n} t\right) + S_{\phi,n} \sin\left(\omega_{\phi,n} t\right)\right] \\
I(t) &= I_0 + \dot{I_0} t + \sum_{n=1}^{N} \left[C_{I,n} \cos\left(\omega_{nut,n} t\right) + S_{I,n} \sin\left(\omega_{nut,n} t\right)\right] \\
\psi(t) &= \psi_0 + \dot{\psi_0} t + \sum_{n=1}^{N} \left[C_{\psi,n} \cos\left(\omega_{nut,n} t\right) + S_{\psi,n} \sin\left(\omega_{nut,n} t\right)\right]
\end{aligned}\right\} \qquad (2.11)$$

In this case, $\dot{\phi_0}$, also indicated as Ω_0 , is the *mean diurnal rotation rate* of the body. The frequency of the sinusoidal terms representing nutation and LOD is modeled as multiple of the natural frequency:

$$\begin{aligned}
\omega_{\phi,n} &= n\,\omega_{\phi,1} \\
\omega_{nut,n} &= n\,\omega_{nut,1}
\end{aligned} \qquad (2.12)$$

Once defined the rotation angles, the transformation from a vector $\boldsymbol{R}_{IE}$, expressed in IERF coordinates, to a vector $\boldsymbol{r}_{MO}$ expressed in MORF coordinates, can be computed as a 3-1-3 rotation:

$$\boldsymbol{r}_{MO} = \Re_z(-\psi)\Re_x(I)\Re_z(-\phi)\,\boldsymbol{R}_{IE} = M_2\,\boldsymbol{R}_{IE} \qquad (2.13)$$

The first rotation is around z axis for an angle - ϕ ; the negative sign is justified by the verse of transformation (from IERF to MORF):

$$\Re_z(-\phi) = \begin{bmatrix} \cos(-\phi) & \sin(-\phi) & 0 \\ -\sin(-\phi) & \cos(-\phi) & 0 \\ 0 & 0 & 1 \end{bmatrix} \qquad (2.14)$$

The second rotation is around x axis of an angle I:

$$\Re_x(I) = \begin{bmatrix} 1 & 0 & 0 \\ 0 & \cos(I) & \sin(I) \\ 0 & -\sin(I) & \cos(I) \end{bmatrix} \qquad (2.15)$$

The third rotation is around z axis of an angle - ψ:

$$\Re_z(-\psi) = \begin{bmatrix} \cos(-\psi) & \sin(-\psi) & 0 \\ -\sin(-\psi) & \cos(-\psi) & 0 \\ 0 & 0 & 1 \end{bmatrix} \qquad (2.16)$$

5.4. From MORF to EMEJ2000

Last transformation from a vector , expressed in MORF coordinates, into a vector , expressed in EMEJ2000 reference frame, requires a 3-1 rotation:

$$\boldsymbol{r}_{EME} = \Re_z(-N)\Re_x(-J)\,\boldsymbol{r}_{MO} = M_3\,\boldsymbol{r}_{MO} \tag{2.17}$$

where:

$$M_3 = \Re_z(-N)\Re_x(-J) \tag{2.18}$$

Only two rotations are required because of the definition of X_{MO}, which is exactly the intersection between the mean orbital plane and the EMEJ2000 vector (Figure 5). The rotation angles are then defined as:

J – inclination of the mean orbital plane of the celestial body with respect to the EMEJ2000 plane;

N – right ascension of the X_{MO} axis with respect to the EMEJ2000 plane; defined positive from X_{EME} axis.

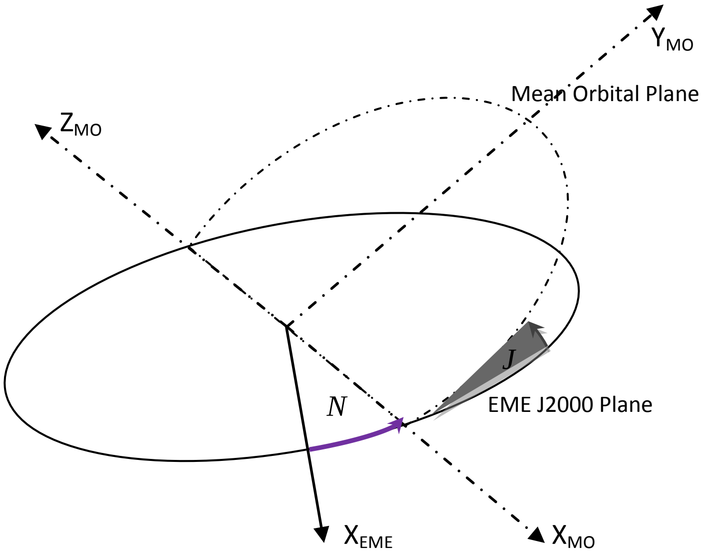

Figure 5 - Inclination J of the mean orbital plane of the body w.r.t. the Earth Mean Equator at J2000 epoch and N angle of line of nodes w.r.t. the vernal direction.

J and N angles are inferred from ephemerides. The relative rotation matrices are defined as:

$$\begin{aligned} \mathfrak{R}_z(-N) &= \begin{bmatrix} \cos(-N) & \sin(-N) & 0 \\ -\sin(-N) & \cos(-N) & 0 \\ 0 & 0 & 1 \end{bmatrix} \\ \mathfrak{R}_x(-J) &= \begin{bmatrix} 1 & 0 & 0 \\ 0 & \cos(-J) & \sin(-J) \\ 0 & -\sin(-J) & \cos(-J) \end{bmatrix} \end{aligned} \tag{2.19}$$

And the complete expression for M_3 is:

$$\begin{aligned} M_3 = \mathfrak{R}_z(-N)\mathfrak{R}_x(-J) &= \\ &= \begin{bmatrix} \cos N & -\sin N \cos J & \sin N \sin J \\ \sin N & \cos N \cos J & -\cos N \sin J \\ 0 & \sin J & \cos J \end{bmatrix} \end{aligned} \tag{2.20}$$

6. Moon EXT model

The model for the Moon is slightly different due to historical reasons and for including librations. In this case the transformation from a vector ($\boldsymbol{R_{TE}}$), initially expressed in lunar TERF coordinates, to a vector ($\boldsymbol{r_{EME}}$) expressed in the EMEJ2000 inertial coordinates, can be defined as:

$$\boldsymbol{r_{EME}} = M_3 M_2 \boldsymbol{R_{TE}} = M_{EXT\_M} \boldsymbol{R_{TE}}$$

where the transformation can be splitted in two distinct phases:

- *BF to Inertial coordinates* - from TERF to MERF (M_2)
- *Passage to standard RF* - from MERF to EMEJ2000 (M_3)

Differently from the other bodies, for historical reasons (e.g. Seidelmann, 2005) the Moon has a dedicated system of reference frames, briefly reported in 6.1 Section. Similarly to IAU and Extended Models, the partial derivatives of M_{EXT_M} with respect to the rotational parameters were analytically developed and they are reported in Annex B.

6.1. The Moon TERF

The definition of the lunar TERF differs from the general reference described in the 2.1 Section because in the Moon case a reference frame coherent with the principal axes of inertia is adopted. The XY reference plane is still the true equator of date, but the X axis direction is identified by the longest axis of inertia (mean direction of the Earth). Z axis is orthogonal to the reference plane while Y axis forms with X and Z a right-handed coordinate system.

6.2. Mean Ecliptic Reference Frame (MERF)

For historical reasons the Mean Ecliptic Reference Frame is used to express the inertial coordinates of a point for the Moon. The XY reference plane is the mean orbital plane of the Earth (Ecliptic) and the X axis direction is the intersection between the Ecliptic and the Earth Mean Equator at J2000.0 epoch (parallel to the J2000.0 vernal equinox of the Earth). The Z axis is orthogonal to the reference plane while Y axis forms with X and Z a right-handed coordinate system.

6.3. From Moon TERF to Mean Ecliptic RF

Similarly to the standard Extended model, the transformation of a vector, expressed in Moon TERF coordinates, into a vector expressed in MERF, consists in a 3-1-3 rotation:

$$M_2 = \mathfrak{R}_z(-\psi)\,\mathfrak{R}_x(\theta)\mathfrak{R}_z(-\phi) \qquad (2.21)$$

where the first rotation around Z axis is:

$$\mathfrak{R}_z(-\phi) = \begin{bmatrix} \cos(-\phi) & \sin(-\phi) & 0 \\ -\sin(-\phi) & \cos(-\phi) & 0 \\ 0 & 0 & 1 \end{bmatrix} \qquad (2.22)$$

the second rotation is around X axis of an angle θ:

$$\mathfrak{R}_x(\theta) = \begin{bmatrix} 1 & 0 & 0 \\ 0 & \cos(\theta) & \sin(\theta) \\ 0 & -\sin(\theta) & \cos(\theta) \end{bmatrix} \qquad (2.23)$$

and finally the third rotation is around z axis of an angle - ψ:

$$\mathfrak{R}_z(-\psi) = \begin{bmatrix} \cos(-\psi) & \sin(-\psi) & 0 \\ -\sin(-\psi) & \cos(-\psi) & 0 \\ 0 & 0 & 1 \end{bmatrix} \qquad (2.24)$$

The three angles ϕ, θ, ψ are so defined (Figure 6):

- ϕ – angle from the descending (w. r. t. the Ecliptic) node N of the lunar equator to the axis X_{TE};
- θ – inclination of the Ecliptic with respect to the lunar equator;
- ψ – longitude (w.r.t. the Ecliptic) of the descending node N of the lunar equator.

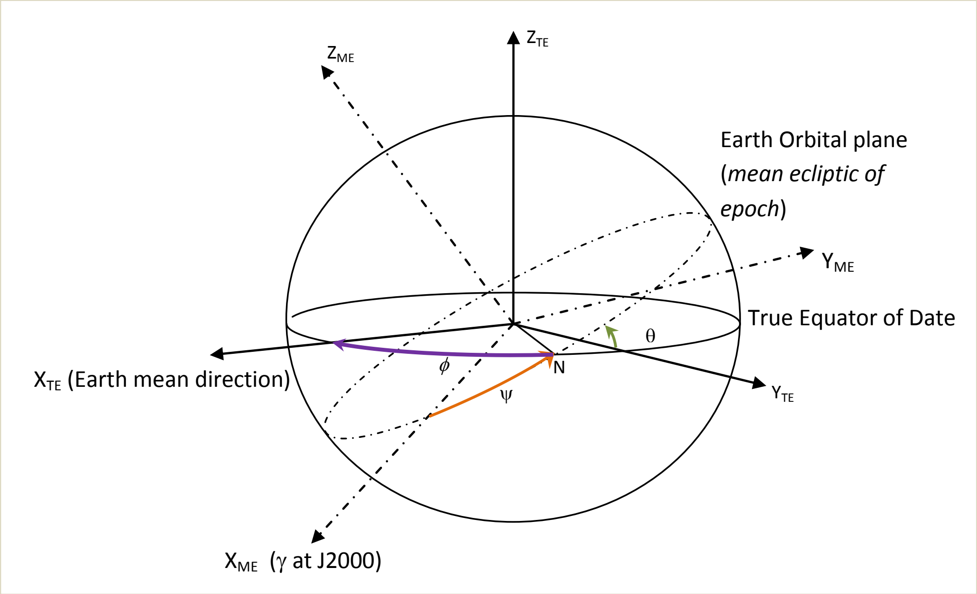

Figure 6 - Moon MERF and TERF, with rotation angles.

These angles can be computed as it follows:

$$\begin{gathered}\theta(t) = I(t) + \rho(t)\\ \psi(t) = \Omega(t) + \sigma(t)\\ \phi(t) = \pi + L(t) - \psi(t) + \tau(t) = \phi_R(t) + \tau(t) - \sigma(t)\end{gathered} \tag{2.25}$$

The angles are formed by regular terms $[(I(t), \Omega(t), \phi(t)]$ which take into account the linear time drift:

$$\begin{gathered}I(t) = I_0 + \dot{I}_0 t\\ \Omega(t) = \psi_0 + \dot{\psi}_0 t\\ \phi_R(t) = \phi_0 + \dot{\phi}_0 t\end{gathered} \tag{2.26}$$

And by the $\rho(t), \sigma(t), \tau(t)$ terms, which describe the libration effects (Figure 7); these angles can be computed by means of sinusoidal terms expressing the libration contribute to the rotation:

Libration in longitude

$$\tau(t) = \tau_1 \sin(M_s) + \tau_2 \sin(M_m) + \tau_3 \sin(2\omega_m) \tag{2.27}$$

Libration in node

$$\begin{aligned}\sigma(t) = {} & \sigma_1 \sin(M_m) + \sigma_2 \sin(M_m + 2\omega_m)\\ & + \sigma_3 \sin(2M_m + 2\omega_m)\end{aligned} \tag{2.28}$$

Libration in inclination

$$\rho(t) = \rho_1 \cos(M_m) + \rho_2 \cos(M_m + 2\omega_m) + \rho_3 \cos(2M_m + 2\omega_m) \tag{2.29}$$

where:

M_s – mean anomaly of the apparent orbit of the Sun w.r.t. the Moon

M_m – mean anomaly of the Moon on its orbit around the Earth

ω_m – argument of the Moon's perigee

6.4. From MERF to EME J2000

For the transformation of a vector, expressed in MERF coordinates, into a vector expressed in EMEJ2000 reference frame only one rotation is necessary:

$$M_3 = \Re_x(-\varepsilon) \tag{2.30}$$

where ε is Earth obliquity, assumed as known and retrieved by the planetary ephemerides.

$$\Re_x(-\varepsilon) = \begin{bmatrix} 1 & 0 & 0 \\ 0 & \cos(\varepsilon) & -\sin(\varepsilon) \\ 0 & \sin(\varepsilon) & \cos(\varepsilon) \end{bmatrix} \tag{2.31}$$

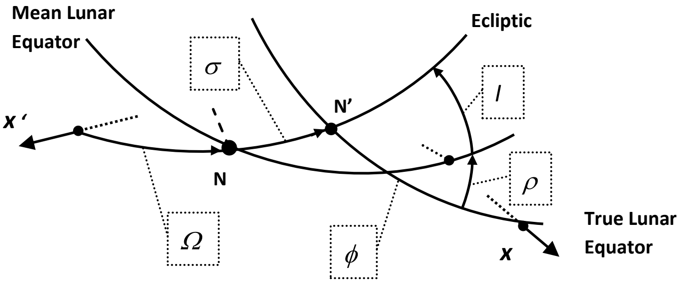

Figure 7 - rotation angles of the Moon Extended Model

7. Libration models

Excluding the Moon, the libration effects are not taken into account into the previous models. This is mainly due to the fact that for several bodies the libration effects are largely unknown. Nevertheless, in the last years several deep space missions or new measurement methods (Margot et al., 2007) increased our knowledge of the rotational state for the relative target bodies, and finally it has been possible to include or try to estimate these effects for other bodies than the Moon.

A modified IAU model including libration terms, valid for every solar system body, is here presented. This model was used for the estimate of the rotational state of Titan from the Cassini data. For Mercury the Margot (2009) model was used as a reference, since this includes the most recent estimates of the libration terms and redefines the prime meridian in order to correct some inconsistencies.

7.1. IAU Modified model

In order to extend the validity of the IAU model and to estimate the amplitude of the physical librations in longitude, an expansion for IAU model is here presented, formerly named the IAU Modified model. The general formulation, coordinate transformation and the rotation matrices included, is the same expressed for the IAU (see Section 4), but the expression for the prime meridian W includes also a term describing the librations in longitude:

$$\begin{cases} \alpha = \alpha_0 + \dot{\alpha}_0 t + \sum_{i=1}^{n} \left[S_i^{\alpha} \sin A_i^{\alpha} + C_i^{\alpha} \cos A_i^{\alpha} \right] \\ \delta = \delta_0 + \dot{\delta}_0 t + \sum_{i=1}^{n} \left[S_i^{\delta} \sin A_i^{\delta} + C_i^{\delta} \cos A_i^{\delta} \right] \\ W = W_0 + \dot{W}_0 d + Q t^2 + \gamma_0 \sin M + \sum_{i=1}^{n} \left[S_i^{W} \sin A_i^{W} + C_i^{W} \cos A_i^{W} \right] \end{cases} \tag{2.32}$$

where the contribute of librations in longitude is referred only to the major perturbing body; γ_0 represents the amplitude for librations in longitude and M is the mean anomaly of the body, computed as:

$$M = n(t - t_0) \tag{2.33}$$

where n is the mean motion and t_0 is the epoch of the passage at the pericenter. The model is not very different from the model developed by Margot (2009) for Mercury.

Since the IAU Modified Model is a linear expansion of the original IAU model, the partial derivatives of $\boldsymbol{R}$ (and consequently M_{IAU}) with respect to the p rotational parameters are coincident with those computed for IAU, with the exception of the libration term, whose partial derivative was analytically calculated and it is reported in the Annex A.

7.2. Margot model of Mercury

(Margot, 2009) proposed an updated rotational model for Mercury including the most recent radar observations (Margot et al., 2007). The updating of the rotation model can be considered necessary in order to improve significantly the level of accuracy. Not considering libration effects for Mercury can imply a positioning error of 0.01° in longitude, or ~ 425 m at the equator. The prime meridian was recomputed as the intersection between the Mercury's equator and the ICRF equator, (W_0 = 329.75°). This value significantly differs from the actual IAU value of 329.548° (Seidelmann et al., 2006), corresponding to the Hun Kal crater, implying a prime meridian 8 km in longitude away from the long axis, with relevant implications not only for georeferencing, but also, for example, for all the gravity spherical harmonic expansions. Coordinate transformation and rotation matrices are also in this case coincident with the general IAU formulation, only the expression for the prime meridian W is modified:

$$\begin{cases} \alpha = 281.0097° - 0.0328°/JC\ t \\ \delta = 61.4143° - 0.0049°/JC\ t \\ W = 329.75° + 6.1385025°/day\ d + +\sum_{i=1}^{5}[\gamma_i \sin M_i] \end{cases} \tag{2.34}$$

where the libration terms ($\gamma_i \sin M_i$) are expressed by a trigonometric series whose amplitude and frequency are reported in the Table 2.

Table 2 – coefficients of the rotational model of Mercury (Margot et al., 2009)

i	γ	***M***
1	0.00993822°	174.791086° + 4.092335°/day *d*
2	-0.00104581°	349.582171° + 8.184670°/day *d*
3	-0.00010280°	164.373257° + 12.277005°/day *d*
4	-0.00002364°	339.164343° + 16.369340°/day *d*
5	-0.00000532°	153.955429° + 20.461675°/day *d*

Chapter III

Observing The Planetary Rotation: Applied Techniques

The rotational state of a body can be estimated by several techniques. Until the first years of 1900 the Earth rotation was estimated using optical astrometric measurements, replaced in 1960's by more accurate VLBI and laser ranging techniques. For the Moon, the laser ranging technique provided very accurate values of body position and rotation (Seidelmann, 2005). Doppler and range measurements of a lander as well as of a probe can be used for the estimation of the rotational parameters as a part of the global fit. For Mars the lander radiotracking from Pathfinder and Viking missions provided relevant information on the rotational state, the polar motion and other effects (Faulkner et al., 1997). For the other bodies of the Solar System the rotational state is unfortunately less well determined. Earth-based radar measurements are currently used for the observation of several bodies, including Mercury, Venus and the Jovian satellites. Recently a new approach developed by (Margot et al., 2007) permitted to reach a high level of accuracy in the case of Mercury. In the case of Venus Davies et al. (1992) proposed the image-based technique, subsequently applied to Titan in the Cassini mission (Stiles et al., 2008). The most used techniques are here reviewed, with a special attention to the reached level of accuracy for each methodology.

1. Observing Earth’s rotation

From 1700 up today several optical astrometric observations were used to determine the rotational state of the Earth. They are listed in the Table 1 with the relative characteristics. Following (Seidelmann, 2005) the methods can be distinguished into two categories: historical and currently applied methods.

1.1. Historical methods

The first technique to be developed was based on the observations of the apparent motion of the stars to estimate the Earth rotation. Since the XVIII century the optical astrometric observations were used to estimate the position of the rotation axis and the spin rate in terms of length of the day. This method is still currently used for comparison with most recent and accurate measurements derived from other methods. Similar to astrometric observations was the Connected-element Radio Interferometry, subsequently substituted by VLBI.

More recent methods include the Doppler radiotracking of satellites and GPS. By the first the position of the satellite and the rotational parameters are determined in a global fit, with an accuracy of few milli-arcseconds. Similarly, the GPS technique makes use of the known positions of a satellite constellation to estimate the position (and the relative variations) of the pole location. Main characteristics of the historical methods are reported in Table 1.

Table 1 - review of the historical methods used to determine Earth's rotation

Technique	Network	Advantages	Disadvantages
Optical Astrometric Observations	100 Optical instruments	Backup on space geodetic techniques	Dependence on the local vertical and the accuracy of the star catalogs
Doppler Satellite Tracking	Variable	Increased accuracy	Dependence from long term drifts
Connected-Element Radio Interferometry	No more	Backup on space geodetic techniques	Substituted by VLBI

1.2. Current methods

Laser Ranging

The laser ranging of a celestial target, first proposed for the Moon in the late '50s and early '60s, is conceptually a very simple observational procedure. A laser beam is directed to a celestial target carrying retroreflectors, such as the Moon or an artificial satellite. Half the round-trip travel time of the light multiplied by the velocity of light gives the distance to the object (subject to the various corrections due to relative motion, refraction, and other effects). These ranges can be compared to their predicted values, and in an adjustment (weighted least squares procedure) the corrections to the involved parameters may be estimated. The considered parameters are the orbital parameters, the position of the station, and the orientation of the Earth.

Actually several satellites are available for laser ranging, but the Laser Geodynamics Satellite (LAGEOS) currently provide the highest accuracy values for the mentioned parameters. LAGEOS is a composite (aluminum shell and brass core) sphere, 60 cm in diameter and with a mass of 407 kg, with 426 (3.8 cm) cube corner retroreflectors embedded in its surface. It is in a nearly circular orbit of about 5900 km (for low atmospheric drag) and an inclination of 109.8°. For its characteristics it is not sensible to short wavelength components of the Earth's gravity field. On Earth, a net of 25 SLR stations regularly obtains observational data, with a precision for the range varying from 1 to 15 cm. Results for Earth rotation are computed at 3-day intervals using data less than a week old, with polar motion accurate to a few milliseconds of arc (Seidelmann, 2005).

Similarly to satellite laser ranging, the lunar laser ranging , with 4 -5 station network, ranging regularly with 3 cm range accuracy. The polar motion is determined with an accuracy of 1.6 mas. The rotational state of the Moon is determined with similar accuracies.

VLBI

In geodetic Very Long Baseline Interferometry (VLBI) a set of extragalactic radio sources is observed in order to determine the Earth rotation. These objects are presumably so distant that their motion is not detectable, forming therefore a fixed celestial reference frame. Currently, 228 sources have positions established within such a system, but only about 74 objects have been observed from more than one network. The VLBI observing networks consist of two to generally four or five radio telescopes that simultaneously track extragalactic radio sources. Each station records X and S band radio signals in digital form on magnetic tape, along with precise time signals provided by hydrogen-maser frequency standards. Typically, 10 to 20 sources are tracked for periods of 3 to 6 minutes several times over the course of a 24-hour observing session. The differences in arrival times of the radio source signals (delays) and their differences in time (delay rates) are determined between each pair of stations. Similar to laser ranging solutions these delays and delay rates are then used in a least squares adjustment in order to estimate a variety of geophysical parameters and the coordinates of the radio sources. Polar motion, nutation and precession corrections have been estimated with an accuracy of ± 1-2 mas.

2. Earth-based radar techniques

In absence of dedicated space missions, Earth-based radar techniques are the first method used to determine the rotational state of the celestial bodies (Ostro, 1999). Derived measurements are then used as a starting point for dedicated on-board experiments or more refined Earth-based techniques, as interferometry.

Radar is a powerful technique which provided otherwise unavailable information about the solar system bodies for three decades. The advantages of radar using in planetary astronomy result from the ability of radar to resolve objects spatially via measurements of the distribution of echo power in time delay and Doppler frequency, and, among other things, the pronounced degree to which delay-Doppler measurements constrain orbits and spin vectors (Ostro, 1999). In addition to providing a wealth of information about the geological and dynamical properties of asteroids, comets, the inner planets, and natural satellites, radar experiments have established the scale of the solar system and contributed significantly to the accuracy of planetary ephemerides.

In principle, echo bandwidth measurements obtained from a sufficiently wide variety of target directions can yield all three scalar components of the spin vector $\boldsymbol{\omega}_S$. This capability derives from the definition of the apparent spin vector $\boldsymbol{\omega}$ as

$$\boldsymbol{\omega} = \boldsymbol{\omega}_s + \boldsymbol{\omega}_0 = \boldsymbol{\omega}_s + \dot{\boldsymbol{e}} \times \boldsymbol{e} \tag{3.1}$$

arising from the changing direction of the target-to-radar unit vector $\boldsymbol{e}$**.** Variations in $\boldsymbol{e}$ and $\dot{\boldsymbol{e}}$, all of which are known, lead to different values of $\boldsymbol{\omega}$ and to the subsequent determination of $\boldsymbol{\omega}_S$. In practice, this process is SNR limited and is coupled to estimation of the target's size, shape, and surface characteristics.For Mercury and Venus, high SNRs are available and size and shape have long been well known (Ostro, 1999).

If compact surface features are prominent in the radar images then observations of their delay-Doppler trajectories provide especially powerful leverage for spin vector refinement.

Table 2 - Solutions for the rotation period and the direction of the spin axis of Venus derived from Earth-Based Radar observations

Period (days)	Right Ascension (deg)	Declination (deg)	Reference
243.026 ± 0.006	272.73 ± 0.09	67.11 ± 0.09	Shapiro et al., 1990
243.022 ± 0.003	272.794 ± 0.14	67.232 ± 0.05	Slade et al., 1990

Analysis of data accumulated over many apparitions leads to the estimate of ω, in part by eliminating certain systematic effects. These various approaches led to the first accurate determinations of the rotations for Venus (Table 2) and Mercury in the '60s and to improved results since then, as telescope sensitivity has increased.

Also the observations of radar speckle patterns can be used to determine the rotational state (Margot et al., 2007). Target body is illuminated by a monochromatic radio signal (for Mercury, λ = 3.5 cm) from transmitting station while echoes are recorded by two distinct receiving stations.

The radar echoes from a solid planet exhibit an irregular wavefront (speckle) generated by the interferences of waves scattered by the irregular surface of the target body. Because of the rotation of the body, the speckles will sweep over the receiving station and give rise to fluctuations of the signal with time (Figure 1). Because the speckles are tied to the rotation of the planet, the time lag δt (~10 sec for Mercury) obtained by cross-correlating the two signals yields a direct measurement of the instantaneous spin rate. Then the cross-correlation of the echoes is performed.

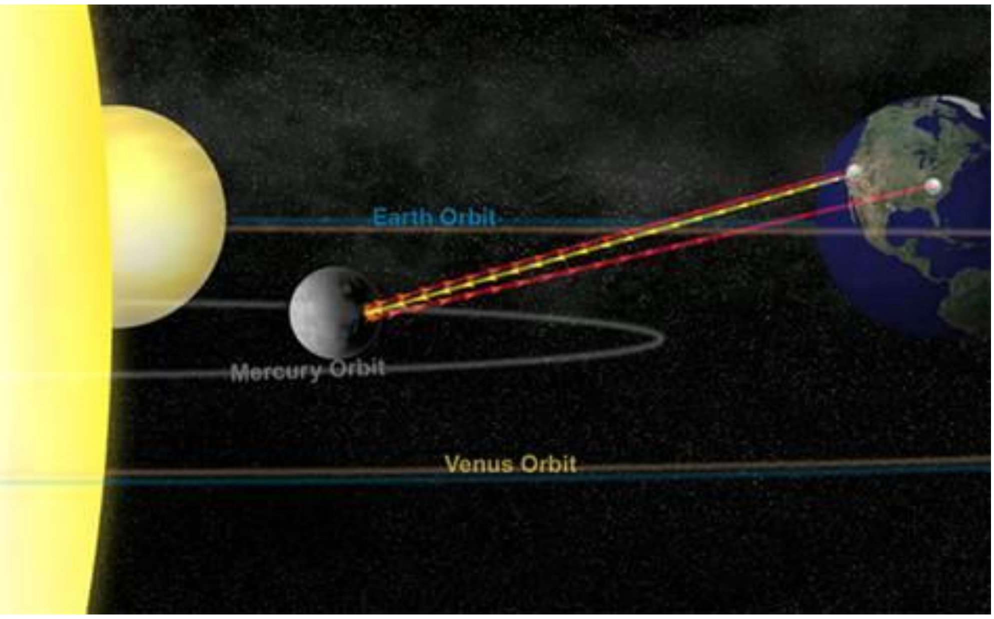

Figure 1 - representation of the Earth-Based radar observations of Mercury (NASA)

A substantial requirement is that both receiving stations must record similar speckle patterns to produce a large correlation, occurring only when the antenna baseline is parallel (ε_T = 0°) to the trajectory of the speckles, as it can be inferred by (Green, 1968):

$$|\delta \boldsymbol{x}| = 2r\omega_s \cos(\varepsilon_T)\, \delta t_{max} \tag{3.2}$$

where $\delta\boldsymbol{x}$ is the orientation of the baseline, r is the range to the target body, $\boldsymbol{\omega}_s$ the sidereal spin rate and ε_T the tilt of the spin vector from perpendicularity with the line of sight. For Mercury (Margot et al., 2007) an uncertainty of 0.1 arc min has been measured for the obliquity and 2 arcsec for the librations amplitude.

3. Lander radiotracking

Another intriguing possibility to determinate the rotational state of a body is the estimation of the rotational parameters by the radiotracking measurements of a lander. (Folkner et al., 1997) applied successfully for the first time this technique to the Pathfinder mission to Mars.

In the experiment the Pathfinder tracking data (July - September 1997) were used in combination with tracking data from the Viking landers (1976 - 1982), including 2 years of Doppler data from the Viking I lander, not included in previous analyses. Due to the large time interval occurred between Viking and Pathfinder missions, the precession motion of the pole of Mars could be easily estimated, in spite of the relatively short span of the Pathfinder data. The Pathfinder and Viking lander tracking measurements were subsequently analyzed to solve for Mars rotation and orbit parameters.

Table 3 - Rotational Parameters Estimation for Mars by Pathfinder and Viking lander radiotracking (Folkner et al., 1997)

Parameter	Value
α_0 (deg)	317.68143 ± 1E-05
$\dot{\alpha}_0$ (deg/JC)	20.1061 ± 7E-04
δ_0 (deg)	52.88650 ± 3E-05
$\dot{\delta}_0$ (deg/JC)	20.0609 ± 4E-04
ω (deg/day)	350.89198226 ± 8E-08

Because the Pathfinder radio system operated at a higher frequency (X band - 8 GHz) than the Viking lander radio systems S-band (2 GHz), the Doppler data are much less affected by fluctuating charged particles in the solar system and in Earth’s ionosphere. Consequently, the Pathfinder Doppler data are affected by a noise about 13 times less than the Viking data, with a value of 0.05 mm/s for data at 60-s intervals.

The solar plasma also affects the round-trip range measurements. Calibrations for the solar plasma for some of the Viking lander data were determined from dual-frequency observations of the Viking orbiters. The Viking ranging data have a residual noise of ~7 m for data with orbiter calibrations and ~ 12 m for data with no orbiter calibrations, against residuals of ~ 3 m of the Pathfinder ranging data. With this technique the obliquity ε of Mars was estimated equal to 25.189417 ± 35E-06 (°) . Obliquity rate was also estimated equal to 1 ± 16 mas/year. The estimate of the rotational parameters is reported in Table 3.

4. Imaging from orbit

Imaging from orbit technique is based on multiple optical or radar observations of the surface of a target body (Figure 2). Georeferenced images of the same area, taken at different times, are compared. If the rotational model used for georeferencing differs from the true model, an apparent shift (*registration error*) can be observed. The rotational parameters are then inferred from the reduction of the registration error by a least squares fit. The geometry of the observations and the mission profile (probe or orbiter) deeply influence the number and the distribution of the observed overlaps. The technique was first developed for the Magellan mission to Venus by (Davies et al., 1992) and subsequently used with a different approach by (Stiles et al., 2008) for a first determination of the rotational state of Titan for the Cassini mission.

In this case several areas are observed twice or more and the crossovers of the images taken at different times are detected. For each crossover at least one tiepoint is selected and the correspondent radar burst is identified.

At the same time, the spacecraft state position and velocity are inferred from the orbit determination process. Subsequently the inertial coordinates of each tiepoint are computed at the appropriate burst time. At this point, two different approaches can be followed, depending on the used observables.

In the first case, the range and Doppler observables are inferred from the inertial coordinates along with the spacecraft ephemerides. The residuals are computed as the difference between the measured and computed coordinates of each tiepoint. The computed coordinates are derived using the range and Doppler resampling coefficients for each burst.

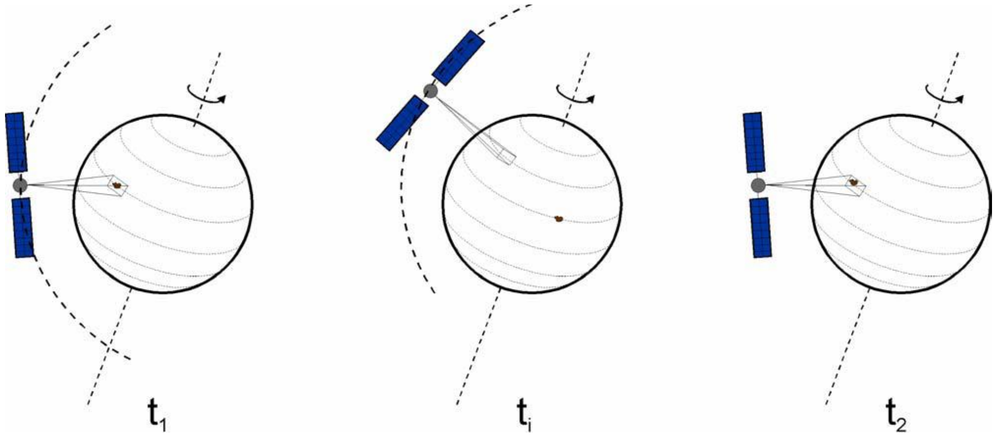

Figure 2 - Imaging from orbit technique

The observables are then combined in a least squares algorithm that minimizes the sum of the squares of the residuals. The computation of the derivatives and the definition of the free parameters is depending on the adopted model. Davies et al. (1992) considered as free parameters the latitude, longitude, and radius of the tiepoints, the right ascension and declination of the pole and the rotation period of Venus, and the Keplerian orbital elements. The precision of the solution significantly depends on the accuracy of the spacecraft ephemeris.

In the second approach the optical observables, intended as the misregistration vectors inferred from the pattern matching of the images, are used. Similarly to the first case the observables are combined in a least squares algorithm minimizing the residuals. As free parameters Stiles et al. (2008) directly estimated the pole location and the spin rate for Titan. As a primary goal of the present work, this approach is reviewed in detail in the Chapter IV.

5. Compared accuracy

Different levels of accuracy for the estimation of the rotational parameters are provided depending on the applied methodology and the specific experiment. It should be taken into account that the accuracy of the measurement is strictly dependent on the accuracy of the spacecraft (orbiter or lander) ephemerides for most of the reported techniques. Several error sources can occur depending on the method and the mission, and the reported accuracy is relative to the specific experiment. A general review of the reached level of accuracy for each technique and/or experiment is reported on Table 4.

Table 4 – comparison of the accuracy obtained for each technique

Methodology	Target	Pole direction Accuracy	Reference
GPS	Earth	3 - 5 mas	Seidelmann, 2006
Laser Ranging	Earth	1 -3 mas	Seidelmann, 2006
	Moon	1.6 mas	Seidelmann, 2006
VLBI	Earth	1 – 2 mas	Seidelmann, 2006
Lander Radiotracking	Mars (Pathfinder)	126 mas	Folkner et al. 1997
Earth-Based Radar	Mercury	6 as	Margot et al., 2007
Imaging from Orbit	Venus (Magellan)	36 as	Davies et al., 1992

Chapter IV

The Imaging From Orbit Technique

The imaging from orbit technique makes use of optical observables to determine the rotational state of a body. Since several missions include a repetitive imaging of the target body, this method can be successfully applied in several cases. The application of the technique can significantly differ depending on the orbit geometry (orbiter or probe), the imaging type (optical or radar), the coverage and the available data volume.
The technique can be divided into three phases:

1. Georeferenced images taken at different times are compared and crossover areas are detected.
2. The crossover areas are matched by different algorithms and the relative registration error is computed. For each crossover a misregistration vector is computed.
3. The misregistration vectors are minimized by a least squares fit, estimating the rotational parameters.

In this chapter the general procedure for the application of the technique is reported, with specific references to the Cassini and BepiColombo missions.

1. Crossover identification

The identification of the crossover areas can be performed with different approaches, depending basically on the available image georeferencing, trajectory and data volume.

1.1. Geometry of the observations

Orbiter
In the case of an orbiter the detection of the crossovers is constrained by the repetitive geometry of the optical/radar observations and the relevant data volume. In this case it is convenient to infer the number and the location of the crossover areas from the ground tracks, the spacecraft trajectory and the camera (or radar) resolution.
The surface of the target body is gridded and for each element the number of passages is computed. Grid dimensions depend on the image resolution. Subsequently all the georeferenced images including a specific crossover area are selected and correlated, generating the correspondent

misregistration vector. This is the procedure actually used for the rotation experiment simulator of BepiColombo mission (Tortora et al., 2011), developed in order to process a relevant data volume.

Fly-bys

If the target body is observed by dedicated fly-bys, the detection of the crossovers is constrained by a different geometry for each fly-by and a reduced data volume. In this case the crossovers are directly inferred from the georeferenced images. For each image the center-track is computed and all the center-tracks are compared in order to detect the intersection points. A crossover is detected where the distance between two points from different center-tracks is minor than a threshold value, depending on the wideness of the optical/radar strip at the surface. This is the method currently applied in the case of Cassini SAR images of Titan. This method can easily be applied in the case of a flyby, with a reduced number of observations; in the case of an orbiter it is not convenient because of the high number of observations.

Often a different cartographic projection is used for each fly-by. In this case the images have to be converted to a common geographical projection in order to allow the cross-over identification and the pattern matching. The analyzed images can also include areas (*dark areas*) without any content because of the image rendering or, more rarely, to data loss. A dark area cross-over can occur very frequently for a flyby operative scenery. For the Cassini analysis we found that ~ 16% of the cross-over number are dark area crossovers.

1.2. Cross-over classification

Crossovers can also be classified into two distinct typologies, named respectively intersections and parallel cross-over.

Intersections

Intersections are the dominant typology in the case of a fly-by scenery, where the coverage is strongly dependant from the orbit geometry. For the Cassini Extended Mission, the 65.5% of crossovers are intersections. They are defined as cross-over areas where the angle between the center tracks is $\neq 0°$ (Figure 1). Intersections are very relevant for the selection of the pattern matching algorithm because the same area is observed from different lines-of-sight. This is a critical point for optical images, where the shadow effects can have a strong impact on pattern matching results.

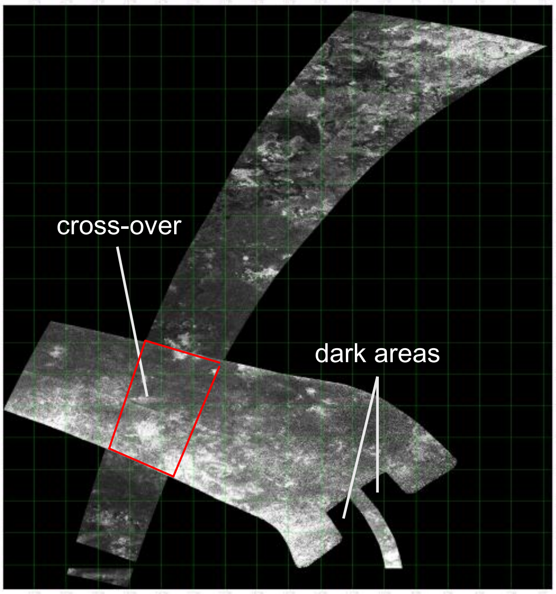

Figure 1 - Intersection between two Cassini SAR images of Titan

Parallel Crossings

Parallel crossings are a very common case for observations from an orbiter, while they are more infrequent in a fly-by scenery. They are defined as an image overlapping where the angle between the center tracks is null. Parallel crossings represent an ideal case for pattern matching, because the effects due to different lines of sight are neglected.

2. Feature classification

For each detected crossover area evident features (landmarks) on the surface are identified. For each landmark a Region-of- Interest (ROI) is retailed from the original image. ROIs observed at different times are then matched to determine the registration error. As it can be observed, in this case the definition of “evident” is an hard matter of discussion. How should it be an “evident” feature? In the absence of pre-determined targets, the definition of “evident” is dependent on the used pattern matching algorithm. Morphological features (craters, rivers, lakes, ridges) are optimal for a visual detection and also for cross-correlation, but not for more refined algorithms; SIFT/SURF features are not recognizable from the human eye. Following this assumption, two different approaches can be applied. The first lies in the selection of a specific type of features depending on the pattern matching algorithm to apply. This is the procedure adopted in the Titan rotation experiment of the Cassini mission. Morphological features were identified from SAR imaging and subsequently 2D cross-correlated.

A second, more complex, approach can be followed. Different types of features can be selected and the optimal pattern matching algorithm for each type is applied. This is the approach adopted by the MORE Team for the BepiColombo mission and the Mercury rotation experiment (see Chapter VIII). Before describing the different pattern matching algorithms, a feature classification is here briefly reported.

- *Morphological features* - craters, lakes, rivers, ridges can be easily observed from both radar and optical instruments (Figure 2). This kind of feature is easy to observe but difficult to correlate: in the case of craters and ridges the image registration may be heavily affected by line-of-sight and shadow effects. Lakes and rivers may be subjected to seasonal variations significantly affecting the pattern matching. Their distribution on the celestial body is generally known. In the case of optical imaging the difference between the phase angles (sun lighting angles) assumes a relevant role: for Mercury craters, only phase angle differences smaller than 35° can provide sub-pixel accuracies (Jorda, 2000).

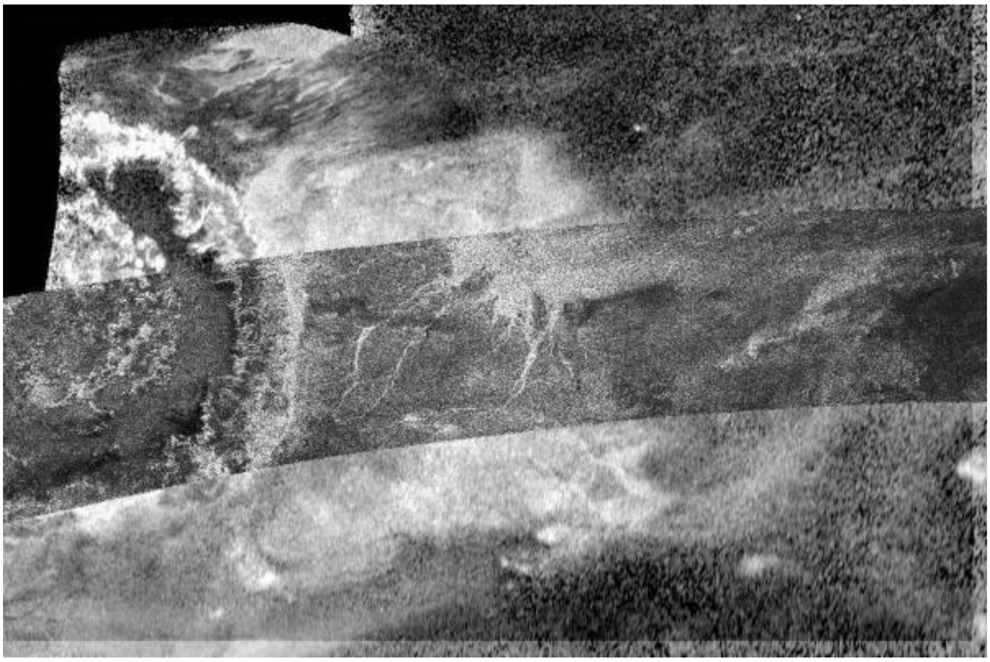

Figure 2 – Cassini SAR image of Titan: Menrva crater (left) and a channel system (right) can be observed (NASA – JPL).

Figure 3 – Mercury: an albedo feature observed from Mariner 10 (NASA - JPL)

- *Albedo features* – areas characterized by a strong contrast in brightness with respect to the adiacent areas (Figure 3). Their brightness depends on the phase angle and, for Mercury, they can reveal the presence of regolith (dust and remains of rocks that cover the planet surface). Albedo features have been considered *"the best candidates to satisfy the required characteristics of a landmark"* because *"their specular reflectivity is very high, allowing them to be slightly influenced by different sun illumination conditions and to present often a low shadowing level"* (Iess et al., 2000). In the case of Mercury, pattern matching can be effected with phase angles more than 10° and less than 70°; it has been also demonstrated (Jorda, 2000) that only phase angles more than 5° and less than 55° can be considered for a sub-pixel accuracy, because of the low contrast on the images for small values and long shadows on the spots for large values. Nevertheless the wide dimensions of albedo features make their use unfeasible for small FOV cameras (as in the case of BepiColombo – SIMBYOSIS).

- *SIFT/SURF features* –points of the image not affected by shadow effects (Figure 4). They are detected using SIFT/SURF tracking algorithm (Gordon, 2004). They can be used in order to reach sub-pixel accuracies for images with an adequate SNR.

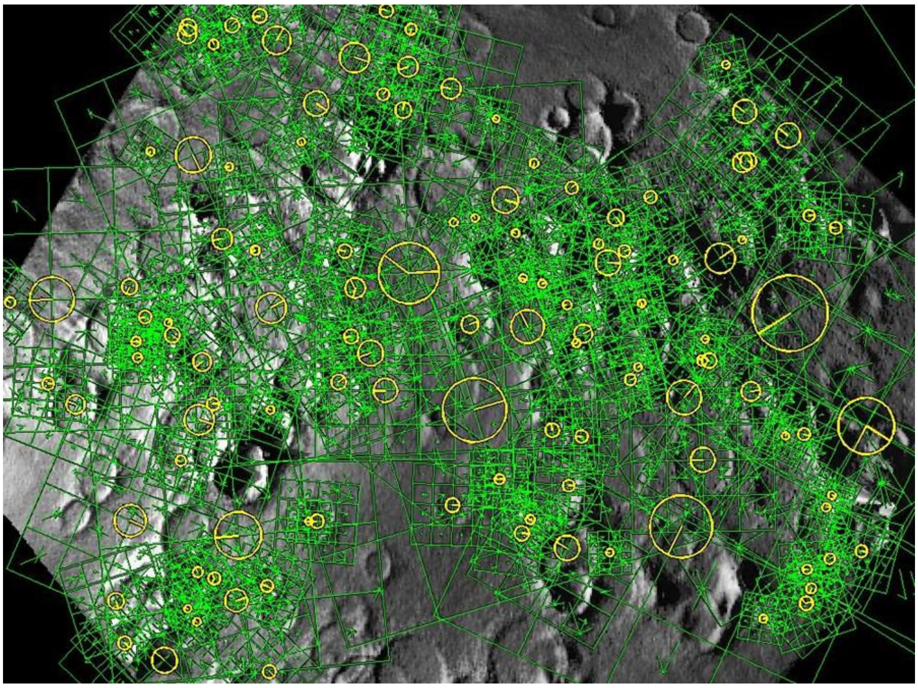

Figure 4 - SIFT features (highlighted in green) in a simulated image of Mercury (Alma Mater Studiorum - Bologna University)

3. Pattern matching

Pattern matching is performed in order to obtain the shift between the observed images for each selected landmark. From the shift the registration error is computed by means of georeferencing. Here it follows a brief review of all the pattern matching algorithms used or test in the present analysis.

Visual Detection

First to be applied, and most common method, it consists into the visual (and manual) detection of evident surface features. It can be applied in the processing of radar images (no shadow effects) and for a limited number of images to be analyzed. It is the method currently used by JPL/USGS for the detection and the correlation of features on the Titan surface (Stiles et al., 2008). The advantages are the possibility to check every step of the identification procedure, while the disadvantages are the dependence on the operator and the impossibility to analyze a significant data volume.

SIFT tracking

In this case some stable natural features are generated from a starting image using the Scale Invariant Feature Transform (SIFT) algorithm, in order to improve the pattern matching process. These features act as descriptors of local image patches: “*They are invariant to image scaling and rotation, and partially invariant to changes in illumination and viewpoint. The distinctiveness of SIFT features, as well as their abundant presence over a large range of image scales, make them suitable for recognition in cluttered and dynamic settings. Feature matching can be performed efficiently*.” (Gordon, 2004). The algorithm can be resumed in three steps:

1. The features are matched to the SIFT feature database obtained from a set of training images. This feature matching is done through a Euclidean-distance based, nearest neighbor approach.
2. All features derived from the same object are clustered in order to increase the robustness to object identification, rejecting the matches left out in the clustering process. This will identify clusters of features that vote for the same object pose in order to increase the probability of a correct interpretation.
3. For each candidate cluster, a least-squares solution for the best estimated affine projection parameters relating the training image to the input image is obtained.

SIFT tracking is a method mostly applied to optical images, it is best suited for high differences in altitude, changes in sun elevations and very limited changes in azimuth. It is independent from morphological features (a critical point of the optical images when changes into the illumination conditions occur) and allows to reach sub-pixel accuracy (Tortora et al., 2011). For the BepiColombo rotation experiment the predicted level of accuracy is of the order of 10E-2 pixel. Nevertheless, the method has a relevant computational cost.

SURF tracking

The SURF (*Speeded Up Robust Feature*) is a robust image tracker, partially inspired by the SIFT, first presented by (H. Bay et al., 2006) and used, among others, into object recognition. The standard version of SURF is several times faster than SIFT and more robust. Similarly to SIFT also SURF it is independent from morphological features and consent to reach sub-pixel accuracy.

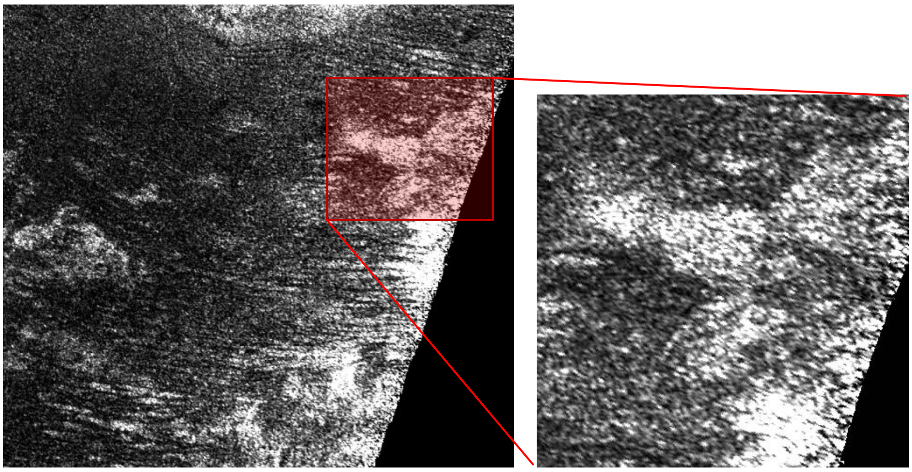

Figure 5 - 1195 X 1320 ROI (left) and retailed (398 X 396) feature from Cassini SAR Image of T25 flyby

Mutual Information

This technique is based on the detection of the maximum mutual information between the two images. The mutual information measures the mutual dependence of two random variables, in this case the pixel value (backscattering or brightness). This technique is widely used in medical imaging for the image registration. For this method a preliminary test was developed with Cassini SAR images of Titan in collaboration with Dr. G. Santilli from “Sapienza” University (Roma). A test feature 1 (398 x 396) was retailed from original ROI (1195 x 1320) (see Figure 5) and subsequently send to the mutual information engine in order to test the accuracy of the pattern matching. ROI was detected (row 220, column 835) with 1 pixel level accuracy, but the computational cost (12 hours) showed the disadvantages to use this technique for a relevant data volume.

2D Cross - Correlation

The 2D cross-correlation is one of the most simple methods used for pattern matching. Similarly to the mutual information, this technique is based on the detection of the maximum cross-correlation between the two images. Because it is based on the direct correlation of the brightness or the backscattering values, it is very sensitive to changes of the phase angles and therefore it is suitable only for the matching of radar images, or also optical images characterized by similar illumination conditions.

If we indicate con A the $N \times M$ matrix registered at first observation and with B the $N \times M$ matrix registered at the second observation, the 2-dimensional cross-correlation function f_c can be written as:

$$f_c(k,q)=\frac{\sum_{i=1}^{N}\sum_{j=1}^{M}\left[A(i,j)-\bar{a}\right]\left[B(i-k,j-q)-\bar{b}\right]}{\sqrt{\sum_{i=1}^{N}\sum_{j=1}^{M}\left[A(i,j)-a\right]^2\sum_{i=1}^{N}\sum_{j=1}^{M}\left[B(i-k,j-q)-\bar{b}\right]^2}} \tag{4.1}$$

where *k* and *q* are the shifting values respectively in the x and y direction; $\bar{a}$ and $\bar{b}$ are the average scattering value of the image, calculated respectively as:

$$\bar{a} = \frac{\sum_{i=1}^{N}\sum_{j=1}^{M} A(i,j)}{X_{\dim} Y_{\dim}} \qquad \bar{b} = \frac{\sum_{i=1}^{N}\sum_{j=1}^{M} B(i,j)}{X_{\dim} Y_{\dim}} \tag{4.2}$$

and where $X_{\dim}$ and $Y_{\dim}$ are the number of pixels in the x and y direction. For the Cassini data analysis NASA IDL libraries were used to perform the cross-correlation between retailed images. An example of a cross-correlation matrix obtained for the Titan rotation experiment is reported in the Figure 6. The identification of the maximum of the correlation matrix *I(k,q)* (also called *correlation index*) allows the computation of the misalignment between the images in terms of pixel shifting *k* and *q*, to not be confused with the registration error, which is instead the difference into the georeferenced position. A reference pixel in A and its correspondent position (provided by the pattern matching) in B is chosen as observed landmark and its georeferencing in terms of coordinates and observation time is extracted from position and time tags. The misregistration vector, expressed in TERF coordinates, is computed directly from the difference between A and B body-fixed coordinates. The inertial coordinates are computed using the relative timetag and the rotation model used for the georeferencing.

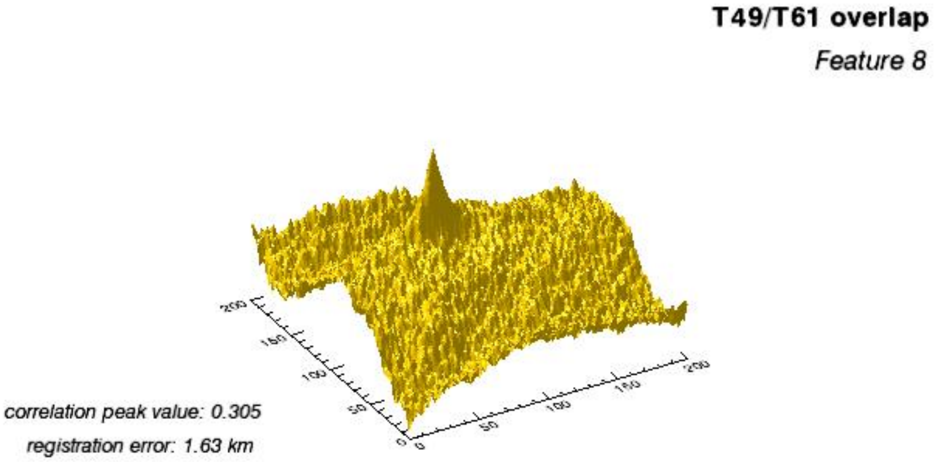

Figure 6 - cross-correlation matrix for T49-T61 cross-over (Titan Rotation Experiment)

4. Estimation process

The rotational parameters are estimated by a least squares method which minimizes the registration errors provided by pattern matching. In this case the misregistration vector is defined as the observable to process.
For a landmark on the surface of the body, if we indicate with $\boldsymbol{R_1}$ its observed body-fixed (TERF coordinates) position at time 1 and with $\boldsymbol{R_2}$ the its observed body-fixed (TERF coordinates) position at time 2, the *misregistration vector* $\Delta\boldsymbol{\rho}$ is defined as:

$$\Delta\boldsymbol{\rho} = \boldsymbol{R}_2 - \boldsymbol{R}_1 \qquad (4.3)$$

In an error-free case, if the correct rotational model is applied, $\Delta\boldsymbol{\rho}$ should be null, because the landmark is tied to the surface and its geodetical coordinates cannot change. A not null value of $\Delta\boldsymbol{\rho}$ comes from a difference between the applied and the true (observed) rotational model.
Since $\boldsymbol{R}$ can be expressed in terms of inertial coordinates ($\boldsymbol{r}$), the dependence of $\Delta\boldsymbol{\rho}$ on time (t) and the i rotational parameters (p_i) can be made explicit by using the rotation matrix M (see also Chapter 2):

$$\Delta\boldsymbol{\rho} = M(p_i, t_2)\boldsymbol{r_2} - M(p_i, t_1)\boldsymbol{r_1} \qquad (4.4)$$

In order to estimate the p_i the misregistration vector $\Delta\boldsymbol{\rho}$ has to be minimized by the application of the well-known least squares method:

$$-2\sum_{j=1}^{N} \frac{\partial \Delta\boldsymbol{\rho}_j}{\partial p_i} \frac{\Xi_j - \Delta\boldsymbol{\rho}_j}{\sigma_i} = 0 \qquad (4.5)$$

where N is the number of the tiepoints, Ξ_i the theoretical values of the mismatching vectors and σ_i the standard deviations associated to the observables. In this particular case Ξ_i are null, due to the fact that, if the correct rotational model is applied and the process is error-free, the misregistration is absent. Expanding this formulation for a dataset, the equation 4.5 can be written in matricial form as:

$$(H^T W H)\boldsymbol{X} = H^T W \boldsymbol{Y} \qquad (4.6)$$

where H is the *Design Matrix*, including the partial derivatives of the observables ($\Delta\boldsymbol{\rho}$) with respect to the solve-for parameters:

$$H = \begin{bmatrix} \frac{\partial \Delta \boldsymbol{\rho}_1}{\partial p_1} & \cdots & \frac{\partial \Delta \boldsymbol{\rho}_1}{\partial p_n} \\ \vdots & \ddots & \vdots \\ \frac{\partial \Delta \boldsymbol{\rho}_n}{\partial p_1} & \cdots & \frac{\partial \Delta \boldsymbol{\rho}_n}{\partial p_n} \end{bmatrix} \tag{4.7}$$

Each element of the Design Matrix can be computed directly by the derivatives of the rotation matrix (respectively at observation times 1 and 2) with respect to the Q-th rotational parameter (*p*):

$$\frac{\partial \Delta \boldsymbol{\rho}}{\partial p} = \frac{\partial \boldsymbol{R}_2}{\partial p} - \frac{\partial \boldsymbol{R}_1}{\partial p} = \frac{\partial M_2}{\partial p}\boldsymbol{r}_2 - \frac{\partial M_1}{\partial p}\boldsymbol{r}_1 \tag{4.8}$$

The expression for the derivatives of the rotation matrix with respect to the solve-for parameters are reported in the Annex A and B.
The observables vector $\boldsymbol{Y}$ is the vector of the observed residuals:

$$\boldsymbol{Y} = \begin{Bmatrix} \Xi_1 - \Delta \boldsymbol{\rho}_1 \\ \vdots \\ \Xi_N - \Delta \boldsymbol{\rho}_N \end{Bmatrix} = \begin{Bmatrix} -\Delta \boldsymbol{\rho}_1 \\ \vdots \\ -\Delta \boldsymbol{\rho}_N \end{Bmatrix} \tag{4.9}$$

The $\boldsymbol{X}$ vector of the Q solve-for parameters is defined as:

$$\boldsymbol{X} = \begin{Bmatrix} \Delta p_1 \\ \vdots \\ \Delta p_Q \end{Bmatrix} \tag{4.10}$$

For IAU model there are at least 15 solve-for parameters, a number which can increase for the IAU-modified model which includes the libration terms. In the Extended Rotational Model almost thirty parameters can be estimated. In order to opportunely assign to each observable the relative weight, it is necessary to define also the *Weight Matrix* (*W*):

$$W = \begin{bmatrix} \frac{1}{\sigma_1^2} & \cdots & 0 \\ \vdots & \ddots & \vdots \\ 0 & \cdots & \frac{1}{\sigma_n^2} \end{bmatrix}$$

Then the solution of the eq. 4.6 can be computed as:

$$\mathbf{X} = \left(H^T W H\right)^{-1} H^T W \mathbf{Y} \tag{4.11}$$

Eq. 4.11 must be numerically solved with an iterative procedure. Calling p the q-th solve-for parameter, the iterative solution will be provided by:

$$\Delta p^{k+1} = p^k + \Delta p \tag{4.12}$$

The analytical expression for the misregistration vector $\Delta\rho$

The TERF coordinates (X, Y, Z) for each tiepoint can be directly related to the rotational parameters using the applied rotational model; in the case of IAU model, the expression will be:

$$\begin{cases} X = -(\cos W \sin\alpha + \sin W \sin\delta \cos\alpha)x + (\cos W \cos\alpha - \sin W \sin\delta \sin\alpha)y + (\sin W \\ Y = (\sin W \sin\alpha - \cos W \sin\delta \cos\alpha)x + (\sin W \cos\alpha - \cos W \sin\delta \sin\alpha)y \ + (\cos W \\ Z = (\cos\delta \cos\alpha)x + \ (\cos\delta \sin\alpha)y + (\sin\delta)z \end{cases} \tag{4.13}$$

Introducing a new symbolism in order to simplify the calculation:

$$\begin{array}{ll} A = \cos W & B = \sin W \\ C = \cos\delta & D = \sin\delta \\ E = \cos\alpha & F = \sin\alpha \end{array} \tag{4.14}$$

The components of the misregistration vector can then be directly expressed as function of the rotational parameters in an analytical formulation:

$$\begin{aligned} \Delta\rho_{\mathrm{x}} &= \mathrm{X}_2 - \mathrm{X}_1 \\ &= \begin{cases} (-A_2F_2 - B_2D_2E_2)x_2 + (A_1F_1 + B_1D_1E_1)x_1 + \\ (A_2E_2 - B_2D_2F_2)y_2 - (A_1E_1 - B_1D_1F_1)y_1 + \\ B_2C_2z_2 - B_1C_1z_1 \end{cases} \end{aligned} \tag{4.15}$$

$$\begin{aligned} \Delta\rho_{\mathrm{y}} &= \mathrm{Y}_2 - \mathrm{Y}_1 \\ &= \begin{cases} (B_2F_2 - A_2D_2E_2)x_2 - (B_1F_1 + A_1D_1E_1)x_1 + \\ -(B_2E_2 + A_2D_2F_2)y_2 + (B_1E_1 + A_1D_1F_1)y_1 + \\ A_2C_2z_2 - A_1C_1z_1 \end{cases} \end{aligned} \tag{4.16}$$

$$\Delta\rho_{\mathrm{z}} = \mathrm{Z}_2 - \mathrm{Z}_1 = \begin{cases} (C_2E_2)x_2 - (C_1E_1)x_1 + \\ (C_2F_2)y_2 - (C_1F_1)y_1 + \\ D_2z_2 - D_1z_1 \end{cases} \tag{4.17}$$

Chapter V

The Rotational State Determination Software

1. Introduction to RSDS

The RSDS (*Rotational State Determination Software*) makes use of the optical observables to estimate the rotational parameters. The software currently include the IAU and IAU Modified model and the EXTended Model, following the formulation previously reported (Chapter II and Chapter IV – 5).
The software was implemented into FORTRAN 95 on a Linux platform. Actually two different versions have been released: 1.0 (2009-2010 upgrade) and 2.0 (2011). Both versions use the observed or simulated observables to estimate the selected rotational parameters with an iterative procedure. The software has the capability to estimate every parameter of the rotational model, even if generally only a narrow range of parameters will be taken into account for the real cases. The release 1.0 was initially developed for the Cassini Rotation Experiment including only the IAU - modified rotational model; the release 2.0, subsequently implemented, has instead no limits on the use of a specific rotational model, which can be inserted with a specific module. Also partial derivative modules can be easily inserted into the SW architecture in order to provide the maximum flexibility to the estimation software. RSDS makes a massive use of the SPICE/NAIF utilities (FORTRAN version) in order to enhance the performances. Planetary and satellite ephemerides, S/C ephemerides, planetary constants (PCK) and leap seconds files are all provided by JPL on the relative page of NAIF web site[1]. Furthermore, IMSL routines are used for the matricial computation and the resolution of linear systems.

---

[1] http://naif.jpl.nasa.gov/naif/

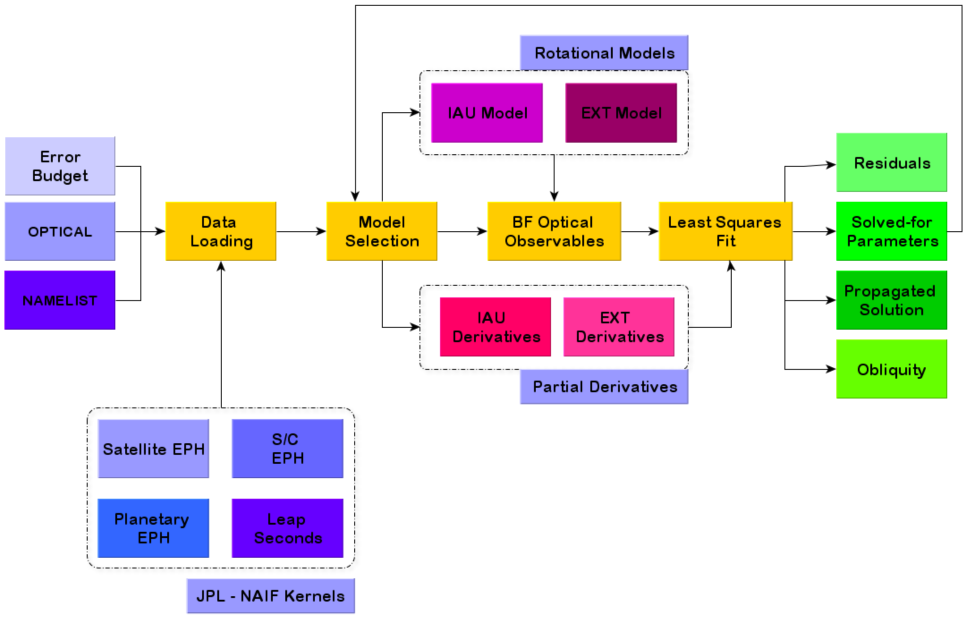

Figure 1 – Top-level block diagram for RSDS

1.1. Input files

In the present release three input files are foreseen: the OPTICAL file containing the observed tiepoints, the NAMELIST file, which includes the general settings, and the ERROR BUDGET ancillary file containing the error budget for the specific case. In the OPTICAL file the following parameters are listed:

- FID - feature ID;
- t_1 – epoch of the first observation;
- t_2 – epoch of the second observation;
- $\mathbf{r_1}$ – EMEJ2000 x,y,z coordinates for the tiepoint observed at t_1;
- $\mathbf{r_2}$ – EMEJ2000 x,y,z coordinates for the tiepoint observed at t_2;
- HC – radius including height corrections from altimetry;
- I - correlation index for the relative image pairs;
- NT - number of tiepoints for the same overlap.

In the NAMELIST file the following parameters are listed:

- *target body* – name or SPICE ID code of the target body;
- *central body* - name or SPICE ID code of the central body;
- *parameters* – list (array) of the solve-for parameters (ID code);
- *number* – number of the parameters to be estimated;
- *iteration* – number of iterations to perform;
- *error* - a nominal error level for the observables (if not otherwise specified from the error budget)
- *model* – name of the rotational model to apply;
- *NAIF_kernels* – filename for the SPICE kernels to load

Also the SPICE NAIF kernels for planetary constants, planetary, S/C and satellite ephemerides and leap seconds file have to be loaded.

1.2. Data processing

The data flow and the processing are reported on Figure 1. All the observations, the SPICE kernels and the ancillary data are loaded at the beginning of the process by a dedicated data manager module. Subsequently, the selected rotational model is activated and the body-fixed coordinates for each observation are computed, generating the optical observables. Similarly, the partial derivatives are computed following the general settings. Then the optical observables and the relative partial derivatives merge into the module of the least squares fit in order to perform the estimate. IMSL routines are used for the solution of the equation 4.11 (see Chapter IV for details). Solved-for parameters and the relative accuracies, computed from the covariance matrix, are reported into the output files, as well as the post-fit residuals. Subsequently the solved-for parameters are used in an updated rotational model in an iterative procedure for a new estimate, up to convergence.

1.3. Output files

Produced RSDS output files include:

- the estimated value and the relative 1-σ accuracy for each parameter (*Solved-for Parameters*);
- the estimated value and the relative 1-σ accuracy for the obliquity (*Obliquity*);
- the estimated spin pole location and the relative 1-σ accuracy at the reference epoch (*Propagated Solution*);
- the post-fit residuals (*Residuals*).

For debugging and testing also a detailed log file is available, generated in order to check the process step by step.

2. Validation

RSDS has been validated using different test levels, in order to ensure the desired level of reliability. A diffusive test campaign was performed on the 1.0 release, which has been also repeated and extended to the 2.0 version. The performed test sessions are reported below.

Single Module check

Each RSDS module is encoded, debugged and checked using a correspondent NAIF test unit; for example, modules containing the analytical formulation for Euler angles and the IAU rotational model were checked by the comparison with the analogue NAIF routines.

Aggregation test

The insertion of each module into the general architecture was thoroughly tested in order to ensure the correct I/O data flow; simple test units expressly dedicated were used to check the correctness of the I/O data format.

Macro-module test

The aggregation of two or more modules generates a macro-module which has to be tested. A macro-module is represented, for example, by the computation of the body-fixed coordinates starting from rotation angles and rotational models. The macro-module was compared to the equivalent transformation computed with NAIF routines.

General test

Once the general architecture was completed an effusive test session was performed in order to check the data flow between the different areas and the production of the desired output.

3. Simulations

Several simulations were performed using the simulated observables and computing the difference between the reference and the estimated values of the rotational parameters. A random distribution of several points on the surface of the target body was used for the generation of the tiepoints. Inertial EMEJ2000 coordinates for each tiepoint were computed at two different, randomly generated, observation times using a reference rotational model.

Table 1 - adopted simulation setup

Parameter	**Set up**
Target Body	Titan
S/C	Cassini
Ephemerides	de407/de421
Reference ellipsoid	Sphere (radius of 2575 km)
Rotational Model	IAU/IAU-modified
Measurement Error	1 - 2 km

Table 2 – Nominal Titan rotational models used in the simulations

SET	α_0 (deg)	δ_0 (deg)	ω (deg/day)	K_0 (deg)
Set 0	36.41	83.94	22.5769768	0.0
Set 1	38.41	83.74	22.5769768	0.0
Set 2	37.41	84.94	22.5780432	0.0

For the simulation setup several different typologies of estimate were selected:

- 2 parameters – pole (α_0, δ_0) estimate
- 3 parameters – pole location and spin rate (ω)
- 4 parameters – pole location and $(\beta_\alpha, \beta_\delta)$ precession terms

The set up for the simulations is those used for the Titan Rotation Experiment and it is reported in the Tab. 1.
Several nominal rotational models were defined in order to perform the simulations (Table 2). Set 0 is the current (Seidelmann, 2006) IAU rotational model for Titan and it was used as first test of the implementation. Set 1 shows variations with respect to IAU only for the pole location, while the set 2 (a typical configuration) also for the spin rate. Set 4 and subsequent present alternative values of the precession rates. The simulated observables were processed with an associated standard deviation of 5 km. Similar results were obtained using smaller standard deviations equalt to 3, 2 and 1 km. In order to calculate the lower limit to the number of useful tiepoints, we used also a data set of 6 landmarks, even if the convergence is naturally faster increasing the number of features.

Table 3 – Residuals and errors for the Case 1

SET	$\alpha_{0est} - \alpha_{0ref}$ (deg)	$\delta_{0est} - \delta_{0ref}$ (deg)	AVG Residuals (km)
Set 0	7.50E-12	1.70E-12	1.47E-9
Set 1	2.67E-11	1.00E-13	1.43E-9
Set 2	3.15E-11	3.00E-13	1.43E-9

3.1. Case 1: α_0 and δ_0 estimate

Simpler configuration to estimate, it was tested with data set 0, 1 and 2 and an error associated to the simulated observables equal to 1 km. A cycle of 10 iterations was performed, but the convergence to the final estimate value is already observed from the 4th iteration. The initial difference between the nominal (used as starting point in the estimation process) and the reference (used to generate simulated observables) rotational model is huge, ~ 1 degree or more for right ascension and up to 1 degree for declination, which correspond to an error on the Titan's surface of ~ 45 km.

Nevertheless the final estimate is very accurate (the differences between the estimated and the reference value are practically null) and the average of the residuals (in terms of the norms computed for each vector) of the order of 1 μm, absolutely negligible (Figure 2). It is possible to notice the level of the numerical noise, in this case of the order 1E-11 degree. It is important to observe that there is no significant difference assuming the nominal rotational model equal to the reference model (Set 0).

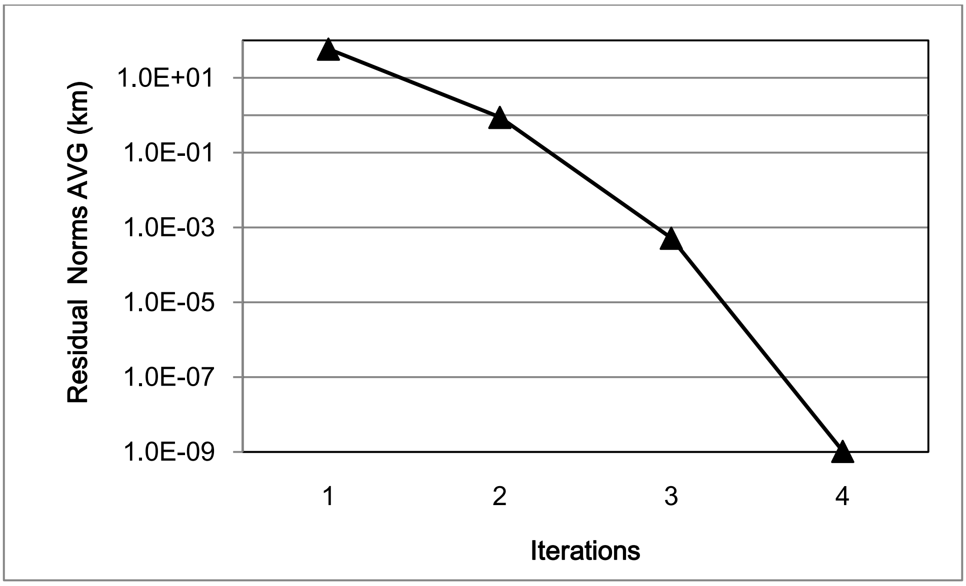

Figure 2 – Case 1: average of the residual norms increasing the iterations (Set 2); the registration error is canceled in 4 runs.

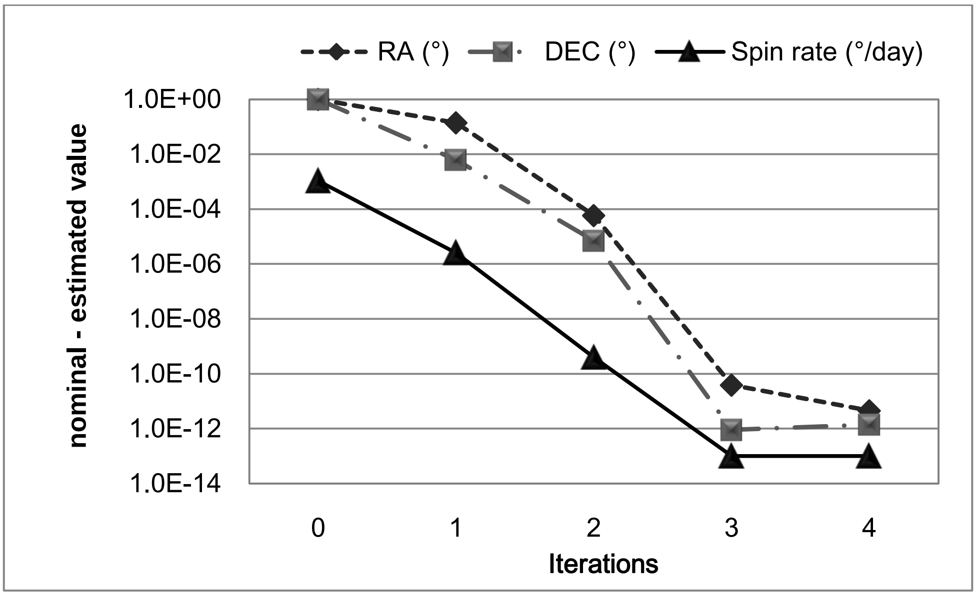

Figure 3 – Case 2: difference between the reference and the estimated value for α_0 (RA), δ_0 (DEC) and ω (Spin rate) using Set 2

3.2. Case 2: α_0, δ_0 and spin rate estimate

In this case Set 2 was used and the difference between the reference and the estimated value for right ascension, declination and spin rate is plotted in Figure 3. It is easy to notice the fast convergence (4 runs) to the nominal value. The better estimate is obtained for ω, with an error of 1E-13 °/day. It is possible to observe that, for the pole location, the level of the numerical noise is 1E-11 degree for RA, 1E-12 degree for DEC and 1E-13 degree/day for the spin rate. Also in this case 10 iterations has been performed but already at 4th iteration the norms of the residuals convert to 10E-9 km, 6 orders of magnitude below the desirable threshold value of 1 m.

3.3. Case 3: precession terms estimate

In this case four parameters are estimated: the center of the precession (α_0, δ_0) and the amplitudes of the precession terms (β_α, β_δ). The reference and the nominal values are reported in Table 4 together with the obtained results. The initial error associated to the observables is equal to 2 km.
All the parameters are estimated with sufficient accuracy. DEC terms are estimated of one order of magnitude with respect to the RA terms.

Table 4 – Case 3: reference and estimated values

Parameter	Reference Value	Nominal Value	Estimated Value
α_0	36.31°	36.35°	36.309° ± 0.025°
δ_0	83.92°	83.924°	83.919° ± 0.004°
β_α	4.66°	4.1°	4.660° ± 0.251°
β_δ	-0.54°	-0.539°	-0.539° ± 0.004°

The post-fit residuals are equal to 26 cm, worst than observed for the previous cases, but still fully compliant. The convergence is slower (6 against 4 runs) with respect to the 2 or 3 parameters fit.

Also in this case 10 iterations has been performed but already at 6th iteration the norms of the residuals convert to the value of 26 cm, to be compared with a the threshold value of 1 m (Figure 4).

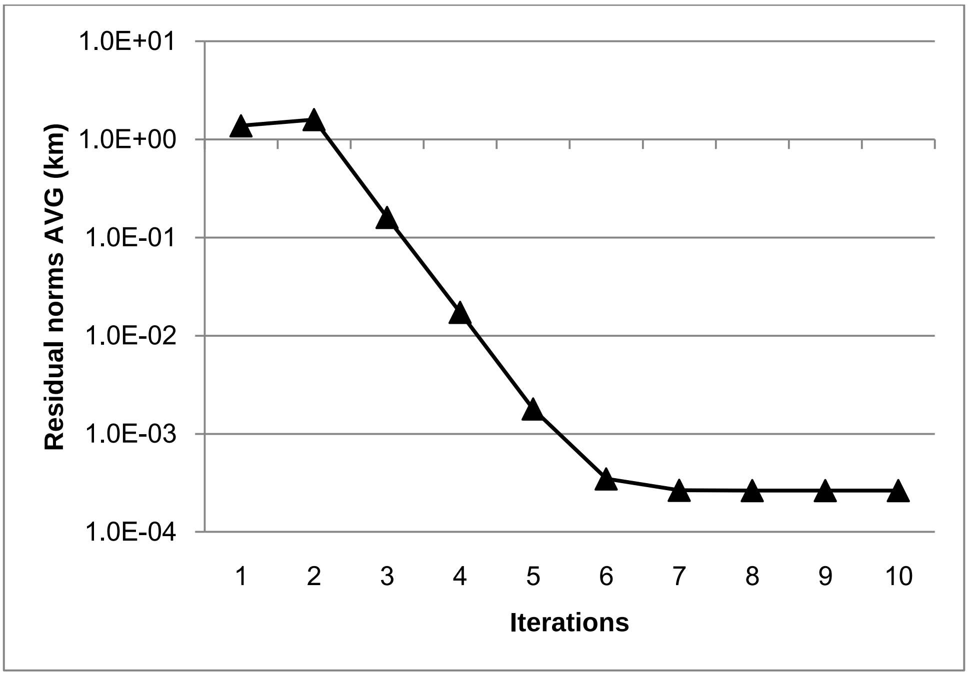

Figure 4 – Case 3: average of the residual norms vs. iteration number.

Table 5 - Simulation result for different systematic error levels σ_n

Parameter	Reference Value	Estimate σ_n = 0.1°	Estimate σ_n = 0.01°	Estimate σ_n = 0.001°
α_0 (°)	37.41	37.4 ± 0.67	37.4 ± 0.67	37.4 ± 0.67
δ_0 (°)	84.94	84.92 ± 0.07	84.94 ± 0.07	84.94 ± 0.07
ω (°/day)	22.5780432	22.5781 ± 3.4E-04	22.5780 ± 3.4E-04	22.5780 ± 3.4E-04

4. Systematic error effects

Simulations were also performed using landmarks affected by a systematic error on position. A data set affected by a systematic error varying from a minimum of 0.001° to a maximum of 0.1° in both longitude and latitude was used. The uncertainty value σ_{obs} was assumed equal to 12 km for the observables, 2.5 times the value of maximum systematic error estimated for the Cassini case (see Chapter VII). This was justified from the fact that, independently from misregistration, georeferencing can be affected by errors on the ephemerides, the assumption of a spherical body and on camera/radar calibration. A complete discussion of the error sources for Cassini and the Titan Rotation Experiment is shown in Chapter VII.

The entity of the systematic error was chosen in order to test the model to estimate the selected parameters using data heavily affected by noise. Nevertheless the parameters are estimated with a sufficient accuracy (Table 5). The linear trend of the residuals depending on the error level can be observed on Table 6. For the case of huge errors (0.1°) on both latitude and longitude, residuals equal to 5 km are perfectly according to the simulated systematic error (4.42 km) (Table 6). The model is able to estimate with sufficient accuracy the rotational parameters, and the residuals are due to the systematic components of error.

Table 6 - Residuals for different systematic error levels

Systematic Error level	$\sigma_n = 0.1°$	$\sigma_n = 0.01°$	$\sigma_n = 0.001°$
Residuals Norms AVG	5.1024 Km	0.5102 Km	5.10 E-002 Km

Chapter VI

Titan And The Cassini Mission

1. Titan

Titan is Saturn’s largest moon, and one of the most interesting celestial bodies of the solar system. With a diameter of 5150 km, larger by volume than Mercury (4879 km) and the Moon (3474 km), Titan is the second largest satellite in the solar system after Ganymede (5268 km). Discovered in 1655 by the Dutch astronomer Christiaan Huygens, as the fifth moon of a planet to be discovered and the first saturnian moon, Titan is the only natural satellite known to have a dense atmosphere and the only object other than Earth for which a clear evidence of surface liquid has been found (Stofan et al., 2007). Before the arrival of Voyager 1 in 1980, Titan was thought to be slightly larger than Ganymede and thus the largest moon in the Solar System; this was an overestimation caused by Titan's dense, opaque atmosphere, which extends many miles above its surface and increases its apparent diameter. With a gravitational constant of 8978 km^3/s^2, Titan has a density of 1881 kg/m^3, similar to those of the Jovian moons Ganymede (1936 kg/m^3) and Callisto (1834 kg/m^3), 80% less dense than the Moon (3346 kg/m^3). Table 1 summarizes the physical and orbital elements of Titan.

Table 1 – Physical and orbital elements of Titan

Parameter	Value	References
Mean surface radius	2575 km	Stiles et al., 2008
Gravitational parameter	8978.1384 km^3/s^2	Iess et al., 2010
Mean density	1881 kg/ m^3	Iess et al., 2006
Orbital semimajor axis	1221865 km	JPL ephemerides
Free orbital eccentricity	0.0288	JPL ephemerides
Mean orbital motion	22.5769768 °/day	Seidelmann et al., 2006
Period of revolution	15.95 days	JPL ephemerides
Period of rotation	15.95 days	JPL ephemerides
Surface temperature	-179.6 °C	Mitri et al., 2007

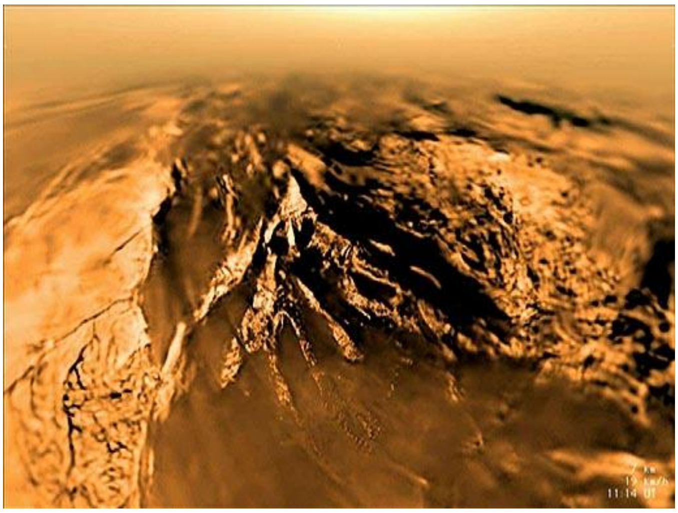

Figure 1 – Titan surface observed from Huygens (NASA – JPL)

1.1 Orbital elements

Titan has an orbital period of 15.95 days and, similarly to Moon and many of the other gas giant satellites, it is expected to be synchronous, with a 1:1 resonance between the orbital and the rotational period. This value is actually predicted by IAU (Seidelmann et al, 2006) to be equal to 22.5769768 degree per day and by JPL to 22.5769756 degree per day. Its orbital eccentricity is 0.0288, and the mean orbital plane is inclined 0.348 degrees with respect to the mean equator of Saturn. The precession period of the normal to the orbital plane is 722.06 years.

Titan is locked in a 3:4 orbital resonance with the small, irregularly shaped satellite Hyperion.

1.2 The surface of Titan

Titan is the only satellite in the Solar System with a thick atmosphere (1.5 bar at the surface). The Titan surface was revealed in detail for the first time from Cassini observations and also from the Huygens probe. The presence of tectonical structures, hydrocarbons lakes, dry rivers, large dune files and structures interpreted as cryovolcanic indicated a complex geological activity.

The geology of Titan is for some aspects very similar to the Earth's: all major geologic processes appear to be represented, including impact cratering, erosion by wind and liquids, tectonism and cryovolcanism. Lakes, rivers and seas of liquid hydrocarbons can be observed; vast dune fields have been detected from radar imaging and also the effects of wind and rain erosion can be recognized. Titan has a methane cycle similar to the Earth hydrological cycle and this characteristic make this satellite very different from the other moons of the Solar System.

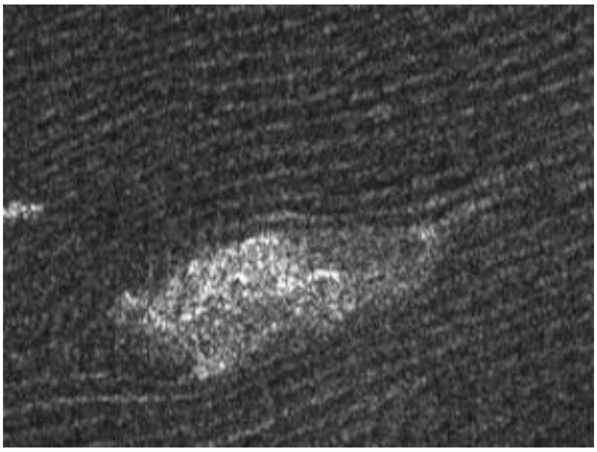

Figure 2 - Dunes on Titan – Cassini SAR Imaging (NASA – JPL)

Dunes

Aeolian features were initially observed in 2004 (Porco et al., 2005), with the observation of streaky boundaries between light and dark terrains, suggesting a possible eastward surface transport due to the aeolian activity, an interpretation subsequently confirmed by radar imaging (Elachi et al., 2006). An example of a dune field is reported on Figure 1. Dune areas are confined to equatorial belt between 20° N and 20° S, a distribution consistent with proposed meteorological models (Mitchell, 2008); nevertheless their distribution, which clearly show an eastwards sands transport, is in contrast with the actual atmospheric circulation models, which suggest instead the presence of westwards flow at low latitudes (Tokano et al, 2006).

Even if actually the measured fraction of Titan's surface covered by dunes is larger than any terrestrial planet, their presence were not predicted for many reasons. First, the low wind speed (~ 1 cm/s), due to many factors (low solar flux, a large column mass of the atmosphere, a relatively small radius), is far below the threshold wind speed required to move sand (assuming an interparticle cohesion similar to terrestrial materials) of 0.5 – 1 m/s.

Second, the sand supply – erosive processes were expected to be weak due to the weak driving sunlight, slow falling rain and small temperature variations (Lorentz et al., 1995). Third, the expected presence of liquid hydrocarbons on Titan's surface might act as traps for any sand that was formed. In any case the dunes could be formed not by fluvial erosion or impact ejecta, but they could have a photochemical origin, with a sand formed from atmospheric haze particles. Spectroscopical analysis shows a lower concentration of water ice compared to other areas, suggesting an organic composition.

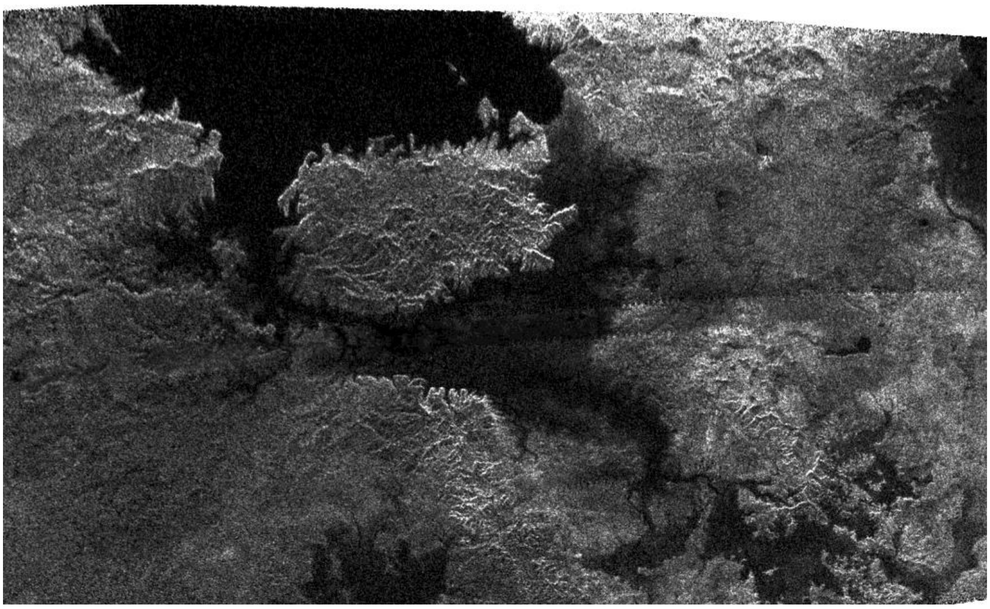

Figure 3 – polar view of the Kraken Mare - Cassini SAR Imaging (NASA – JPL)

Lakes and Seas

Before the Cassini mission the presence of liquid hydrocarbons on the surface had been predicted (Lunine et al., 1983), basing on the necessity to have reservoirs to resupply the atmospheric methane and to feed up the methane cycle; otherwise the atmospheric methane would be totally broken down into more complex hydrocarbons on timescales of ~ $10^7 – 10^8$ years by photochemical processes, the same which give rise to the thick atmospheric haze (Lorenz and Lunine 2005).

With the Cassini mission venue, the optical images gave evidence of several dark surface features, subsequently identified by RADAR observations as formed by liquid methane, likely mixed with liquid ethane (Stofan et al., 2007). All the identified lakes and seas occur at high latitudes, with myriad lakes observed at high northern latitudes (Hayes et al., 2008).

Significant variations in size and morphology can be observed. Size range varies from < 1 km^2 to the 400’000 km^2 of the Kraken Mare shown in the Figure 2 (for comparison, the Mediterranean Sea is 1.2 million km^2 wide). Morphologically the lakes are extremely diverse, with rough shorelines or representing flooded river valleys or still existing within depressions with smooth, rounded sides. In addition to morphological differences, also radar backscattering varies from very low values (liquid filled basins) to high values similar to terrain backscattering, indicating dry lakebeds (Mitri et al., 2007).

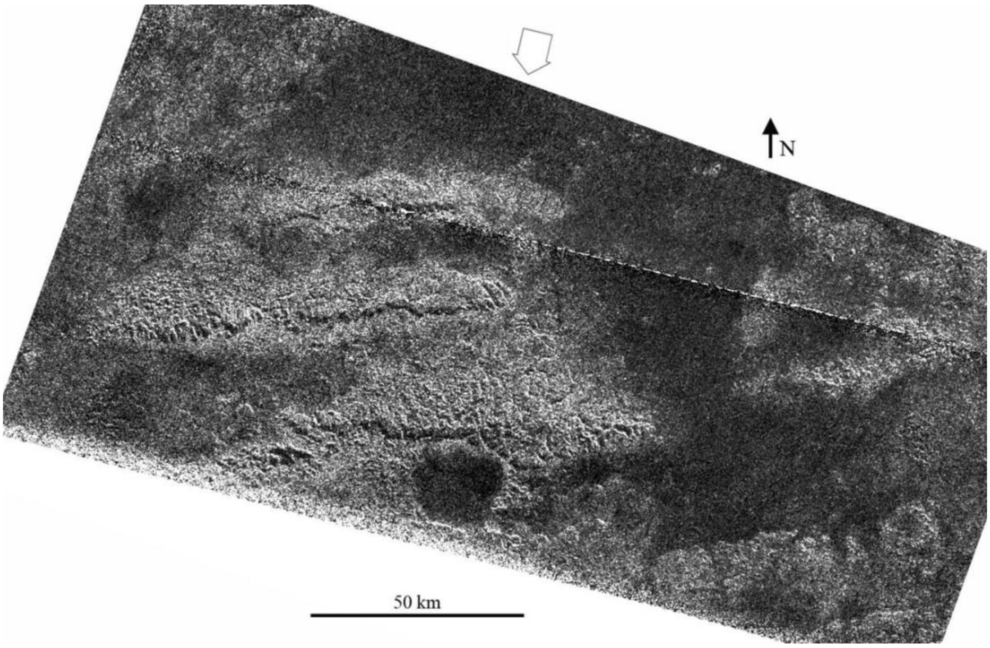

Figure 4 – ridges observed by Cassini SAR at 2°S 127°W (Xanadu Regio) on 2008 (NASA – JPL)

Cryovolcanism

The existence of cryovolcanism on Titan was predicted (Lorenz and Lunine, 1996) before Cassini, with an high probability of the presence of effusive features and flows and domes. Several surface features which could be interpreted as cryovolcanic have been observed by Radar Mapper (Lopes et al., 2007) and by VIMS (Visible and Infrared Mapping Spectrometer) (Sotin et al., 2005), including flow features and caldera-like depressions, these last all associated with lobate deposits. Several ridges can be observed into the Figure 3.Most putative cryovolcanic features are located at mid to high northern latitudes, characterized by lobate boundaries and relatively uniform radar properties, with flow features brighter than their surroundings. Cryovolcanic flows are quite limited in area compared to the more extensive dune fields or lakes. Most famous are *Rohe Fluctus* (41°W, 47°N), a caldera-like with a diameter of ~ 13 km and radar-bright edges, with a lobate deposit of at least 40 km long; *Ara Fluctus* (118°W, 39°N), an irregularly shaped depression, about 18 km across and oval in shape, with a flow like deposit of 53 km and with a radar-bright rim around the periphery; *Winia Fluctus* (46°W, 49°N), a series of flow-like deposits, whose origin is not clear from RADAR data, covering an area of at least 23700 km^2. *Hotei Regio* (78° W, 26°S) is another region considered to be currently volcanically active. Explanations for cryovolcanism for Titan are various. Mitri et al. (2008) proposed a model for ammonia-water resurfacing which involves cracking at the base of the ice shell and a subsequent formation of liquid pockets in the ice. Thermal convection in the superficial ice-I shell can also play an important role in ensuring the resurfacing activity.

Fluvial features

Fluvial features have been observed on Titan (Jaumann et al., 2008) and can be observed in Figure 4. Valley-like features are known from Cassini observations. Traces of fluvial erosion cover the entire surface of Titan and individual channels or networks could be found at the equator, at mid-latitudes and at the North Pole. On the other hand, there are regions where channels are almost entirely missing, like the equatorial dune fields (Prockter et al., 2010).

Due to the extremely low (94 K) superficial temperature, only methane and ethane among fluids can stay liquid on the surface, and only methane has a high enough vapor pressure to participate in a hydrological cycle (Lorenz et al., 2008). And although methane has a short lifetime of about ~ 100 years its high concentration in the atmosphere implies that the atmosphere itself is recharged by reservoirs on the surface and subsurface (Tobie et al., 2006).

Figure 5 - Image of the southern canyons taken at 240° W 71° S, Dimensions are 335 X 289 km. SAR illuminated this area from the top of the image at 18 degrees incidence angle. Such a morphological configuration is typical of other regions observed in several flybys near Titan's south pole (NASA [1])

---

[1] http://www.nasa.gov/mission_pages/cassini/multimedia/pia12036.html

In this case these fluvial features are part of the cycle and should be common on Titan. Sediment on Titan would consist of water ice, derived from outer icy crust and broken up by impact cratering, mass wasting and fluvial processes, and organic material, which settles from the atmosphere after formation by photochemical reactions of hydrocarbons (Lorenz and Lunine 2005). Furthermore, precipitation rates as estimated from the current atmospheric might not exceed 1 cm/year (Tokano et al., 2006), comparable to terrestrial deserts; consequently, heavy rainstorms should be infrequent and could not be considered the first methane refilling for liquids on the surface.

Impact Craters

Due to the presence of a thick atmosphere and of a hydrological methane-based cycle very few evidences of impact craters have been identified. Basing on the analysis of the 22% of the surface imaged by SAR, (Wood et al., 2010) identified 5 certain impact craters and 44 additional probable impact craters. These craters are quite similar to those detected on both rocky and icy satellites. Often craters appear eroded or partially covered by dune deposits and their distribution is not uniform. Xanadu has a crater density from 2 up to 9 times greater than other areas. The paucity of recognizable craters implies that Titan’s surface is quite young and it is likely that dynamical geological processes have destroyed most of its early history and that multiple processes clearly continue to modify its surface.

Mountains and tectonic features

Possible tectonic features on Titan include linear and ridge-like formations, probably chains of hills (Lopes et al., 2010) and dark, sub-parallel and branching lineaments (virgae), probably tectonic fractures later used by liquids as fluvial channels (Perry et al., 2007). SAR images showed possible tectonic features as linear chains of radar-bright terrain and irregularly shaped fragments of radar bright terrain as Xanadu (Radebaugh et al., 2010). Following (Lopes et al., 2010) both types are part of the hummocky and mountainous terrain, more exposed in the equatorial regions, the oldest geomorphological unit to have been identified on Titan. A possible explanation for contractional tectonism has been proposed by Mitri et al. (2010).

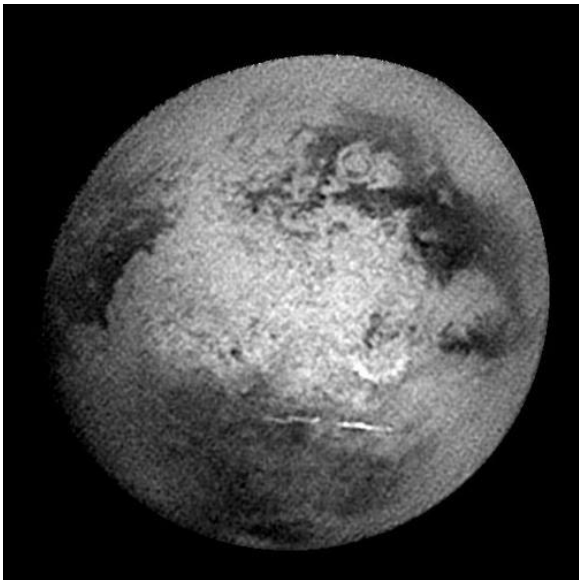

Figure 6 – Xanadu region by SAR Imaging (NASA – JPL)

Xanadu

Xanadu is a plateau-like region of highly reflective water ice centered at 10°S 100°W on the southern hemisphere, identified for the first time in 1994 by the Hubble Space Telescope in the infrared spectrum, and imaged in detail by Cassini along all the mission extension (Porco et al., 2005). The extension of Xanadu Regio is about 3400 km, ~ 5% of Titan superficial area. It is characterized by a complex geological history (Radebaugh et al., 2011). Recently Brown et al. (2011) proposed that Xanadu is an impact crater. An evident albedo boundary can be observed on the western side of Xanadu (Figure 5), exhibiting linear and angular shapes whose form and orientation suggest that the dark material have embayed the bright terrain (Porco et al., 2005).

1.3 Interior models

Titan is primarily composed of water ice and rocky material, similar in composition to the other Saturnian satellites Dione and Enceladus, but denser (1.88 g/cm^3 versus 1.47 g/cm^3 and 1.60 g/cm^3 respectively). Formation and thermal models indicate that Titan should be at least partially differentiated with a multi-layer internal structure divided into a deep interior, a high-pressure ice (HP) layer, an ammonia-water subsurface ocean, and an outer ice-I shell (e.g., Grasset et al., 2000; Sohl et al., 2003; Tobie et al., 2006; Mitri and Showman, 2008a). Some models, developed before Cassini mission (Grasset et al, 2000, Sohl et al., 2003), can be still considered valid even if used parameters should be updated.

Table 2 – Physical Properties for the Saturnian Satellites (Jacobson et al., 2006)

Saturnian Satellites - Physical Properties

Body	*Radius (km)*	*Mass (10^{22} g)*	*Density (g/cm^3)*
Mimas	198.30 ± 0.30	3.7493 ± 0.0031	1.1479 ± 0.0053
Enceladus	252.10 ± 0.10	10.8022 ± 0.0101	1.6096 ± 0.0024
Tethys	533.00 ±0.70	61.7449±0.0132	0.9735±0.0038
Dione	561.70 ± 0.45	109.5452±0.0168	1.4757 ±0.0036
Rhea	764.30 ± 1.10	230.6518 ± 0.0353	1.2333 ± 0.0053
Titan	**2575.50 ± 2.00**	**13452.0029±2.0155**	**1.8798±0.0044**
Hyperion	133.00 ± 8.00	0.5584 ± 0.0068	0.5667 ± 0.1025
Iapetus	735.60 ±1.50	180.5635 ± 0.0375	1.0830 ± 0.0066
Phoebe	106.60 ± 1.00	0.8292 ± 0.0010	1.6342 ±0.0460

Actual Titan interior models are based on:

- the observed *mean density*, derived from the GM estimate (Jacobson, 2006) and equal to 1881 kg/m^3;

- the *Moment of Inertia*, equal to 0.34 and recently inferred from the measurements of 3x3 gravity field (Iess et al., 2010); the estimate of the quadrupole moment (J_2, C_{22}) shows that Titan is mostly relaxed to hydrostatic equilibrium (J_2/C_{22} = 3.186 ± 0.042 compared to the value of 3.33 for hydrostatic quadrupole);

- the high value of the *eccentricity* (0.0288), which can be explained referring to the tidal energy dissipation on the surface and within the interior (Tobie et al., 2005). In this perspective, -only interior models including a few percent of ammonia (and not zero) in the composition of the subsurface ocean can limit the damping of the eccentricity over the age of the Solar System;

- the *obliquity*, inferred from the SAR Rotation Experiment and scientific goal of the present work. Actually from previous measurements (Stiles et al., 2008) the measured obliquity is equal to 0.3, a value not compatible (Bills and Nimmo, 2008) with the MoI value inferred from gravity measurements. The determination of the obliquity and the relative standard deviation could provide relevant information on the interior and the core-shell decoupling.

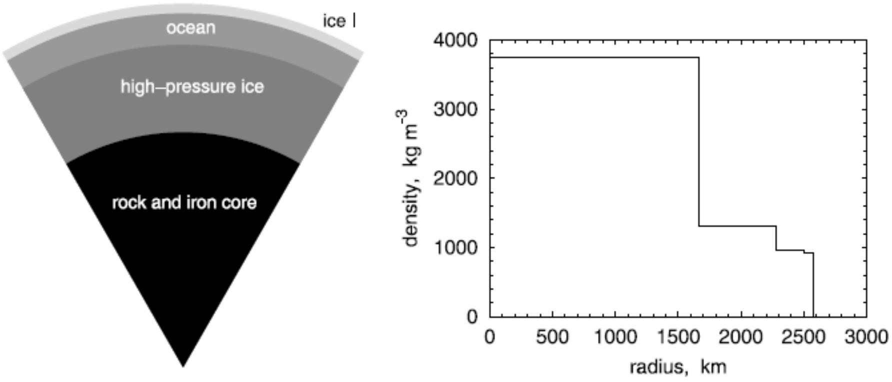

Figure 7 – Titan's interior structure and density profile (Sohl et al., 2003)

1.3.1 2000 -2010 : density based models

Until (Iess, 2010) the only available measure useful to the development of an interior model was the measured mean density of 1881 kg/m^3. These models are still considered valid even if they do not impose constraints on the value of MoI.

Grasset model

(Grasset, 2000) model includes a thick water ice layer and two possible structures: a core as a well-convecting silicate sphere (CI chondrites case) or a layered structure composed of a liquid iron inner core surrounded by a slowly convecting silicate layer (EH enstatite chondrites). The volume of the iron core relative to the silicate layer depends on the initial amount of metallic iron in chondrites. The icy layer can be composed of several sublayers, since the range of the pressure encountered from the surface to the top of the core allows the existence of several high-pressure polymorphs of ice. Furthermore, a deep liquid layer could exist below an ice I outer layer.

Sohl model

Sohl et al., (2003) provided an interior model of a differentiated Titan which includes an outer icy shell, an internal ammonia-water ocean and a rocky core (Figure 6). Assuming thermal and mechanical equilibrium. Sohl et al. calculated the structure of the interior as a function of the thickness of outer ice I shell, the moment of inertia factor and the tidal Love numbers. In particular, Love numbers are linearly dependent on the thickness of the ice I shell at constant rheology parameters but decrease by one order of magnitude in the absence of an internal ocean.

The interior structure model is optimized to satisfy the bulk rock-to-ice ratio of 55:45 and includes four layers:

- □ *an Ice I layer* – with a thickness 65 ÷70 km, a density of 920 kg/m^3 , assumed entirely conductive;
- □ *the subsurface ocean* - composed by 15 wt.% NH_3 and extending over a depth range of 224 km;
- □ *an High-Pressure Ice layer*: 612 km thickness, density ~1200 kg/m^3
- □ *a rocky core* - with a radius of 1671 km and a mean density of 3800 kg/ m^3.

Ice shell thicknesses are between 90 and 105 km for models with 5 wt.% ammonia and for core densities between 3500 and 4500 kg/ m^3. In the model the thickness of the ocean is found to be inversely proportional with respect to those of the icy shell. Core sizes vary from 1500 to 1800 km radius. The model is using a viscosity parameterization which is strongly temperature-dependent. The density distribution is associated with a MoI factor of 0.304, distant from the actual value of 0.34 (Iess et al., 2010).

Tobie model

Tobie et al. (2005, 2006) model of a possible present-day structure of Titan's interior includes a fully differentiated structure, formed by a silicate core, an high-pressure layer, a liquid water layer, and an ice I superficial layer. To verify the present-day value of the mean density (ρ = 1881 kg/m^3), the silicate core radius is set to 1900 km and the total H_2O mass M_{H2O} to 4.82×10^{22} kg. In the Table 3 the density values for each layer are reported.

Table 3 – Density profile for Titan's interior (Tobie et al., 2005)

Layer	**Density (kg/m^3)**
Ice I outer shell	920
Subsurface ocean (liquid water)	1000
High pressure Ice VI	1310
Silicates Core	3000

1.3.2 After 2010: MoI based models

Mitri model

(Mitri et al., 2010) interpreted the estimated MoI = 0.34 as an indication of a partially differentiated structure, with a deep interior composed of a mixture of ice and rock. In this case Titan must be formed relatively late (> 2.6 Myr) and the accretion should have occurred on a timescale > 0.1 Myr. In this case two cases are predicted, respectively a two and a three layer structure. The first includes an icy shell, a subsurface water ocean (with the presence of ammonia and salts), an high pressure icy layer and an undifferentiated core with a radius equal to 2100 km and a low density equal to 2560 kg/m^3 . In the second case (three layer model) the undifferentiated deep interior is divided in two parts: an intermediate layer with density < 2560 kg/m^3, and a silicate or metallic core with a radius of a few hundred kilometers and an averaged density $\sim$ 3300 kg/m^3 .

Castillo and Lunine model

(Castillo and Lunine, 2010) rather interpreted the MoI from gravity as due to a fully differentiated structure, with a thickness of the icy shell variable between 50 and 100 km, a subsurface ocean, a hydrated silicate layer (2400 – 2800 kg/m^3) and a deeper core of anhydrous silicates. In this case the presence of anhydrous silicates puts a constraint on the ocean density and its chemical composition, with $\sim$ 10% of ammonia and a relevant percentage of potassium and other salts in order to limit the dehydration of the core. In this case Titan must be formed relatively late (> 2.6 Myr) and the accretion should have occurred on a timescale > 0.1 Myr.

Existence of a subsurface ocean

(Lunine, 1993) has shown that a subsurface ocean is the only structure that is consistent with all of the known constraints (chemical, tidal, ground-based radar and near-infrared observations). If Titan contains a thick ocean, its density can reach 1300 kg/m^3 at the interface with the high pressure ice layer and could even be greater if one assumes the presence of solutes and of small silicate particles in suspension (Kirk and Stevenson, 1987). Thus whether Titan’s shell is frozen or contain a thick liquid layer, its density profile is about the same, and its mass fraction 40% (Castillo, 2010). An alternative evidence for the presence of the ocean has recently been uncovered by the measurements of extremely low frequency (ELF) radio waves in Titan's atmosphere. Titan's surface is thought to be a poor reflector of ELF waves, so they may instead be reflecting off the liquid-ice boundary of a subsurface ocean (Simoes et al., 2007).

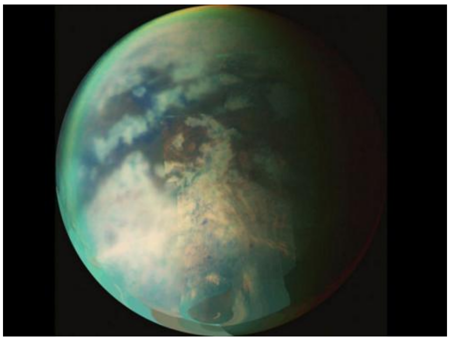

Figure 8 – Cassini composite image of Titan's atmosphere (NASA – JPL)

1.4 Atmosphere

Titan is the only moon in the solar system with a thick atmosphere (Figure 6). Due to Titan mean density (1881 kg/m^3 against 5515 kg/ m^3 for the Earth), its gravity doesn't hold onto its gaseous envelope as tightly as the Earth and the atmosphere extends to an altitude of about 600 km. In 1980 the Voyager 1 spacecraft showed that the air pressure at the surface is one-and-a-half times that of Earth at sea level and four times the density. Titan's atmosphere is formed by nitrogen for the 98.4 % (the only dense, nitrogen-rich atmosphere in the Solar System aside from the Earth's) and by methane for 1.4 % and by hydrogen for 0.1–0.2%, with small amounts of other carbon-rich compounds (ethane, propane) and of other gases (CO_2, Ar, He). In the upper atmosphere layers the methane and nitrogen molecules dissociation, due to the UV sunlight components and to the high-energy particles accelerated by Saturn's magnetic field, occurs producing a thick orange smog. The subsequent combination of chemical products gives rise to a variety of organic molecules.

1.5 Seasons and weather

As on Earth, the climate is driven mostly by changes in the amount of sunlight depending on the seasons, 7 years long on Titan. Large fields of puffy clouds have been observed near the south polar region by both Cassini spacecraft and the Hubble Space Telescope. These cloud formations were plentiful near the time of that hemisphere's summer solstice, not long before Cassini arrived in the Saturn system, but then became scarce as autumn approached. In the intervening years Cassini has observed streak-like clouds at middle latitudes in both the northern and southern hemispheres, as well as a giant cloud of ethane that formed over the northern polar region. The timing of the observed breakup of Titan's south polar cloud system along with the resurgence of clouds at generally lower southern latitudes ($\sim 55^\circ$ S) is consistent with the timing of the seasonal shift of the location of maximum solar insolation away from the south pole (Schaller et al., 2006).

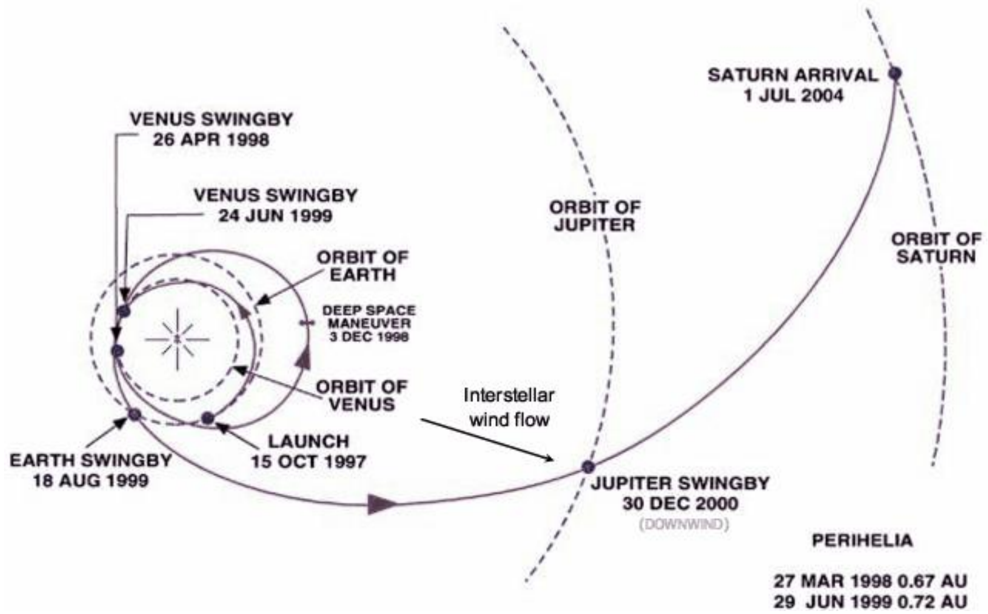

Figure 9 – Mission profile for Cassini spacecraft (NASA – JPL)

2. The Cassini mission

Cassini/Huygens is a NASA/ESA/ASI joint mission to Saturn. The spacecraft was launched on October 15, 1997 from Cape Canaveral (Florida) with a Titan IVB-Centaur rocket and its seven-years journey to Saturn included two Venus (respectively on April 36, 1998 and on June 24, 1999), Earth (August 18, 1999) and Jupiter (December 30, 2000) gravity assists. On July 1, 2004 Cassini/Huygens successfully completed the 627 m/s SOI (*Saturn Orbit Insertion*) maneuver and it was inserted into an highly eccentric, 166 day orbit around Saturn (Figure 8). The event marked the beginning of an in-depth exploration of the Saturnian system, which produced a wealth of scientific discoveries. About six months later, on December 25, 2004 the Huygens probe separated from the spacecraft and penetrated into Titan’s atmosphere just 20 days later (January 14, 2005), completing successfully its two-hour parachute descent.

The 4-years Prime Mission (completed on June 20, 2008) included 74 orbits around Saturn, 45 Titan flybys and several encounters with other icy satellites. The first two-years Extended Mission (Equinox Mission), ended on July 2010, included 60 additional orbits, 26 Titan flybys, 7 Enceladus flybys and one fly-by for Dione, Rhea and Helene. The third mission’s extension, which goes through September 2017, is named Solstice Mission for the Saturnian summer solstice occurring in May 2017. Since Cassini arrived at Saturn just after the planet's northern winter solstice, the extension allows for the first study of a complete seasonal period.

2.1 Spacecraft design

Information about Cassini design can be retrieved from (Henry, 2002) and the mission website[2]. Cassini is the largest interplanetary spacecraft ever built by NASA, with its 6 m high and a launch weight of 5655 kg, with respectively 2523 kg for the dry mass and 3132 kg for the propellant. At the top of the S/C there is the High Gain Antenna (HGA), which is a fixed 4 m diameter, parabolic cassegrain feed antenna constructed of graphite epoxy layers and aluminum honeycomb core. The HGA assembly also includes the first Low Gain Antenna (LGA1), a pair of sun sensors, several feeds for the RADAR instrument and a receive path for the Huygens Probe signal. The HGA Antenna is the primary antenna for telecommunications and is one of the key elements for the RADAR instruments. Equipment for a total of twelve different science instruments is carried onboard the Cassini orbiter while other six found place on the Huygens probe. On-board instruments for the Cassini Orbiter are reported on Table 4. The remote sensing pallet (RSP) and fields and particles pallet (FPP) are two aluminum structures attached to the USS that support science instruments. The RSP supports the ISS NAC, ISS WAC, VIMS, CIRS, UVIS, and two stellar reference units.

Table 4 – On-Board Instruments for the Cassini Orbiter (Henry, 2002)

Instruments (*sensors*)	**Abbreviation**
Cassini Plasma Spectrometer	CAPS
Composite Infrared Spectrometer	CIRS
Cassini radar	RADAR
Radio Frequency Instrument Subsystem	RFIS
Magnetometer	MAG
Imaging Science Subsystem	ISS
Wide Angle Camera	WAC
Narrow Angle Camera	NAC
Visible and Infrared Mapping Spectrometer	VIMS
Radio and Plasma Wave Science	RPWS
Ion and Neutral Mass Spectrometer	INMS
Magnetospheric Imaging Instrument	MIMI
Charge –Energy Mass Spectrometer	CHEMS
Low Energy Magnetospheric Measurement System	LEMMS
Ion and Neutral Camera	INCA
Cosmic Dust Analyzer	CDA
Ultraviolet Imaging Spectrograph	UVIS

---

[2] http://saturn.jpl.nasa.gov/index.cfm

The fields and particles pallet supports the INMS, the CAPS, MIMI CHEMS, and MIMI LEMMS.

The propulsion module subsystem attaches to the bottom of the USS. The primary structure is a cylindrical, semi-monocoque, aluminum shell. Housed within this shell are 2 tanks for bipropellants. Attached to the outside of the shell are a helium tank, spherical monopropellant tank, four thruster booms, two main engines, two pressurant control components assemblies, two propellant isolation components assemblies, and an electronics bay.

The bottom of the spacecraft, also made of aluminum, is named the Lower equipment Module (LEM). Attached to the LEM there are 3 radioisotope Thermoelectric Generators (RTG), 3 reaction wheels and the second low gain antenna (LGA2). The spacecraft design can be observed in the Figure 9.

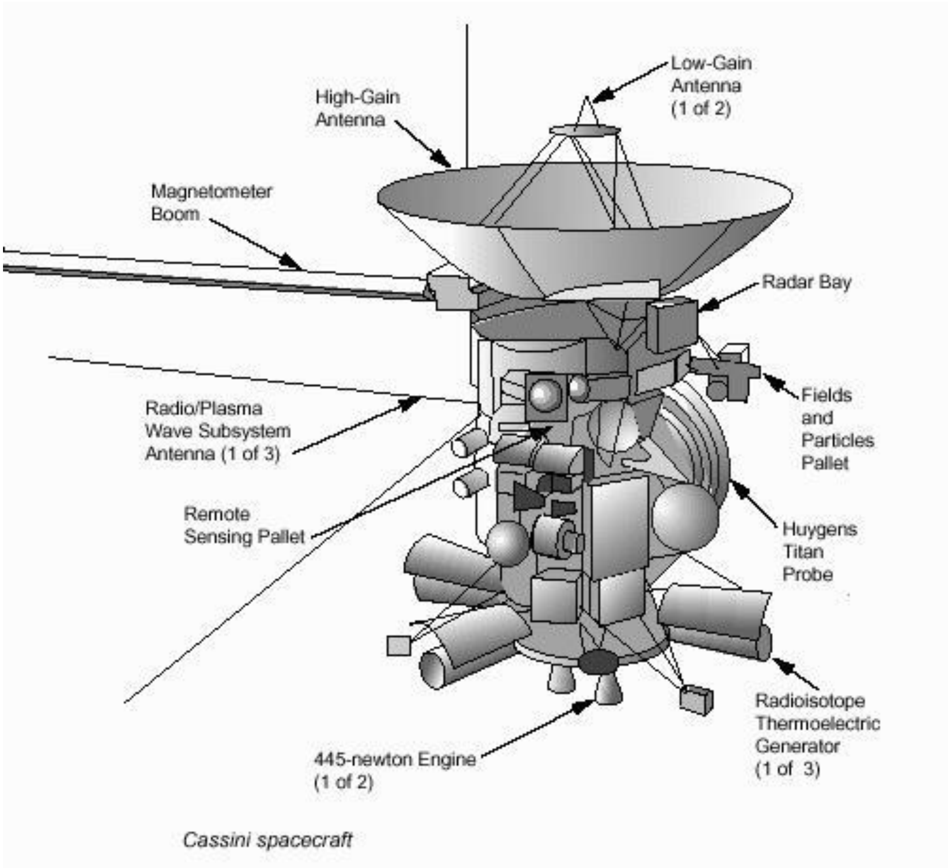

Figure 10 – A perspective view of the Cassini spacecraft (NASA – JPL)

2.2 Scientific goals

As for Titan, during the Primary and Extended mission Cassini investigated the frigid surface revealing vast methane lakes, sand dunes, impact craters and an hydrological activity based on hydrocarbons. Also the structure and complex organic chemistry of Titan's thick, smog-filled atmosphere were thoroughly analyzed. During the Solstice mission the spacecraft will look for signs of seasonal climate change as well as evidence of cryovolcanism.

Between the primary targets for the exploration of the Saturnian System there is Enceladus, a small icy satellite but of great scientific interest because of the presence of active plumes on the surface. Cassini discovered an icy plume, of complex organic composition, shooting from the south pole of the moon, likely due to tidal heating. Saturn magnetosphere also is characterized by a particular activity, deeply influenced by the Enceladus plumes. The water from the jets loads up the magnetosphere, influencing radio and auroral activity, modifying also the rotation of the magnetic field itself.

During the Solstice Mission the spacecraft will also perform repeated dives between Saturn and its rings, in order to obtain in depth knowledge of the gas giant. During these close encounters, the spacecraft will study the internal structure of Saturn, its magnetic fluctuations, and the mass of the rings. Furthermore Cassini will revisit many of Saturn’s icy moons along the Solstice Mission, studying the bright and dark surfaces of Dione and Rhea and the unique thermal features recently discovered on Mimas.

2.3 The RADAR system

During its 7-years mission Cassini has overflight Titan for 71 flybys, and produced 31 RADAR images of the Titan surface. Cassini RADAR instrument is a 13.8 GHz burst mode radar and it produced, in SAR (Synthetic aperture radar) mode, 2000 km long for 200 km wide image strips for each flyby, with an actual total coverage > 30 % of the surface.

RADAR Sensing Instruments

Since the RADAR operates almost exclusively during close flybys of its targets, altitudes will change rapidly throughout the data collection periods. Under such conditions, operations in a multiplicity of modes are a necessity (Elachi, 2005). The instrument was designed to incorporate four modes: imaging (either high or low resolution), altimetry, scatterometry, and radiometry. The basics of operations in these modes are outlined below. An optimal Titan flyby operating scenery, in which all RADAR modes are exercised and a maximum volume of data is collected, calls for about 10 h of uninterrupted operations.

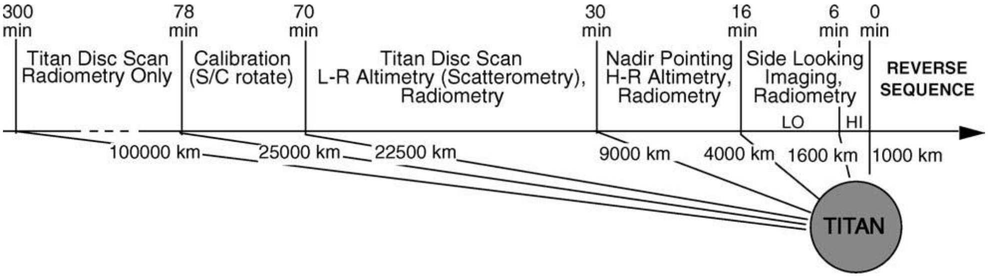

Figure 11 – Operative sequence for a Cassini RADAR flyby (Elachi et al., 2005)

At 5 h away from the closest approach, the spacecraft is about 100,000 km from Titan (Figure 10). At that distance the RADAR is used in the radiometer-only mode. As the spacecraft approaches Titan, the remaining modes are activated; first scatterometry, followed by altimetry, and, finally, imaging. The relative four RADAR sub-systems are:

- Synthetic Aperture Radar Imager [SAR] (13.78 GHz Ku-band; 175 m to 1.4 km resolution)
- Altimeter (13.78 GHz Ku-band; 24 to 27 km horizontal, 90 to 150 m vertical resolution)
- Scatterometer (13.78 GHz Ku-band, 0.1 MHz bandwidth)
- Radiometer (13.78 GHz passive Ku-band; 7 to 310 km resolution)

In the imaging (SAR) mode of operation, radar is mapping the surface of Titan from different incidence angles, providing backscattering images of the target. SAR is used for mapping because of the thick, cloud-infested atmosphere of Titan. Furthermore, in order to improve the surface coverage, the HGA includes a switched, multiple Ku-band, antenna feed array structure, which allows the formation of five antenna beams, used to enlarge the wideness of the image strip. Each of these beams is characterized by a different pointing angle, relative to the antenna reflector's focal axis. The characteristics of SAR system and operation mode are described in 2.4.

In the altimetry mode, the RADAR produced more than 20 altitude profiles of Titan surface; altimetric data, jointly to SAR data, allowed the determination of a global large scale topography (Zebker et al., 2010). In this case the instrument is transmitting energy nearly vertically to the body surface below and records the received echo as a function of time. Then the mean return is used to estimate the mean surface height. The altimetry mode is typically employing only the central, narrow antenna beam, to make time-of-flight measurements of the relative surface elevations along suborbital (nadir) tracks (Elachi et al., 2005). A tight spacecraft pointing toward Titan’s center of mass is required during the time altimetric observations. Last measurements indicating a maximum elevation on the reference sphere equal to +/- 800 m (Zebker et al., 2010).

Table 5 – RADAR Altimeter Mode characteristics (Elachi et al., 2005)

RADAR - High resolution altimetry mode	
Carrier Frequency	13.78 GHz
Carrier wavelength	2.17 cm
Burst period	3333 ms
Pulse width	150 µs
Pulse repetion frequency	4700-5000 Hz
Antenna 3dB beamwidth	0.35 deg
Chirp bandwidth	4.25 MHz
Sample rate	10 MHz
Transmit time	1.4-1.8 ms
Peak transmitted power	48.084 W
Peak antenna gain	50.7 dB
Vertical resolution	35 m
Horizontal resolution	24-27 km

Altimetry corrections can be used into image georeferencing process in order to avoid parallax effects and induced systematic errors.

In the backscatter mode of operation, radar bounces pulses off Titan's surface and then measure the intensity of the energy returning. From the recorded backscatter several information about the surface composition can be inferred. Measurements (Elachi, 2006) show a very geologically varied surface, modified by a mix of processes including strong fluvial, impact, and cryovolcanism.

Finally, in the radiometry mode the radar is passively operating, recording the energy emanating from the surface of Titan and estimating the latent heat in the atmosphere, providing relative calibrations.

During imaging, altimetry, and backscatter operations the radar is transmitting linear, frequency-modulated, Ku-band pulsed signals toward the surface of Titan using the HGA. These signals, after reflection from the surface, are captured by the same antenna and detected by the Radio Frequency Electronics Subsystem. During radiometry operations, the instrument is not transmitting any radar signals, but the HGA is again used for radiometric observations.

Table 6 – Operational modes for Cassini HGA (Henry, 2002)

Antenna	Mode	Frequency (GHz)	Function
HGA			
X-band	Transmit	7.175 ±0.025	Telecommunications
	Receive	8.425 ±0.025	Telecommunications
Ka-band	Transmit	32.028 ±0.1	Science (RFIS)
	Receive	34.316 ±0.1	Science (RFIS)
Ku-band	Transmit & Receive	13.7765±0.005	Science (RADAR)
	Receive	13.8000 ± 0.1	Science (RADAR)
S-band	Transmit	2.298 ± 0.005	Science (RFIS)
	Receive	2.097 ± 0.005	Probe Relay
	Receive	2.118 ± 0.005	Probe Relay
LGAs			
X-band	Transmit	7.175 ±0.025	Telecommunications
	Receive	8.425 ±0.025	Telecommunications

RADAR System specs

The Cassini telecommunication system is formed by the Antenna and Radio Frequency Subsystems. The antenna subsystem includes the High Gain Antenna (HGA) and the two Low Gain Antennas(LGA1, LGA2) plus the associated waveguides. The HGA and LGA1 are mounted on top of the spacecraft facing along the −Z axis. The LGA2 is mounted on the lower equipment module facing along the −X axis (Henry, 2002). The operational modes for Cassini HGA are reported on Table 6, while the functions and associated frequencies are reported on the Table 7 (Henry, 2002).

Table 7 – High and low gain antenna: general features (Henry, 2002)

Antenna	*TX/RX Band*	*Value*
HGA on axis gain	X-band TX	>46.1 dB
HGA on axis gain	X-band RX	>44.3 dB
HGA half power beam width	X-band TX	9.77 ± 0.35 mrad
HGA half power beam width	X-band RX	11.34 ± 0.35 mrad
LGA1 on axis gain	X-band TX/RX	>7.3 dB
LGA1 gain 90 degrees off axis	X-band TX/RX	>−14.0 dB
LGA2 on axis	X-band TX/RX	>4.2 dB
LGA2 gain 90 degrees off axis	X-band TX/RX	>−13.5 dB

The HGA was dedicated to both engineering and science functions (RADAR and Gravity experiments) while the LGAs were assigned to pure engineering functions, but at the moment the possibility to use LGAs also for science purposes is analyzed for the next extension of the mission (Solstice Mission).

2.4 SAR imaging

The primary target for RADAR observations is Titan. Due to its thick, hazy atmosphere the surface was not successfully imaged by previous missions (Pioneer and Voyager) and Cassini RADAR is the first instrument to produce backscatter and altimeter sounding of the surface. Transmitted frequency is equal to 13.78 GHz; for imaging, the bandwidth varies between 0.425 MHz and 0.85 MHz with a data rate of 365 kbps and a peak power of 86 W.

2.4.1 BIDR images

Actually SAR data are processed by JPL in order to produce gridded (raster) maps of Titan and stored as PDS image files, namely called BIDR (*Basic Image Data Records*) products. They are characterized by different bit types and resolutions; provided resolutions are 2,8, 32, 128 and 256 pixels per degree, with map scales respectively of 22.5 km, 5.62 km, 1.40 km, 351 m and 175 m. In the present analysis, only images with 256 pixel per degree resolution were used.

Each BIDR is georeferenced by an oblique cylindrical coordinate system in which the ground track of the spacecraft is defined to be 0° latitude (Stiles, 2008). Its extent will be the minimum bounding rectangle of the coverage area in this projection. Oblique cylindrical projection was chosen because of the highly variable geometry of the Titan flybys from Cassini and the elongated shape of the SAR image footprints. Each pixel in the BIDR image represent the normalized backscatter cross-section, computed using the well-known radar equation:

$$\sigma_0 = \frac{64 P_r \pi^3 L r^4}{P_t G_r G_{ar} G_{at} A \lambda^2} \tag{6.1}$$

where:

P_r - received power for the pixel

P_t - transmitted power

G_r - receiver gain

G_{at} - antenna gain of the pixel at transmit time

L - system loss

r - range to the pixel

λ - the wavelength of the radar signal

G_{ar} - antenna gain of the pixel at receive time

A - area of a nominal pixel projected onto the surface of a sphere

Each pixel in the incidence angle back-plane image is the angle and the antenna look vector. The latitude (longitude) back-planes specify the ordinary latitude (longitude) of each pixel in the IAU standard coordinate system for Titan. This coordinate system is a planetographic latitude *west longitude* system. Image georeferencing is consistent. Furthermore, the reference figure for Titan is chosen to be consistent with IAU recommendations, namely a reference sphere of radius 2575 km. Height corrections are separately applied by a dedicated procedure and are not included into BIDR files.

During the mission the reference rotation model used for georeferencing has been changed several times, into need to adapt new estimates deriving from data with new produced data; for this reason rotational model change (also dramatically) between different versions of the same image or between different phases of the mission. For flybys from Ta up to T36 in the old versions IAU georeferencing (Seidelmann et al., 2006) were used:

$$\begin{aligned} \alpha &= 36.41^\circ - 0.036t + 2.66^\circ \sin(29.80^\circ - 52.1t) \\ \delta &= 83.94^\circ - 0.004^\circ t - 0.30^\circ \cos(29.80^\circ - 52.1t) \\ W &= 189.64^\circ + 22.5769768\,{}^{\circ}\!/_{d}\, d + 2.64^\circ \sin(29.80^\circ - 52.1t) \end{aligned} \qquad (6.2)$$

while for flybys from Ta up to T30 (new release) a specific rotational model determined for the period from (Stiles et al., 2008) was used:

$$\begin{aligned} \alpha &= 41.4644^\circ - 30.1t \\ \delta &= 83.4279^\circ \\ W &= 187.9996^\circ + 22.574677\,{}^{\circ}\!/_{day}\, d + 0.00000071184\,{}^{\circ}\!/_{day^2}\, d^2 \end{aligned} \qquad (6.3)$$

finally, for flybys from T39 up today the a synchronous spin rate model with an updated pole location (Stiles, 2008) is used:

$$\begin{aligned} \alpha &= 39.4827^\circ \\ \delta &= 83.4279^\circ \\ W &= 186.5855^\circ + 22.5769768\,{}^{\circ}\!/_{day}\, d \end{aligned} \qquad (6.4)$$

BIDR Reference Frames

The IAU approved two different types of coordinate systems for planetary mapping:

- *planetocentric* – this reference frame uses planetocentric latitude, defined as the angle between a point, the center of the body and the equatorial plane, and *positive eastward* longitude. This reference frame is universally used in cartographic calculations and it is coincident with the standard right-handed spherical polar coordinate system of mathematics;

- *planetographic* – this reference frame uses planetographic latitude, defined as the angle between the perpendicular to the reference surface at a point and the equatorial plane, and longitude with a positive direction chosen so that the longitude of the disk center increases with time as seen by an observer fixed in the inertial space; for prograde rotators as most of the planets and Titan, this longitude is westward.

This two reference frames are coincident in altitude but opposite for longitude: this is a crucial part of the georeferencing process and the computation of the inertial coordinates.

2.4.2 BIDR Georeferencing

The location of each pixel (in terms of line and sample index in the file) can be inferred from the geographical oblique coordinates using the following equations:

$$\begin{aligned} l &= NINT\left(LPO + \lambda_o(a) * RES + 1\right) \\ s &= NINT\left(SPO + \phi_o(a) * RES + 1\right) \end{aligned} \tag{6.5}$$

l	line index		LPO	line projection offset
s	sample index		SPO	sample projection offset
λ_o	longitude in the oblique cylindrical projection		RES	map resolution
ϕ_o	latitude in the oblique cylindrical projection			

where NINT stands for “nearest integer”. Oblique coordinates can be inferred directly from the pixel location. This is the actually applied procedure to compute the georeferencing directly from the images. Subsequently, the oblique coordinates are converted into the standard body-fixed coordinates (TERF, see Chapter 2) using the opportune rotation matrix:

$$\mathbf{X}_A = M\mathbf{X}_B \tag{6.6}$$

where, for each point (pixel), $\boldsymbol{X}_B$ is the position vector of the point expressed into spherical(indicating with λ the longitude and with ϕ the latitude) body-fixed coordinates:

$$\mathbf{X}_B = \left\langle R\cos\phi\cos\lambda, R\cos\phi\sin\lambda, R\sin\phi\right\rangle^T \tag{6.7}$$

while $\boldsymbol{X}_A$ is the position of the point on oblique coordinates:

$$\mathbf{X}_A = \left\langle R\cos\phi_o \cos\lambda_o, R\cos\phi_o \sin\lambda_o, R\sin\phi_o \right\rangle^T \tag{6.8}$$

The transformation matrix M can be directly inferred from the Cassini state vector:

$$M = \begin{bmatrix} \dfrac{\mathbf{X}_c}{\|\mathbf{X}_c\|} & \dfrac{\mathbf{V}_c}{\|\mathbf{V}_c\|} & \dfrac{\mathbf{X}_c}{\|\mathbf{X}_c\|} \times \dfrac{\mathbf{V}_c}{\|\mathbf{V}_c\|} \end{bmatrix} \tag{6.9}$$

where $\boldsymbol{X}_c$ and $\boldsymbol{V}_c$ are representing respectively the position and the body-relative velocity directions of the Cassini spacecraft in the regular body-fixed reference frame at the time of closest approach. M can be also be written as a 3-2-3 rotation in terms of longitude and latitude of the north pole of the rotated system.

Chapter VII

Results: Titan And The Cassini Rotation Experiment

From 2004 to 2009 the Cassini SAR observations of Titan produced 31 georeferenced images, used to detect 44 crossovers and 243 evident features on the Titan surface. For each feature an apparent shift on the surface (registration error) was observed, due to the differences between the model of Titan rotation used for the georeferencing and the real rotational state.

We analyzed how the position of these features apparently change during time, in order to estimate the pole location and the spin rate of Titan by using the misregistration vectors. The analysis provided useful information on the obliquity, the occupancy of a Cassini state, and, indirectly, the differentiation level of the interior (Bills and Nimmo, 2008).

Since Titan surface is rich with morphological features (lakes, mountains, craters), several features were visually detected and relative regions-of-interest (ROI) were retailed from the SAR images. The ROIs have been cross-correlated in order to compute the relative misregistration vectors. Finally, the optical observables were processed by RSDS with a weighted least squares method in order to estimate the rotational parameters of interest.

1. Background

Before the present analysis the rotation of Titan was known partially from astronomical observations (Seidelmann et al., 2006) and partially from the results of the prime mission (Lorenz et al., 2008). Some of these results were discussed for their geophysical implications and are at the origin of the decision to effort a new, complete estimate of the rotational state. For these reasons the state of the art is briefly reported in the next sections.

1.1. Obliquity and pole location

Before the Cassini mission, the only available rotational model was that provided by IAU (Seidelmann et al., 2006), based on astronomical observations. In this model a null obliquity is assumed and only the precession effects are included. The occupancy of a Cassini State (see Chapter I) is also assumed and the spin axis is supposed to be coincident with the normal to the orbital plane.

Nevertheless, during the Cassini prime mission Stiles et al. (2008) estimated an obliquity value equal to 0.3° and an averaged pole location (α=39.483°, δ=83.428°) referred to the epoch of the observations. This pole location is not compatible with the occupancy of a Cassini state. This is a crucial point, since, if the occupancy of a Cassini state is verified, the obliquity ε can provide information about the polar MoI c (Bills and Nimmo, 2008). Actually c derived from gravity measurements is equal to 0.34, indicating a not homogeneous interior structure and a low density gradient (Iess et al., 2010). The obliquity derived from this measure is equal to 0.115°, far below the estimated value. The missing correspondence between the gravity and the rotation data suggests the presence of a differentiated structure of the interior, but it is actually not explained. For this reason the obliquity and the pole location need to be determined with an improved level of accuracy.

1.2. Spin rate

Before Cassini the spin rate of Titan was derived assuming a synchronous rotation equal to 22.57697 deg/day. First results from the prime mission erroneously showed a super-rotation of 22.5780 deg/day (Lorenz et al., 2008), corrected afterwards into a value equal to 22.57731 ± 0.00011 deg/day (Stiles et al., 2010). Super-rotation was at first explained using the Tokano et al. (2008) circulation model of the atmosphere. Lorenz et al. (2008) showed how the seasonal exchange of angular momentum between the surface and Titan's dense atmosphere allows a shift up to 0.36°/year in apparent longitude for a shell decoupled from the core. In this case the observed deviations from the synchronous value were interpreted as an evidence of a sub-surface ocean. Subsequently the existence of a super-rotation was discussed. Karatekin et al. (2008) showed that for a shell decoupled from the core the gravitational coupling prevents Titan from large deviations from synchronous rotation. In this case the residual not-synchronous rotation due to seasonal changes varies from -0.02 up to 0.04 °/year for the period between 2004 and 2010, one order of magnitude below the observed value. Karatekin et al. (2008) also observed that the forced librations in longitude due to the gravitational attraction of Saturn and the finite eccentricity of Titan cause an additional non-synchronous rotation variation with a much shorter period, equal to the orbital period of Titan around Saturn (15.9454 day).

Also the Goldreich and Mitchell (2009) model of elastic icy shells for Titan and Europa tends to exclude significant deviations from synchronous rotation. If a super-rotation occurred, the tides raised by Saturn on Titan would generate an additional torque tending to restore the synchronous spin. In any case the tidal torque would overwhelm the atmospheric torque. For all these reasons the spin rate is considered as a crucial parameter to estimate.

2. Data processing

Georeferenced SAR (BIDR) images, with a resolution of 175 m, not corrected for the line of sight and reporting the original scattering value σ_0, were used to produce the optical observables.

SAR images were converted from the native oblique cylindrical projection (relative to each observed area), to a rectangular lon/lat projection of the entire satellite (or into a polar stereographic projection in the case of the polar regions), in order to detect the cross-over areas. Once displayed the general map, the most evident features were visually detected. This step is the only non-automatic procedure present in the analysis process and it is consistent with similar methods used by Stiles et al. (2008).

Several pairs of Regions-of Interest (ROI) including the same area but observed at different times were retailed and then matched using 2D cross-correlation as pattern matching algorithm (see Chapter IV for details).

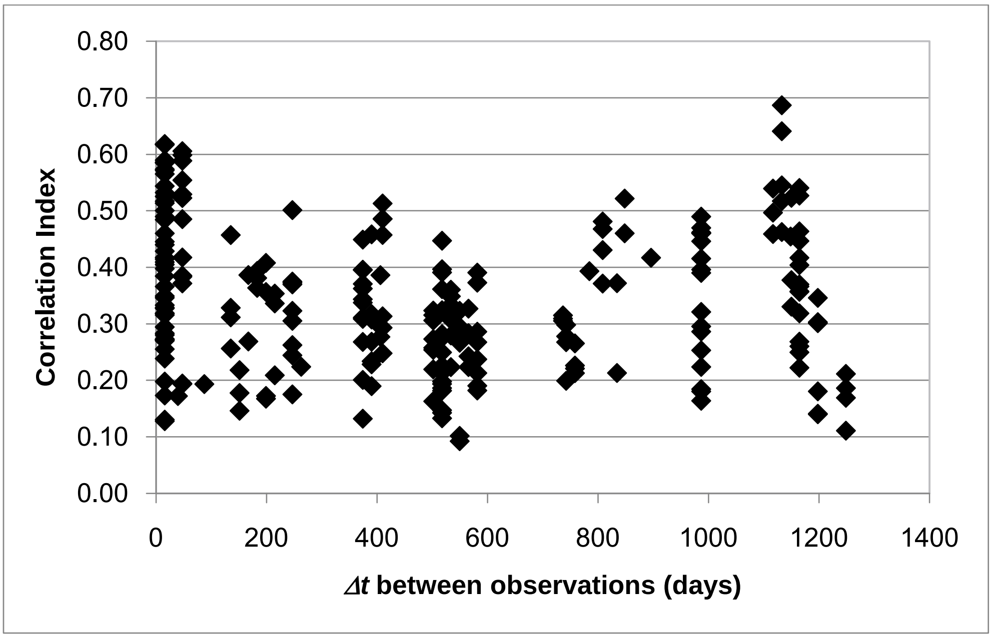

Figure 1 - distribution of I for the time span occurred between the observations

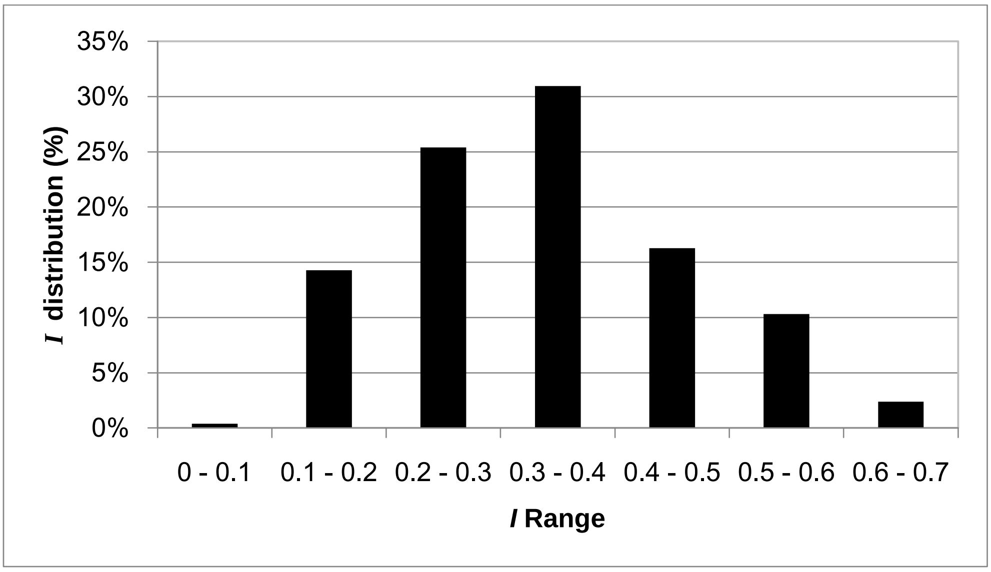

Figure 2 – percentage distribution of I for different correlation ranges

In the specific case the cross-correlation was preferred because of the robustness of the method and the short computational times (few minutes against several hours of elaboration for the mutual information), assuring 1 pixel accuracy (~170 m), sufficient for our purposes.

For the data set of 243 tiepoints the correlation index *I* vary from 0.09 up to 0.7, where 31 % of tiepoints are included in a range between 0.3 and 0.4. Low correlation index were expected for the effects of not – corrected line of sight on the image quality, but 60% of the tiepoints typified by I > 0.3 and 50% of these has a correlation index >0.4, indicating a sufficient consistency of the data. In order to analyze dependencies from time interval (Δt) between observations the temporal distribution of the observations with respect to *I* (Fig. 2) has been calculated, showing a uniform distribution over the analyzed time range (up to 1400 days) and the independence from observational Δt.

2.1. Error budget

In a theoretical error-free case the maximum reachable precision of the applied model is equal to the image resolution (~ 170 m) and it would be reasonable to expect residuals of the order of a few hundreds of meters. Nonetheless, data are affected by systematic error components.

The errors on the determination of Cassini ephemeris in terms of position and velocity can give rise to not negligible errors in the georeferencing. A preliminary study by Stiles et al. (2008) for the prime mission provided an estimate for the ephemeris error < 100 m. For this work an analysis of the covariance matrix provided by Cassini Navigation Team for the RADAR flybys was performed, determining uncertainties of the Cassini position vector between 100 and 200 m.

Similarly, the systematic effects due to transmission errors, echo delay and other effects were also estimated (Stiles et al., 2008) ~ 100 m. The error budget is reported on Table 1. It can be observed that the most relevant systematic error component is tied to the topography. Assuming a spherical Titan could lead to an error of 400-500 m in pixel location for an altitude error equal to 200 m, and up to 1 km and more, if the error is larger (Stiles et al., 2008). For this reason we asked to the RADAR team to provide the height correction for the produced dataset in order to remove the error source (Meriggiola et al., 2011). The corrections derived from the combination of the Doppler and Ranging values with topography are not applied. The correlation error has also to be taken into account. In this case it was assumed a 1 pixel accuracy for the current analysis, resting upon a dedicated pattern matching test. In order to calculate the uncertainty associated to the observables (misregistration vectors) and the relative weight matrix all the previously mentioned error sources have to be considered. A conservative value equal to 2 km was assumed for the uncertainty σ_0 associated to the observables, taking into account all the error sources. This is the actual configuration used for the estimate.

Table 1 – Error budget for the Titan Rotation Experiment

Error Sources	Estimate	Description	Reference
Georeferencing	0.1÷ 0.2 km	Error on the determination of Cassini ephemerides	NAV
Transmission	0.1 km	Echo delay and other effects	Stiles et al. 2008
Line of sight correction	0.1 km	Angle of incidence effects	Stiles et al. 2008
Height correction	0.4 ÷ 2 km	Spherical Titan assumption	Stiles et al. 2008
Correlation	0.2 km	Correlation error	Estimated
Total	1 km ÷ 3 km		

Several tests were also performed to compute the uncertainty of each observable σ_{obs} by using the correlation index as an amplification factor:

$$\sigma_{obs} = \frac{\sigma_0}{I} \tag{7.1}$$

where, if *I* is equal to 1 (max correlation) the weight of the observable is equal to the threshold value given by σ_0. In any other case σ_{obs} is linearly amplified by *I*. This quite conservative method to define the uncertainty associated to the observables is predicted to be used in order to assign a different weight to each observable.

3. Data analysis

The analysis includes 243 features with registration errors between 400 m and 40 km. The time span of the observations goes from 2004 to 2009, covering both the Cassini prime and extended mission. For the Prime (PM) Mission (2004-2007) the observed landmarks are mainly distributed on northern hemisphere, while during the Extended Mission (EM) the coverage of the southern hemisphere was significantly improved (Figure 3). This difference into the coverage should be taken into account when considering the estimate for the spin axis direction and the spin rate. All results here provided were obtained using the height corrected tiepoints.

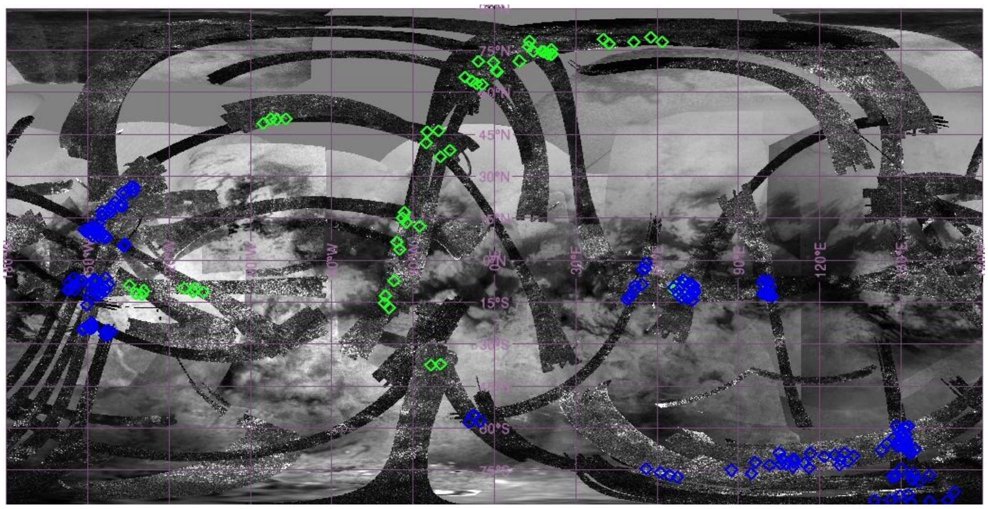

Figure 3 – current SAR coverage and detected landmarks for Titan; the green tiepoints are relative to Prime mission , while the blue are derived from Extended mission data.

3.1. Observation periods and applied models

Data were analyzed dividing the observations for mission phase:

- Prime Mission (PM, 2004 -2007),
- Extended Mission (EM, 2007-2009),
- Prime + Extended mission (P+E, 2004-2009).

Considering the nature of the technique, the PM includes strictly observations between 2004 and 2007, while the EM dataset is including only the observations where at least one of the tiepoints was observed on the EM period. The P+E dataset is the sum of the PM and EM dataset.

Used Rotational Models

Three different rotational models were used into the estimate process, in order to analyze the differences and to improve the residuals. Initially only the spin rate and the pole location in terms of right ascension and declination were estimated, without considering any precession term or time drift. So the *Estimate at the Observation Epoch* was performed. This is a shot of the observations at an average epoch (2007), used to be compared with the previous estimate (Stiles et al., 2008). Nevertheless in this case the results cannot be strictly considered a rotation model. For this reason two available models were used and some of their coefficients estimated, in order to provide their updated versions. The first is the *IAU Model,* still used for georeferencing, which includes the time drift and the precession effects. The second is a model considering also the nutation terms. Nutations and other short period effects (librations, seasonal variations tied to the atmosphere) could have a relevant impact on the residuals and they should be included at least in the model, if not in the estimate. This is the reason why the *NAV model* was introduced. This model has been developed at JPL (R. Jacobson, private communication) to be used by Cassini Navigation team and it is a further refinement of the IAU model.

3.2. Preliminary analysis and generation of the dataset

The *General* dataset (243 features) was the first to be analyzed. Due to different epoch of data production, the set includes also uncalibrated data (T43 and T44 flyby), affected by a potential error level between 2 and 4 km (Stiles, private communication), and for this reason subsequently removed. After preliminary tests, also 8 outliers were detected into the General dataset. Finally, a systematic component of error for the tiepoints of a specific crossover (T55-T56) was detected. Since other observables derived from T55 and T56 flybys are perfectly able to fit the model, this trend could be explained by an error in the correlation process. The *Calibrated* data set (160 features) does not include the uncalibrated data, the outliers, and the T55-T56 crossover tiepoints.

In order to analyze the quality of the fit for each tiepoint it is possible to defining the *reduction factor* (RF) as the percentage difference between the pre-fit and post-fit norms of the misregistration vectors ($\Delta\boldsymbol{\rho}$) :

$$RF = \frac{\|\Delta\boldsymbol{\rho}\|_{prefit} - \|\Delta\boldsymbol{\rho}\|_{postfit}}{\|\Delta\boldsymbol{\rho}\|_{prefit}} \tag{7.2}$$

The percentage reduction of the registration error shows an average value of 85 %, with peaks of 95 % (Figure 4). For the landmarks characterized by an initial registration error smaller to 1 km the error reduction is null (15% or less) or negative. This is due to the fact that for these features the observed (pre-fit) registration error is below the 1 km threshold for the systematic errors predicted by the error budget and confirmed by post-fit residuals.

In the calibrated dataset an average post-fit error level equal to ~ 4 km involving some specific flybys (T3, T7, T21, T41 and T61) can be observed. A deep investigation of these flybys showed some common characteristics:

- all crossing the equatorial belt
- presenting for 45% SARTopo height corrections < 100 m
- showing postfit residuals with a reduction factor 60% (vs. 85-90% for the other tiepoints)

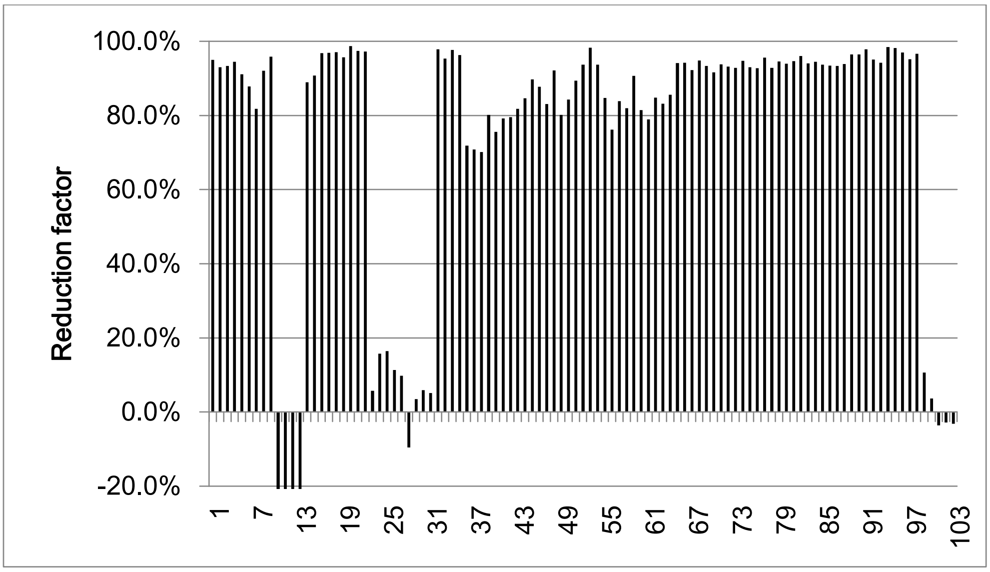

Figure 4 – Reduction factor for the Benchmark dataset

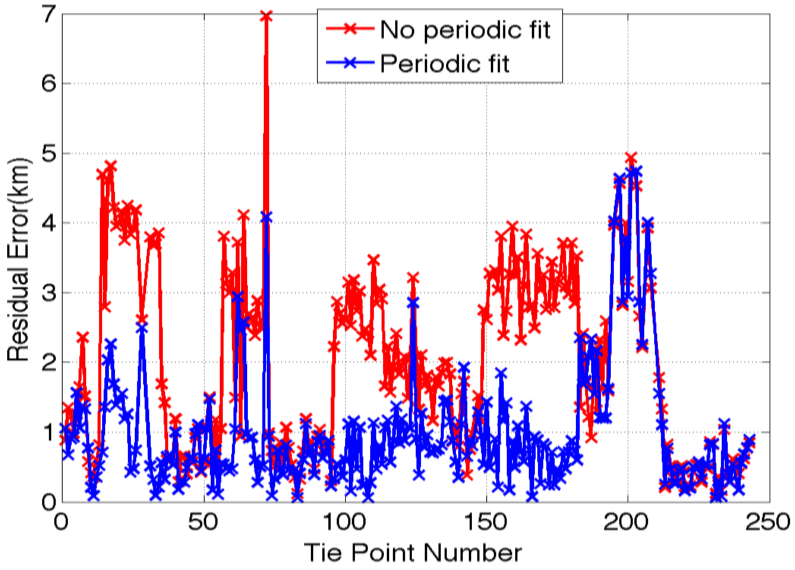

Figure 5 - Residuals trend for the Calibrated dataset with and without periodic terms (B.W. Stiles, a courtesy of NASA - JPL)

Short period oscillations could be added as a possible explanation for this trend. An improvement in the residuals up to 1.5 km can be observed including an a-priori half Saturn year periodic terms (Figure 5) in the formulation. It is possible that the couple of observations on a time scale (2004-2009) comparable to the nutation period could be heavily affected from the missing nutation modeling. For the previous reasons, three distinct data sets were selected to be used in the estimate process:

- *General* (243 features) - includes all the available data;
- *Calibrated* (160 features) - includes only the calibrated data;
- *Benchmark* (103 features) - data not affected by short period effects.

Residuals varying 0.7 - 1 km for the Benchmark and 1.7 - 2 km for the General data set. Taking into account the results of the simulations (Chapter V) and the previous considerations about the error sources, the Benchmark post-fit residuals show a value fully compatible with the estimated error budget (see 4.1, 5.1.1, 5.2.1, 6.1.1, 6.2.1). Actually the benchmark case could be considered as the best available estimate. The presence of short period oscillations affect the solution, even if the rotational parameters can be estimated with sufficient accuracy (see Section 4). Tiepoints with best postfit residuals use most recent data, georeferenced using (Stiles et al., 2008) estimate of the pole location and a synchronous value for the spin rate. This has reduced the residual error in the fit.

4. Estimate at Observation Epoch

In this case a simplified model was used in order to estimate an average value of the pole location and the spin rate along the time span of the observations. The estimate is performed not considering the contribution of the time drift, the precession or the short period variations. For these reasons α, δ and ω were directly estimated from the observables.

4.1. Residuals

General dataset including not calibrated data shows (Figure 6) as expected the worst residuals, with an average of the residual norms varying from 1.7 (PM) up to 2.3 km (P + E). The residuals for the Calibrated dataset are varying from 1 to 1.7 km, with a reduction of the error around 30%. The contribution of the error due to the missing calibration (for some data) can then be quantified in an average value ~ 600 m. The residuals for the Benchmark dataset are < 1 km, varying between 700 (PM) and 900 m (P+E). It should be observed that for the Calibrated dataset the most relevant component of error is relative to EM. This is likely due to the effects of short period oscillations.

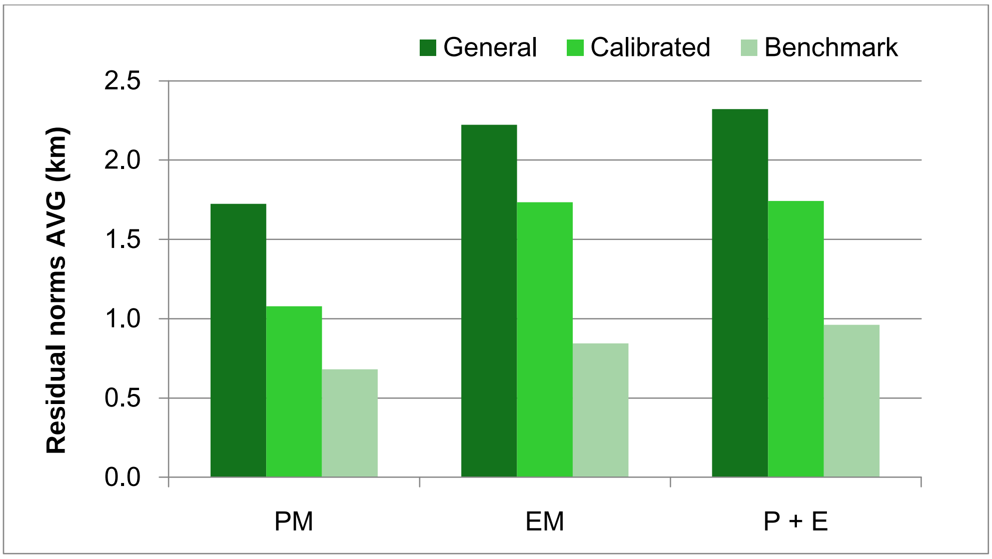

Residual norms AVG (km)			
Dataset	General	Calibrated	Benchmark
PM	1.72	1.08	0.68
EM	2.22	1.74	0.84
P+E	2.32	1.74	0.96

Figure 6 - Average of the residual norms for the Estimate at the Observation Epoch case

4.2. Pole location

The only previous available estimate (Stiles, 2008) for the position of the pole is based on the analysis of PM data and it is an averaged value strongly dependant from the epoch of the observations. Furthermore, it does not take into account the precession effects, but only the linear drift terms. This first estimate was subsequently corrected on (Stiles, 2010) but the first version is still currently used for part of the SAR image georeferencing. In this section we will show the results of the correspondent estimate using also the data for the EM and the P+E. The aim is to compare the results with (Stiles et al., 2008). The estimate of the pole location allows to determine the obliquity of the satellite, one of the goals of the current analysis.

Right Ascension

The Right Ascension at the Epoch (α) for P+E case is equal to 39.41° ± 0.036°, compatible with the previous estimate of 39.483° ± 0.025° (Stiles et al., 2008). Benchmark solution (39.45°) is even closer to the previous estimate, included in 1-σ range for all the solutions (Figure 7). Differences between PM and EM are likely due to the short period oscillations.

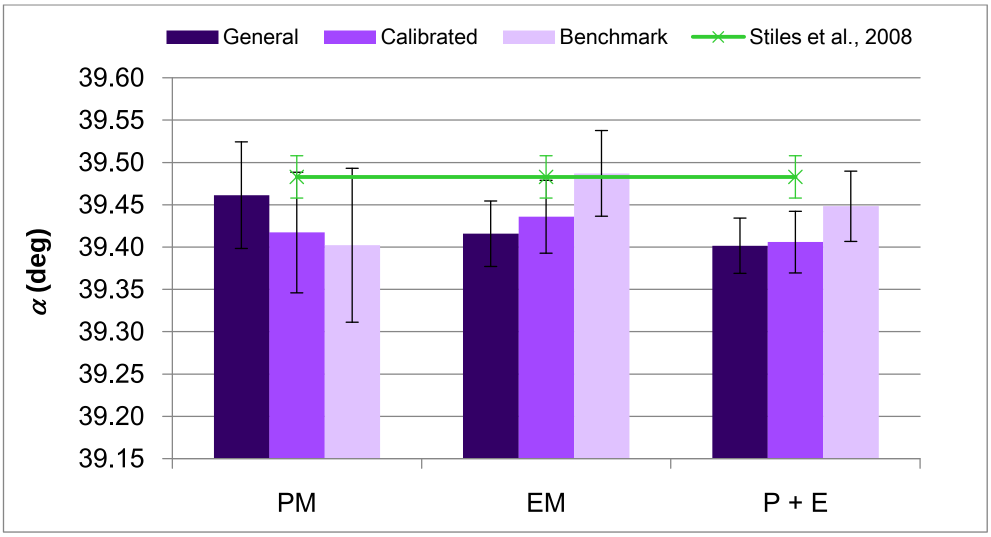

Estimate at Observation Epoch: α (deg)

	General	St.Dev.	Calibrated	St.Dev.	Benchmark	St. Dev
PM	39.46	6.3E-02	39.42	7.1E-02	39.40	9.1E-02
EM	39.42	3.9E-02	39.44	4.3E-02	39.49	5.1E-02
P+E	39.40	3.3E-02	39.41	3.6E-02	39.45	4.2E-02

Figure 7 - RA estimated values for the Estimate at Observation Epoch case

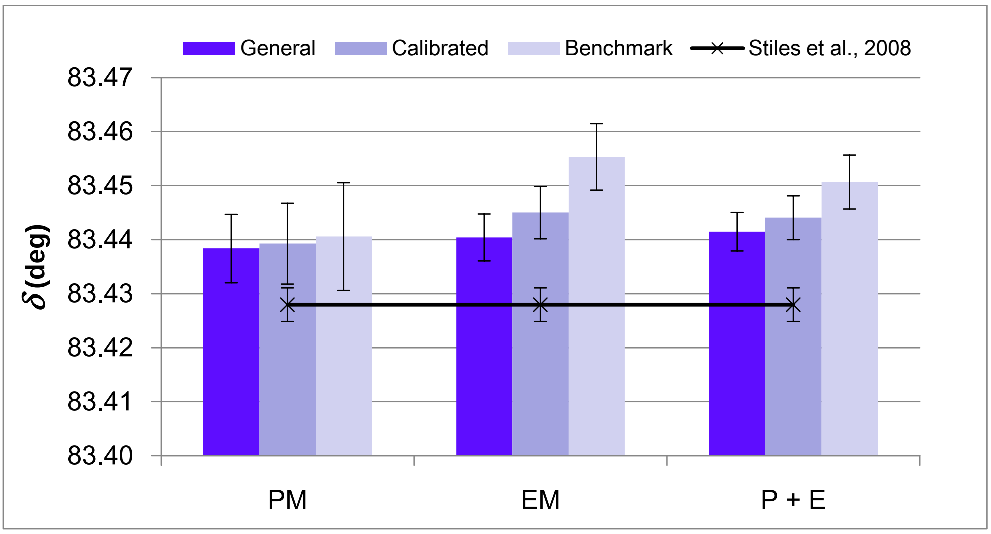

δ (deg)						
	General	St.dev.	Calibrated	St.dev.	Benchmark	St. Dev.
PM	83.438	6.3E-03	83.439	7.5E-03	83.441	1.0E-02
EM	83.440	4.3E-03	83.445	4.8E-03	83.455	6.1E-03
P+E	83.442	3.6E-03	83.444	4.1E-03	83.451	5.0E-03

Figure 8 - DEC estimated values for the Estimate at Observation Epoch case

Declination

Declination is varying from 83.44° to 83.45°, with an average value of 83.445° included into 1-σ range for all estimated values (Figure 8). Estimated values are compatible with (Stiles et al., 2008) estimate (83.428° ± 0.003°) in 1-σ range for the PM and 2-σ range for EM and P+E, respectively. Declination is very sensitive to changes into the observation period and selected dataset. A difference of 0.02° can be observed for Calibrated data between PM and EM; the difference is wider for the Benchmark data. Such differences can be likely ascribed to short period effects.

Error ellipses

From the covariance matrix of the system we computed also the error ellipses for the pole location; we reported the P+E case in the Figure 9. The error ellipses are reported at 1-σ range. It can easily observed the almost null cross-correlation between the estimated values of right ascension and the declination. The most relevant difference between Benchmark dataset and the other estimates is a difference equal to ~ 0.008° in declination and equal to ~ 0.04° in right ascension. The (Stiles et al., 2008) estimate is out of the error ellipses in all the three cases, but it is included in the case of error ellipses at the 3-σ range.

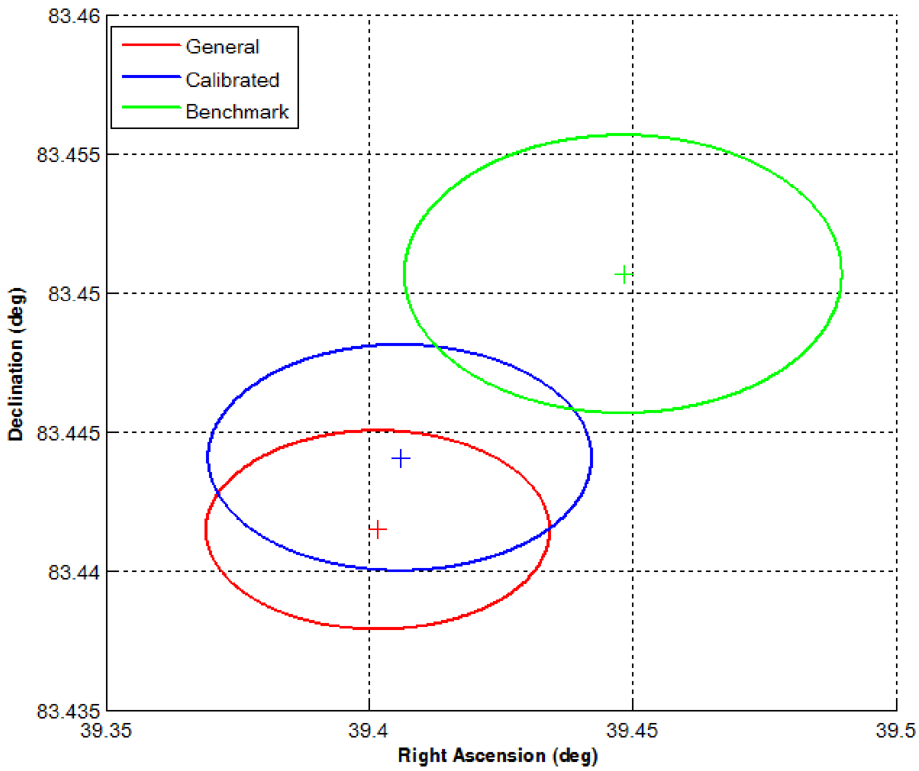

Figure 9 - Error ellipses at 1-σ range for the P+E Estimate at Observation Epoch

4.3. Spin rate

In this case the measured spin rate is estimated not including any precession term into the formulation for the prime meridian W:

$$W = W_0 + \dot{W}_0 d = W_0 + \omega d \tag{7.3}$$

where the Prime Meridian at the J2000 Epoch W_0 is assumed as known and equal to 189.64° (Seidelmann et al., 2006). *d* is the time expressed in days while the spin rate ω is expressed in deg/day. The most remarkable result of the estimate is the compatibility with the synchronous rotation (Figure 10). For the PM the estimates include the IAU predicted value for the spin rate into 1-σ range, while for the EM the difference is wider, and the synchronous solution is included into 3-σ range. The residual non-synchronous rotation (NSR) is below 0.02 deg/year for the PM and about -0.02 deg/year for the EM, and it is possible to observe a sign inversion between the PM and the EM. This sign inversion has been predicted by (Karatekin et al., 2008) and could likely be explained by the atmospheric seasonal changes which occur during the 2004 -2010 time span (see 8.2 for details).

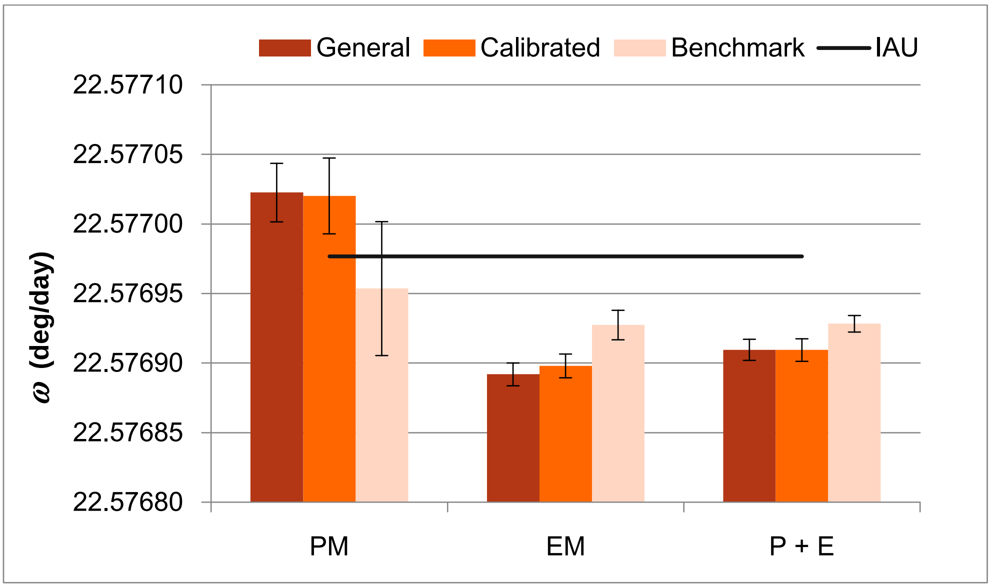

Spin Rate (deg/day)						
Dataset	General	St.dev.	Calibrated	St.dev.	Benchmark	St. Dev.
PM	22.57702	2.1E-05	22.57702	2.7E-05	22.57695	4.8E-05
EM	22.57689	8.2E-06	22.57690	8.5E-06	22.57693	1.1E-05
P+E	22.57691	7.6E-06	22.57691	8.1E-06	22.57693	5.9E-06

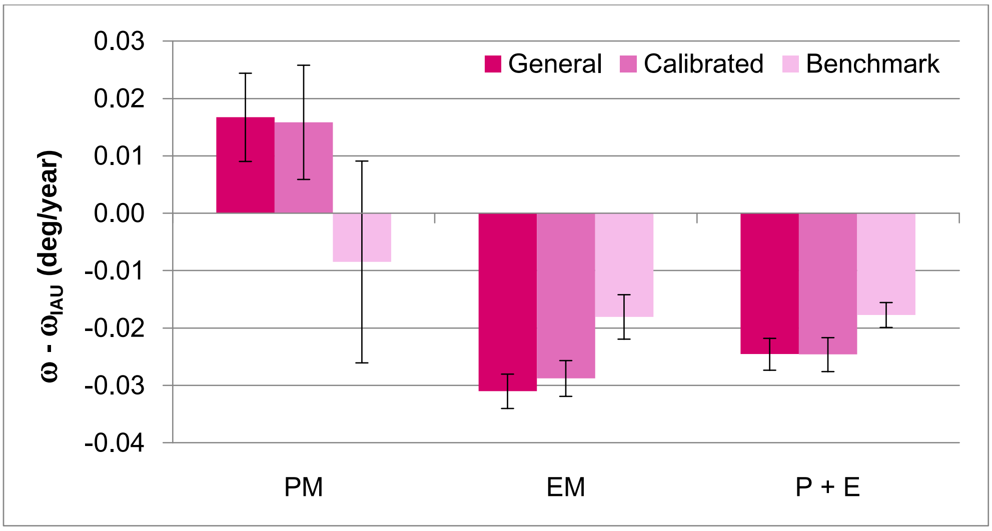

Not Synchronous Rotation (deg/year)						
Dataset	General	St.Dev.	Calibrated	St.Dev.	Benchmark	St.Dev.
PM	0.017	7.7E-03	0.016	1.0E-02	-0.008	1.8E-02
EM	-0.031	3.0E-03	-0.029	3.1E-03	-0.018	3.9E-03
P+E	-0.025	2.8E-03	-0.025	3.0E-03	-0.018	2.2E-03

Figure 10 - Estimated spin rate and NSR for the Estimate at Observation Epoch

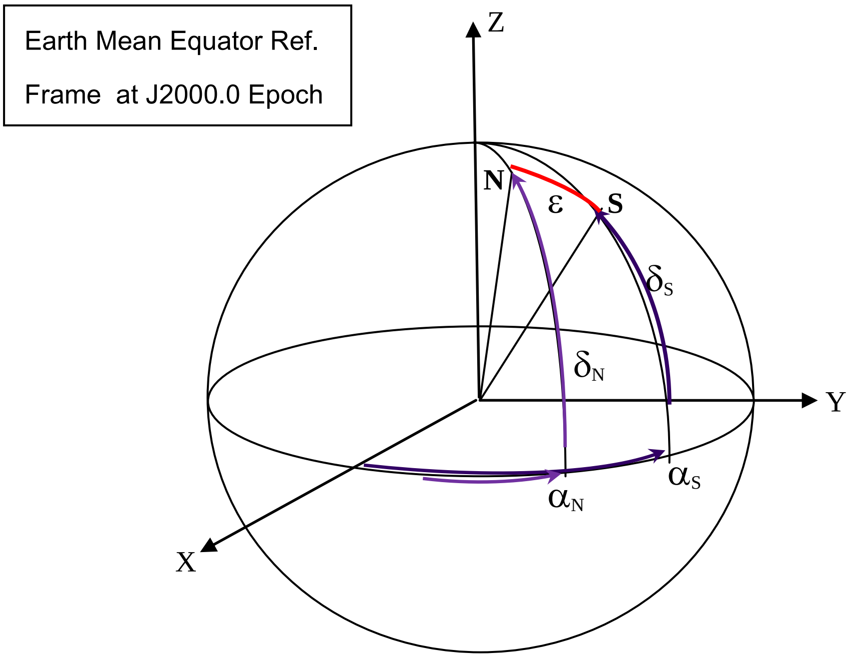

Figure 11 - Spin axis (S), normal to the orbital plane (N) and obliquity (ε) in the EMEJ2000 reference frame. Please notice the relative spherical coordinates, expressed in terms of right ascension (α) and declination (δ).

4.4. Obliquity

The obliquity ε is defined as the angle between the plane of the equator and the mean orbital plane (Figure 11). Subsequently ε can be computed as the angle between the normal to the orbital plane (**N**) and the spin axis (**S**), expressed in the EMEJ2000 coordinates. The normal to the orbital plane is computed using the JPL DE421 ephemeris; the spin axis direction is expressed in terms of right ascension (α) and declination (δ) at the reference epoch. As reference epoch was selected an average epoch between the observations for each dataset. Obliquity ε was then computed directly from the estimated α and δ at reference epoch. Obliquity is computed as the dot-product of **N** and **S**:

$$\cos\varepsilon = \mathbf{N}\cdot\mathbf{S} = N_x S_x + N_y S_y + N_z S_z \qquad (7.4)$$

where N_i and S_i are the rectangular EMEJ2000 coordinates. For a unit sphere it is possible to make explicit the dependence of ε from α and δ as:

$$\varepsilon = \arccos\begin{pmatrix} \cos\delta_N \cos\alpha_N \cos\delta_S \cos\alpha_S + \\ \cos\delta_N \sin\alpha_N \cos\delta_S \sin\alpha_S + \\ \sin\delta_N \sin\delta_S \end{pmatrix} = \arccos\left(f_{\alpha,\delta}\right) \qquad (7.5)$$

where $\alpha_{N,S}$ and $\delta_{N,S}$ indicate respectively the right ascension and the declination of **N** and **S**.

Error propagation for the obliquity

It is then possible to compute the standard deviation associated to ε from the well-known theory of error propagation as:

$$\sigma_{\varepsilon}^2 = \left|\frac{\partial \varepsilon}{\partial \alpha_S}\right|^2 \sigma_{\alpha S}^2 + \left|\frac{\partial \varepsilon}{\partial \delta_S}\right|^2 \sigma_{\delta S}^2 + 2\frac{\partial \varepsilon}{\partial \alpha_S}\frac{\partial \varepsilon}{\partial \delta_S}\operatorname{cov}(\alpha_S, \delta_S) \tag{7.6}$$

Partial derivates of the obliquity with respect to α and δ are then calculated as:

$$\begin{aligned} \frac{\partial \varepsilon}{\partial \alpha_S} &= -\frac{1}{\sqrt{1 - f^2{}_{\alpha,\delta}}}\frac{\partial f_{\alpha,\delta}}{\partial \alpha_S} \\ \frac{\partial \varepsilon}{\partial \delta_S} &= -\frac{1}{\sqrt{1 - f^2{}_{\alpha,\delta}}}\frac{\partial f_{\alpha,\delta}}{\partial \delta_S} \end{aligned} \tag{7.7}$$

where:

$$\begin{aligned} \frac{\partial f_{\alpha,\delta}}{\partial \alpha_S} &= -\cos\delta_N \cos\alpha_N \cos\delta_S \sin\alpha_S + \cos\delta_N \sin\alpha_N \cos\delta_S \cos\alpha_S \\ \frac{\partial f_{\alpha,\delta}}{\partial \delta_S} &= -\cos\delta_N \cos\alpha_N \sin\delta_S \cos\alpha_S - \cos\delta_N \sin\alpha_N \sin\delta_S \sin\alpha_S + \sin\delta_N \cos\delta_S \end{aligned} \tag{7.8}$$

For the P+E case the obliquity is equal to 0.310° ± 0.005° (Benchmark), an estimate included into 1-σ range for all the considered datasets (Figure 12). The estimates for EM are practically equivalent (0.31°). In the PM case, an average larger value is estimated (0.32° ± 0.008° for Benchmark dataset) but still compatible into 2-σ range with the other estimates. The solutions are compatible with the previous estimate of 0.3° (Stiles et al., 2008). Variations of the obliquity between the PM and the EM could be likely added to the effect of short period oscillations.

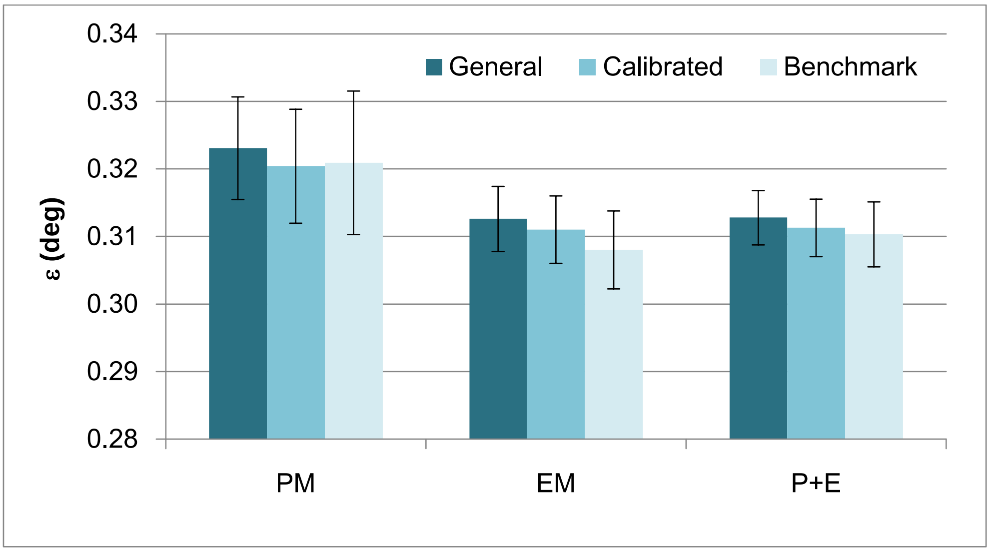

Obliquity (deg) - Ref epoch

Dataset	General	St.Dev.	Calibrated	St. Dev.	Benchmark	St.Dev.
PM	0.323	7.6E-03	0.320	8.4E-03	0.321	1.1E-02
EM	0.313	4.8E-03	0.311	5.0E-03	0.308	5.8E-03
P+E	0.313	4.0E-03	0.311	4.3E-03	0.310	4.8E-03

Figure 12 - Estimated values of the obliquity for the Estimate at Observation Epoch

5. Estimate by the IAU Model

In this case the IAU rotational model (see Chapter II) was used, in order to describe the spin motion along the observational period. The Prime Meridian at J2000 Epoch, the precession period and the time drift of the pole are assumed as known. The following formulation was adopted for the model:

$$\alpha = \alpha_0 + \dot{\alpha}_{0\,IAU} t + \beta_{\alpha\,IAU} \sin\left(\gamma_{IAU} + \chi_{IAU} t\right) \tag{7.9}$$

$$\delta = \delta_0 + \dot{\delta}_{0\,IAU} t + \beta_{\delta\,IAU} \cos\left(\gamma_{IAU} + \chi_{IAU} t\right) \tag{7.10}$$

$$W = W_0 + \omega_{0\,IAU} d + \beta_{W\,IAU} \sin\left(\gamma_{IAU} + \chi_{IAU} t\right) \tag{7.11}$$

For Titan the IAU model includes only the precession terms (first order of the trigonometric series) while the nutation terms are not provided.

Table 2 - IAU numerical coefficients of the Titan rotational model

Parameter	Value	Unit
α_0	36.41	Deg
δ_0	83.94	Deg
W_0	189.64	Deg
$\dot{\alpha}_0$	-0.036	deg/century(s)
$\dot{\delta}_0$	-0.004	deg/century(s)
ω	22.5769768	deg/day

The numerical coefficients for the parameters are reported in the Table 2, while the numerical coefficients for the precession terms are reported in the Table 3. Two different types of estimate are here reported. In the first, the *3 parameters fit,* the precession terms are assumed as known. This assumption is then partially removed in the *4 parameters fit*, where the amplitudes of the precession terms for RA and DEC are estimated.

5.1. The 3 parameters fit

Differently from the previous case, where the averaged values for the pole location (α, δ) and the spin rate (ω) were directly estimated for the observational period, in this case we tried to determine the rotational parameters for a model which is a function of the time. We estimated the right ascension and declination of the pole ($\alpha_{0,}\delta_0$) and ω, assuming as known the time drift ($\dot{\alpha}_0$, $\dot{\delta}_0$), the position of the Prime Meridian (W_0) and the precession terms. This assumption is a linear approximation around the observed point and it is valid for the linear drift terms and the precession period, but it has its own limitation into the precession amplitude. Since the numerical values of the IAU model are provided for the case with null obliquity, the fixed amplitude of the precession terms will generate an "over estimation" of the pole location. In any case the estimate it is still useful to determine a limit to the estimated values of α_0 and δ_0 and to observe any change of the estimated ω.

Table 3 - IAU Numerical coefficients for the precession terms

Order	Term	β (deg)	$\gamma + \chi t$ (deg + deg/centuries t)	Period (years)
1	$\beta_{\alpha,1}$	2.66	29.80 - 52.1 t	722
	$\beta_{\delta,1}$	-0.30		
	$\beta_{W,1}$	-2.64		

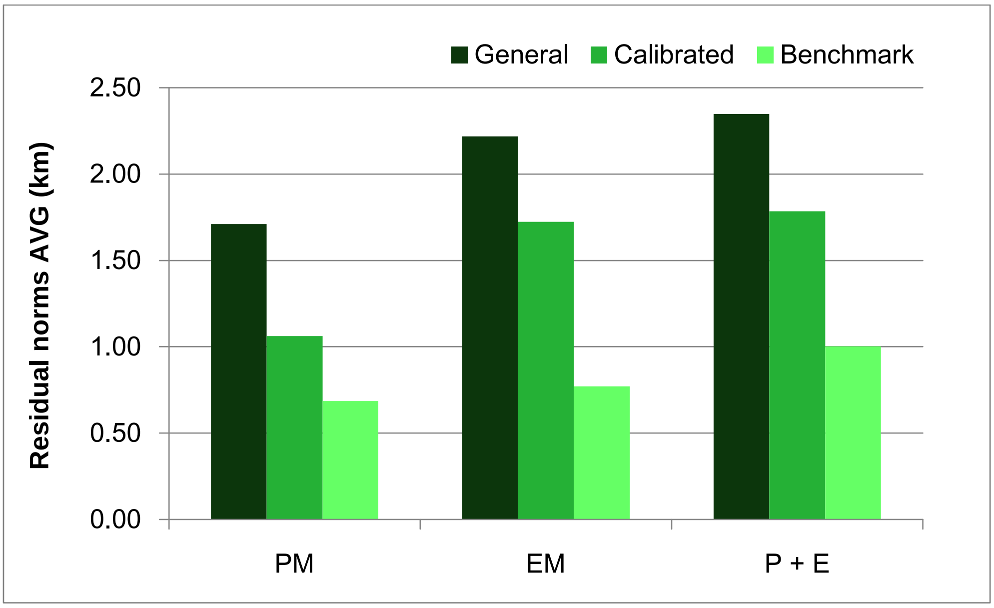

Residual norms AVG (km)			
Dataset	General	Calibrated	Benchmark
PM	1.71	1.06	0.69
EM	2.22	1.72	0.77
P+E	2.35	1.78	1.00

Figure 13 - Average of the residual norms for the 3 parameter fit - IAU model

5.1.1. Residuals

For the PM the residuals vary from 690 m to 1.71 km, where both Calibrated and Benchmark dataset show a level of accuracy minor or equal to the best case value (900 m) of the error budget (Figure 13). In this case the PM estimates show a slight (5%) improvement with respect to the Estimate at the Observation Epoch. This slight improvement is confirmed also for the Extended mission, where the residuals vary from 770 m to 1.72 km. For the P+E case the residuals vary from 1 to 2.35 km. Similarly to the previous estimate, the EM and the P+E trend is likely due to the short period effects not included in the model.

5.1.2. Pole location

Right Ascension

For the PM the estimated α_0 vary between 38.23° (Benchmark) and 38.29° (General). The Calibrated solution is equal to 38.25° ± 0.071°. For the EM the solution is stable for General data set, but it rises up for Calibrated (38.30°) and Benchmark (38.35°) datasets.

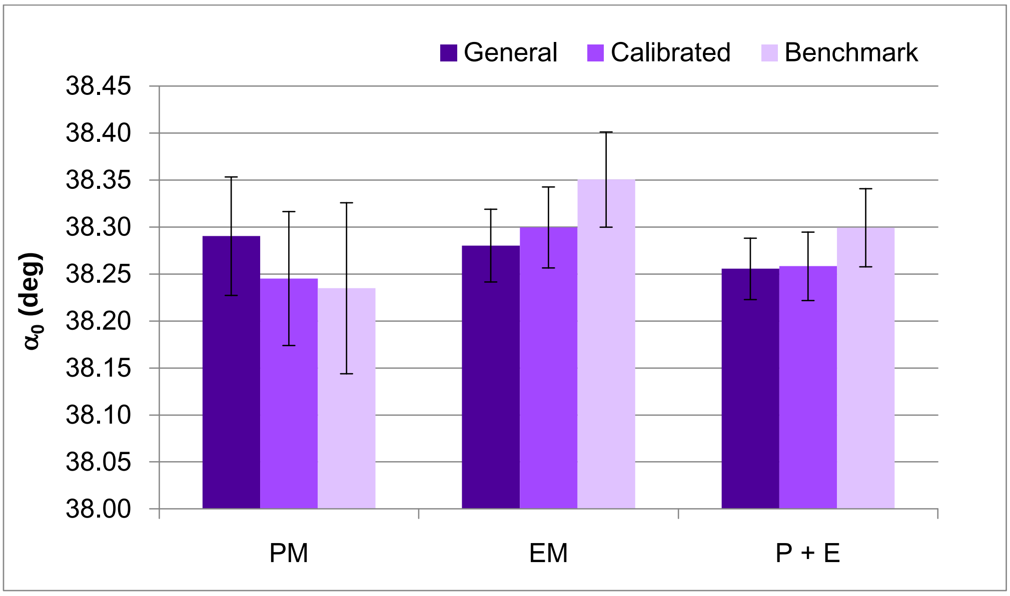

IAU Model - α_0 (deg)

Dataset	General	St.Dev.	Calibrated	St. Dev	Benchmark	St. Dev.
PM	38.29	6.3E-02	38.25	7.1E-02	38.23	9.1E-02
EM	38.28	3.8E-02	38.30	4.3E-02	38.35	5.1E-02
P + E	38.26	3.3E-02	38.26	3.6E-02	38.30	4.2E-02

Figure 14 – Estimated α_0 for the 3 parameters fit - IAU Model

Finally, considering the P+E case, the estimated value (Benchmark) for α_0 is equal to 38.30° ± 0.042°, a value included in a 2-σ range of all the analyzed datasets and observational periods (Figure 14). These values are 1.5° far from the initial, estimated value of 36.41° (Seidelmann et al., 2006), but they can be explained with the fixed amplitudes for the precession terms, computed assuming a null obliquity. In this case the α_0 variation is larger than the real value to compensate the missing contribution of the precession terms. Furthermore, short period oscillations are not included.

Declination

δ_0 is estimated at a level of accuracy of 10^{-3} deg, an order of magnitude better than α_0. For the PM the estimated values vary between 83.708° (General and Calibrated) and 83.710° (Benchmark). In the EM case the estimated solutions vary between 83.713° (General) and 83.728° (Benchmark). A 0.01° difference between the PM and the EM can be observed (Figure 15). For the P+E the estimated value (Benchmark) for α_0 is equal to 83.722° ± 0.005° (General: 83.713 ± 0.004°), a value included in a 2-σ range for all the analyzed datasets. For the reasons previously provided for the right ascension, all the estimates differ significantly from actual IAU value equal to 83.94° (Seidelmann et al., 2006).

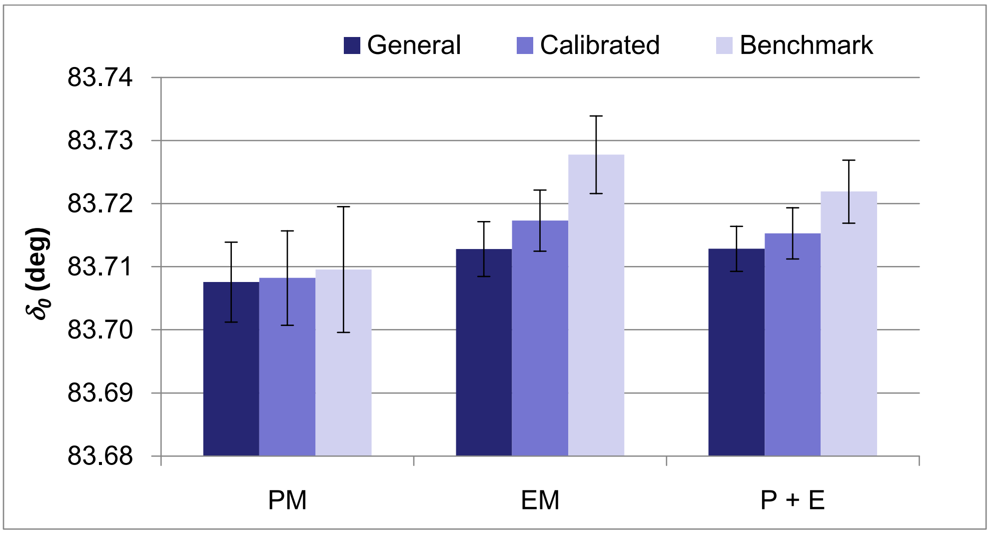

IAU Model: δ0 (deg)						
Dataset	General	St.Dev.	Calibrated	St. Dev.	Benchmark	St. Dev.
PM	83.708	6.3E-03	83.708	7.5E-03	83.710	1.0E-02
EM	83.713	4.3E-03	83.717	4.8E-03	83.728	6.1E-03
P+E	83.713	3.6E-03	83.715	4.1E-03	83.722	5.0E-03

Figure 15 – Estimated δ_0 value for the 3 parameters fit - IAU Model

5.1.3. Spin rate

The new estimate of ω for both General and Benchmark data set are compatible (Figure 16) with the synchronous condition (reference value: ω = 22.5769768 deg/day) predicted by IAU (Seidelmann, 2006) for a 1:1 resonance. For the P+E case the estimated value is 22.57693 °/day (General: ω = 22.57691 °/day); the contribution of NSR (Non-Synchronous Rotation) is < 0.02 °/year. All the analyzed data sets show an estimated value compatible with the IAU value, 3-σ included for EM and P+E and 1-σ included for PM, closer to the reference. This is likely due to the relevant presence of polar features in the EM data set, whose contribution to the determination of ω is lesser than equatorial tiepoints.

The observed NSR is equivalent to that observed with the Estimate at Observation Epoch, confirming that there is no correlation between the estimation of the spin rate and those of the pole location. The negative trend along the time span of the mission is coherent with the theoretical predictions of (Karatekin et al., 2008) (see 7.2).

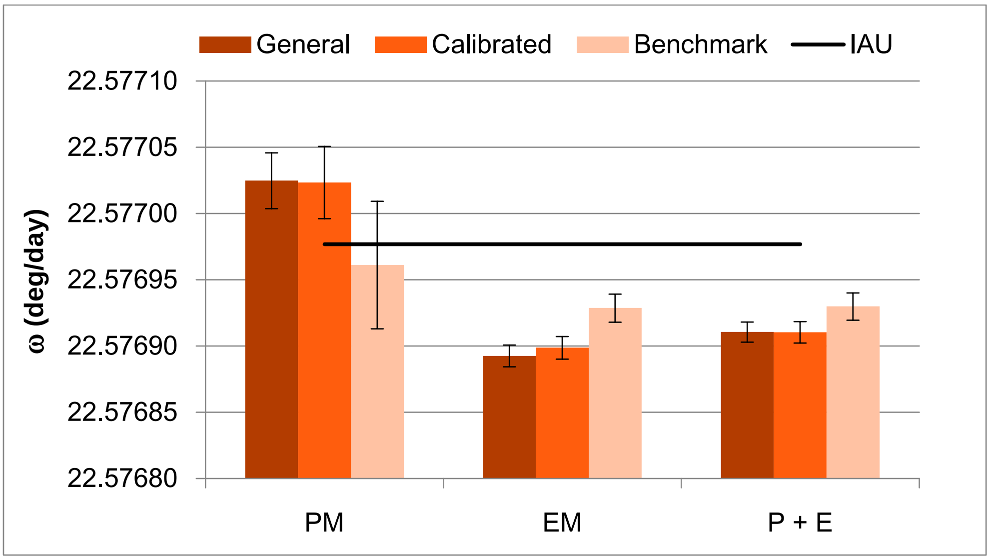

Spin Rate (deg/day)						
Dataset	General	St.dev.	Calibrated	St. Dev.	Benchmark	St. Dev.
PM	22.57702	2.1E-05	22.57702	2.7E-05	22.57696	4.81E-05
EM	22.57689	8.20E-06	22.57690	8.5E-06	22.57693	1.06E-05
P+E	22.57691	7.6E-06	22.57691	8.1E-06	22.57693	1.0E-05

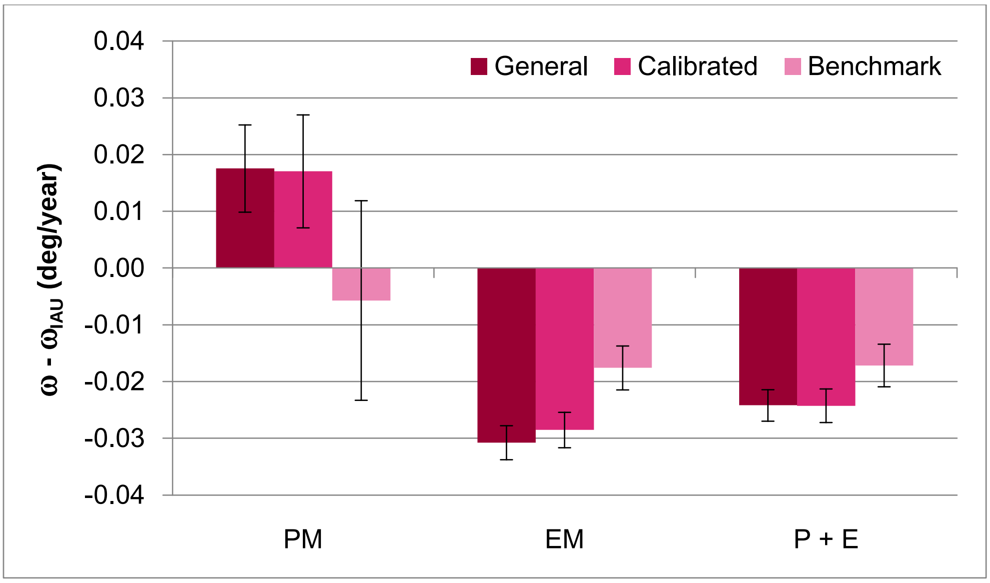

Not Synchronous Rotation (deg/year)						
Dataset	General	St. Dev.	Calibrated	St. Dev.	Benchmark	St. Dev.
PM	0.018	7.7E-03	0.017	1.0E-02	-0.006	1.8E-02
EM	-0.031	3.0E-03	-0.029	3.1E-03	-0.018	3.9E-03
P+E	-0.024	2.8E-03	-0.024	3.0E-03	-0.017	3.8E-03

Figure 16 - Estimated ω and NSR for the 3 parameters fit - IAU Model

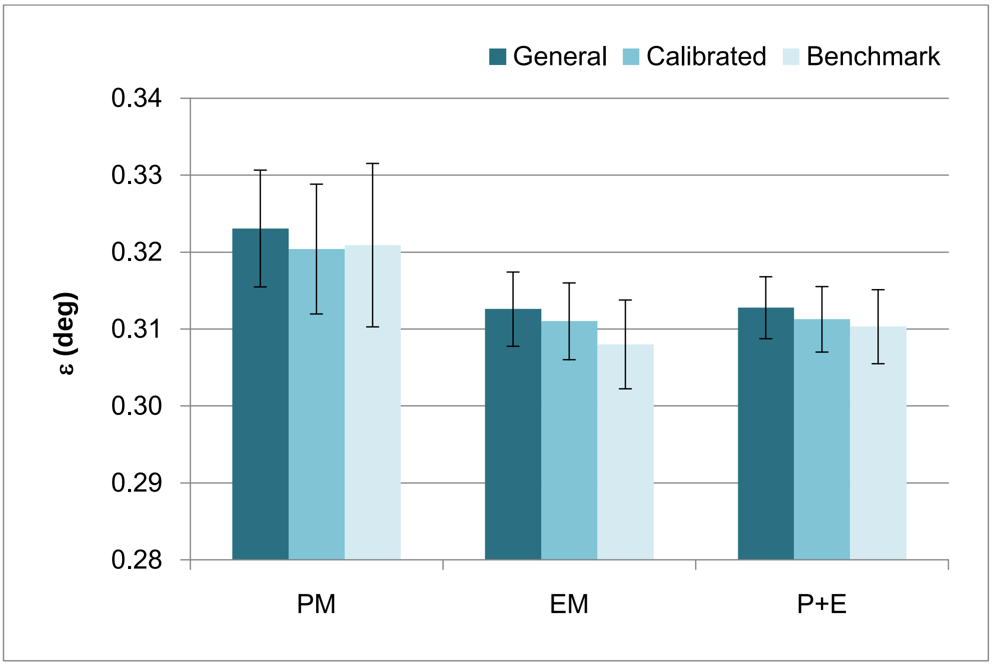

Obliquity (deg) - Ref epoch

Dataset	General	St.Dev.	Calibrated	St. Dev.	Benchmark	St.Dev.
PM	0.323	7.6E-03	0.320	8.4E-03	0.321	1.1E-02
EM	0.313	4.8E-03	0.311	5.0E-03	0.308	5.8E-03
P+E	0.313	4.0E-03	0.311	4.3E-03	0.310	4.8E-03

Figure 17 - Estimated ε for the 3 parameters fit - IAU Model

5.1.4. Obliquity

In this case the propagated pole location at an averaged reference epoch (2006 - 2007) for each dataset was used to compute ε. This computation can be considered a test of the previous results obtained for the obliquity. In any case, the estimated values are fully consistent with the estimate at reference epoch (Figure 17). Estimated ε is equal to 0.310° ± 4.8E-03° (P+E, Benchmark). The PM estimates are 1-σ range compatible but 0.01° larger than EM estimated values.

5.2. The 4 parameters fit

In the 4 parameters fit the pole location (α_0, δ_0) and the amplitude of the precession terms (β_α, β_δ) are estimated. This is an approximation of the real case, where also the precession term for the Prime Meridian (β_W) has an influence on the estimate. Preliminary tests with a 5 parameter fit (α_0, δ_0, β_α, β_δ , β_W) indicated the impossibility to estimate with sufficient accuracy all the precession terms with the available data; consequently, only the position of the pole and the precession terms for RA and DEC have been estimated. The spin rate ω is assumed as synchronous, and the IAU value equal to 22.5769768 deg/day is used for the fit. We made this assumption considering the results of the 3 parameters fit, where the estimated NSR is compatible with the synchronous value.

5.2.1. Residuals

The residuals are substantially equivalent to those obtained for the 3 parameter fit (Figure 18). For the PM the residuals vary from 690 m to 1.72 km, with a good level of accuracy for both Calibrated and Benchmark dataset. Both show a slight (5%) improvement with respect to the Estimate at the Observation Epoch. For the EM the situation is equivalent to the 3 parameters fit, where the residuals vary from 760 m to 1.75 km. Residuals slightly get worst for the P+E case, varying from 1 to 2.39 km.

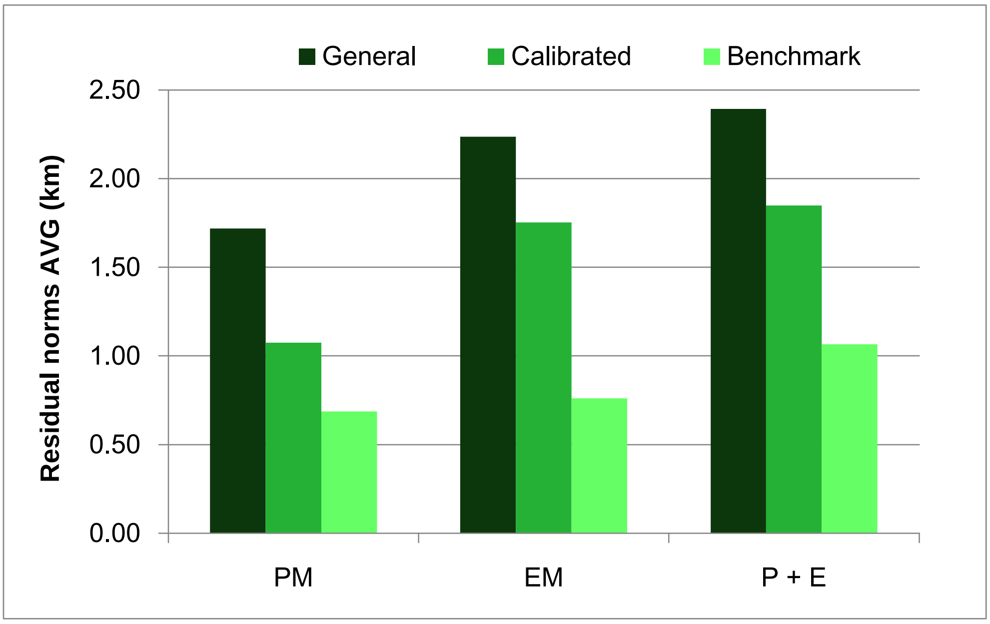

Residual norms AVG (km)			
Dataset	General	Calibrated	Benchmark
PM	1.72	1.07	0.69
EM	2.24	1.75	0.76
P+E	2.39	1.85	1.07

Figure 18 - Average of the residual norms for the 4 parameters fit - IAU Model

5.2.2. Pole location

Right Ascension

Significant differences with the 3 parameters fit can be observed into the estimation of the right ascension (Figure 19). A great variability of the estimated solutions can be observed, with relevant differences (from 1° to 2.5°) between the PM and the EM solutions. For the PM the estimated α_0 vary between 37.27° (Benchmark) and 39.11° (General). For the EM the solutions vary between 36.58° and 37.34°, with a difference > 1° with respect to the 3 parameters fit. Most of all, the solutions for the EM are closer to the predicted IAU value of 36.41° (Seidelmann et al., 2006), even if they do not include this value. It can be observed that the estimation of the precession terms concurred to a more accurate estimation of α_0, closer to the expected value. For the P+E, the estimated values vary between 36.92° and 37.34°. Benchmark solutions show generally larger values. The accuracy is improved of almost an order of magnitude for most of cases; in any case α_0 is estimated with an accuracy better than the correspondent 3 parameter fit solution.

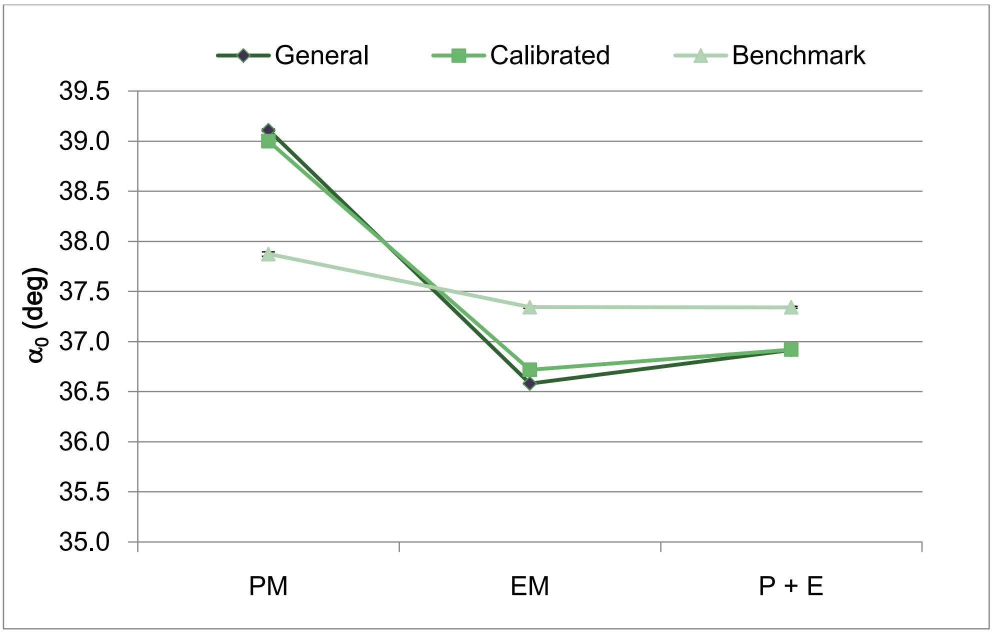

IAU Model - α_0 (deg)

Dataset	General	St.Dev.	Calibrated	St. Dev	Benchmark	St. Dev.
PM	39.11	1.4E-02	39.00	1.6E-02	37.87	2.2E-02
EM	36.58	9.2E-03	36.72	1.0E-02	37.34	1.2E-02
P + E	36.92	7.5E-03	36.92	8.4E-03	37.34	9.5E-03

Figure 19 – Estimated α_0 for the 4 parameters fit - IAU Model

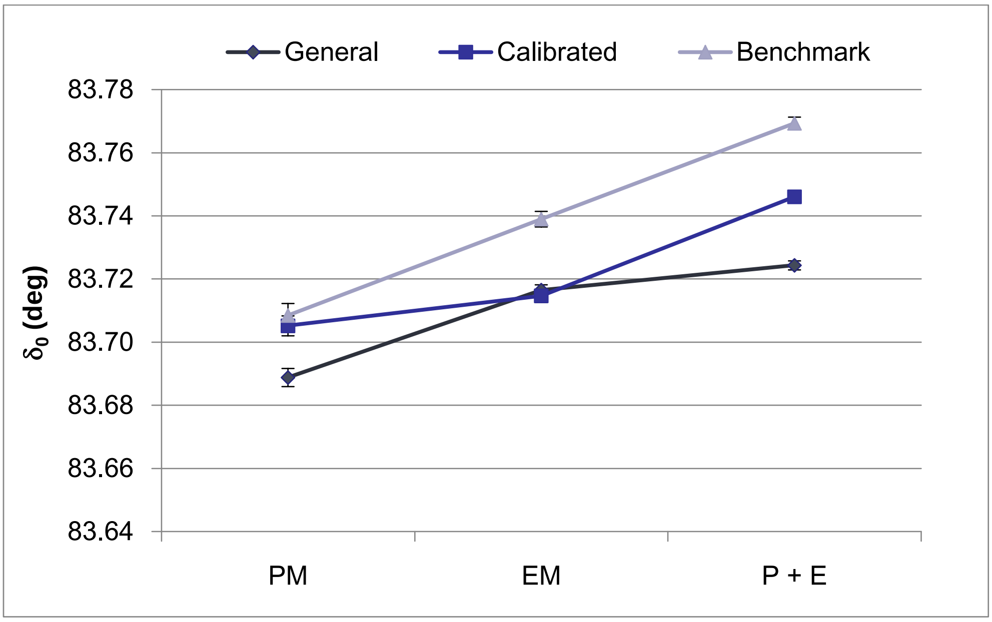

IAU Model: δ_0 (deg)						
Dataset	General	St.Dev.	Calibrated	St. Dev.	Benchmark	St. Dev.
PM	83.689	2.9E-03	83.705	3.2E-03	83.708	3.8E-03
EM	83.717	1.7E-03	83.715	2.1E-03	83.739	2.5E-03
P+E	83.724	1.4E-03	83.746	1.7E-03	83.769	2.0E-03

Figure 20 –Estimated δ_0 for the 4 parameters fit - IAU Model

Declination

A great variability of the solution is observed also for δ_0; PM solutions vary between 83.689° (General) and 83.708° (Benchmark), with a variation of 0.01° with respect to the 3 parameter fit (Figure 20). For the EM the estimate varies significantly, being included in a range between 83.717° (General) and 83.739° (Benchmark). For the P+E mission, the estimated values are larger and vary between 83.724° and 83.769°. A 0.01° difference between PM, EM and P+E can be observed. One of the reasons for the observed difference between PM and EM is likely due to the presence of several polar features for the EM data set. Furthermore, short period oscillations are not taken into account into the model. P+E solutions are closer, but still not compatible with the predicted IAU value equal to 83.94° (Seidelmann et al., 2006). The accuracy is generally improved, passing from 0.005° to 0.002°.

5.2.3. Precession terms

Since the observed obliquity is not null, precession terms are expected to significantly differ from initial values. These expectations are substantially confirmed.

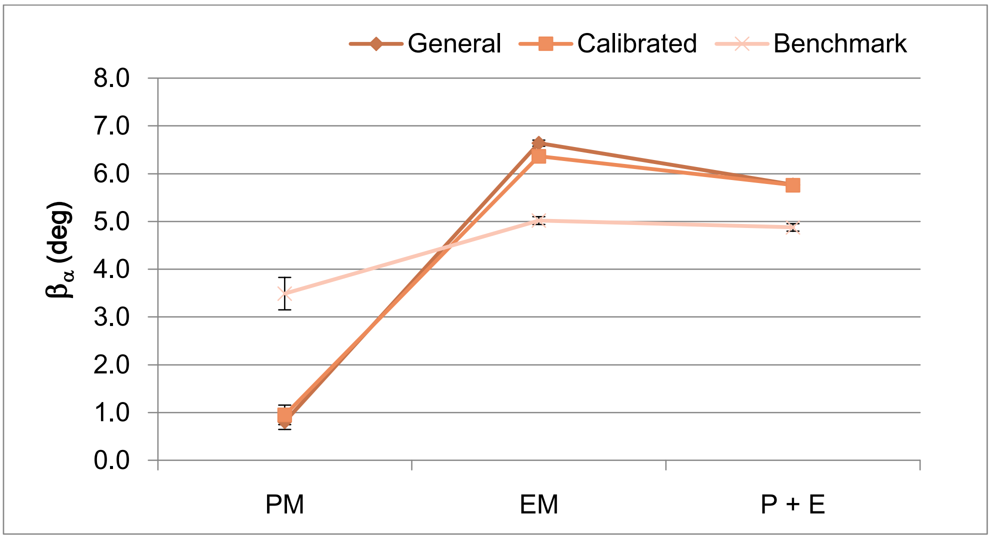

β_α (deg)						
Dataset	General	St.dev.	Calibrated	St. Dev.	Benchmark	St. Dev.
PM	0.81	1.6E-01	0.95	2.0E-01	3.49	3.4E-01
EM	6.64	6.4E-02	6.37	6.7E-02	5.02	8.1E-02
P+E	5.77	5.9E-02	5.76	6.3E-02	4.88	7.8E-02

Figure 21 - Estimated β_α for the 4 parameters fit - IAU Model

Right Ascension

For the PM, the estimated β_α vary from 0.81° up to 3.49°, with an accuracy equal to ~ 0.2°. As a particular case, in the General case β_α is not estimated with sufficient accuracy (Figure 21). For the EM the estimated values vary between 5.02° (Benchmark) and 6.64° (General), with an improved accuracy equal to ~ 0.07°, an order of magnitude better than the PM case. For the P+E, the estimated β_α vary from 4.88° (Benchmark) up to 5.77° (General), similar to EM trend but with improved accuracies. It is easy to compare Figure 19 with Figure 21 to observe the complementarity between the estimated α_0 and the values obtained for β_α.

Declination

Estimated solutions for β_δ are stable around the initial, predicted value equal to -0.30°, with accuracies of the order of 0.002°. In this case the expected variation due to not null obliquity is addressed to δ_0 with respect to the precession term, as it is possible to observe from δ_0 trend (Figure 22).

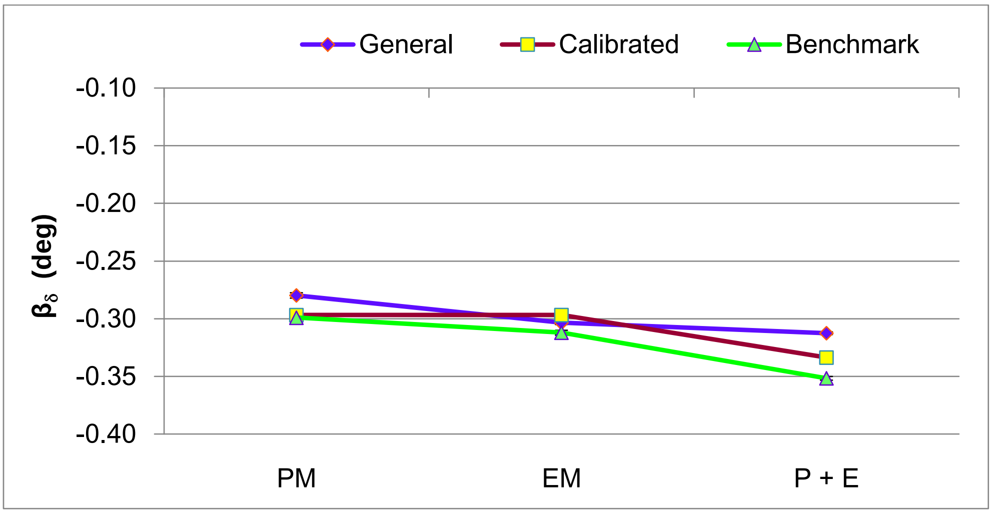

βδ (deg)						
Dataset	General	St. Dev.	Calibrated	St. Dev.	Benchmark	St. Dev.
PM	-0.280	2.3E-03	-0.297	2.5E-03	-0.299	2.8E-03
EM	-0.304	1.4E-03	-0.297	1.9E-03	-0.312	2.1E-03
P+E	-0.312	1.2E-03	-0.334	1.5E-03	-0.352	1.6E-03

Figure 22 - Estimated β_δ for the 4 parameters fit - IAU Model

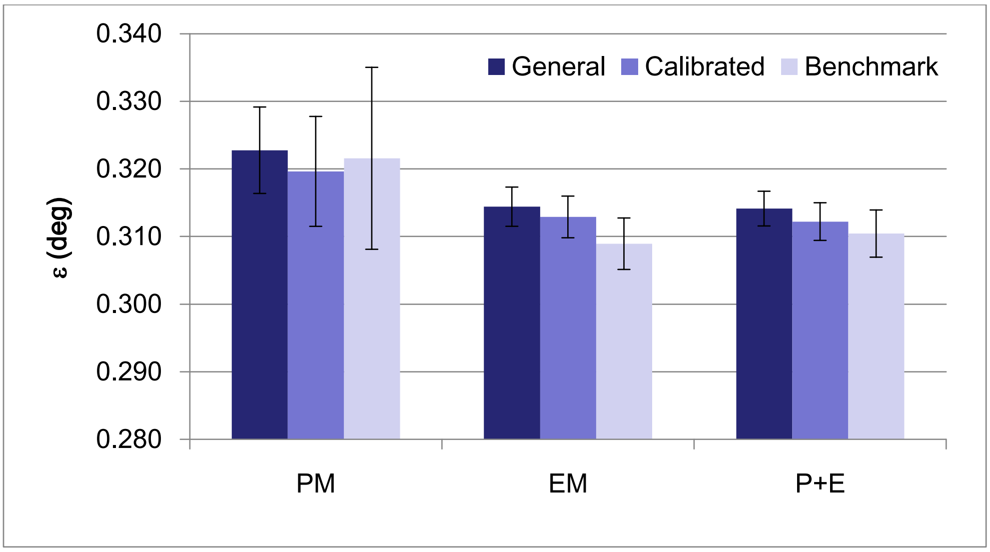

Obliquity (deg) - Ref epoch

Dataset	General	St.Dev.	Calibrated	St. Dev.	Benchmark	St.Dev.
PM	0.323	6.4E-03	0.320	8.1E-03	0.322	1.3E-02
EM	0.314	2.9E-03	0.313	3.1E-03	0.309	3.8E-03
P+E	0.314	2.6E-03	0.312	2.8E-03	0.310	3.5E-03

Figure 23 - Estimated ε for the 4 parameters fit - IAU Model

5.2.4. Obliquity

For the 4 parameters fit the estimates of obliquity remain substantially unchanged, but it is possible to observe (Figure 23) an improvement for the accuracy for EM and P+E cases (from 0.005° to 0.003°). As in the 3 parameters fit, we used the pole location at an averaged reference epoch (2006 - 2007) for each dataset to compute ε. In any case, results are fully consistent also with the estimate at the observation epoch.

6. Estimate by the NAV Model

Since the previous estimates using the IAU model show evident limitations into the determination of α_0 and δ_0, which should be coincident with the Laplace pole, it is significant to fit the parameters introducing the nutation terms into the rotational model. This will allow to search for improvements in the residuals and in the accuracy of the estimated parameters. For these reasons the NAV rotational model was used into the estimate process.

NAV model includes updated values for the pole, the linear drift and the precession terms, and also four additional nutation terms, by means of the following formulation:

$$\alpha = \alpha_0 + \dot{\alpha}_{0\,NAV} t + \sum_{i=1}^{5} \beta_{\alpha\,NAV,i} \sin\left(\gamma_{NAV,i} + \chi_{NAV,i} t\right) \tag{7.12}$$

$$\delta = \delta_0 + \dot{\delta}_{0\,NAV} t + \sum_{i=1}^{5} \beta_{\delta\,NAV,i} \cos\left(\gamma_{NAV,i} + \chi_{NAV,i} t\right) \tag{7.13}$$

$$W = W_0 + \omega_{0\,NAV} d + \sum_{i=1}^{5} \beta_{W\,NAV,i} \sin\left(\gamma_{NAV,i} + \chi_{NAV,i} t\right) \tag{7.14}$$

The numerical values of the parameters are reported in Table 4.

Table 4 - Numerical coefficients for the NAV Model and correspondent IAU values

Parameter	NAV Value	IAU Value
α_0	36.33°	36.41°
δ_0	83.981°	83.94°
W_0	191.76°	189.64°
$\dot{\alpha}_0$	-0.0423°/cent	-0.036°/cent
$\dot{\delta}_0$	-0.0044°/cent	-0.004°/cent
ω	22.5769792°/day	22.5769768°/day

Table 5 - Numerical values for the NAV precession terms

Order	Term	β (deg)	$\gamma + \chi t$ (deg + deg/centuries t)	Period (years)
1	$\beta_{\alpha,1}$	2.919475	26.350485 - 49.4802860 t	727.5624
	$\beta_{\delta,1}$	-0.331428		
	$\beta_{W,1}$	-2.817196		

The numerical values for the precession terms are reported in Table 5, while the nutation terms (terms with i = 2…5) are reported in Table 6.

Nutation terms

Following the NAV formulation for the coefficients, it is possible to compute the general amplitude of the nutations for the observational period. The results are relevant: for RA, the amplitude of the contribution due to nutation is ~ 4-6 km, a huge value (Figure 24). If these nominal values were confirmed, the maximum amplitude would be equal to ~ 10 km between the 2004 and the 2009. For the DEC the results are similar, with a general amplitude of the oscillations ruled by the order 2 term and with a max amplitude equal to 600 m; in this case it is possible to observe that in the observational period (2004 – 2009) the value varies of about 400 m (Figure 25).

Table 6 - Numerical values for the NAV nutation terms

Order	Term	β (deg)	$\gamma + \chi t$ (deg + deg/centuries t)	Period (years)
2	$\beta_{\alpha,2}$	- 0.120326	343.352452 + 2448.4031887 t	14.7034
	$\beta_{\delta,2}$	0.013190		
	$\beta_{W,2}$	0.127783		
3	$\beta_{\alpha,3}$	0.025088	117.291775 + 1219.6475091 t	29.5167
	$\beta_{\delta,3}$	0.001224		
	$\beta_{W,3}$	-0.015665		
4	$\beta_{\alpha,4}$	0.015504	122.555879 + 3676.2976707 t	8.1604
	$\beta_{\delta,4}$	-0.001604		
	$\beta_{W,4}$	-0.014928		
5	$\beta_{\alpha,5}$	0.001642	82.621514 + 4881.7480179 t	7.3744
	$\beta_{\delta,5}$	-0.000171		
	$\beta_{W,5}$	-0.001887		

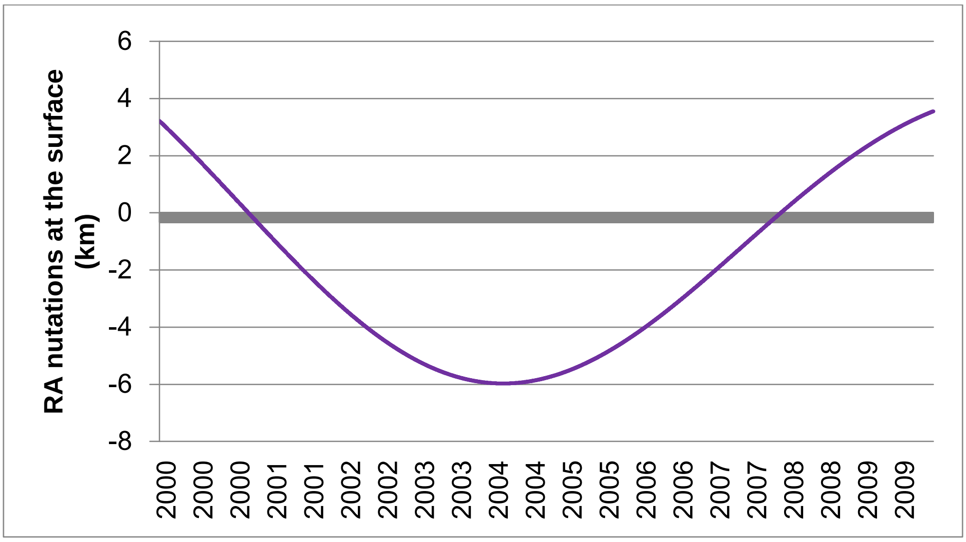

Figure 24 - trend for the RA nutation terms at the surface between 2000 and 2009

In this case not considering the nutation terms could cause an over-estimation of the rotational parameters, trying to fit this contribution. This is compatible with the results obtained from the IAU model, where the solution for α_0 and δ_0 is closer but not compatible with the predicted values. Considered the relevant entity of these terms, the nutation terms cannot be excluded from the model, and it is highly probable that their not perfect determination is heavily affecting the residuals.

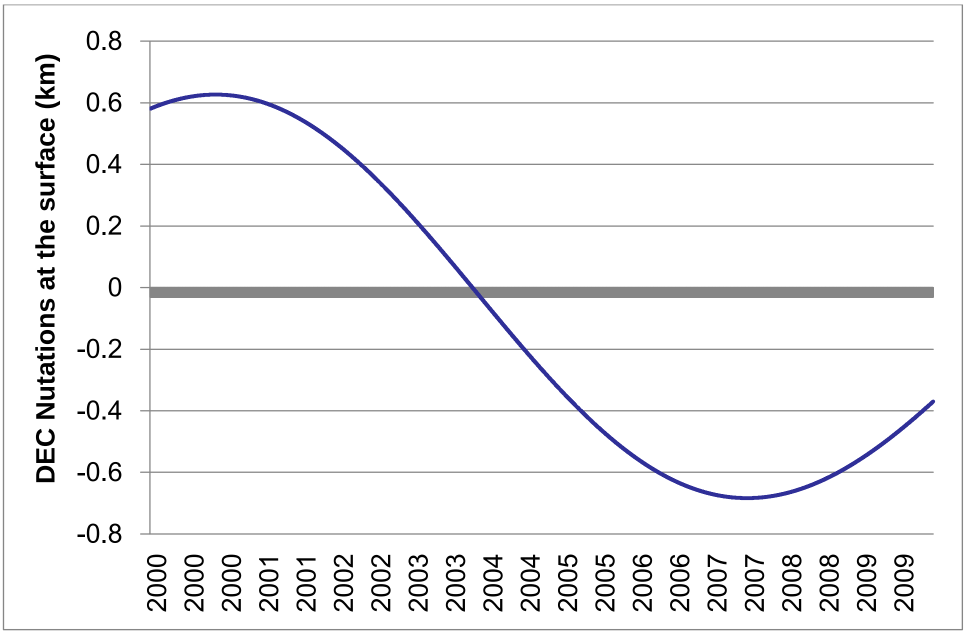

Figure 25 - trend for the DEC nutation terms at the surface between 2000 and 2009

6.1. The 3 parameters fit

Similarly to IAU case, in the 3 parameters fit only α_0, δ_0 and ω were estimated; the results of the fit are a linear approximation of the rotational model for the observational period.

6.1.1. Residuals

In this case there are no significant improvements in the residuals, which are substantially unchanged with respect to the correspondent IAU 3 parameters fit (Figure 26). For the PM the residuals vary from 760 m up to 1.77 km, 60 m worst than the estimate for the IAU model. A similar trend (from 940 m to 2.24 km) is confirmed also for the EM, where the Benchmark case is worst of about 170 m. For the P+E case the residuals are analogue to those shown for the IAU model (from 1 to 2.34 km). Including the nutation terms (with the nominal values) does not improve the residuals.

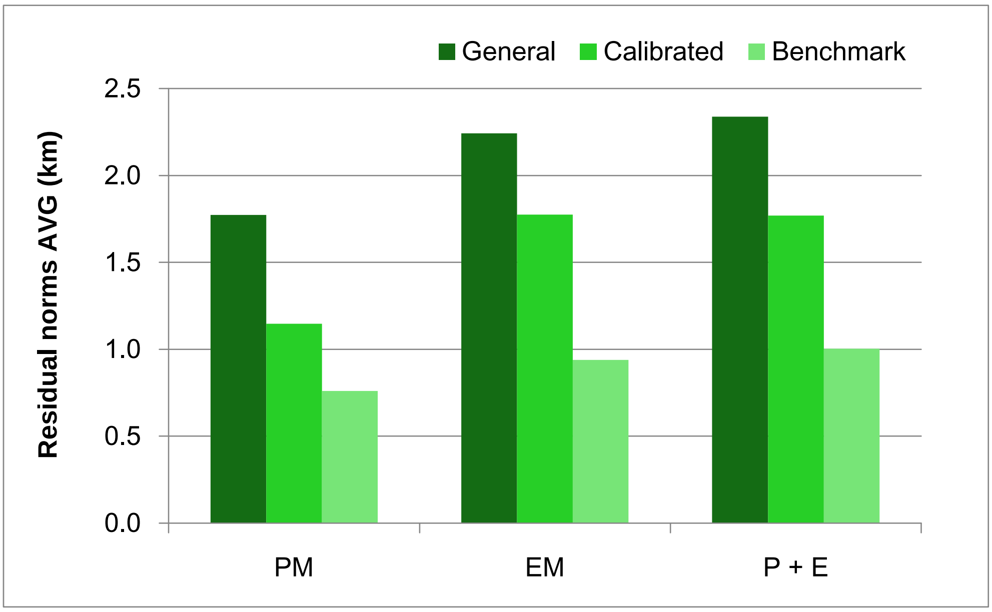

Residual norms AVG (km)			
Dataset	General	Calibrated	Benchmark
PM	1.77	1.15	0.76
EM	2.24	1.78	0.94
P+E	2.34	1.77	1.00

Figure 26 - Average of the residual norms for the 3 parameters fit - NAV model

6.1.2. Pole location

The same considerations for the IAU 3 parameter fit are valid also in this case. Not estimating the precession terms will cause an “over-estimation” of the pole location, because of the not null obliquity. This is also the reason why the estimated values are compatible with the solutions of the IAU 3 parameters fit.

Right Ascension

Estimated values vary between 38.29° and 38.38°, with an averaged accuracy equal to ~0.05°. Solutions are 1-σ range compatible with the correspondent IAU solutions, with no significant variations due to nutation terms (Figure 27). For the General datasets the differences between IAU and NAV are of the order of 0.09°, reduced to 0.01° - 0.04° in the other cases. For the P + E the Benchmark case (38.34° + 0.042°) is included into 1-σ range of all solutions.

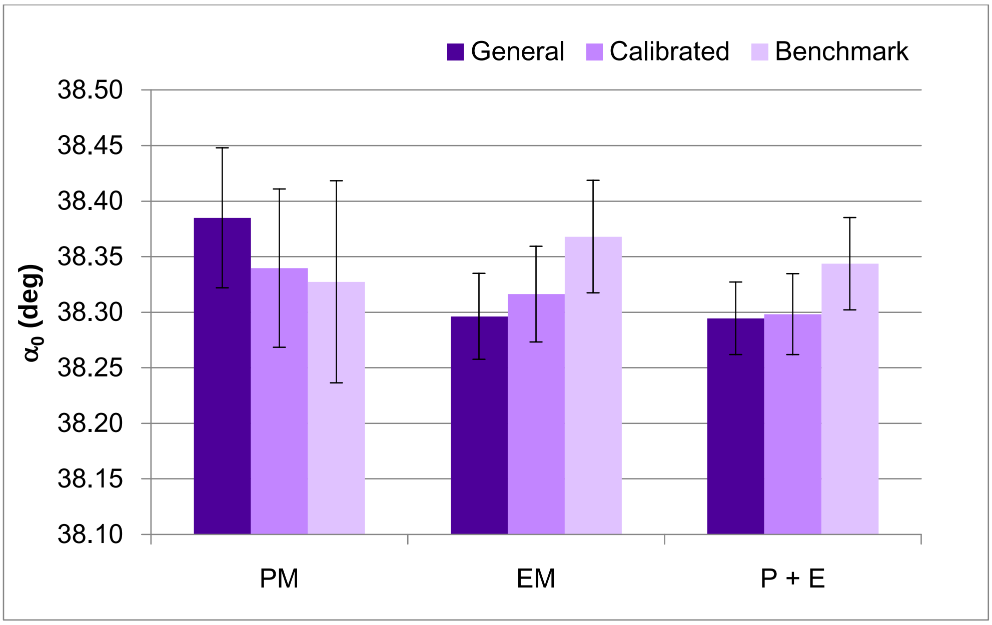

NAV Model - α_0 (deg)

Dataset	General	St.Dev.	Calibrated	St. Dev.	Benchmark	St. Dev.
PM	38.38	6.3E-02	38.34	7.1E-02	38.33	9.1E-02
EM	38.30	3.9E-02	38.32	4.3E-02	38.37	5.1E-02
P + E	38.29	3.3E-02	38.30	3.6E-02	38.34	4.2E-02

Figure 27 – Estimated α_0 for the 3 parameters fit - NAV Model

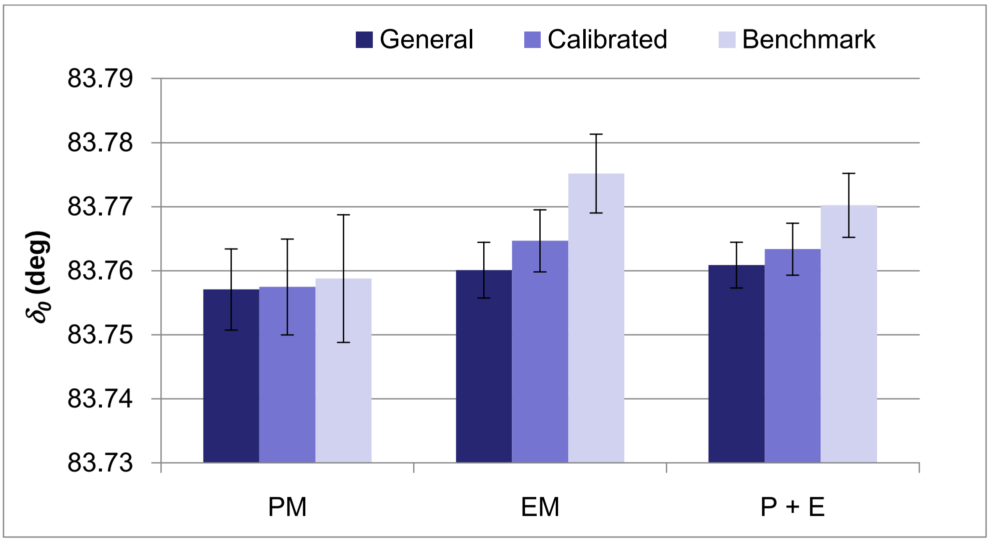

NAV Model: δ0 (deg)						
Dataset	General	St.dev.	Benchmark	St. Dev.	Calibrated	St.Dev.
PM	83.757	6.3E-03	83.759	1.0E-02	83.757	7.5E-03
EM	83.760	4.3E-03	83.775	6.2E-03	83.765	4.8E-03
P+E	83.761	3.6E-03	83.770	5.0E-03	83.763	4.1E-03

Figure 28 – Estimated δ_0 for the 3 parameters fit - NAV Model

Declination

A significant variation of 0.05° between IAU and NAV can be observed (Figure 28). NAV solution is closer but not compatible with the predicted value (83.94° - 83.98°). For the PM the estimate is in agreement for all the analyzed datasets of 83.757°; for the EM (and also P+E) the solutions vary significantly between 83.760° and 83.775°; it should be observed that the Benchmark dataset has an larger percentage of polar features with respect to the other data sets.

6.1.3. Spin rate

The NAV solutions for ω are 1-σ range compatible with the IAU and the Estimate at the Observation Epoch estimated values, and, for the Benchmark case, closer to the synchronous value for ~ 1-σ (Figure 29). The sign inversion for the NSR is observed also in this case, with a residual NSR varying between 0.02 deg/year and -0.02 deg/year. The confirmed trend for residual NSR for all the different estimate types is strengthening the estimated solution and the assumption of a synchronous rotation for Titan.

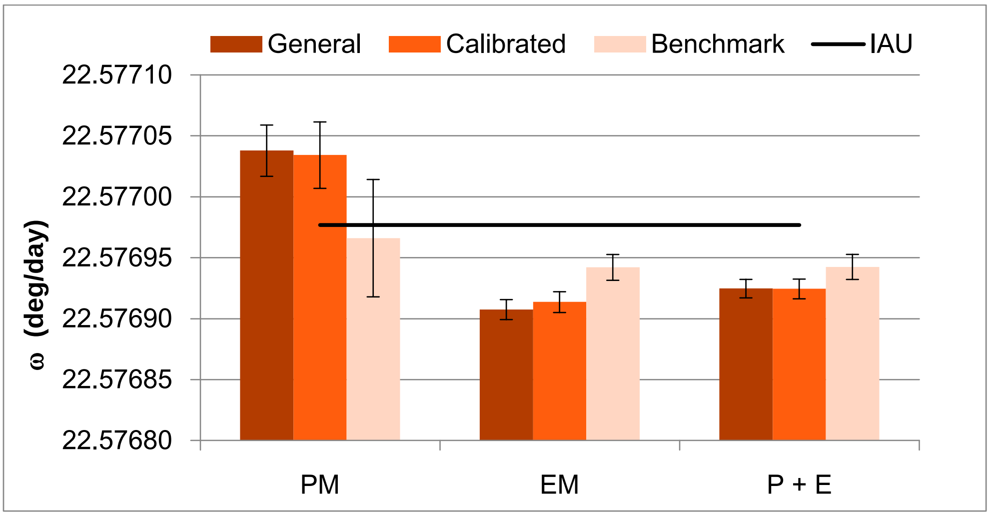

Spin Rate (deg/day)						
Dataset	General	St.dev.	Calibrated	St. Dev.	Benchmark	St. Dev.
PM	22.57704	2.1E-05	22.57703	2.7E-05	22.57697	4.8E-05
EM	22.57691	8.2E-06	22.57691	8.5E-06	22.57694	1.1E-05
P+E	22.57692	7.6E-06	22.57692	8.1E-06	22.57694	1.0E-05

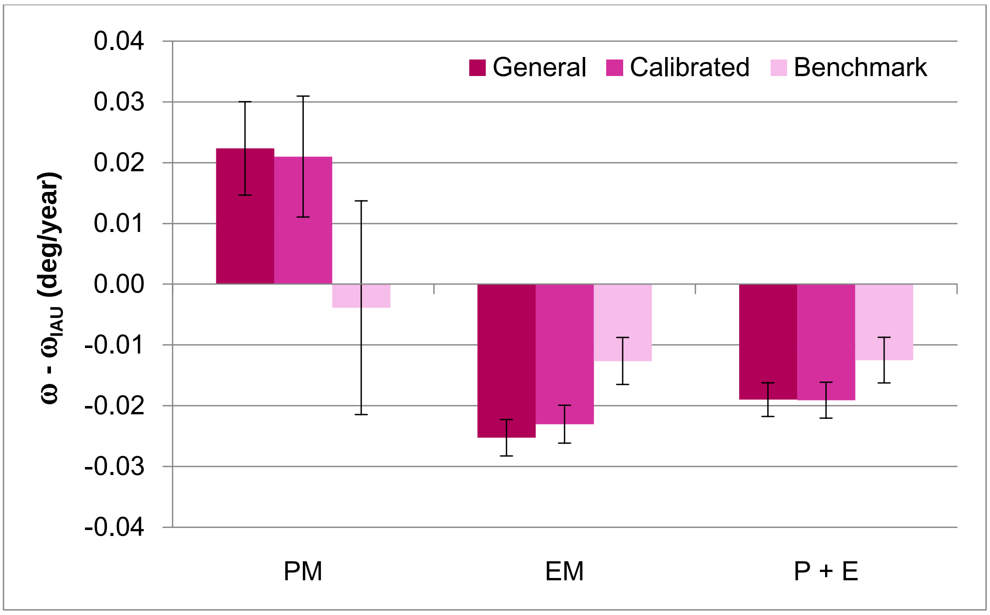

Not Synchronous Rotation (deg/year)						
Dataset	General	St. Dev.	Benchmark	St. Dev.	Calibrated	St. Dev.
PM	0.022	7.7E-03	-0.004	1.8E-02	0.021	1.0E-02
EM	-0.025	3.0E-03	-0.013	3.9E-03	-0.023	3.1E-03
P+E	-0.019	2.8E-03	-0.013	3.8E-03	-0.019	3.0E-03

Figure 29 – Estimated ω and NSR for the 3 parameters fit - NAV Model

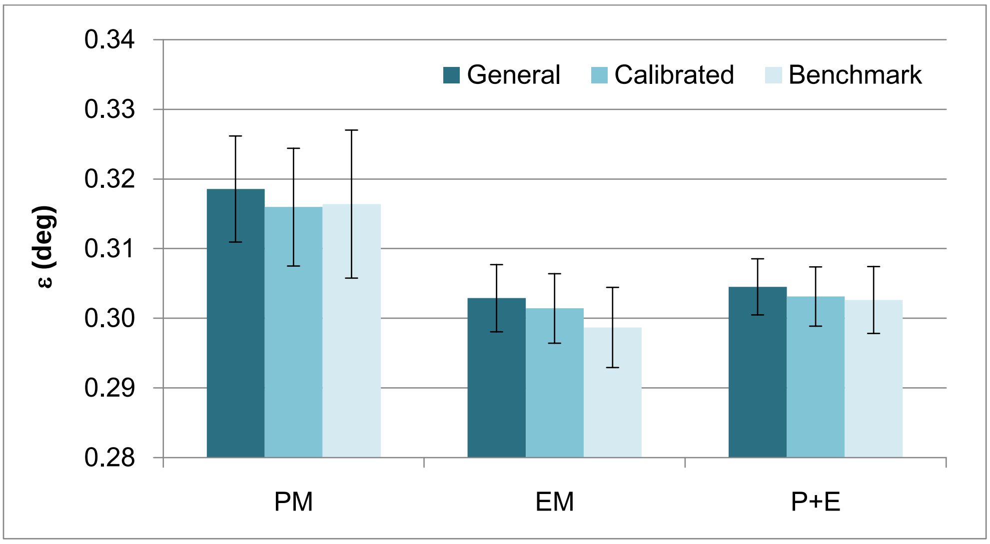

Obliquity (deg) – Reference epoch						
Dataset	General	St. Dev.	Calibrated	St. Dev.	Benchmark	St. Dev.
PM	0.319	7.6E-03	0.316	8.4E-03	0.316	1.1E-02
EM	0.303	4.8E-03	0.301	5.0E-03	0.299	5.8E-03
P+E	0.305	4.0E-03	0.303	4.3E-03	0.303	4.8E-03

Figure 30 – Estimated ε for the 3 parameters fit - NAV Model

6.1.4. Obliquity

Similarly to the IAU case, a pole location at an averaged reference epoch (2006 - 2007) for each dataset was used to compute ε. For the PM the estimated values are 1-σ range compatible with the IAU and the Estimate at the Observation Epoch solutions (Figure 30). For the EM and P+E instead the observed obliquity is 0.005° minor than estimated for the IAU and the EOE cases, but still 2-σ range compatible with previous estimates. For the EM and P+E the accuracy is significantly improved of almost 1 order of magnitude.

6.2. The 4 parameters fit

Similarly to IAU case, in the 4 parameters fit the Laplace Pole (α_0, δ_0) and the amplitude of the precession terms (β_α, β_δ) are estimated. The spin rate ω is assumed as synchronous and the NAV value is used for the fit. We made this assumption considering the results for the 3 parameters fit, where the estimated NSR is compatible with synchronous condition. Also in this case only 4 parameters were estimated.

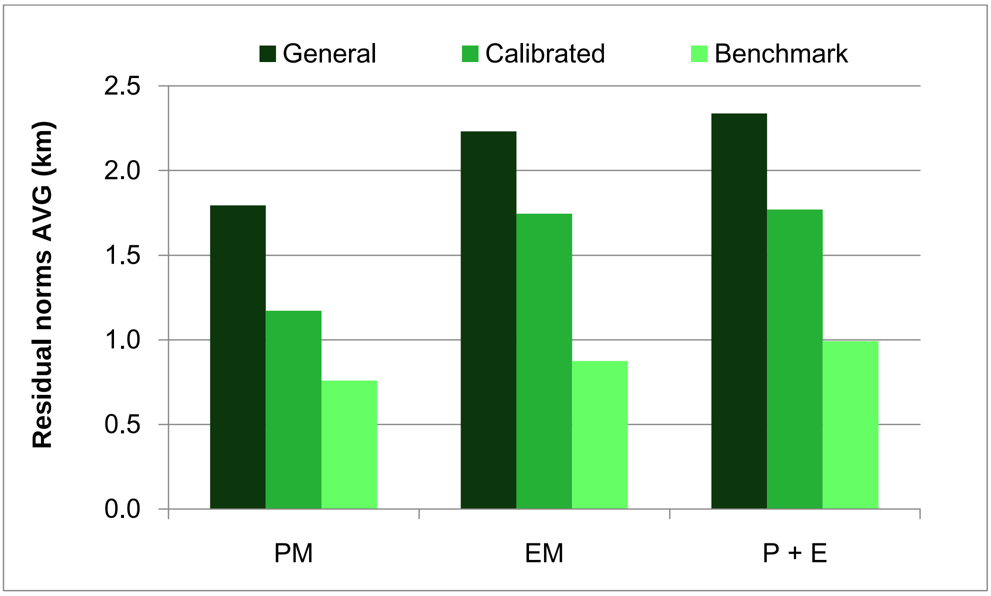

Residual norms AVG (km)			
Dataset	General	Calibrated	Benchmark
PM	1.79	1.17	0.76
EM	2.23	1.75	0.87
P+E	2.34	1.77	0.99

Figure 31 - Average of the residual norms for the 4 parameters fit - NAV model

6.2.1. Residuals

No significant improvements can be observed for the 4 parameters case (Figure 31), using the nominal values for the nutation terms. Residuals for General and Calibrated datasets are unchanged, while a 50 m improvement can be observed for the Benchmark case (760 - 990 m).

6.2.2. Pole location

Right Ascension

In this case it is observed the same trend of the correspondent IAU case (Figure 32). While the solutions for the 3 parameters fit vary around the 38.30°, for the 4 parameter fit differences up to 2° can be observed between the PM and the EM solutions. For the PM the estimated α_0 (38.10° - 39.39°) is quite different from . The EM estimated values (37.05° - 37.71°) differ for ~ 1° with respect to the correspondent solutions for the 3 parameters fit.

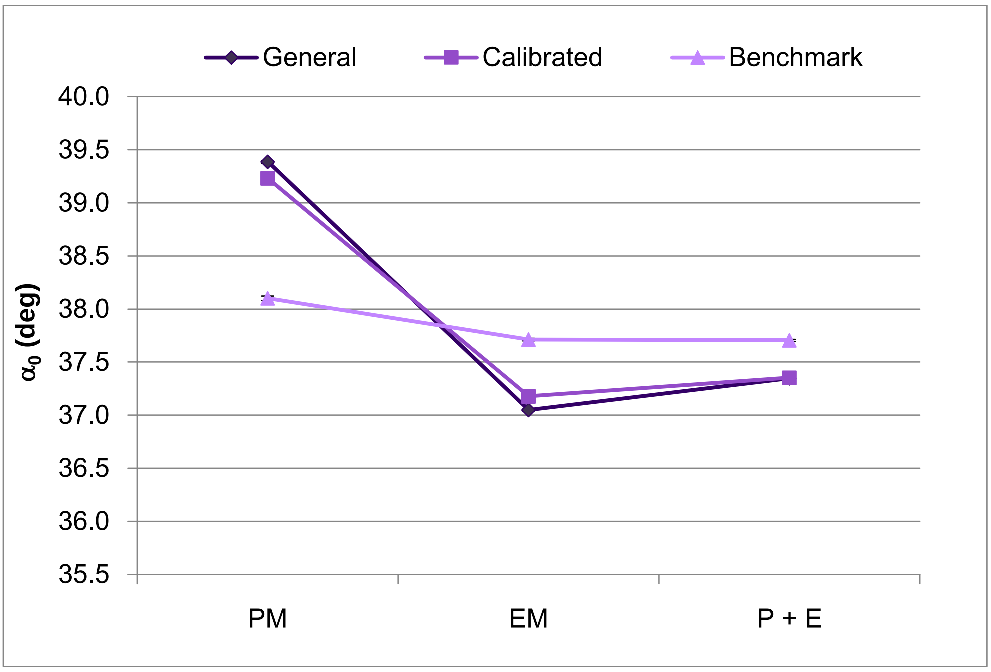

NAV Model - α_0 (deg)						
Dataset	General	St.Dev.	Calibrated	St. Dev.	Benchmark	St. Dev.
PM	39.39	1.4E-02	39.23	1.6E-02	38.10	2.2E-02
EM	37.05	9.2E-03	37.18	1.0E-02	37.71	1.2E-02
P + E	37.35	7.5E-03	37.35	8.4E-03	37.71	9.5E-03

Figure 32 – Estimated α_0 for the 4 parameters fit - NAV Model

The solutions for the EM are closer, but not compatible, to the NAV predicted value (36.33°). In this sense, IAU solution is closer to the expected value with respect to the NAV. Also in this case it can be observed that the contribution of the precession terms into the estimate is leading the estimation of α_0 through the expected value. Furthermore, the accuracy is improved of almost an order of magnitude for most of cases; in any case α_0 is estimated with an accuracy better than the correspondent 3 parameter fit solution.

Declination

A great variability of the estimated solutions (83.742° - 83.793°) is observed also for δ_0 (Figure 33). A 0.04° - 0.05° difference between PM, EM and P+E cases can be observed. Benchmark solutions (83.766° - 83.793°) are closer but not compatible with the predicted NAV value (83.98°). Similarly to IAU case, the accuracy is generally improved, passing from 0.005° to 0.002°.

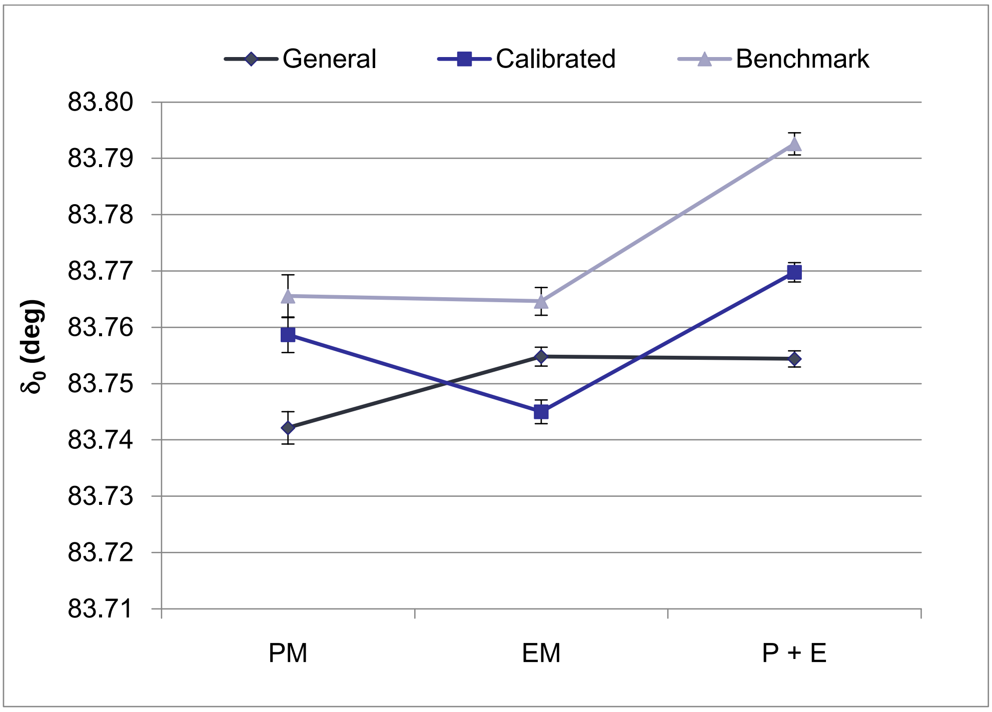

NAV Model: δ_0 (deg)						
Dataset	General	St.dev.	Calibrated	St. Dev.	Benchmark	St.Dev.
PM	83.742	2.9E-03	83.759	3.2E-03	83.766	3.8E-03
EM	83.755	1.7E-03	83.745	2.1E-03	83.765	2.5E-03
P+E	83.754	1.4E-03	83.770	1.7E-03	83.793	2.0E-03

Figure 33 – Estimated δ_0 for the 4 parameters fit - NAV Model

6.2.3. Precession terms

As observed for the IAU case, since the observed obliquity is not null, precession terms are expected to significantly differ from initial values. These expectations are substantially confirmed.

Right Ascension

Trend is similar to those shown for the IAU case. The PM solutions differs significantly from EM and β_α is not estimated with sufficient accuracy for the PM General and Calibrated dataset (Figure 34). The EM estimated values (4.66°- 6.23°) are 0.2° - 0.4° minor than the correspondent IAU solutions. This difference is likely due to the contribution of the nutation terms. EM and P+E accuracies are equal to ~ 0.07°, an order of magnitude better than the PM case.

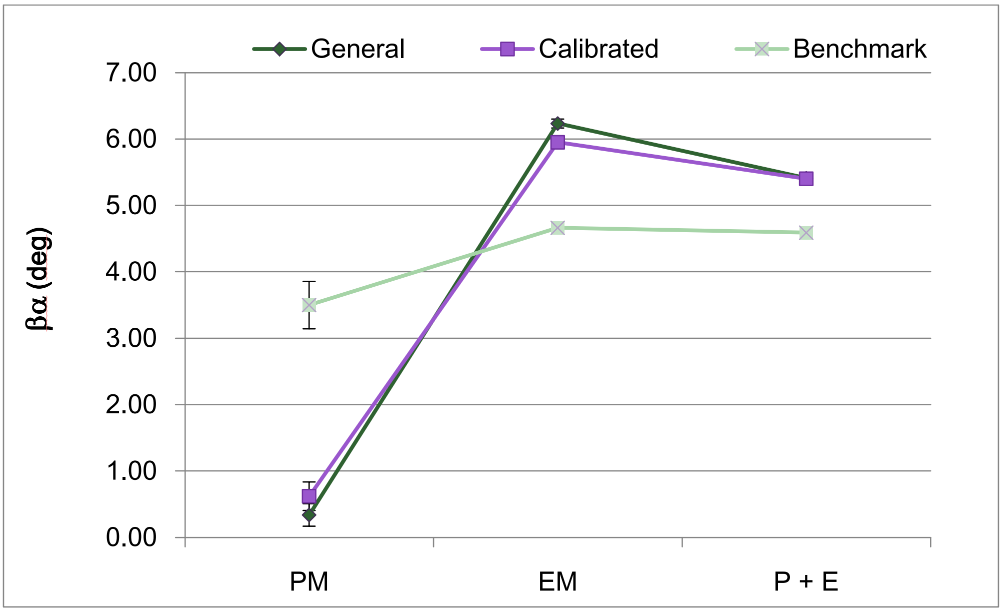

β_α(deg)

Dataset	General	St.dev.	Calibrated	St. Dev.	Benchmark	St. Dev.
PM	0.34	1.7E-01	0.62	2.1E-01	3.50	3.6E-01
EM	6.23	6.7E-02	5.95	7.0E-02	4.66	8.6E-02
P+E	5.41	6.2E-02	5.40	6.6E-02	4.59	8.2E-02

Figure 34 - Estimated β_α for the 4 parameters fit - NAV Model

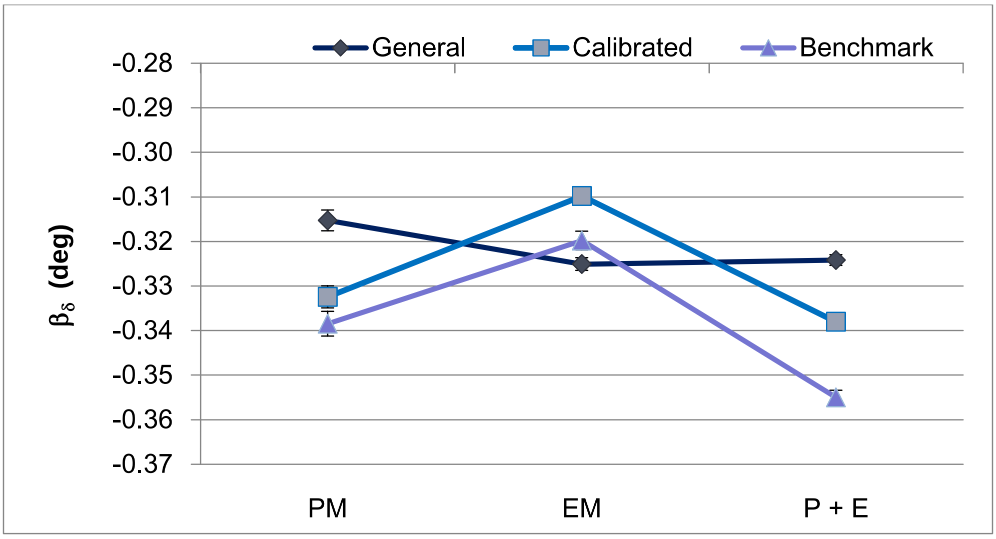

β_δ (deg)

Dataset	General	St. Dev.	Calibrated	St. Dev.	Benchmark	St. Dev.
PM	-0.32	2.3E-03	-0.332	2.5E-03	-0.338	2.8E-03
EM	-0.33	1.4E-03	-0.310	1.9E-03	-0.320	2.1E-03
P+E	-0.32	1.2E-03	-0.338	1.5E-03	-0.355	1.6E-03

Figure 35 - Estimated β_δ for the 4 parameters fit - NAV Model

Declination
Similarly to IAU case, the estimated solutions for β_δ vary around the initial, predicted value, in this case equal to -0.33°, with accuracies of ~ 0.002° (Figure 35). In this case the expected variation due to not null obliquity is addressed to δ_0 with respect to the precession term, as it is possible to observe from δ_0 trend (Fig. 33).

6.2.4. Obliquity

For the 4 parameters fit the estimates of obliquity remain substantially unchanged (Figure 36), but it is possible to observe an improvement for the accuracy for EM and P+E cases (from 0.005° to 0.003°). As in the 3 parameters fit, we used the pole location at an averaged reference epoch (2006 - 2007) for each dataset to compute ε. In any case, results are fully consistent also with the estimate at the observation epoch. For the EM and P+E the observed obliquity is 0.005° lesser than the estimated value for the IAU, but it is still 2-σ range compatible with previous estimates. For the EM and P+E the accuracy is significantly improved of almost 1 order of magnitude.

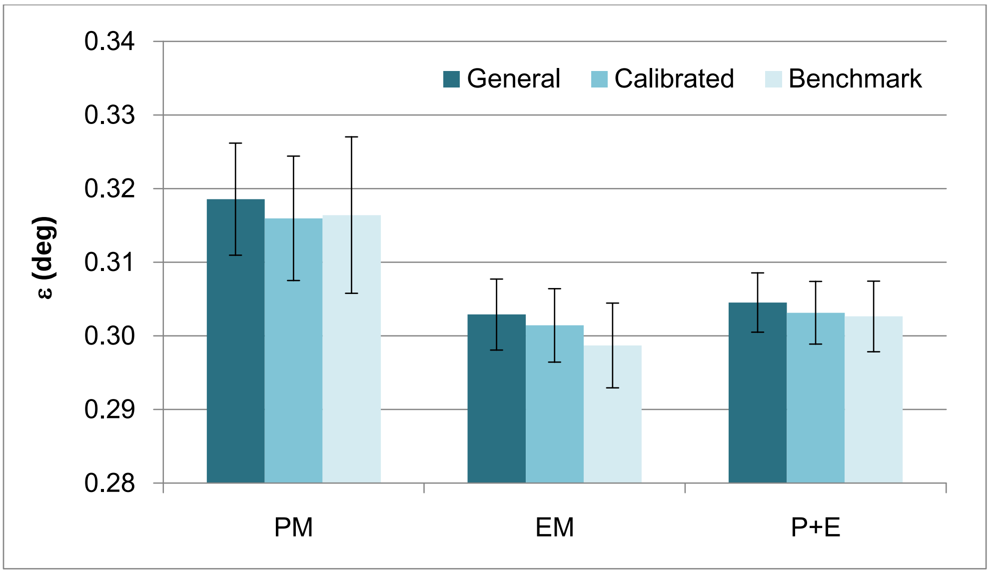

Obliquity (deg) – Reference epoch						
Dataset	General	St. Dev.	Calibrated	St. Dev.	Benchmark	St. Dev.
PM	0.318	6.2E-03	0.315	7.9E-03	0.317	1.3E-02
EM	0.305	2.8E-03	0.303	3.0E-03	0.300	3.6E-03
P+E	0.306	2.5E-03	0.304	2.7E-03	0.303	3.4E-03

Figure 36 – Estimated ε for the 4 parameters fit - NAV Model

7. Summary of the results

The residuals obtained for the Benchmark dataset are < 1 km and are at the moment the best available result for the estimate of the rotational state. The residuals of the Calibrated dataset are larger, between 1 and 1.7 km. The difference is likely due to the short period effects (nutations, librations, seasonal variations) which can heavily affect some observations. 40-200 m improvements can be observed estimating the precession terms (4 parameters fit).

The estimation at the Observation Epoch allowed to determine an averaged pole location for the prime and extended mission. The estimated solution is compatible with the previous estimate (Stiles et al., 2008), which was relative only to PM. The observed pole location is at $\alpha = 39.45° \pm 0.042°$ and $\delta = 83.451° \pm 0.005°$. The estimate is fully compatible with the propagated pole location obtained by IAU and NAV solutions.

The estimate by IAU Model allowed to provide a rotational model which includes precession effects and takes into account the estimated obliquity. The time drift terms are assumed as known, as well as the precession period (~ 700 years). the amplitudes for the precession terms (RA, DEC) have been estimated. The location of the pole is found at $\alpha_0 = 37.34° \pm 0.009°$ and $\delta_0 = 83.769° \pm 0.002°$ (Benchmark). The correspondent amplitudes for the precession terms are $\beta\alpha = 4.48° \pm 0.08°$ and $\beta\delta = -0.352° \pm 0.002°$ (Benchmark).

The estimate by NAV Model allowed to provide a rotational model which takes into account also the nutation terms. The numerical coefficients of the NAV Model differ from the correspondent IAU values, and the estimate reflects these differences. Time drift terms and the precession period are assumed as known. Nutation terms are considered but not estimated. The nominal values for nutation periods are respectively 14.7, 29.5, 8.2 and 7.4 years. In this case the location of the pole is found at $\alpha_0 = 37.71° \pm 0.009°$ and $\delta_0 = 83.793° \pm 0.002°$ (Benchmark). The correspondent amplitudes for the precession terms are $\beta\alpha = 4.59° \pm 0.08°$ and $\beta\delta = -0.355° \pm 0.002°$ (Benchmark). Considering the nutation terms does not improve the residuals. Nominal values are not effective on the estimate and in the future the nutation terms will be included into the estimate process.

The estimated obliquity ε is stable into 1-σ range around 0.31° (0.32° for the PM). The estimated obliquity is $\varepsilon = 0.31 \pm 0.005°$ (Benchmark) for both the Estimate at the Observation Epoch and the IAU model. For the NAV model the estimated ε decreases to 0.305°, likely due to the presence of the nutation terms.

For all the analyzed cases the spin rate ω has been estimated compatible into 1 or 2-σ range with synchronous value. Residual NSR vary from + 0.02 deg/year (PM) to - 0.02 deg/year (EM). A sign inversion is observed passing from the PM (2004 - 2007) to the EM (2007 - 2009).

8. Geophysical implications

Significant geophysical implications can be inferred from the estimated solutions. The occupancy of a Cassini State for the estimated pole location, as well as the implications about the obliquity and the structure of the interior, and a possible interpretation for the observed NSR are here reported.

8.1. Pole location and the Cassini state

For the estimated spin pole location the possible occupancy of a Cassini State has been analyzed (Figure 37). In this case it should be remembered that, since the provided estimates were obtained as a linear approximation in the time span of the observations, the validity of the rotation models is restricted to a limited time range. For the estimates obtained using the IAU model, the spin pole location for both 3 and 4 parameters fit are compatible with the occupancy of a Cassini State 1. In the computation a local Laplace pole was used[1], following JPL indications. The estimates for the spin pole are computed at the J2000 epoch. The normal to the orbital plane, computed for 600 years, from 2000 to 2600 ET, using DE421 JPL satellite ephemerides, is also reported. A weak deviation (~ 2°) from the perfect alignment can be observed, likely due to the definition of Laplace pole, whose uncertainty is not known. As it can be observed, both IAU and NAV models use different numerical values for the position and the linear drift of the Laplace pole; the numerical values should be considered valid only for a restricted time span (100 years or less). The same concept is applied to the estimated rotational models here provided.

---

[1] NASA Solar System dynamics: http://ssd.jpl.nasa.gov/

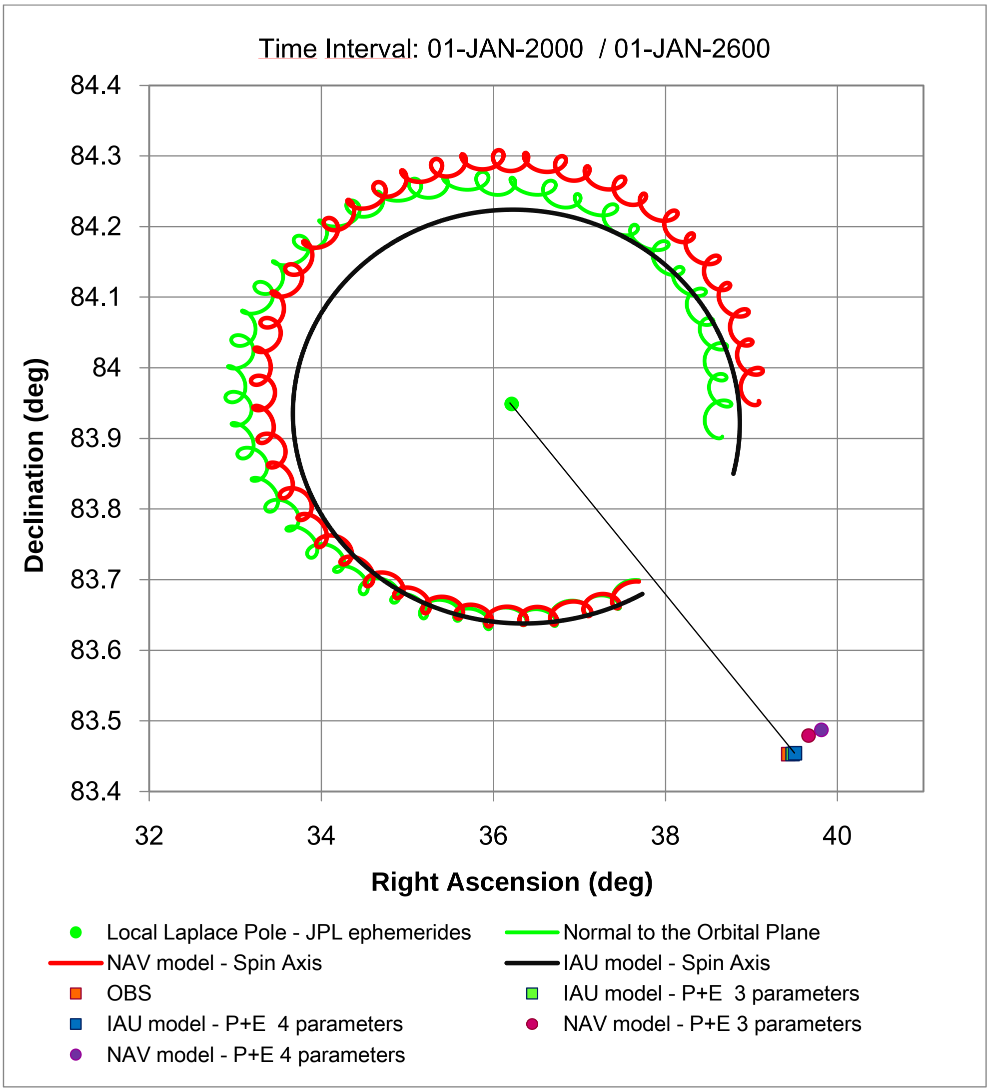

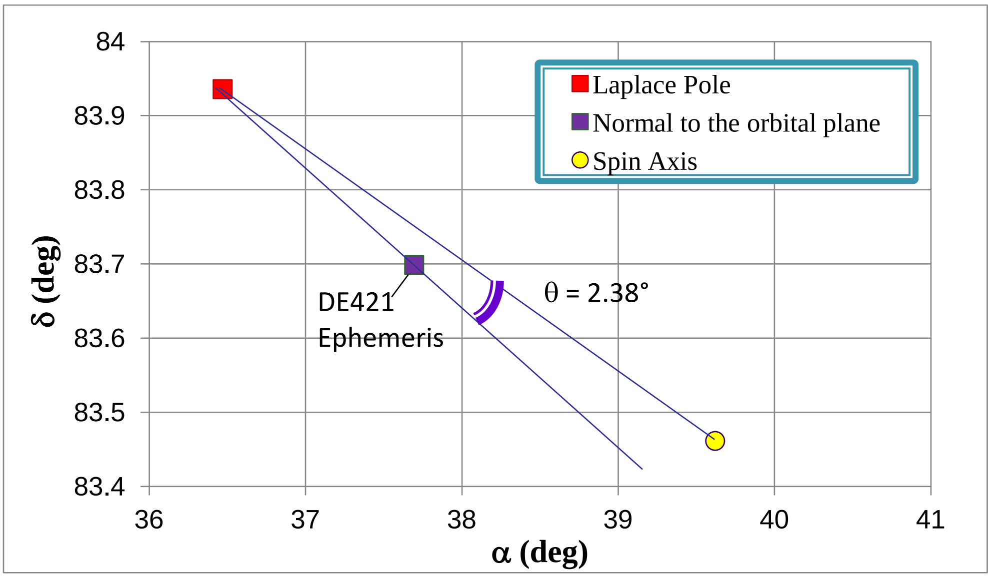

Figure 37 – Occupancy of the Cassini State 1 for Titan at J2000 Epoch

8.2. Seasonal variations of the spin rate

All the estimated values for ω are compatible with the synchronous rotation, but a residual NSR is still observed. This component show a sign inversion between the PM and the EM and it has an amplitude between + 0.02 deg/year and - 0.02° /year. A possible explanation for this result could be provided by (Karatekin et al., 2008) work on the Titan rotation. Karatekin et al. (2008) suggests that an icy shell, decoupled from the core, could be subject to variations of the spin rate due to the atmospheric torque acting on the surface. In this case the response of the crust to the atmospheric torque can be expressed by the ratio:

$$\frac{2K\frac{(C_i + C_s)}{C_i}}{\omega^2 C_s} \approx \frac{2K}{\omega^2 C_s} \tag{7.15}$$

where K is the strength of the gravitational coupling between the core and the shell and C_i, C_s are respectively the polar moment of inertia for the core and the shell. K is depending on the interior structure (the flattening and the densities of the core and the shell). The outer shell is rotationally decoupled from the interior when this ratio is much smaller than unity ($K < 10^{17}$ Nm) and the rotation variations are resonantly amplified when it is close to unity ($K \sim 10^{18}$ Nm). For the actual models of the interior this ratio varies between about 10 and 100, suggesting that the gravitational coupling ($K \sim 10^{20}$ Nm) is strong enough to lock the rotations of the outer shell and the solid interior; the only deviation from the synchronous condition could derive from seasonal changes of the atmospheric angular momentum. These changes are reported in Figure 38, where a sinusoidal variation with a maximum amplitude of 0.08 deg/year can be observed. The estimated values obtained for all three models (Estimate at Epoch, IAU, NAV) are compatible with this prediction, following also the sign inversion. This could be a valid explanation for the residual NSR observed into the estimate process.

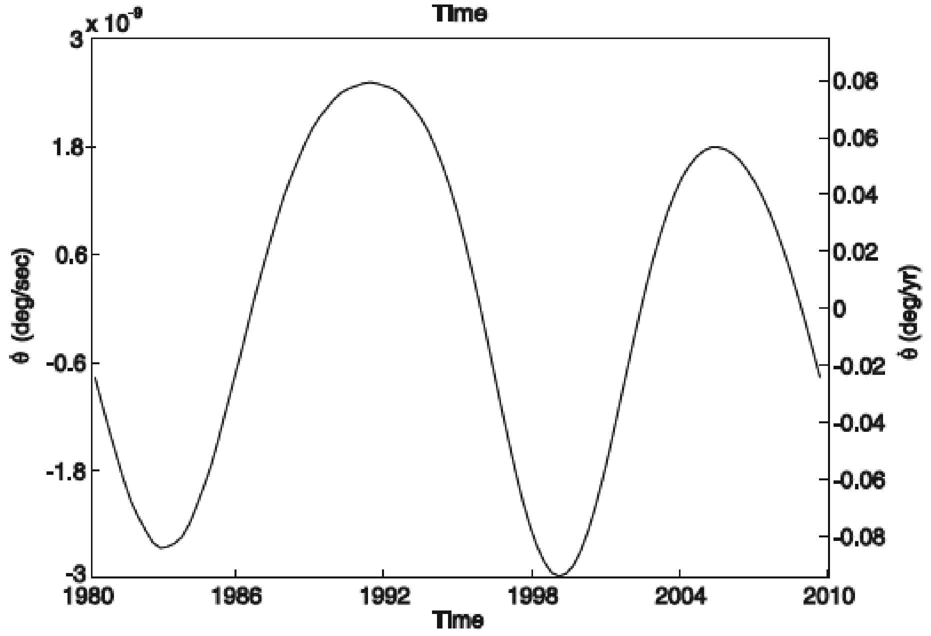

Figure 38 – Seasonal variations for the spin rate (Karatekin et al., 2008)

8.3. Estimated obliquity and the core-shell decoupling

The estimated value of ε (0.31°) confirm the previous estimate of (Stiles et al., 2008) and call the attention on the disagreement between the gravity and the rotation data. Following (Bills and Nimmo, 2008) we computed the polar MoI from the obliquity (see also Chapter I), estimating a MoI equal to 0.63, clearly considered an unphysical value. The difference between the two values could be explained observing that ε is derived from superficial measurements, whereas *c* is computed from gravity data referred to the whole satellite. If data from superficial observations are not consistent with gravity data, it is possible that the outer icy shell is decoupled from the core. But is it possible a core-shell decoupling for Titan? The gravitational coupling for Titan was studied by (Karatekin et al., 2008) in order to investigate the possible existence of a super-rotation. The strength of the gravitational coupling will prevent any deviation from the synchronous rotation > 0.05°, but inside this range some oscillations of the icy shell could be verified. If the core and the shell were partially decoupled, the obliquity inferred from rotation data would be relative only to the shell and this could explain the divergence between the gravity and the rotation data.

Chapter VIII

Results: Mercury and the BepiColombo Rotation Experiment

1. Mercury

Mercury is the innermost and smallest planet in the solar system, orbiting the Sun once every 87.969 Earth days. The orbit of Mercury has the highest eccentricity (0.206) of all the solar system planets, and the smallest obliquity (0.1°). Its orbital motion is characterized by a 3:2 resonance and by a precession of the perihelion around the Sun at a rate equal to 43 arcsec/century.

All available information about Mercury derived from ground-based observations and from two dedicated missions, Mariner 10 (1974-1975) and Messenger (2011). Mariner 10 was the first spacecraft to reach the planet, mapping about 45% of the planet's surface, providing a quadrupole gravity field and revealing the presence of a magnetosphere. The second is the MESSENGER probe, which attained orbit around Mercury on March 2011.

At a first sight Mercury is similar to the Moon, heavily cratered with regions of smooth plains. It does not have natural satellites and a substantial atmosphere. The large density (5441 kg/m^3), second in the solar system only to the Earth, and the magnetic field suggest the presence of a large iron core. The surface temperatures range from about 90 (bottoms of craters at the poles) to 700 K (subsolar point).

1.1. Interior

Mercury's distinctive features inspired different formation models, based on the high bulk density (5441 kg/m^3), quite impressive considering that Mercury is ~ 20 times less massive than the Earth. Such a large value suggests that 60 % of the planet's mass consists of iron, with a large size of the core and an apparently low percentage of FeO on the surface. Static models suggest a differentiated structure of the interior, with an iron core extending out to 75% of the planet's radius, a rocky mantle with a thickness ~ 600 km, and a lithosphere with a thickness equal to ~ 200 km.

Early formation

Weidenschilling (1978) presented the idea of aerodynamic fractionation during the accretion phase, which would separate metal from silicate and increase the abundance of metal in the formation region of Mercury. The high percentage of iron would be explained by the formation in the hot region close to the Sun, predicting a very limited presence of FeO in the rocks (< 3 %) . This model also predicts that Mercury should have higher concentrations of refractory elements (calcium and aluminium) with respect to volatile elements such as sodium and potassium.

Impact theory

In order to explain the absence of a large rocky mantle several authors (e.g. Wetherill,1988) propose models where Mercury was hit by a large object, likely wandering planetesimals come from as far away as Mars or the inner asteroid belt, after its differentiation, stripping away the silicate mantle. The impact ejected and possibly vaporized a great part of the mantle, increasing the amount of metallic core. When the large iron core started to cool, it contracted and the rigid outer crust collapsed and formed the unique scarps observed all over Mercury. The investigation of the surface composition and the measurement of the size of the core could provide crucial information on the formation history of the planet.

Molten core

Infrared and radio observations indicate a general lack of basaltic iron and titanium rich material, suggesting that deep-seated widespread volcanism shut off early in Mercury's formation history. If true, it suggests a very slow cooling of the iron core, which may still be partially molten. If the core consists of a mixture of Fe and FeS rather than pure iron, the melting temperature would be lower, strengthening the assumption of a partially molten core. A molten convective core could also sustain a magnetohydrodynamic dynamo system needed to generate the magnetic field detected around Mercury. Size seems to be an important feature of the intensity and duration of the melting processes.

The thermal evolution is characterized by the growth of a massive lithosphere on top of the convecting mantle. Following (Benkhoff et al., 2010) the lower mantle and the core cool comparatively little and temperatures stay between 1900 and 2000 K until about 2.0 Ga. After only 0.5 billion years convection structures become relatively small. The flow patterns in the early evolution show that mantle convection is characterized by numerous up-welling plumes fed by the heat flow from the cooling core. These up-wellings are relatively stable in terms of their spatial position. As the core cools down the temperature anomalies become colder but not less numerous (Benkhoff et al., 2010).

The large core of Mercury compared to the other terrestrial planets makes its thermal history very unique. Due to the weak constraints of important parameters (e.g. sulphur content of the core, mantle rheology, amount and distribution of radiogenic heat sources, planetary contraction, thermal conductivity) several models are required to understand the importance and influence of the mentioned variables. Generally the interior models are essential for the data analysis and for science mission planning.

1.2. The surface of Mercury

The knowledge of Mercury's surface is based mostly on the Mariner 10 data, which covers only ~ 50% of the surface, and on data recently received from MESSENGER. The morphology of the surface includes several craters, smooth plains, linear valleys and scarps. Mercury has been often compared to the Moon for the surface age and composition.

Even if several craters were observed, the smooth plains cover approximately 40% of the observed surface (Denevi et al., 2009). Evidences of large expanses of plains suggest that a substantial portion of the crust came about volcanically. Some very old plains lay between the largest old craters and it has been suggested that the plains have a volcanic origin. There are apparently color differences between the younger units (possible pyroclastics and volcanic flows) and the older inter-crater plains, which may be considered as representing the average crust of Mercury. In any case testing the idea of volcanism requires a more exhaustive knowledge about the chemical composition of Mercury.

Unlike on Earth, very few features on Mercury are clearly related to the tectonic forces that reshaped the surface, even if several observed features are thought to have been formed by compression. Linear valleys can be observed on the side of the planet opposite to the largest crater, Caloris Basin. They may have been formed when the planet's shape focused seismic energy from the impact into concentrated regions. Hapke et al. (1975) suggested that the surface of Mercury has very low contents of FeO and TiO_2, basing on the analysis of the albedo features observed on Mariner10 images. An extreme case of surface composition may be the complete absence of FeO.

Similarly to the lunar regolith, Mercury's surface should be modified by space weathering (micrometeoritic bombardment and solar wind particle precipitation), most probably to a greater extent than on the Moon. The expected optical effects of lunar-like space weathering are the formation of glassy agglutinates and submicroscopic Fe particles formed due to reduction of FeO in silicates. These tiny Fe particles lead to the darkening of the surface, a reduction of the spectral contrast and reddening of the spectral slope in the VIS–NIR spectral regions (Hapke, 2001).

1.3. Mercury's exosphere

The atmosphere of Mercury is very tenuous, with a pressure of a fraction of pico-bar, and is non-collisional so that atmospheric neutral particles move on ballistic orbits (Benkhoff et al., 2010). Therefore the atmosphere is called an exosphere. FromMariner10 UV and Earth-based optical spectroscopy measurements, six elements have been identified: Ca, Na, K, H, He and O. Measurements of MESSENGER should confirm these findings (Solomon et al.,2008).

Other species are expected such as H_2, OH (possibly released by impacting bodies) and noble gases (both non-radiogenic (Ne) and radiogenic (40Ar,129Xe)). The dynamics of Mercury's exosphere are complex due to the interaction of several factors such as the solar wind, the solar radiation, atmosphere, magnetosphere, planetary magnetic field and the rocky surface of the planet. This leads to high temporal and spatial variations in the exosphere, characterized by global asymmetries between day and night side as well as between the northern and southern hemispheres.

The determination of the composition, the structure and the dynamics of Mercury's exosphere is one of the scientific goals of the BepiColombo mission.

1.4. Mercury's magnetosphere (Benkhoff et al., 2010)

The physics of the magnetosphere of Mercury has been modeled resting upon the analogy with the Earth's. Currently the solar wind environment at the orbit of the planet and the fact that Mercury possesses a small intrinsic magnetic field are the only available information. A peculiarity of Mercury's magnetosphere is that the planet's surface is close to the day side magnetospheric boundary. Step-like increases in the ram pressure associated with solar wind disturbances will generate large-scale induction currents. These induction currents are such that they will temporarily add closed magnetic flux to the day side magnetosphere and effectively enhance the magnitude of Mercury's intrinsic magnetic field. Accordingly, the solar wind interaction with Mercury's dayside magnetosphere may be governed by more complicated physics than occurs at Earth. While the overall structure of the magnetosphere seems to be well predicted by the scaling arguments, which are the only possible ones with the currently available information, the dynamic aspects will be likely subjected to modifications due to MESSENGER and BepiColombo observations.

2. BepiColombo mission

The BepiColombo is a ESA/JAXA joint mission to Mercury, named after Professor Giuseppe (Bepi) Colombo (1920-1984), the first to observe the 3:2 resonance for Mercury. It will be launched on Ariane V on 2015 on escape trajectory to reach heliocentric orbit for Earth flyby after 1 year. The estimated launch mass is 4100 kg, including two probes: the Mercury Planetary Orbiter (MPO), led by ESA, and the Mercury Magnetospheric Orbiter (MMO), led by JAXA. The orbital transfer to the cruise trajectory will be performed by the Solar Electric Propulsion Module (SEPM) plus seven gravity assists: Earth, Venus (twice) and Mercury (four times). During the 6 year cruise phase to Mercury several instrument calibrations and a test of Einstein's theory of general relativity will be performed. The capture and the orbit insertion will be performed by chemical propulsion engines within the MPO, with the subsequent release of the MMO in a polar orbit (400 x 11824 km, 9.3 hr period). The MPO will then be inserted into a lower polar orbit (400 x 1508 km, 2.3 hr period). The nominal mission will extend for one year, with an optional one year extension. The main goals of the mission are:

- the investigation for the origin and evolution of Mercury;
- the determination of the gravity field and the topography;
- the determination of the interior structure and the geology, analyzing the chemical composition of the surface;
- the analysis of the composition and dynamics of the exosphere;
- the determination of the origin, structure and dynamics of the magnetosphere;
- the investigation of the polar deposits;
- Test of Einstein’s theory of general relativity.

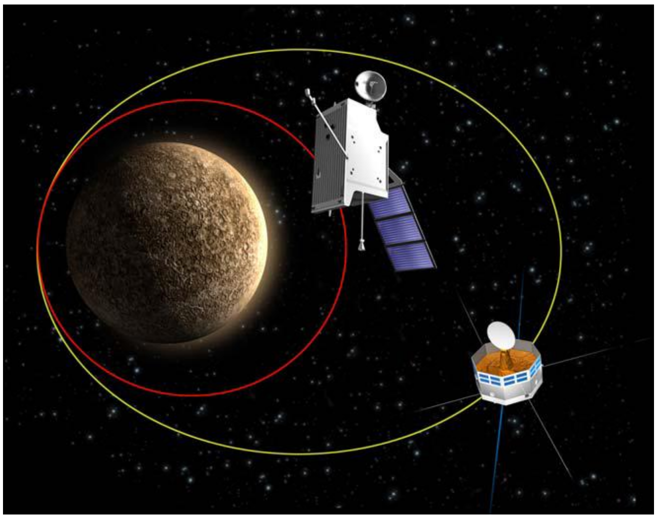

Figure 1 - MPO and MMO orbit

2.1. Orbit design

The full high-resolution mapping coverage of Mercury is one of the main scientific goals of the mission. For this reason polar orbits at low altitude were chosen. Nevertheless the proximity of the spacecraft to the Mercury surface implies a large (up to ~ 10 solar constants) thermal load due to the planet infrared emission and the albedo (Benkhoff et al., 2010). The MPO final orbit, a compromise between the scientific goals and the thermal load on the spacecraft, is a polar orbit at 400 x 1508 km with a 2.3-h period, with the apoherm on the equator on the sun side when Mercury is in its perihelion (Figure 1). This is a sub-solar point where the thermal load on the spacecraft is at its maximum. Half a Mercury year later, at aphelion, the sub-solar point occurs when the spacecraft is at its minimum distance to the planet.

For the MMO a highly eccentric orbit at 400 × 11824 km was selected, coplanar with the MPO orbit, in order to allow the mapping of the magnetic field and the investigation of the magnetosphere, covering the bow-shock, the magnetotail and the magnetopause.

Table 1 – general features of the MPO and MMO

	Mercury Planetary Orbiter	**Mercury Magnetospheric Orbiter**
Stabilisation	3-axis stabilised	15-rpm spin-stabilised
Orientation	Nadir pointing	Spin axis at 90° to Sun
Spacecraft Mass	4100 kg (at launch) 1075 kg (in Mercury orbit)	275 kg (in Mercury orbit)
Payload Mass	80 kg	45 kg
Payload Power	100-150 W	90 W
TM band	X/Ka-band	X-band
Data volume (downlink)	1550 Gbits/year	160 Gbits/year
Equivalent average data rate	50 kbits/s	5 kbits/s
Antenna	High-temperature resistant 1.0 m X/Ka-band high-gain steerable antenna	0.8 m X-band phased array high-gain antenna

2.2. Spacecraft design

Several information about BepiColombo characteristics can be inferred from (Benkhoff, 2010) and from ESA web site[1].

The MPO is a three-axis stabilized and nadir pointing spacecraft with an instrument suite of 11 experiments, while the MMO is a spinning spacecraft carrying a payload of five instruments (Table 1).

The MPO payload will include 11 instruments, comprising cameras, spectrometers (IR, UV, X-ray, γ-ray, neutron), radiometer, laser altimeter, magnetometer, particle analyzers, Ka-band transponder, and accelerometer.

Table 2 - List of the instruments and relative acronyms for MPO and MMO

INSTRUMENT	ABBREVIATION
MPO	
BepiColombo Laser Altimeter	BELA
Italian Spring Accelerometer	ISA
Mercury Magnetometer	MERMAG
Mercury Thermal Infrared Spectrometer	MERTIS-TIS
Mercury Gamma ray and Neutron Spectrometer	MGNS
Mercury Imaging X-ray Spectrometer	MIXS
Mercury Orbiter Radio science Experiment	MORE
Probing of Hermean Exosphere by Ultraviolet Spectroscopy	PHEBUS
Search for Exosphere Refilling and Emitted Neutral Abundances (Neutral and ionized particle analyzer)	SERENA
Spectrometers and Imagers for MPO BepiColombo Integrated Observatory System (High resolution and stereo cameras, Visual and NIR spectrometer)	SIMBIO-SYS
Solar Intensity X-ray Spectrometer	SIXS
MMO	
Mercury Magnetometer	MERMAG-M/MGF
Mercury Plasma Particle Experiment	MPPE
Plasma Wave Instrument	PWI
Mercury Sodium Atmospheric Spectral Imager	MSASI
Mercury Dust Monitor	MDM

---

[1] http://www.esa.int/science/bepicolombo

The MMO will carry a payload of five advanced scientific experiments, including a magnetometer, ion spectrometer, electron energy analyzer, cold and energetic plasma detectors, plasma wave analyzer, and imager. The full list of MPO and MMO instruments with the related abbreviations is reported on Table 2.

2.3. High resolution imaging system

The remote-sensing experiments will use the MPO three-axis stabilized, nadir-pointing platform to perform optical observations of the surface. The orbit eccentricity (0.163229) and low altitude (400 km at pericenter) are designed for high resolution mapping. The observations have to ensure the total coverage of the planet at a resolution sufficient to identify major landforms. A good phase angle coverage has also to be provided in order to allow the derivation of surface photometric properties and further improvements of the knowledge of local topography. Some stereo capability may also be useful to provide even stronger constraints; this should be traded-off against acquisition of topographic profiles by other dedicated means such as a laser altimeter (Benkhoff et al., 2010).
The preliminary assessment of the requirements suggests that the imaging system on MPO needs to provide:

- a surface global mapping with a resolution < 200 m,
- the imaging of selected areas (2-5% of the surface) at a resolution equal to ~20 m,
- a phase angles range (from 0 to 120°) in order to derive surface photometric properties for specific areas,
- a dynamic range between 12 and 14 bits per pixel in order to distinguish subtle variations of the surface properties.

Since the requirement of a global coverage and a high resolution system are not strictly compatible, a wide angle system will also be provided, supplemented either as a sub-system of the high resolution camera or as a separate system. The integrated package for the imaging and spectroscopic investigation of Mercury's surface is the *Spectrometer and Imagers for MPO BepiColombo Integrated Observatory System* (SIMBIO-SYS). The scientific goals of SIMBIO-SYS include the investigation of the surface age and composition, the volcanism and the global tectonics of Mercury. It incorporates capabilities to perform a global mapping in stereo and color imaging at medium-spatial resolution, using two pan-chromatic and three broad-band filters. Also a high-spatial resolution imaging with pan-chromatic and three broad-band filters can be performed, as well as the imaging spectroscopy in the spectral range 400–2000 nm (Flamini et al., 2009).

SIMBIO-SYS is made up to:

- *Stereo Channel (STC)* - providing the global color coverage in full stereo at 50 m/pixel resolution, in order to define the main geological units and large-scale features;
- *High spatial Resolution Imaging Channel (HRIC)* - providing high-resolution images (~ 5 m/pixel from 400 km altitude) in four different bands, for special surface targets;
- *Visible Infrared Hyperspectral Imager Channel (VIHI)* - a hyperspectral imager in the visible and near-infrared range providing the global mapping of the global mineralogical composition of the surface.

Line-scan cameras can be proficiently used in the case of nadir-pointing S/C performing near-circular orbits. These devices can perform the required tasks and accommodate additional lines with color filters to provide mineralogical information without moving parts. For a good coverage, around 6 additional colors should be incorporated into the focal plane. The data volume is reduced by normally operating the color lines in a binned (2 x 2) mode. The HRIC features are reported on Table 3.

Table 3 - HRIC general features

Parameter	Value
Focal length	330 mm
Aperture	38 mm
Design	Cassegrain-like, line scan
Central obscuration	30 %
Effective f-ratio	10.4
Typical filter bandwidth (nm)	100 nm
Pixel pitch	9 μm
Full-well capacity	1.5 E05 electron
IFOV	27.3 μrad /px
Minimum number of pixels	2048
Swath width at periapsis	21 km (3.2°)
Peak quantum efficiency	40 %
Scale from 0.16 RM	10 m/px
Typical phase angle for observation	45°
Maximum exposure time at 0.16 RM	3.5 ms
Single line data acquisition rate at 0.16 RM	7.0 Mb/s
Number of colours	7
Wavelength range	350-1000 nm

3. MORE rotation experiment

The Mercury Orbiter Radio-science Experiment (MORE) attends to several scientific goals in geodesy, geophysics and fundamental physics:

- reconstruction of the planet's gravity field (up to degree and order 25) and the Love number k2 (*gravimetry experiment*). The expected accuracies range from SNR of 104 for degree 2 to SNR of 10 for degree 20 (Genova et al., 2010);
- determination of the post-Newtonian parameters, the mass and the oblateness of the Sun, and the upper limits to the temporal variation of the gravitational constant G (*relativity experiment*);
- estimation of the obliquity and the amplitude of the physical librations in longitude (*rotation experiment*). These measurements, carried out in collaboration with the HRIC team, will provide information on the polar moments of inertia of the whole planet and its mantle.

These scientific goals will be achieved by means of several data types, generated at the ground station or on board by the relative instruments (BELA, ISA and SIMBIO-SYS) using the attitude determination and control system. The Rotation Experiment will be performed by the interaction of MORE with the SIMBIO-SYS experiment, using the imaging from orbit technique described in the Chapter IV.

The method used to estimate Mercury's rotational state makes use of a combination of HRIC optical images, MORE radio tracking data and ISA readings. The registration errors are computed by matching pairs of HRIC optical images of the same area, taken at different times. The images will be georeferenced by using MORE, ISA and telemetry data and correlated applying different pattern matching algorithms. Then the rotational parameters will be estimated by the minimization of the registration errors.

A delicate aspect to assess the achievable accuracy of the method sketched above is the setup of realistic error models for all the measurements involved in the process.

The models include several error sources: the accuracy of the spacecraft ephemeris and the attitude determination, the camera misalignment, timetag errors and the accuracy of the pattern matching algorithms. Error sources and models are reported in 3.2 Section.

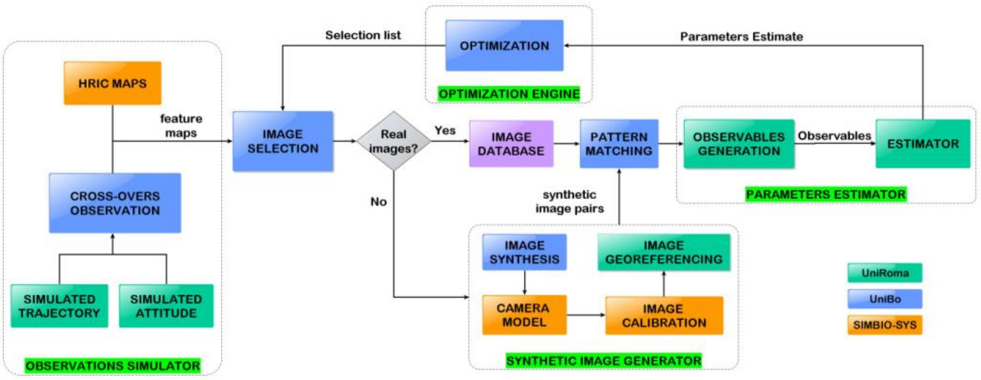

Figure 2 - Architectural design for the Rotation Experiment Simulator

3.1. RES: the Rotation Experiment Simulator

Accurate simulations of the experiment are required in order to determine the effects of the several error sources on the accuracy of the measurement. For this reason an end-to-end Mercury Rotation Experiment Simulator (RES) has been developed by a joint MORE/HRIC team. RES includes:

- a Mercury simulated digital elevation model
- a HRIC optics and electronics simulator
- a S/C attitude simulator
- several image processing and pattern matching algorithms
- a rotational state estimator (RSDS)

As a by-product, the simulator is designed to allow the optimization of the HRIC images acquisition scheduling, in particular those focused to the rotation experiment, a feature which may offer significant advantages for the limitation of MPO data volume (Tortora et al., 2011). RES is at the same time a simulator of the experiment and a processor of the real data. Are involved in the experiment the MORE Team, represented by the Radio Science Lab (Università Sapienza - Roma), and the Alma Mater Studiorum University - Bologna (UniBo), jointly to the SIMBIO-SYS HRIC Team. The contribution relative to each team is reported in the RES block diagram (Figure 2). RES is a modular, cross-platform stand-alone application where the following operations are performed:

- a global mapping of the predicted crossover areas is generated from the S/C trajectory and attitude. The spacecraft ephemerides and attitude are available from dedicated simulations. Crucial information as illumination angles, observation times and number of passages are also stored. The mapping is subsequently matched with the scheduling of the camera observations in order to provide the available crossovers. These are send to the selection module.

- A crossover dataset is selected following the constraints provided by the optimization module. They rely on the illumination conditions, the altitude of the orbit, the geographical distribution and their combined effect on the estimate. In the real mode all the images including the selected crossovers are detected in the database and send to the pattern matching module. In the simulation mode the crossovers are send to the synthetic image generator.
- In the simulation mode only, for each crossover a pair of synthetic images is generated. Information on the altitude and the illumination angles are processed by the synthetic image generator. The HRIC model and calibration are applied to every image. The images are georeferenced using a nominal rotational model and shifted by a simulated registration error, before to be send to the pattern matching module.
- For each crossover the images are matched by a specific algorithm, selected according to illumination conditions and altitude. Several pattern matching algorithms will be available, from SIFT/SURF to combined matching and shape from shading algorithms. The (real or simulated) offset with the relative accuracy is computed and send to the module for the generation of the observables.
- The observables (misregistration vectors) are computed using the registration error. The error associated to the observables is computed considering the several error sources affecting the process. Subsequently the observables are send to the RSDS.
- The rotational parameters of interest are estimated using the (real or simulated) produced observables by a weighted least squares method. Ancillary data relative to obliquity, Cassini State and residuals are also provided. The estimation results are send to the optimization module.
- The results of the estimation are processed by the optimization module. Indications for an improved estimate in terms of altitude, illumination angles and geographical distribution are provided by the application of a cost function. The estimation is iteratively improved.

Each step of the process is reported in detail in the following sections.

3.1.1. Observation simulator

The observation simulator (Tortora et al., 2011) provides a global mapping of the crossovers. The simulated trajectory (Genova et al., 2010) and the attitude of the spacecraft have been provided taking into account the currently predicted operative scenery.

The dynamical model used for the simulated trajectory takes into account non-gravitational perturbations, blackout periods and desaturation maneuvers of reaction wheels. The task has been accomplished by means of range rate measurements accurate to 0.003 mm/s (at 1000 s integration times), enabled by highly stable, multi-frequency radio links in X and Ka band (Genova et al., 2010). The best results were obtained with a batch-sequential filter, which proves to cope well the complexity of the noise and dynamical models. The crossover mapping was generated by gridding the Mercury surface and numbering S/C observations for each point of the grid. Ancillary data (observation epoch, altitude of the orbit, illumination angles) have been also associated to each point of the grid. Currently a 770 × 1540 grid (9 km resolution at the equator) is used, not considering latitudes over 85° in order to exclude a part of frequent but not significant polar crossovers. The mapping of all the potential crossovers needs to be matched with HRIC scheduling of the observations, in order to detect the predicted observations and provide the mapping of the observed crossovers.

3.1.2. Data selection and storage

A dataset can be generated from the available crossovers following the constraints provided by the optimization module. The process is performed by the selection module, which uses the output of the optimization module to guide the data selection. Since the optimization is following the estimate process in the first open-loop simulations it is not applied and data selection is guided only by simple filtering criteria, in order to ease the simulation process. Actually filtering criteria are based on:

- *altitude* - S/C radial distance from surface, directly related to the image resolution. The pattern matching of images at different resolutions requires robust algorithms and it is a more complex process than matching images at the same resolution. Filtering for similar S/C altitude will allow to obtain images at the same resolution.
- *illumination angles* – the illumination conditions lead the choice of the pattern matching algorithm to apply. For each pattern matching technique a sufficient level of accuracy is provided only for a predefined range of illumination angles (Sun azimuth and elevation). In general, images taken at similar light conditions should be preferred in order to compute the registration errors with a sub-pixel level of accuracy.
- *geographical distribution* – the distribution of the observations directly affect the estimate. The estimation of the spin rate as well as the amplitude of the physical librations in longitude can be improved by equatorial observations. On the contrary, polar observations positively affect the estimation of the obliquity. Since MPO will be inserted on a polar orbit, the distribution of the crossover observations will be concentrated on high latitude regions.

The global mapping of the observations and the relative images are stored in a dedicated database. In an operative scenery the real images are selected and send to the pattern matching module. In a simulation the observations are used to generate synthetic images, stored in the database and send to pattern matching module.

3.1.3. Synthetic image generator

The Synthetic Image Generator provides for each crossover a pair of synthetic images using the ancillary data (location, observation epoch, altitude, illumination conditions). The generator is made of four modules: image synthesis, camera model, image calibration and image georeferencing, here briefly introduced.

Image Synthesis

Gherardi (2010) developed a Digital Elevation Model (DEM) in order to simulate the real conditions. The synthetic image generation procedure is divided in three steps. Initially a fractional Brownian motion algorithm generates a plain surface according to a $1/f^n$ pink noise. This procedure allows to define the coarser texture level free from any other feature (craters, ridges or bumps) at each scale.

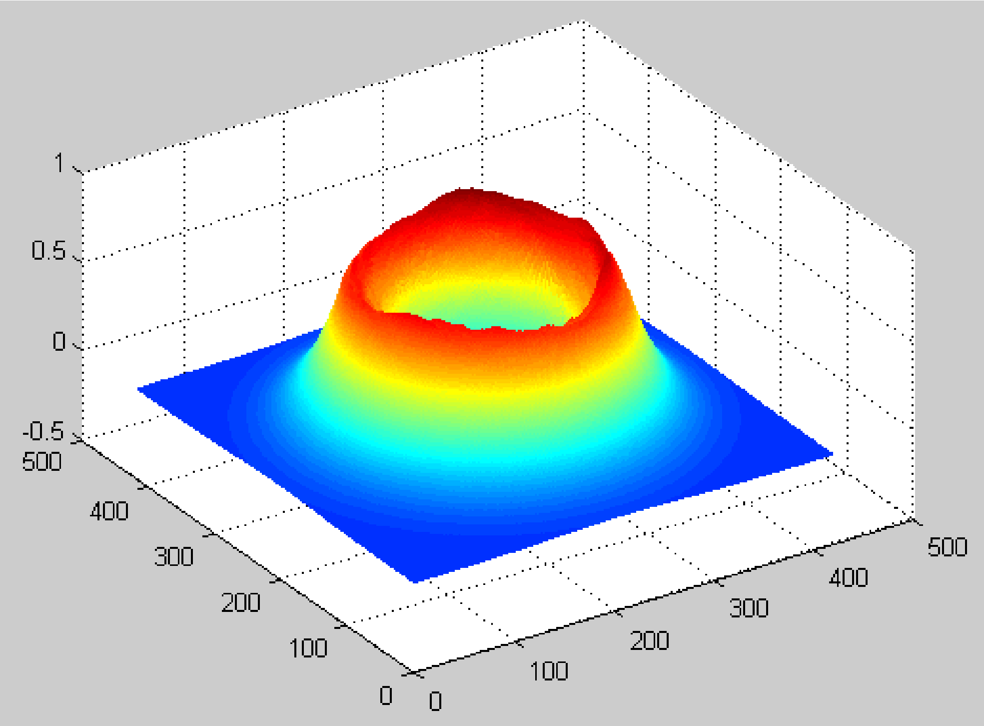

Figure 3 - Digital Elevation Model for crater simulations

Figure 4 - the simulated Mercury surface (A courtesy of Bologna University)

Subsequently a random number of craters, defined by variable size and density, is added randomly to the coarse DEM shape (Figure 3). Crater size and density were estimated by analyzing images acquired by Messenger and Mariner10 and taking into account the HRIC ground resolution.

Finally, the previous two steps are iterated until the resulting DEM is generated (Figure 4). The illumination is modeled using the sun elevation and azimuth angles, defined in the HRIC reference frame. The offsets along the two principal directions of the DEM are used to position the camera. A zoom parameter adjusts the field of view of the camera according to the altitude of the probe.

3.1.4. 3.2.4 - Image georeferencing

Provided synthetic images need to be georeferenced with a nominal rotational model. For the simulations as well as for the real data processing the IAU rotational model will be used for georeferencing. Nevertheless, in the first case the registration error needs to be simulated.

Crossover mapping is produced using the IAU rotational model: consequently, any deviation from this model will provide an offset in the image pair.

$$\Delta\boldsymbol{\rho}_{\boldsymbol{IAU}} = M_{IAU}(t_2)\boldsymbol{r}_2 - M_{IAU}(t_1)\boldsymbol{r}_1 = 0 \qquad (7.1)$$

The expected offset $\Delta\boldsymbol{\rho}_{\boldsymbol{IAU}}$ for the IAU model is null because crossovers were calculated using this rotational model (theoretical case). Since in a real case the “true” rotational model is different from the nominal model used for georeferencing, a reference model (M_{REF}) is used to simulate the registration error ($\Delta\boldsymbol{\rho}_{SIM}$):

$$\Delta\boldsymbol{\rho}_{\boldsymbol{SIM}} = M_{REF}(t_2)\boldsymbol{r}_2 - M_{REF}(t_1)\boldsymbol{r}_1 \tag{7.2}$$

The $\Delta\boldsymbol{\rho}_{SIM}$ offset, expressed in body-fixed coordinates, is reported on camera coordinates and then applied to images simulating the registration error. Final images are georeferenced by IAU and include the offset computed for the reference rotational model.

3.1.5. Pattern matching

Different PM algorithms have been implemented in order to test the robustness of each algorithm for different altitude and illumination conditions; they are reported on Table 4. SIFT and SURF algorithms (see Chapter IV) have been used for the crossovers characterized by significant differences in the altitude (resolution), while more complex algorithms (which require the image preprocessing) were used in the case of large variations of the illumination conditions.

1.1.1. Generation of the observables

Pattern matching provides the computed offset for an image pair. Take a reference point in the first image. Since images are georeferenced, the body-fixed coordinates of the point are known. From the offset it is possible to compute the position of this point in the second image. Also in this case the coordinates can be inferred from georeferencing. The difference between the observed positions of the same point is the optical observable (see equation 7.2).

Table 4 –pattern matching robustness to changes of scale and illumination

PM Method	**ΔAltitude**	**Sun ΔElevation**	**Sun Δ Azimuth**	**Notes**
SIFT/SURF Features	High	Limited	Very limited	*No dependance on surface features*
Geometric Features	Moderate	Moderate	Limited	*Preprocessing required*
Transformed feature shape + combined matching and shape from shading	Moderate	High	High	*Preprocessing required*

In this module the optical observables are computed, as well as the associated error. Currently:

- the position error is inserted directly in the S/C ephemerides (perfectly simulating real operative mode); in this case in the computation of the weight of the observables the average value of along-track and across-track error is taken into account;
- the attitude error is inserted directly in the S/C attitude kernel (simulating real operative mode). Currently only the Gaussian, white noise component of the error is inserted, while the systematic component is under investigation and is taken into account with an adequate contribute to the weight associated to the observables;
- time tagging error has been considered negligible at the moment;
- the pattern matching error is inserted directly into the generation of the observables.

The definition of the error models is reported in 3.2.8.

1.1.2. Estimator

Optical observables are processed by RSDS in order to minimize the registration error estimating the rotational parameters with a least squares method. The architecture and the functions of the estimator have been extensively described in Chapter IV and V. Different rotational models and estimation setup can be taken into account. Actually the preferred setup includes 1 parameter (libration in longitude), 3 parameters (pole location and spin rate) and 4 parameters (pole location, spin rate and libration amplitude). The estimates (central value and relative accuracy) are then send to the optimization module.

1.2. Error models

In order to analyze all the effects which can provide a contribute to the error budget, several error sources have been taken into account:

- S/C position and orbit determination;
- S/C attitude determination;
- HRIC focal axis misalignments with respect to S/C reference frame;
- image time-tagging errors;
- accuracy of the pattern matching algorithms;
- systematic error sources.

The first three error sources refer to the inaccuracy in the determination of absolute position of the S/C and the camera, the fifth is due to the pattern matching process, while the last refers to the systematic effects due to thermoelastic deformations.

Position error

The determination of the accuracy of the spacecraft ephemeris is crucial for the rotation experiment because the georeferencing is heavily dependent from the position and the attitude of the probe. In the latest orbit determination simulations performed by Genova et al. (2010), currently used in the experiment simulator, the position errors are consistently found below 10 m for both the along and across track components, while much better accuracies (~ 1 cm) are obtained for the radial component. The along- and across-track accuracies are compatible with a required accuracy of 2 arcsec for the estimate of the amplitude of physical librations in longitude. An improvement in the orbit determination is required to measure the amplitude of the physical librations with an accuracy < 1 arcsecond.

Attitude error

The final accuracy of this experiment relies not only on an accurate determination of the spacecraft trajectory, but also on the quality of the attitude reconstruction. The attitude error represents the misalignment of the camera with respect to the nominal position (nadir pointing) due to an error in the attitude determination or control. This kind of error creates a shifting of the surface image captured from the camera with respect to the center of the nominal nadir image.

Basically two distinct components of attitude errors need to be taken into account: a white-noise, Gaussian component and a component due to the presence of systematic effects into the attitude determination/control systems. Following (Iess et al., 2003) the Gaussian component of the attitude error has been modeled as a misalignment of the pointing direction with respect to the nadir position, characterized by a randomly generated direction and a modulus equal to 2.5 arcsec. More recently, the onboard star trackers and gyroscopes should allow for the Gaussian component an accuracy of 1-2 arcsec. In addition, the spacecraft design ensures a high stability of the optical alignment between the star trackers and the camera.

Camera misalignment

The effect of the temperature on the spacecraft can cause a deformation of the structure and a consequence misalignment of the camera pointing. To model this error a simple relationship has been adopted:

$$\delta\alpha = a_0 + a\cos E_M - b_0 - b\cos E_{S/C} \tag{7.3}$$

where $\delta\alpha$ is the angular misalignment of the camera, a_0 ,b_0 represent the error bias and a,b represent the coefficient of hit reemission of Mercury and the direct influence of the sun on the spacecraft heating.

Following (Iess et al., 2003) the misalignment may assume a maximum value equal to ~ 5 arcsec.

Time tagging error

The time tagging error indicates a discrete error due to the wrong time clock reference on board. Generally the clock can randomly precede or delay the correct time by a tick at a time, giving rise to an error of +1, –1 or zero, if the clock is synchronized with the real time. The clock error then generates a shifting vector in the along-track direction, defined as the product between the S/C velocity vector per the step time. For an error of 1 s the correspondent maximum error on the surface is ~ 2 meters, below the maximum HRIC resolution.

Pattern Matching error

In this case the error is tied to the algorithm chosen to perform the pattern matching. The error depends on the resolution, the illumination conditions and also on the software code used for the correlation itself. Quite conservative (Iess et al., 2003) estimated variance for a 2D Correlation is ~ 2 arcsec. More recently UniBo performed preliminary tests based on SIFT features extracted from images with limited differences in phase angles (elevation $\varphi < 30$ deg and azimuth $\theta < 40$ deg). Results show a sub-pixel accuracy (less than 1/10 of a pixel) (Gherardi, 2010). SIFT and SURF applied methods (see Chapter IV) show a good capability on tracking features at different scales, such as when considering images taken at the periherm and apoherm side. Nevertheless at the moment several other methods are under investigation in order to be employed when severe differences in phase angles are present.

1.3. Simulations

Preliminary simulations have been performed with a reduced number of crossovers. This is due to the computational weight of the synthetic image generator, which is partially under development. Observations vary between January and December 2021.

3 Parameters configuration

A simulation campaign has been performed in order to estimate the pole location and the spin rate. The reference rotational model was an IAU modified model where the values of right ascension and declination of the pole and the spin rate were changed, holding fixed the other IAU parameters. Pattern matching on rendered DEMs was executed on 5 image pairs with SIFT features tracking (Figure 5). A sub-pixel accuracy level was reached in this case.

In order to ease the generation of the synthetic images and the pattern matching process some constraints were applied in the establishment of the simulation set up.

Two different constraints were applied on the illumination angles (Sun elevation and azimuth) in order to compare images with similar illumination conditions. A limit on the altitude difference was also imposed in order to compare images with compatible resolutions. A minimum value of the difference between predicted libration amplitudes is also imposed. Furthermore, a spherical Mercury is imposed, being negligible in this phase the altimetry data (from Mariner 10 data, the difference between the ellipsoid axes a-c = 200 m and a-b = 150 m). The simulation setup is reported on Table 5.

Table 5 - Simulation setup and imposed constraints

ID	*Constraint*	*Value*	*Notes*
C1	*Elevation angle:*	between 35° and 85°	Imposed to compare images with similar illumination conditions
C2	*Max elevation difference:*	10°	Imposed to compare images with similar illumination conditions
C3	*Max difference in azimuth:*	free parameter	Not constrained.
C4	*Altitude max difference:*	700 km	Imposed to compare images with compatible resolutions.
C5	*Minimum libration difference*:	50 m	The expected libration amplitude for Mercury is around 400 m.
C6	*Spherical Mercury*	R = 2439.7 km	From Mariner 10 data, the difference a-c = 200 m, a-b = 150 m.

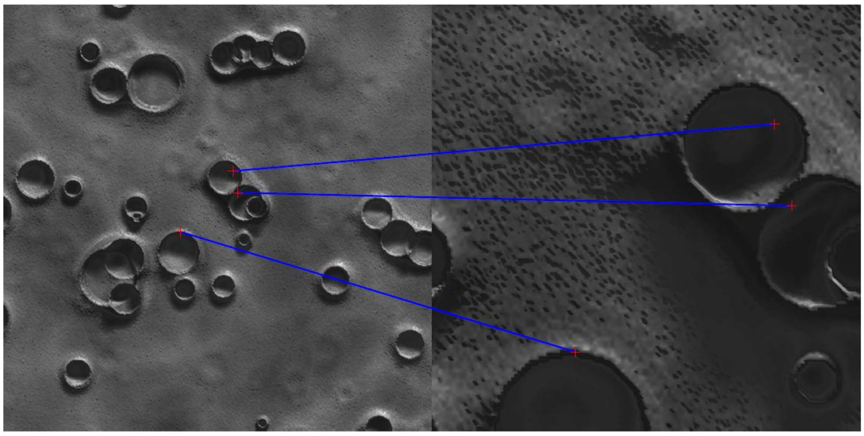

Figure 5 - pattern matching of simulated features. Please notice the different light conditions and resolutions due to different altitudes.

Different pseudo-true rotational models were used in order to test the capability of the simulator to correctly estimate the rotational parameters through different error levels; Estimate results for the worst case are reported on Table 6. The initial registration error was ~ 100 m, very huge if compared to the maximum HRIC solution of 5 m at the periherm (400 km). The registration error included also the pattern matching error, estimated in this case with a sub-pixel accuracy. The weight associated to the observables was equal to 10 m. Post-fit residuals are < 0.5 m, with a misregistration reduction factor equal to 99.73% (Figure 6).

Table 6 - RES simulations: estimated values for the worst case

Parameter	Estimate	Reference	Unit
α_0	280.010 ± 7.123E-002	280.01	deg
δ_0	61.351 ± 5.230E-002	61.35	deg
ω	6.13851768 ±1.093E-06	6.1385176	deg/day

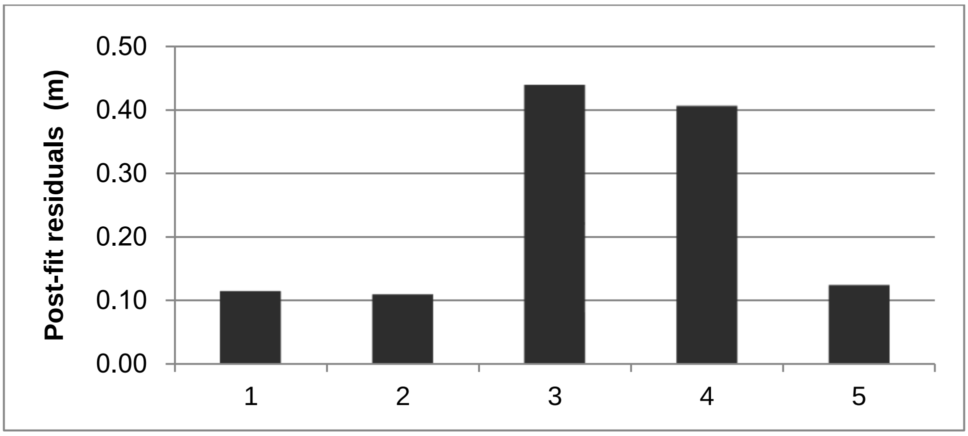

Figure 6 – Simulations: post-fit residuals

Conclusions

In the present work four different goals have been reached: an in-depth review of the imaging from orbit technique, the development of rotational models matched to the experimental accuracies, the design and realization of a numerical code for the estimate of the rotational parameters and, finally, the application of models and codes to the determination of the rotational state of Titan and Mercury.

The imaging from orbit technique was widely reviewed in order to reach better accuracies and to optimize the data processing. Different pattern matching algorithms were proposed and their efficiency for different cases has been reported. Crucial aspects such as the crossover identification, the feature classification and the differences between the usage of the optical and radar images were analyzed. A complete formulation for the application of the weighted least-squares method for the determination of the rotational state has also been provided, as well as several guidelines for the optimization of the rotation experiment using the imaging from orbit technique.

Available rotational models have been reviewed and an extended (EXT) rotational model was developed in order to describe with improved accuracy the rotational state, including the polar motion and the length-of-day variations. Furthermore, also a modified version of the IAU model for satellites was provided in order to include physical librations.. The analytical expressions of the partial derivatives of the optical observables with respect to the rotational parameters have been provided for each model.

One of the main goals of the present work was to design and write a numerical code able to estimate the rotational parameters by means of optical observables. The developed estimator (RSDS) incorporates different rotational models and the associated analytical expressions for the partial derivatives. Extensive numerical simulations showed the capability of the code to accurately estimate the spin pole location and the spin rate also when the observables are affected by systematic errors. The RSDS has been used for both Titan (Cassini) and Mercury (BepiColombo) Rotation Experiment.

Cassini mission: Titan Rotation Experiment

The described technique and RSDS have been successfully applied to the Titan Rotation Experiment of the Cassini mission. 243 optical observables were produced by from the available set of radar images in order to obtain the first available estimate from the extended mission data. The obtained residuals vary from an average value lower than one kilometer (benchmark case) up to 1.7 km. These large residuals (as compared to the expected experimental accuracy) have been attributed to the effects of the unmodeled short period oscillations, (nutations and librations).

The spin axis direction has been estimated by different types of data fitting. The averaged pole location obtained by the estimate at the observation epoch is compatible with the previous estimate (Stiles et al., 2008), with a pole location (α = 39.45° ± 0.042°, δ = 83.451° ± 0.005°) observed at a reference epoch (27 March 2007). Since the validity of the estimated pole location is restricted to the epoch of the observations, this estimate cannot be strictly considered as a rotational model valid over long time scales, such as the precession period. An updated version of the IAU rotational model has been provided, obtained by the estimate of the precession terms. The model is a linear approximation where the precession does not occur about the true Laplace pole. The location of the Laplace pole is at α_0 = 37.34° ± 0.009° and δ_0 = 83.769° ± 0.002°, while the amplitudes of the precession terms are respectively β_α = 4.48° ± 0.08° for RA and β_δ = -0.352° ± 0.002° for DEC. Also the Titan rotation model used by the Cassini Navigation Team has been updated taking into account, but not estimating the nutation terms. In this case the location of the Laplace pole is estimated at α_0 = 37.71° ± 0.009° and δ_0 = 83.793° ± 0.002° and the amplitudes for the precession terms are β_α = 4.59° ± 0.08° for RA and β_δ = -0.355° ± 0.002° for DEC, respectively. Relevant differences can be observed between the estimated values for the Laplace pole location and the expected values, likely due to unestimated short period effects.

A spin rate equal to 22.57693 deg/day has been estimated. This value is compatible at a 3σ level with the synchronous rotation value depending on the used dataset, in agreement with the predicted 1:1 orbital resonance. The measure significantly differs from the previous estimates (Stiles et al., 2008) of 22.5780 deg/day. The residual non-synchronous rotation (NSR) vary from + 0.02 deg/year to - 0.02 deg/year, depending on the data set used (prime mission, 2004 – 2007, or extended mission data, 2007 - 2009). The existence of such a component of super-rotation is fully compatible with those predicted by (Karatekin et al., 2008), due to the presence of an atmospheric torque acting on an icy shell gravitationally decoupled from the core.

The estimated obliquity is ε = 0.31 ± 0.005°, (ε =0.32° ± 0.01°, considering only the data from the prime mission). The moment of inertia factor (MoI) inferred from the estimated obliquity (0.63) is not compatible with the MoI inferred from gravity field measurements (0.34, Iess et al., 2010). This discrepancy suggests that some of the hypotheses of the Cassini state model are not valid. For example, a decoupling between the outer icy shell and the core would lead to different results. Given its relevant geophysical implications, it should be explored in future work..

The estimated spin pole location is not fully compatible with the occupancy of Cassini state 1, as predicted from (Bills & Nimmo, 2008). Weak deviations from Cassini state could be added to the definition of the Laplace pole.

Further improvements could be reached by estimating also the nutation terms and a modeling of the short period effects, (librations, atmospheric variations of the spin rate). However, the inclusion of nutation terms at the actual nominal values does not improve the residuals. Better results may be obtained by including the nutation terms in the estimate.

Mercury Rotation Experiment - BepiColombo Mission

In this case the optical imaging from orbit technique was applied to the realization of a rotation experiment simulator. The simulator includes all steps of the data processing, from the generation of the optical observables to the parameter estimator. We provided the general architecture and modules for the georeferencing and the simulation of the registration error. As part of the simulation, realistic kernels od the spacecraft attitude were also produced. The core of the estimation process (RSDS) was integrated with the other elements of the simulator and used in preliminary simulations of the rotation experiment.

The simulator has been used to identify an error budget of the rotation experiment, allocating contributions for errors in the spacecraft orbit, spacecraft attitude, misalignments between the camera and the star trackers, pattern matching. The allocation was carried out in order to meet a target accuracy of 1 arcsec in the amplitude of Mercury’s librations in longitude. Future work should address also the systematic errors in the onboard attitude determination system and the effects of thermoelastic deformations of the camera.

References

Bay, H., Tuytelaars, T., And Van Gool, L., "SURF: Speeded Up Robust Features", *Computer Vision – ECCV 2006* , Lecture Notes in Computer Science, **3951**/2006, 404-417, 2006, doi: 10.1007/11744023_32

Benkhoff, J., Casteren, J., Hayakawa H., Fujimoto, M., Laakso, H., Novara, M., Ferri P., Middleton, H. R., Ziethe, R., "Comprehensive Science Investigations of Mercury: The scientific goals of the joint ESA/JAXA mission BepiColombo", *Planetary and Space Science*, **58**, Issues 1-2, Pages 2-20, January 2010. doi:10.1016/j.pss.2009.09.020

Bills, B.G. and Nimmo, F., "Forced obliquity and moments of inertia of Titan", *Icarus,* **196**, 293–296, 2008. doi:10.1016/j.icarus.2008.03.002

Castillo-Rogez, J.C. and Lunine, J.I., "Evolution of Titan's rocky core constrained by Cassini observations", *Geophysical Research Letters*, **37**, L20205, 2010 doi:10.1029/2010GL044398

Davies, M. E., Colvin, T. R. , Rogers, P. G. , Chodas, P. W. , Sjogren, W. L., Akim, E. L., Stepanyantz, V. A., Vlasova, Z. P. and Zakharov, A. I., "The Rotation Period, Direction of the North Pole, and Geodetic Control Network of Venus", *J. Geophys. Res.*, **97**(E8), 13,141–13,151, 1992. doi:10.1029/92JE01166.

Denevi, B.W., Robinson, M.S., Solomon, S.C., Murchie, S.L., Blewett, D.T., Domingue, D.L., McCoy, T.J., Ernst, C.M., Head, J.W., Watters, T.R., Chabot, N.L., "The evolution of Mercury's crust: a global perspective from MESSENGER". *Science*, **324**, 613–618, 2009.

Elachi, C., Allison, M.D., Borgarelli, L., Encrenaz, P., Im, E., Janssen, M.A., Johnson, W.T.K., Kirk, R.L., Lorenz, R.D., Lunine, J.I., Muhleman, D.O., Ostro, S.J., Picardi, G., Posa, F., Rapley, C.G., Roth, L.E., Seu, R., Soderblom, L.A., Vetrella, S., Wall, S.D., Wood, C.A., Zebker, H.A., "RADAR: The Cassini Titan Radar Mapper", *Space Science Reviews,* **117**, 71-110 (2005) doi: 10.1007/s11214-004-1438-9

Elachi., C., Wall, S.D., Janssen, M.A., Stofan, E., Lopes, R., Kirk, R.L., Lorenz, R.D., Lunine, J.I., Paganelli, F., Soderblom, L.A., Wood, C.A., Wye, L., Zebker, H.A., Anderson, Y., Ostro, S.J., Allison, M.D.,Boehmer, R., Callahan, P., Encrenaz, P., Flamini, E., Francescetti, G., Gim, Y., Hamilton, G., Hensley, S., Johnson, W.T.K., Kelleher, K., Muhleman, D.O., Picardi, G., Posa, F., Roth, L., Seu, R., Shaffer, S., Stiles, B.W., Vetrella, S., West, “Titan Radar Mapper observations from Cassini’s T3 flyby ” R., *Nature*, **441**, 709-713 (2006) doi:10.1038/nature04786

Flamini, E., Capaccioni, F., Colangeli, L., Cremonese, G., Doressoundiram, A., Josset, J.L., Langevin Josset, Y., Debei, S., Capria, M.T., De Sanctis, M.C., Marinangeli, L., Massironi, M., Epifani, E.M., Naletto, G., Palumbo, P., Eng, P., Roig, J.F., Caporali, A., Da Deppo, V., Erard, S., Federico, C., Forni, O., Sgavetti, M., Filacchione, G., Giacomini, L., Marra, G., Martellato, E., Zusi, M., Cosi, M., Bettanini, C., Calamai, L., Zaccariotto, M., Tommasi, L., Dami, M., Veltroni, J.F., Poulet, F., Hello, Y.,. the SIMBIO-SYS Team. "SIMBIO-SYS: the Spectrometer and Imagers Integrated Observatory SYStem for the BepiColombo Planetary Orbiter", *Planetary and Space Science*, 56, 125–143, 2009.

Folkner, W. M., Yoder, C. F. , Yuan, D. N. , Standish, E. M. and Preston, R. A., " Interior Structure and Seasonal Mass Redistribution of Mars from Radio Tracking of Mars Pathfinder", *Science*, Vol. 278 no. 5344 pp. 1749-1752, 5 December 1997. DOI: 10.1126/science.278.5344.1749

Grasset, O., Sotin, C., and Deschamps, F., “On the internal structure and dynamics of Titan”, *Planetary and Space Science*, **48**, Issues 7-8, 617-636, 2000 doi:10.1016/S0032-0633(00)00039-8

Gross, R. S., “The excitation of the Chandler wobble”, *Geophys. Res. Lett.*, 27(15), 2329–2332, 12 May 2000. doi:10.1029/2000GL011450.

Hapke, B., Danielson Jr., G.E., Klaasen, K., Wilson, L., "Photometric observations of Mercury from Mariner 10", *J. Geophys. Res.*, **80**, 2431–2443, 1975.

Henry, C.A., “An introduction to Cassini design”, *Space Science Reviews*, **104**, no. 1-4, 129-153, 2002 doi:10.1016/S0032-0633(00)00039-8

Iess, L., Rappaport, N.J., Jacobson, R.A., Racioppa, P., Stevenson, D.J., Tortora, P., Armstrong, J.W., Asmar, S.W., “Gravity Field, Shape, and Moment of Inertia of Titan”, *Science*, **327**, no. 5971, 1367 – 1369, March 2010 DOI: *10.1126/science.1182583*

Jacobson, R. A., Antreasian, P. G., Bordi, J. J., Criddle, K. E., Ionasescu, R., Jones, J. B., Mackenzie, R. A., Meek, M. C., Parcher, D., Pelletier, F. J., Owen Jr., W. M., Roth, D. C., Roundhill, I. M., and Stauch, J. R., "The Gravity Field of the Saturnian System from Satellite Observations and Spacecraft Tracking Data", *The Astronomical Journal*, **132**, Issue 6, 2520 doi:10.1086/508812

Karatekin, Ö., T. Van Hoolst, and T. Tokano (2008), "Effect of internal gravitational coupling on Titan's non-synchronous rotation", *Geophys. Res. Lett.*, **35**, L16202, doi:10.1029/2008GL034744.

Lorenz, R.D., Lunine, J.I., Grier, J.A. and Fisher, M.A., "Prediction of aeolian features on planets: Application to Titan paleoclimatology", *Journal of Geophysical Research*, **100** (E12), 26377-26386.

Lorenz, R.D., Lunine, J.I., "Titan's surface before Cassini", *Planetary Space Science*, **53**, Issue 5, pp. 557-576, 2005. doi:10.1016/j.pss.2004.06.004

Lorenz, R.D., Stiles, B.W., Kirk, R.L., Allison, M.D., Persi del Marmo, P., Iess, L., Lunine, J.I., Ostro, S.J., and Hensley, S., "Titan'sRotation Reveals an Internal Ocean and changing Zonal Winds" , *Science*, **319**, no 5870, 1649-1651, March 2008 doi: 10.1126/science.1151639

Lopes, R., Mitchell, K.L., Wall, S.D., Mitri, G., Janssen, M.A., Ostro, S.J., Kirk, R.L., Hayes, A.G., Stofan, E., Lunine, J.I., Lorenz, R.D., Wood, C.A., Radebaugh, J., Paillou, P., Zebker, H.A., and Paganelli, F., "The Lakes and Seas of Titan", *EOS*, **88**, no. 51, 569-570, 18 December 2007. DOI : 10.1029/2007EO510001

Lopes, R., Stofan, E.R., Peckyno, R., Radebaugh, J. , Mitchell, K.L., Mitri, G., Wood, C.A. , Kirk, R.L., Wall, S.D., Lunine, J.I., Hayes, A., Lorenz, R., Farr, T., Wye, L., Craig, J. , Ollerenshaw, R.J., Janssen, M., LeGall, A., Paganelli, F., West, R., Stiles, B.W., Callahan, P., Anderson, Y., Valora, P., and Soderblom, L., "Distribution and interplay of geologic processes on Titan from Cassini RADAR data", Icarus, 205, Issue 2, 540 – 588, February 2010 doi:10.1016/j.icarus.2009.08.010

Lunine, J.I., Stevenson, D. J., and Yung, Y.L., "Ethane ocean on Titan", *Science*, **222**, no 4629, pp. 1229-1230, 1983 DOI: 10.1126/science.222.4629.1229

Lunine, J.I., “Does Titan have an ocean? A review of current understanding of Titan’s surface”, *Reviews of Geophysics*, **31**, no. 2, 133-150, 1993 doi:10.1029/92RG02794

Margot, J. L., Peale, S. J., Jurgens, R. F. , Slade, M. A., Holin, I. V., “Large Longitude Libration of Mercury Reveals a Molten Core”, *Science*, **316** 5825 710-714, 4 May 2007. DOI: 10.1126/science.1140514.

Margot, J.L., "A Mercury Orientation model including non-zero obliquity and librations", *Celestial Mechanics and Dynamical Astronomy* , **105**, no 4, 329-336, 2009 DOI: 10.1007/s10569-009-9234-1

Mitchell, J.L., “The drying of Titan’s dunes: Titan’s methane hydrology and its impact on atmospheric circulation”, *Journal of Geophysical Research*, **113**, E08015, 22 PP., 2008. doi:10.1029/2007JE003017

Mitri, G., Showman, A., Lunine, J.I., and Lorenz, R.D., “Hydrocarbon lakes on Titan”, *Icarus*, **186**, Issue 2, 385-394, February 2007 doi:10.1016/j.icarus.2006.09.004

Mitri, G., Lunine, J.I., G., Showman, A., and Lopes, R., “Resurfacing of Titan by ammonia-water cryomagma” , *Icarus*, **196**, issue 1, pages 216-224, 2008. doi:10.1016/j.icarus.2008.02.024

Nakiboglu, S.M., “Hydrostatic theory of the Earth and its mechanical implications”, Phys. *Earth Planet. Int.*, **28**, 302-311, 1982

Ostro, S.J., “Planetary Radar Astronomy”, *Rev.Mo d. Phys.*, Volume 65, Issue 4, 1235–1279, 1993. DOI:10.1103/RevModPhys.65.1235

Peale, S., Phillips, R.J., Solomon, S.C., Smith, D. E., Zuber, M., “A procedure for determining the nature of Mercury’s core”, *Meteoritics & Planetary Science*, **37**, 1269-1283, 2002

Porco, C.C., Baker, E., Barbara, J., Beurle, K., Brahic, A., Burns, J.A., Charnoz, S., Cooper, N., Dawson, D.D., Del Genio, A.D., Denk, T., Dones, L., Dyudina, U., Evans, M.W., Fussner, S., Giese B., Grazier, K., Helfenstein, P., Ingersoll, A.P., Jacobson, R.A., Johnson, T.V., McEwen, A., Murray, C.D., Neukum, G., Owen, W., Perry, J., Roatsch, T., Spitale, J., Squyres, S., Thomas, P., Tiscareno, M., Turtle, E.P., Vasavada, A.R., Veverka, J., Wagner, R., and West, R., “Imaging of Titan from the Cassini spacecraft”, *Nature*, **434**, 159-168, 2005 doi:10.1038/nature03436

Radebaugh R., Lorenz, R.D, Wall, S.D., Kirk, R.L., Wood, C.A. , Lunine, J.I.,Stofan, E.R., Lopes, R., Valdora, P., Farr, T.G., Hayes, A., Stiles, B.W., Mitri, G., Zebker, H.A., Janssen, M., Wye, L., LeGall, A., Mitchell, K.L., Paganelli, F., West, R., Schaller, E.L., and Cassini RADAR Team, "Regional geomorphology and history of Titan's Xanadu province", Icarus, 211, Issue 1, 672-685, January 2011 doi:10.1016/j.icarus.2010.07.022

Seidelmann, P.K., Archinal, B.A., A'Hearn, M.F., Conrad, A., Consolmagno, G.J., Hestroffer, D., Hilton, J.L., Krasinsky, G.A., Neumann, G., Oberst, J., Stooke, P., Tedesco, E.F., Tholen, D.J., Thomas, P.C., Williams, I. P., "Report of the IAU/IAG Working Group on cartographic coordinates and rotational elements: 2006", *Celestial Mechanics and Dynamical Astronomy*, **98**, 155-180, 2006, DOI 10.1007/s10569-007-9072-y

Schaller, E.L., Brown, M.E., Roe, H.G., Bouchez, A.H., and Trujillo, C.A., "Dissipation of Titan's south polar clouds", *Icarus*, **184**, Issue 2, 517-523, October 2006 doi:10.1016/j.icarus.2006.05.025

Shapiro, I. I., Chandler, J. F., Campbell, D. B., Hine, A. A., and Stacy, N.J.S., "The spin vector of Venus", *Astronomical Journal*, **100**, 1363-1368, 1990.

Simoes, F., R. Grard**,** M. Hamelin**,** J.J. López-Moreno**,** K. Schwingenschuh**,** C. Béghin**,** J.-J. Berthelier**,** B. Besser**,** V.J.G. Brown**,** M. Chabassière**,** P. Falkner**,** F. Ferri**,** M. Fulchignoni**,** R. Hofe**,** I. Jernej, J.M. Jeronimo, G.J. Molina-Cuberos, R. Rodrigo, H. Svedhem, T. Tokano, R. Trautner, "A new numerical model for the simulation of ELF wave propagation and the computation of eigenmodes in the atmosphere of Titan: Did Huygens observe any Schumann resonance?", Planetary and Space Science, 55, Issue 13, 1978-1989, November 2007 doi:10.1016/j.pss.2007.04.016

Slade, M.A., Zohar, S., and Jurgens, R. F., "Venus: Improved spin vector from Goldstone radar observations", *Astronomical Journal*, **100**, 1369-1374, 1990.

Soler, T., "A new matrix development of the potential and attraction at exterior points as a function of the inertia tensors", *Celest. Mech.*, **32**, 257-296, 1984

Solomon, S.C., McNutt, R.L., Gold, R.E., Acun˜a, M.H., Baker, D.N., Boyton, W.V., Chapman, C.R., Cheng, A.F., Gloeckler, G., Head ,J.W., Krimigis, S.M., McClintock, W.E., Murchie, S.L., Peale, S.J., Philips, R.J., Robinson, M.S., Slavin, J.A., Smith, D.E., Strom, R.G., Trombka, J.I., Zuber, M.T.,."The MESSENGER mission to Mercury: scientific objectives and implementation", *Planetary Space Sciences*,**49**,1445–1465, 2001.

Sotin, C., Jaumann, R., Buratti, B. J., Brown, R. H., Clark, R. N., Soderblom, L. A., Baines, K. H., Bellucci, G., Bibring, J.P., Capaccioni, F., Cerroni, P. , Combes, M., Coradini, A., Cruikshank, D. P., Drossart, P., Formisano, V., Langevin, Y., Matson, D. L., McCord, T. B., Nelson, R. M., Nicholson, P. D., Sicardy, B., LeMouelic, S., Rodriguez, S., Stephan, K. , and Scholz, C. K., " Release of volatiles from a possible cryovolcano from near-infrared imaging of Titan", *Nature* **435**, 786-789 (9 June 2005) | doi:10.1038/nature03596

Stofan, E.R., Elachi, C., Lunine, J.I., Lorenz, R.D., Stiles, B.W., Mitchell, K.L., Ostro, S., Soderblom, L., Wood, C., Zebker, H., Wall, S., Janssen, M., Kirk, R., Lopes, R., Paganelli, F., Radebaugh, J. ,Wye, L.,Anderson, Y., Allison, M., Boehmer, R., Callahan, P., Encrenaz, P., Flamini, E., Francescetti, G., Gim, Y., Hamilton, G., Hensley, S., Johnson, W.T.K., Kelleher, K., Muhleman, D., Paillou, P., Picardi, G., Posa, F., Roth, L., Seu, R., Shaffer, S., Vetrella, S., and West, R., "The Lakes of Titan", *Nature*, **445**, 61-64, 4 January 2007, doi:10.1038/nature05438

Stiles, B.W., Kirk, R.L., Lorenz, R.D., Hensley, S., Lee, E., Ostro, S.J., Allison, M.D., Callahan, P., Gim, Y., Iess, L., Persi del Marmo, P., Hamilton, G:, Johnson, W.T.K., West, R. and the Cassini RADAR Team, "Determining Titan's Spin State from Cassini RADAR images" , *The Astronomical Journal*, **135**, 1669-1680, May 2008 doi:10.1088/0004-6256/135/51669

Stiles, B.W., Kirk, R.L., Lorenz, R.D., Hensley, S., Lee, E., Ostro, S.J., Allison, M.D., Callahan, P., Gim, Y., Iess, L., Persi del Marmo, P., Hamilton, G:, Johnson, W.T.K., West, R. and the Cassini RADAR Team, "ERRATUM: Determining Titan's Spin State from Cassini RADAR images" , *The Astronomical Journal*, **139**, 311, 2010 doi:10.1088/0004-6256/139/1/311

Tobie, G., Grasset, O., Lunine, J.I., Mocquet, A., and Sotin, C., "Titan's internal structure inferred from a coupled thermal-orbital model", *Icarus*, **175**, pages 496-502, 2005 doi:10.1016/j.icarus.2004.12.007

Tobie, G., Lunine, J.I., and Sotin, C., "Episodic outgassing as the origin of atmospheric methane on Titan", *Nature*, **440**, pages 61-64, 2006 doi:10.1038/nature04497

Tokano, T., McKay, C.P., Neubauer, F.M., Atreya, S.K., Ferri, F., Fulchignoni, M. and Niemann, H.B., "Methane drizzle on Titan", Nature, 442, 432 -435, 2006 | doi:10.1038/nature04948

Van Hoolst, T., Rambaux, N., Karatekin, O., and Baland, R.M., "The effect of gravitational and pressure torques on Titan's length-of-day variations", *Icarus*, **200** , 256 – 264, 2009

Ward, W.R., "Past orientation of the lunar spin axis", *Science*, **189**, 377–379, 1975.

J. Wahr, "The effects of the atmosphere and oceans on the Earth's wobble", *Geophys. J. R. Astron. Soc.*, **70**, 349-372, 1982

Weidenschilling, S.J., "Iron /silicate fractionation and the origin of Mercury", *Icarus*, **35**, Issue 1, Pages 99-111, July 1978, doi:10.1016/0019-1035(78)90064-7

Wetherill, G.W., "Accumulation of Mercury from planetesimals", Mercury (A89-43751 19-91), University of Arizona Press, p. 670-691, 1988

Wood, C.A., Lorenz, R.D., Kirk, R.L., Lopes, R., Mitchell, K., and Stofan, E., "Impact craters on Titan", *Icarus*, **206**, Issue 1, 334-344, 2010 doi:10.1016/j.icarus.2009.08.021

Zebker, H.A., Stiles, B.W., Hensley, S., Lorenz, R.D., Kirk, and Lunine, J.I., "Size and Shape of Saturn's moon Titan", *Science*, **324**, no. 5929, pp. 921 – 923, 2009 DOI: *10.1126/science.1168905*

Conferences

Genova, A., Marabucci, M., Iess, L., "A batch-sequential filter for the BepiColombo Radio Science Experiment ", *ISSFD*, 2010

Gordon, I. and Lowe, D.G., "Scene Modelling, Recognition and tracking with Invariant Image Features", *Int Symp on Mixed and Augmented Reality*, 2004.

Hayes, A.G., Aharonson, O., Stevenson, D.J., Lunine, J.I., Lorenz, R.D., Kirk, R.L., Stiles, B.W., Wall, S.D., Sotin, C., Le Gall, A., Lopes, R., Janssen, M.A., and Cassini RADAR Team, "Joint Analysis of Titan's Surface Using The Cassini VIMS and RADAR Instruments.", *Division for Planetary Sciences*, annual meeting, Ithaca, abstract #34-06, 2008

Meriggiola, R., Iess, L., and Stiles, B.W., "The rotation of Titan by latest Cassini data", *AGU* Fall Meeting 2011, P33E-1802, December 2011

Perry, J.E., Turtle, E.P., McEwen, A.S., and Dawson, D.D., “Cassini ISS Observations of Titan: the Titan-20 Flyby”, *38th Lunar and Planetary Science Conference*, Houston, Abstract #2219, 2007

Tortora, P., Bevilacqua, A., Carozza, L., Genova, A., Gherardi A., Iess, L., Meriggiola, R., Palli, A., Palumbo, P. and Zusi, M., "Simulation of BepiColombo’s Mercury Rotation Experiment", *Geophysical Research Abstracts*, EGU General Assembly 2011, Vol. 13, EGU2011-13565, 2011

Books

Grasset., O., Blanc, M., Coustenis, A., Durham, W.B., Hussmann, H., Pappalardo, R.T., Turrini, D., “Satellites of the Outer Solar System – Exchange processes Involving the Interiors”, Springer, 2010 ISBN 978-1-4419-7438-9

Green, P.E,, "Radar Astronomy", Chapter I, McGraw-Hill, New York, 1968

Murray, C.D. and Dermott, S.F., “Solar System Dynamics”, Cambridge University Press, 1999 |ISBN 978-0-521-57597-3

Seidelmann, K.P., "Explanatory Supplement to the Astronomical Almanac", revised edition, University Science Books, 2005, ISBN-13: 978-1891389450

Technical Reports

Gherardi A., " Bepi-Colombo Rotation Experiment: Mercury's Albedo Features and Synthetic Images for Feature Generation and Pattern Matching", *ESA Technical Report* #1, ARCES - Università di Bologna - MORE, 22 November 2010.

Jorda, L. and Thomas, N., "The accuracy of pattern matching techniques for the radio science experiment of ESA's Mercury Cornerstone mission", Preliminary study, Max-Planck Institute for Aeronomie, Katlenburg-Lindau, Germany, 2000.

Iess, L., Mercolino, M., Persi, P., and Tortora, P., "BepiColombo Rotation Experiment", *ESA Internal Report*, June 2003.

Stiles, B.W., “Cassini Radar Basic Image Data Records SIS”, Version 2.0, *Cassini RADAR Instrument Team Technical Report*, D-27889, April 2008.

Appendix A

Partial derivatives for the IAU Model

In this section the analytical formulation for the partial derivatives of a body-fixed vector ***R***, expressed in TERF coordinates, with respect to the IAU rotational parameters, will be reported. ***r*** is the correspondent inertial vector, expressed in EMEJ2000 coordinates.

1. Derivative with respect to α_0

The derivative of the body-fixed vector ***R*** with respect to α_0 angle can be calculated as it follows:

$$\frac{\partial \boldsymbol{R}}{\partial \alpha_0} = \left[\frac{\partial M_{IAU}}{\partial \alpha_0}\right] \boldsymbol{r}$$

where the derivative of M_{IAU} with respect to α_0 can be expressed as:

$$\frac{\partial M_{IAU}}{\partial \alpha_0} = \frac{\partial [\Re_z(w)\Re_x(d)\Re_z(a)]}{\partial \alpha_0} = \Re_z(w)\Re_x(d)\frac{\partial \Re_z(a)}{\partial \alpha_0}$$

and $\Re_z(a)$ can be differentiated as:

$$\frac{\partial \Re_z(a)}{\partial \alpha_0} = \begin{bmatrix} -\sin(a) & \cos(a) & 0 \\ -\cos(a) & -\sin(a) & 0 \\ 0 & 0 & 0 \end{bmatrix}$$

where it was assumed that:

$$\frac{\partial a}{\partial \alpha_0} = \frac{\partial \left(\frac{\pi}{2} + \alpha\right)}{\partial \alpha_0} = \frac{\partial \alpha}{\partial \alpha_0} = 1$$

2. Derivative with respect to δ_0

The derivative of the body-fixed vector ***R*** with respect to δ_0 angle can be calculated as it follows:

$$\frac{\partial \boldsymbol{R}}{\partial \delta_0} = \left[\frac{\partial M_{IAU}}{\partial \delta_0}\right] \boldsymbol{r}$$

Where the derivative of M_{IAU} with respect to δ_0 can be expressed as:

$$\frac{\partial M_{IAU}}{\partial \delta_0} = \frac{\partial[\Re_z(w)\Re_x(d)\Re_z(a)]}{\partial \delta_0} = \Re_z(w)\frac{\partial \Re_x(d)}{\partial \delta_0}\Re_z(a)$$

and $\Re_x(d)$ can be differentiated as:

$$\frac{\partial \Re_x(d)}{\partial \delta_0} = \begin{bmatrix} 0 & 0 & 0 \\ 0 & \sin(d) & -\cos(d) \\ 0 & \cos(d) & \sin(d) \end{bmatrix}$$

where it was assumed that:

$$\frac{\partial d}{\partial \delta_0} = \frac{\partial\left(\frac{\pi}{2} - \delta\right)}{\partial \delta_0} = -\frac{\partial \delta}{\partial \delta_0} = -1$$

3. Derivative with respect to W$_0$

The derivative of the body-fixed vector $\boldsymbol{R}$ with respect to W_0 angle can be calculated as it follows:

$$\frac{\partial \boldsymbol{R}}{\partial W_0} = \left[\frac{\partial M_{IAU}}{\partial W_0}\right] \boldsymbol{r}$$

Where the derivative of M_{IAU} with respect to w_0 can be expressed as:

$$\frac{\partial M_{IAU}}{\partial W_0} = \frac{\partial[\Re_z(w)\Re_x(d)\Re_z(a)]}{\partial W_0} = \frac{\partial \Re_z(w)}{\partial W_0}\Re_x(d)\Re_z(a)$$

and $\Re_z(w)$ can be differentiated as:

$$\frac{\partial \Re_z(w)}{\partial W_0} = \begin{bmatrix} -\sin(w) & \cos(w) & 0 \\ -\cos(w) & -\sin(w) & 0 \\ 0 & 0 & 0 \end{bmatrix}$$

where it was assumed that:

$$\frac{\partial w}{\partial W_0} = \frac{\partial W}{\partial W_0} = 1$$

4. Derivative with respect to $\dot{\alpha}_0$

The derivative of the body-fixed vector $\boldsymbol{R}$ with respect to $\dot{\alpha}_0$ angle can be calculated as it follows:

$$\frac{\partial R}{\partial \dot{\alpha}_0} = \left[\frac{\partial M_{IAU}}{\partial \dot{\alpha}_0}\right] \boldsymbol{r}$$

Where the derivative of M_{IAU} with respect to α_0 can be expressed as:

$$\frac{\partial M_{IAU}}{\partial \dot{\alpha}_0} = \frac{\partial[\Re_z(w)\Re_x(d)\Re_z(a)]}{\partial \dot{\alpha}_0} = \Re_z(w)\Re_x(d)\frac{\partial \Re_z(a)}{\partial \dot{\alpha}_0}$$

and $\Re_z(a)$ can be differentiated as:

$$\frac{\partial \Re_z(a)}{\partial \dot{\alpha}_0} = \begin{bmatrix} -t\sin(a) & t\cos(a) & 0 \\ -t\cos(a) & -t\sin(a) & 0 \\ 0 & 0 & 0 \end{bmatrix}$$

where:

$$\frac{\partial a}{\partial \dot{\alpha}_0} = \frac{\partial\left(\frac{\pi}{2}+\alpha\right)}{\partial \dot{\alpha}_0} = \frac{\partial \alpha}{\partial \dot{\alpha}_0} = t$$

5. Derivative with respect to $\dot{\boldsymbol{\delta}}_0$

The derivative of the body-fixed vector ***R*** with respect to $\dot{\delta}_0$ angle can be calculated as it follows:

$$\frac{\partial \boldsymbol{R}}{\partial \dot{\delta}_0} = \left[\frac{\partial M_{IAU}}{\partial \dot{\delta}_0}\right]\boldsymbol{r}$$

Where the derivative of M_{IAU} with respect to δ_0 can be expressed as:

$$\frac{\partial M_{IAU}}{\partial \dot{\delta}_0} = \frac{\partial[\Re_z(w)\Re_x(d)\Re_z(a)]}{\partial \dot{\delta}_0} = \Re_z(w)\frac{\partial \Re_x(d)}{\partial \dot{\delta}_0}\Re_z(a)$$

and $\Re_x(d)$ can be differentiated as:

$$\frac{\partial \Re_x(d)}{\partial \dot{\delta}_0} = \begin{bmatrix} 0 & 0 & 0 \\ 0 & t\sin(d) & -t\cos(d) \\ 0 & t\cos(d) & t\sin(d) \end{bmatrix}$$

where:

$$\frac{\partial d}{\partial \dot{\delta}_0} = \frac{\partial\left(\frac{\pi}{2}-\delta\right)}{\partial \dot{\delta}_0} = -\frac{\partial \delta}{\partial \dot{\delta}_0} = -t$$

6. Derivative with respect to $\dot{\mathbf{W}}_0$

The derivative of the body-fixed vector ***R*** with respect to $\dot{W}_0$ angular velocity can be calculated as it follows:

$$\frac{\partial \boldsymbol{R}}{\partial \dot{W}_0} = \left[\frac{\partial M_{IAU}}{\partial \dot{W}_0}\right]\boldsymbol{r}$$

Where the derivative of M_{IAU} with respect to $\dot{W}_0$ can be expressed as:

$$\frac{\partial M_{IAU}}{\partial \dot{W}_0} = \frac{\partial[\mathfrak{R}_z(w)\mathfrak{R}_x(d)\mathfrak{R}_z(a)]}{\partial \dot{W}_0} = \frac{\partial \mathfrak{R}_z(w)}{\partial \dot{W}_0}\mathfrak{R}_x(d)\mathfrak{R}_z(a)$$

and $\mathfrak{R}_z(w)$ can be differentiated as:

$$\frac{\partial \mathfrak{R}_z(w)}{\partial \dot{W}_0} = \begin{bmatrix} -t\sin(w) & t\cos(w) & 0 \\ -t\cos(w) & -t\sin(w) & 0 \\ 0 & 0 & 0 \end{bmatrix}$$

where:

$$\frac{\partial w}{\partial \dot{W}_0} = \frac{\partial W}{\partial \dot{W}_0} = t$$

7. Derivative with respect to K$_0$

The derivative of the body-fixed vector $\boldsymbol{R}$ with respect to the amplitude of the physical librations in longitude K$_0$ can be calculated as it follows:

$$\frac{\partial \boldsymbol{R}}{\partial \mathrm{K}_0} = \left[\frac{\partial M_{IAU}}{\partial \mathrm{K}_0}\right]\boldsymbol{r}$$

where the derivative of M_{IAU} with respect to $\dot{W}_0$ is:

$$\frac{\partial M_{IAU}}{\partial \mathrm{K}_0} = \frac{\partial[\mathfrak{R}_z(w)\mathfrak{R}_x(d)\mathfrak{R}_z(a)]}{\partial \mathrm{K}_0} = \frac{\partial \mathfrak{R}_z(w)}{\partial \mathrm{K}_0}\mathfrak{R}_x(d)\mathfrak{R}_z(a)$$

and $\mathfrak{R}_z(w)$ can be differentiated as:

$$\frac{\partial \mathfrak{R}_z(w)}{\partial \mathrm{K}_0} = \begin{bmatrix} -K_d\sin(w) & K_d\cos(w) & 0 \\ -K_d\cos(w) & -K_d\sin(w) & 0 \\ 0 & 0 & 0 \end{bmatrix}$$

where:

$$\frac{\partial w}{\partial \mathrm{K}_0} = \frac{\partial W}{\partial \mathrm{K}_0} = \sin M = K_d$$

8. Derivative with respect to Q

The derivative of the body-fixed vector $\boldsymbol{R}$ with respect to the angular acceleration Q can be calculated as it follows:

$$\frac{\partial \boldsymbol{R}}{\partial Q} = \left[\frac{\partial M_{IAU}}{\partial Q}\right]\boldsymbol{r}$$

where the derivative of M_{IAU} with respect to Q is:

$$\frac{\partial M_{IAU}}{\partial Q}=\frac{\partial[\Re_z(w)\Re_x(d)\Re_z(a)]}{\partial Q}=\frac{\partial \Re_z(w)}{\partial Q}\Re_x(d)\Re_z(a)$$

and $\Re_z(w)$ can be differentiated as:

$$\frac{\partial \Re_z(w)}{\partial Q}=\begin{bmatrix}-t^2\sin(w) & t^2\cos(w) & 0\\ -t^2\cos(w) & -t^2\sin(w) & 0\\ 0 & 0 & 0\end{bmatrix}$$

where:

$$\frac{\partial w}{\partial Q}=\frac{\partial W}{\partial Q}=t^2$$

9. Derivative with respect to $\mathbf{C_i^\alpha}$, $\mathbf{C_i^\delta}$, $\mathbf{C_i^W}$

The derivative of the body-fixed vector $\boldsymbol{R}$ with respect to the coefficients C_i^χ $(\chi = \alpha,\delta,W)$ can be calculated as it follows:

$$\frac{\partial \boldsymbol{R}}{\partial C_i^\alpha}=\left[\frac{\partial M_{IAU}}{\partial C_i^\alpha}\right]\boldsymbol{r}$$

$$\frac{\partial \boldsymbol{R}}{\partial C_i^\delta}=\left[\frac{\partial M_{IAU}}{\partial C_i^\delta}\right]\boldsymbol{r}$$

$$\frac{\partial \boldsymbol{r}_L^B}{\partial C_i^W}=\left[\frac{\partial M_{IAU}}{\partial C_i^W}\right]\boldsymbol{r}$$

where the derivative of M_{IAU} with respect to C_i^χ is:

$$\frac{\partial M_{IAU}}{\partial C_i^\alpha}=\frac{\partial[\Re_z(w)\Re_x(d)\Re_z(a)]}{\partial C_i^\alpha}=\Re_z(w)\Re_x(d)\frac{\partial \Re_z(a)}{\partial C_i^\alpha}$$

$$\frac{\partial M_{IAU}}{\partial C_i^\delta}=\frac{\partial[\Re_z(w)\Re_x(d)\Re_z(a)]}{\partial C_i^\delta}=\Re_z(w)\frac{\partial \Re_x(d)}{\partial C_i^\delta}\Re_z(a)$$

$$\frac{\partial M_{IAU}}{\partial C_i^W}=\frac{\partial[\Re_z(w)\Re_x(d)\Re_z(a)]}{\partial C_i^W}=\frac{\partial \Re_z(w)}{\partial C_i^W}\Re_x(d)\Re_z(a)$$

where:

$$\frac{\partial \Re_z(a)}{\partial C_i^\alpha}=\begin{bmatrix}-\sin(a) & \cos(a) & 0\\ -\cos(a) & -\sin(a) & 0\\ 0 & 0 & 0\end{bmatrix}\cos(\mathrm{A_i^\alpha})$$

$$\frac{\partial \mathfrak{R}_x(d)}{\partial C_i^{\delta}} = \begin{bmatrix} 0 & 0 & 0 \\ 0 & \sin(d) & -\cos(d) \\ 0 & \cos(d) & \sin(d) \end{bmatrix} \cos\left(\mathrm{A}_\mathrm{i}^{\delta}\right)$$

$$\frac{\partial \mathfrak{R}_z(w)}{\partial C_i^{W}} = \begin{bmatrix} -\sin(w) & \cos(w) & 0 \\ -\cos(w) & -\sin(w) & 0 \\ 0 & 0 & 0 \end{bmatrix} \cos\left(\mathrm{A}_\mathrm{i}^{\mathrm{W}}\right)$$

10. Derivative with respect to $\mathbf{S}_\mathbf{i}^{\boldsymbol{\alpha}}$, $\mathbf{S}_\mathbf{i}^{\boldsymbol{\delta}}$, $\mathbf{S}_\mathbf{i}^{\mathbf{W}}$

The derivative of the body-fixed vector ***R*** with respect to the coefficients S_i^{χ} $(\chi = \alpha, \delta, W)$ can be calculated as it follows:

$$\frac{\partial \boldsymbol{R}}{\partial S_i^{\alpha}} = \left[\frac{\partial M_{IAU}}{\partial S_i^{\alpha}}\right] \boldsymbol{r}$$

$$\frac{\partial \boldsymbol{R}}{\partial S_i^{\delta}} = \left[\frac{\partial M_{IAU}}{\partial S_i^{\delta}}\right] \boldsymbol{r}$$

$$\frac{\partial \boldsymbol{R}}{\partial S_i^{W}} = \left[\frac{\partial M_{IAU}}{\partial S_i^{W}}\right] \boldsymbol{r}$$

Where the derivative of M_{IAU} with respect to S_i^{χ} can be expressed as:

$$\frac{\partial M_{IAU}}{\partial S_i^{\alpha}} = \frac{\partial [\mathfrak{R}_z(w)\mathfrak{R}_x(d)\mathfrak{R}_z(a)]}{\partial S_i^{\alpha}} = \mathfrak{R}_z(w)\mathfrak{R}_x(d)\frac{\partial \mathfrak{R}_z(a)}{\partial S_i^{\alpha}}$$

$$\frac{\partial M_{IAU}}{\partial S_i^{\delta}} = \frac{\partial [\mathfrak{R}_z(w)\mathfrak{R}_x(d)\mathfrak{R}_z(a)]}{\partial S_i^{\delta}} = \mathfrak{R}_z(w)\frac{\partial \mathfrak{R}_x(d)}{\partial S_i^{\delta}}\mathfrak{R}_z(a)$$

$$\frac{\partial M_{IAU}}{\partial S_i^{W}} = \frac{\partial [\mathfrak{R}_z(w)\mathfrak{R}_x(d)\mathfrak{R}_z(a)]}{\partial S_i^{W}} = \frac{\partial \mathfrak{R}_z(w)}{\partial S_i^{W}}\mathfrak{R}_x(d)\mathfrak{R}_z(a)$$

where:

$$\frac{\partial \mathfrak{R}_z(a)}{\partial S_i^{\alpha}} = \begin{bmatrix} -\sin(a) & \cos(a) & 0 \\ -\cos(a) & -\sin(a) & 0 \\ 0 & 0 & 0 \end{bmatrix} \sin(\mathrm{A}_\mathrm{i}^{\alpha})$$

$$\frac{\partial \mathfrak{R}_x(d)}{\partial S_i^{\delta}} = \begin{bmatrix} 0 & 0 & 0 \\ 0 & \sin(d) & -\cos(d) \\ 0 & \cos(d) & \sin(d) \end{bmatrix} \sin\left(\mathrm{A}_\mathrm{i}^{\delta}\right)$$

$$\frac{\partial \mathfrak{R}_z(w)}{\partial S_i^{W}} = \begin{bmatrix} -\sin(w) & \cos(w) & 0 \\ -\cos(w) & -\sin(w) & 0 \\ 0 & 0 & 0 \end{bmatrix} \sin\left(\mathrm{A}_\mathrm{i}^{\mathrm{W}}\right)$$

11. Derivative with respect to $\boldsymbol{\gamma_i^\alpha, \gamma_i^\delta, \gamma_i^W}$

The derivative of the body-fixed vector $\boldsymbol{R}$ with respect to $\gamma_i^\chi (\chi = \alpha, \delta, W)$ angles can be calculated as it follows:

$$\frac{\partial \boldsymbol{R}}{\partial \mathrm{\gamma_i^\alpha}} = \left[\frac{\partial M_{IAU}}{\partial \mathrm{\gamma_i^\alpha}}\right]\boldsymbol{r}$$

$$\frac{\partial \boldsymbol{R}}{\partial \mathrm{\gamma_i^\delta}} = \left[\frac{\partial M_{IAU}}{\partial \mathrm{\gamma_i^\delta}}\right]\boldsymbol{r}$$

$$\frac{\partial \boldsymbol{R}}{\partial \mathrm{\gamma_i^W}} = \left[\frac{\partial M_{IAU}}{\partial \mathrm{\gamma_i^W}}\right]\boldsymbol{r}$$

Where the derivative of M_{IAU} with respect to γ_i^χ can be expressed as:

$$\frac{\partial M_{IAU}}{\partial \mathrm{\gamma_i^\alpha}} = \frac{\partial [\Re_z(w)\Re_x(d)\Re_z(a)]}{\partial \mathrm{\gamma_i^\alpha}} = \Re_z(w)\Re_x(d)\frac{\partial \Re_z(a)}{\partial \mathrm{\gamma_i^\alpha}}$$

$$\frac{\partial M_{IAU}}{\partial \mathrm{\gamma_i^\delta}} = \frac{\partial [\Re_z(w)\Re_x(d)\Re_z(a)]}{\partial \mathrm{\gamma_i^\delta}} = \Re_z(w)\frac{\partial \Re_x(d)}{\partial \mathrm{\gamma_i^\delta}}\Re_z(a)$$

$$\frac{\partial M_{IAU}}{\partial \mathrm{\gamma_i^W}} = \frac{\partial [\Re_z(w)\Re_x(d)\Re_z(a)]}{\partial \mathrm{\gamma_i^W}} = \frac{\partial \Re_z(w)}{\partial \mathrm{\gamma_i^W}}\Re_x(d)\Re_z(a)$$

In particular:

$$\frac{\partial \Re_z(a)}{\partial \mathrm{\gamma_i^\alpha}} = \begin{bmatrix} -\sin(a) & \cos(a) & 0 \\ -\cos(a) & -\sin(a) & 0 \\ 0 & 0 & 0 \end{bmatrix} [S_i^\alpha \cos(A_i^\alpha) - C_i^\alpha \sin(A_i^\alpha)]$$

$$\frac{\partial \Re_x(d)}{\partial \mathrm{\gamma_i^\delta}} = \begin{bmatrix} 0 & 0 & 0 \\ 0 & \sin(d) & -\cos(d) \\ 0 & \cos(d) & \sin(d) \end{bmatrix} [S_i^\delta \cos(A_i^\delta) - C_i^\delta \sin(A_i^\delta)]$$

$$\frac{\partial \Re_z(w)}{\partial \mathrm{\gamma_i^W}} = \begin{bmatrix} -\sin(w) & \cos(w) & 0 \\ -\cos(w) & -\sin(w) & 0 \\ 0 & 0 & 0 \end{bmatrix} [S_i^W \cos(A_i^W) - C_i^W \sin(A_i^W)]$$

12. Derivative with respect to $\boldsymbol{\omega_{IAU,i}}$

The derivative of the body-fixed vector $\boldsymbol{R}$ with respect to $\omega_{IAU,i}$ can be calculated as it follows:

$$\frac{\partial \boldsymbol{R}}{\partial \mathrm{\omega_{IAU,i}^\alpha}} = \left[\frac{\partial M_{IAU}}{\partial \mathrm{\omega_{IAU,i}^\alpha}}\right]\boldsymbol{r}$$

$$\frac{\partial \boldsymbol{R}}{\partial \omega_{\mathrm{IAU,i}}^{\delta}} = \left[\frac{\partial M_{IAU}}{\partial \omega_{\mathrm{IAU,i}}^{\delta}}\right]\boldsymbol{r}$$

$$\frac{\partial \boldsymbol{R}}{\partial \omega_{\mathrm{IAU,i}}^{\mathrm{W}}} = \left[\frac{\partial M_{IAU}}{\partial \omega_{\mathrm{IAU,i}}^{\mathrm{W}}}\right]\boldsymbol{r}$$

Where the derivative of M_{IAU} with respect to $\omega_{IAU,i}$ can be expressed as:

$$\frac{\partial M_{IAU}}{\partial \omega_{\mathrm{IAU,i}}^{\alpha}} = \frac{\partial[\Re_z(w)\Re_x(d)\Re_z(a)]}{\partial \omega_{\mathrm{IAU,i}}^{\alpha}} = \Re_z(w)\Re_x(d)\frac{\partial \Re_z(a)}{\partial \omega_{\mathrm{IAU,i}}^{\alpha}}$$

$$\frac{\partial M_{IAU}}{\partial \omega_{\mathrm{IAU,i}}^{\delta}} = \frac{\partial[\Re_z(w)\Re_x(d)\Re_z(a)]}{\partial \omega_{\mathrm{IAU,i}}^{\delta}} = \Re_z(w)\frac{\partial \Re_x(d)}{\partial \omega_{\mathrm{IAU,i}}^{\delta}}\Re_z(a)$$

$$\frac{\partial M_{IAU}}{\partial \omega_{\mathrm{IAU,i}}^{\mathrm{W}}} = \frac{\partial[\Re_z(w)\Re_x(d)\Re_z(a)]}{\partial \omega_{\mathrm{IAU,i}}^{\mathrm{W}}} = \frac{\partial \Re_z(w)}{\partial \omega_{\mathrm{IAU,i}}^{\mathrm{W}}}\Re_x(d)\Re_z(a)$$

In particular:

$$\frac{\partial \Re_z(a)}{\partial \omega_{\mathrm{IAU,i}}^{\alpha}} = \begin{bmatrix} -\sin(a) & \cos(a) & 0 \\ -\cos(a) & -\sin(a) & 0 \\ 0 & 0 & 0 \end{bmatrix} [S_i^{\alpha}\cos(A_i^{\alpha}) - C_i^{\alpha}\sin(A_i^{\alpha})]t$$

$$\frac{\partial \Re_x(d)}{\partial \omega_{\mathrm{IAU,i}}^{\delta}} = \begin{bmatrix} 0 & 0 & 0 \\ 0 & \sin(d) & -\cos(d) \\ 0 & \cos(d) & \sin(d) \end{bmatrix} \left[S_i^{\delta}\cos\left(A_i^{\delta}\right) - C_i^{\delta}\sin\left(A_i^{\delta}\right)\right]t$$

$$\frac{\partial \Re_z(w)}{\partial \omega_{\mathrm{IAU,i}}^{\mathrm{W}}} = \begin{bmatrix} -\sin(w) & \cos(w) & 0 \\ -\cos(w) & -\sin(w) & 0 \\ 0 & 0 & 0 \end{bmatrix} [S_i^{W}\cos(A_i^{W}) - C_i^{W}\sin(A_i^{W})]t$$

13. Derivative with respect to $\beta_{\mathrm{IAU,i}}$

The derivative of the body-fixed vector $\boldsymbol{R}$ with respect to $\beta_{IAU,i}$ can be calculated as it follows:

$$\frac{\partial \boldsymbol{R}}{\partial \beta_{\mathrm{IAU,i}}^{\alpha}} = \left[\frac{\partial M_{IAU}}{\partial \beta_{\mathrm{IAU,i}}^{\alpha}}\right]\boldsymbol{r}$$

$$\frac{\partial \boldsymbol{R}}{\partial \beta^{\delta}_{\mathrm{IAU,i}}} = \left[\frac{\partial M_{IAU}}{\partial \beta^{\delta}_{\mathrm{IAU,i}}}\right]\boldsymbol{r}$$

$$\frac{\partial \boldsymbol{R}}{\partial \beta^{\mathrm{W}}_{\mathrm{IAU,i}}} = \left[\frac{\partial M_{IAU}}{\partial \beta^{\mathrm{W}}_{\mathrm{IAU,i}}}\right]\boldsymbol{r}$$

where the derivative of M_{IAU} with respect to $\beta_{IAU,i}$ can be expressed as:

$$\frac{\partial M_{IAU}}{\partial \beta^{\alpha}_{\mathrm{IAU,i}}} = \frac{\partial[\Re_z(w)\Re_x(d)\Re_z(a)]}{\partial \beta^{\alpha}_{\mathrm{IAU,i}}} = \Re_z(w)\Re_x(d)\frac{\partial \Re_z(a)}{\partial \beta^{\alpha}_{\mathrm{IAU,i}}}$$

$$\frac{\partial M_{IAU}}{\partial \beta^{\delta}_{\mathrm{IAU,i}}} = \frac{\partial[\Re_z(w)\Re_x(d)\Re_z(a)]}{\partial \beta^{\delta}_{\mathrm{IAU,i}}} = \Re_z(w)\frac{\partial \Re_x(d)}{\partial \beta^{\delta}_{\mathrm{IAU,i}}}\Re_z(a)$$

$$\frac{\partial M_{IAU}}{\partial \beta^{\mathrm{W}}_{\mathrm{IAU,i}}} = \frac{\partial[\Re_z(w)\Re_x(d)\Re_z(a)]}{\partial \beta^{\mathrm{W}}_{\mathrm{IAU,i}}} = \frac{\partial \Re_z(w)}{\partial \beta^{\mathrm{W}}_{\mathrm{IAU,i}}}\Re_x(d)\Re_z(a)$$

In particular:

$$\frac{\partial \Re_z(a)}{\partial \beta^{\alpha}_{\mathrm{IAU,i}}} = \begin{bmatrix} -\sin(a) & \cos(a) & 0 \\ -\cos(a) & -\sin(a) & 0 \\ 0 & 0 & 0 \end{bmatrix} [S_i^{\alpha}\cos(A_i^{\alpha}) - C_i^{\alpha}\sin(A_i^{\alpha})]t^2$$

$$\frac{\partial \Re_x(d)}{\partial \beta^{\delta}_{\mathrm{IAU,i}}} = \begin{bmatrix} 0 & 0 & 0 \\ 0 & \sin(d) & -\cos(d) \\ 0 & \cos(d) & \sin(d) \end{bmatrix} \left[S_i^{\delta}\cos\left(A_i^{\delta}\right) - C_i^{\delta}\sin\left(A_i^{\delta}\right)\right]\mathrm{t}^2$$

$$\frac{\partial \Re_z(w)}{\partial \beta^{\mathrm{W}}_{\mathrm{IAU,i}}} = \begin{bmatrix} -\sin(w) & \cos(w) & 0 \\ -\cos(w) & -\sin(w) & 0 \\ 0 & 0 & 0 \end{bmatrix} [S_i^{W}\cos(A_i^{W}) - C_i^{W}\sin(A_i^{W})]t^2$$

Appendix B

Partial derivatives for the Extended Model

In this section the analytical formulation for the partial derivatives of a body-fixed vector ***R***, expressed in TERF coordinates, with respect to the EXT rotational parameters, will be reported. ***r*** is the correspondent inertial vector, expressed in EMEJ2000 coordinates.

1. Polar motion parameters

In this paragraph are computed the derivatives of the inertial EMEJ2000 vector ***r*** with respect to the parameters describing the polar motion effects.

1.1. Derivative with respect to $\mathrm{C_{x,n}}$

The derivative of the body-fixed vector ***R*** with respect to the polar motion x_p angle can be calculated by the formula:

$$\frac{\partial \boldsymbol{R}}{\partial \mathrm{C_{x,n}}} = \left[M_3 M_2 \frac{\partial M_1}{\partial \mathrm{C_{x,n}}}\right]^T \boldsymbol{r}$$

Where the only term differentiable with respect to y_p is M_1, which can be expressed as:

$$\frac{\partial M_1}{\partial \mathrm{C_{x,n}}} = \frac{\partial\left[\mathfrak{R}_y(x_p)\mathfrak{R}_x(y_p)\right]}{\partial \mathrm{C_{x,n}}} = \frac{\partial \mathfrak{R}_y(x_p)}{\partial \mathrm{C_{x,n}}} \mathfrak{R}_x(y_p)$$

where the expression of the derivative of $\mathfrak{R}_y(x_p)$ with respect to x_p is:

$$\frac{\partial \mathfrak{R}_y(x_p)}{\partial \mathrm{C_{x,n}}} = \frac{\partial \mathfrak{R}_y(x_p)}{\partial x_p}\frac{\partial x_p}{\partial \mathrm{C_{x,n}}} = \begin{bmatrix} -\sin(x_p) & 0 & -\cos(x_p) \\ 0 & 0 & 0 \\ \cos(x_p) & 0 & -\sin(x_p) \end{bmatrix} \frac{\partial x_p}{\partial \mathrm{C_{x,n}}}$$

where:

$$\frac{\partial x_p}{\partial \mathrm{C_{x,n}}} = \cos(\omega_n t)$$

1.2. Derivative with respect to $\mathbf{S_{x,n}}$

The derivative of the body-fixed vector $\boldsymbol{R}$ with respect to the polar motion x_p angle can be calculated by the formula:

$$\frac{\partial \boldsymbol{R}}{\partial \mathrm{S}_{\mathrm{x,n}}} = \left[M_3 M_2 \frac{\partial M_1}{\partial \mathrm{S}_{\mathrm{x,n}}} \right]^T \boldsymbol{r}$$

where the only term differentiable with respect to y_p is M_1, which can be expressed as:

$$\frac{\partial M_1}{\partial \mathrm{S}_{\mathrm{x,n}}} = \frac{\partial \left[\mathfrak{R}_y(x_p) \mathfrak{R}_x(y_p) \right]}{\partial \mathrm{S}_{\mathrm{x,n}}} = \frac{\partial \mathfrak{R}_y(x_p)}{\partial \mathrm{S}_{\mathrm{x,n}}} \mathfrak{R}_x(y_p)$$

the expression of the derivative of $\mathfrak{R}_y(x_p)$ with respect to $\mathrm{S}_{\mathrm{x,n}}$is:

$$\frac{\partial \mathfrak{R}_y(x_p)}{\partial \mathrm{S}_{\mathrm{x,n}}} = \frac{\partial \mathfrak{R}_y(x_p)}{\partial x_p} \frac{\partial x_p}{\partial \mathrm{S}_{\mathrm{x,n}}} = \begin{bmatrix} -\sin(x_p) & 0 & -\cos(x_p) \\ 0 & 0 & 0 \\ \cos(x_p) & 0 & -\sin(x_p) \end{bmatrix} \frac{\partial x_p}{\partial \mathrm{S}_{\mathrm{x,n}}}$$

where:

$$\frac{\partial x_p}{\partial \mathrm{S}_{\mathrm{x,n}}} = \sin(\omega_n t)$$

1.3. Derivative with respect to $\mathbf{C_{y,n}}$

The derivative of the body-fixed vector $\boldsymbol{R}$ with respect to the polar motion $\mathrm{C}_{y,\mathrm{n}}$ angle can be calculated by the formula:

$$\frac{\partial \boldsymbol{R}}{\partial \mathrm{C}_{y,\mathrm{n}}} = \left[M_3 M_2 \frac{\partial M_1}{\partial \mathrm{C}_{y,\mathrm{n}}} \right]^T \boldsymbol{r}$$

Where the only term differentiable with respect to $\mathrm{C}_{y,\mathrm{n}}$ is M_1, which can be expressed as:

$$\frac{\partial M_1}{\partial \mathrm{C}_{y,\mathrm{n}}} = \frac{\partial \left[\mathfrak{R}_y(x_p) \mathfrak{R}_x(y_p) \right]}{\partial \mathrm{C}_{y,\mathrm{n}}} = \mathfrak{R}_y(x_p) \frac{\partial \mathfrak{R}_x(y_p)}{\partial \mathrm{C}_{y,\mathrm{n}}}$$

Where the expression of the derivative of $\mathfrak{R}_x(y_p)$ with respect to $\mathrm{C}_{y,\mathrm{n}}$ is:

$$\frac{\partial \mathfrak{R}_x(y_p)}{\partial \mathrm{C}_{y,\mathrm{n}}} = \frac{\partial \mathfrak{R}_x(y_p)}{\partial y_p} \frac{\partial y_p}{\partial \mathrm{C}_{\mathrm{y,n}}} = \begin{bmatrix} 0 & 0 & 0 \\ 0 & -\sin(y_p) & \cos(y_p) \\ 0 & -\cos(y_p) & -\sin(y_p) \end{bmatrix} \frac{\partial y_p}{\partial \mathrm{C}_{\mathrm{y,n}}}$$

where:

$$\frac{\partial y_p}{\partial \mathrm{C_{y,n}}} = \cos(\omega_n t)$$

1.4. Derivative with respect to $\mathrm{S_{y,n}}$

The derivative of the body-fixed vector ***R*** with respect to the polar motion $\mathrm{S}_{y,\mathrm{n}}$ angle can be calculated by the formula:

$$\frac{\partial \boldsymbol{R}}{\partial \mathrm{S}_{y,\mathrm{n}}} = \left[M_3 M_2 \frac{\partial M_1}{\partial \mathrm{S}_{y,\mathrm{n}}}\right]^T \boldsymbol{r}$$

Where the only term differentiable with respect to $\mathrm{S}_{y,\mathrm{n}}$ is M_1, which can be expressed as:

$$\frac{\partial M_1}{\partial \mathrm{S}_{y,\mathrm{n}}} = \frac{\partial\left[\Re_y(x_p)\Re_x(y_p)\right]}{\partial \mathrm{S}_{y,\mathrm{n}}} = \Re_y(x_p)\,\frac{\partial \Re_x(y_p)}{\partial \mathrm{S}_{y,\mathrm{n}}}$$

Where the expression of the derivative of $\Re_x(y_p)$ with respect to $\mathrm{S}_{y,\mathrm{n}}$ is:

$$\frac{\partial \Re_x(y_p)}{\partial \mathrm{S}_{y,\mathrm{n}}} = \frac{\partial \Re_x(y_p)}{\partial y_p}\frac{\partial y_p}{\partial \mathrm{S_{y,n}}} = \begin{bmatrix} 0 & 0 & 0 \\ 0 & -\sin(y_p) & \cos(y_p) \\ 0 & -\cos(y_p) & -\sin(y_p) \end{bmatrix} \frac{\partial y_p}{\partial \mathrm{S}_{y,\mathrm{n}}}$$

where:

$$\frac{\partial y_p}{\partial \mathrm{S}_{y,\mathrm{n}}} = \sin(\omega_n t)$$

1.5. Derivative with respect to $\mathrm{C_{CW,x}}$

The derivative of the body-fixed vector ***R*** with respect to the polar motion $\mathrm{C}_{CW,x}$ angle can be calculated by the formula:

$$\frac{\partial \boldsymbol{R}}{\partial \mathrm{C}_{CW,x}} = \left[M_3 M_2 \frac{\partial M_1}{\partial \mathrm{C}_{CW,x}}\right]^T \boldsymbol{r}$$

The only term differentiable with respect to $\mathrm{C}_{CW,x}$ is M_1, which can be expressed as:

$$\frac{\partial M_1}{\partial \mathrm{C}_{CW,x}} = \frac{\partial\left[\Re_y(x_p)\Re_x(y_p)\right]}{\partial \mathrm{C}_{CW,x}} = \frac{\partial \Re_y(x_p)}{\partial \mathrm{C}_{CW,x}}\Re_x(y_p)$$

Where the expression of the derivative of $\Re_y(x_p)$ with respect to $\mathrm{C}_{CW,x}$ is:

$$\frac{\partial \Re_y(x_p)}{\partial \mathrm{C}_{CW,x}} = \begin{bmatrix} -\sin(x_p) & 0 & -\cos(x_p) \\ 0 & 0 & 0 \\ \cos(x_p) & 0 & -\sin(x_p) \end{bmatrix} \frac{\partial x_p}{\partial \mathrm{C}_{CW,x}}$$

where:

$$\frac{\partial x_p}{\partial \mathrm{C}_{CW,x}} = \cos(\omega_{CW} t)$$

1.6. Derivative with respect to $\mathbf{S}_{\mathbf{CW,x}}$

The derivative of the body-fixed vector $\boldsymbol{R}$ with respect to the polar motion $\mathrm{S}_{CW,x}$ angle can be calculated by the formula:

$$\frac{\partial \boldsymbol{R}}{\partial \mathrm{S}_{CW,x}} = \left[M_3 M_2 \frac{\partial M_1}{\partial \mathrm{S}_{CW,x}}\right]^T \boldsymbol{r}$$

Where the only term differentiable with respect to $\mathrm{S}_{CW,x}$ is M_1, which can be expressed as:

$$\frac{\partial M_1}{\partial \mathrm{S}_{CW,x}} = \frac{\partial\left[\Re_y(x_p)\Re_x(y_p)\right]}{\partial \mathrm{S}_{CW,x}} = \frac{\partial \Re_y(x_p)}{\partial \mathrm{S}_{CW,x}}\Re_x(y_p)$$

Where the expression of the derivative of $\Re_y(x_p)$ with respect to $\mathrm{C}_{CW,y}$ is:

$$\frac{\partial \Re_y(x_p)}{\partial \mathrm{S}_{CW,x}} = \begin{bmatrix} -\sin(x_p) & 0 & -\cos(x_p) \\ 0 & 0 & 0 \\ \cos(x_p) & 0 & -\sin(x_p) \end{bmatrix} \frac{\partial x_p}{\partial \mathrm{S}_{CW,x}}$$

where:

$$\frac{\partial x_p}{\partial \mathrm{S}_{CW,x}} = \sin(\omega_{CW} t)$$

1.7. Derivative with respect to $\mathrm{C}_{\mathrm{CW,y}}$

The derivative of the body-fixed vector ***R*** with respect to the polar motion $\mathrm{C}_{CW,\mathrm{y}}$ angle can be calculated by the formula:

$$\frac{\partial \boldsymbol{R}}{\partial \mathrm{C}_{CW,\mathrm{y}}} = \left[M_3 M_2 \frac{\partial M_1}{\partial \mathrm{C}_{CW,\mathrm{y}}}\right]^T \boldsymbol{r}$$

Where the only term differentiable with respect to $\mathrm{C}_{CW,\mathrm{y}}$ is M_1, which can be expressed as:

$$\frac{\partial M_1}{\partial \mathrm{C}_{CW,\mathrm{y}}} = \frac{\partial\left[\mathfrak{R}_y(x_p)\mathfrak{R}_x(y_p)\right]}{\partial \mathrm{C}_{CW,\mathrm{y}}} = \mathfrak{R}_y(x_p)\,\frac{\partial \mathfrak{R}_x(y_p)}{\partial \mathrm{C}_{CW,\mathrm{y}}}$$

Where the expression of the derivative of $\mathfrak{R}_x(y_p)$ with respect to $\mathrm{C}_{CW,\mathrm{y}}$ is:

$$\frac{\partial \mathfrak{R}_x(y_p)}{\partial \mathrm{C}_{CW,\mathrm{y}}} = \begin{bmatrix} 0 & 0 & 0 \\ 0 & -\sin(y_p) & \cos(y_p) \\ 0 & -\cos(y_p) & -\sin(y_p) \end{bmatrix} \frac{\partial y_p}{\partial \mathrm{C}_{CW,\mathrm{y}}}$$

where:

$$\frac{\partial y_p}{\partial \mathrm{C}_{CW,\mathrm{y}}} = \cos(\omega_{CW} t)$$

1.8. Derivative with respect to $\mathrm{S}_{\mathrm{CW,y}}$

The derivative of the body-fixed vector ***R*** with respect to the polar motion $\mathrm{S}_{CW,y}$ angle can be calculated by the formula:

$$\frac{\partial \boldsymbol{R}}{\partial \mathrm{S}_{CW,y}} = \left[M_3 M_2 \frac{\partial M_1}{\partial \mathrm{S}_{CW,y}}\right]^T \boldsymbol{r}$$

Where the only term differentiable with respect to $\mathrm{S}_{CW,y}$ is M_1, which can be expressed as:

$$\frac{\partial M_1}{\partial \mathrm{S}_{CW,y}} = \frac{\partial\left[\mathfrak{R}_y(x_p)\mathfrak{R}_x(y_p)\right]}{\partial \mathrm{S}_{CW,y}} = \mathfrak{R}_y(x_p)\,\frac{\partial \mathfrak{R}_x(y_p)}{\partial \mathrm{S}_{CW,y}}$$

Where the expression of the derivative of $\mathfrak{R}_x(y_p)$ with respect to $\mathrm{S}_{y,\mathrm{n}}$ is:

$$\frac{\partial \mathfrak{R}_x(y_p)}{\partial \mathrm{S}_{CW,y}} = \begin{bmatrix} 0 & 0 & 0 \\ 0 & -\sin(y_p) & \cos(y_p) \\ 0 & -\cos(y_p) & -\sin(y_p) \end{bmatrix} \frac{\partial y_p}{\partial \mathrm{S}_{CW,y}}$$

where:

$$\frac{\partial y_p}{\partial \mathrm{S}_{CW,y}} = \sin(\omega_{CW} t)$$

1.9. Derivative with respect to $\boldsymbol{\omega}_\mathbf{n}$

The derivative of the body-fixed vector ***R*** with respect to the polar motion ω_n frequency can be calculated by the formula:

$$\frac{\partial \boldsymbol{R}}{\partial \omega_n} = \left[M_3 M_2 \frac{\partial M_1}{\partial \omega_n} \right]^T \boldsymbol{r}$$

Where the only term differentiable with respect to $\mathrm{S}_{CW,y}$ is M_1, which can be expressed as:

$$\frac{\partial M_1}{\partial \omega_n} = \frac{\partial \Re_y(x_p)}{\partial \omega_n} \Re_x(y_p) + \Re_y(x_p) \frac{\partial \Re_x(y_p)}{\partial \omega_n}$$

Where the expression of the derivative of $\Re_y(x_p)$ with respect to ω_n is:

$$\begin{aligned} \frac{\partial \Re_y(x_p)}{\partial \omega_n} &= \frac{\partial \Re_y(x_p)}{\partial x_p} \frac{\partial x_p}{\partial \omega_n} \\ &= \frac{\partial \Re_y(x_p)}{\partial x_p} t \left[\sum_{n=1}^{N} n \left(S_{x,n} \cos(n\omega_n t) - C_{x,n} \sin(n\omega_n t) \right) \right] \end{aligned}$$

While the expression of the derivative of $\Re_x(y_p)$ with respect to ω_n is:

$$\begin{aligned} \frac{\partial \Re_x(y_p)}{\partial \omega_n} &= \frac{\partial \Re_x(y_p)}{\partial y_p} \frac{\partial y_p}{\partial \omega_n} \\ &= \frac{\partial \Re_x(y_p)}{\partial y_p} t \left[\sum_{n=1}^{N} n \left(S_{y,n} \cos(n\omega_n t) - C_{y,n} \sin(n\omega_n t) \right) \right] \end{aligned}$$

where:

$$\frac{\partial \Re_y(x_p)}{\partial \omega_\mathrm{n}} = \begin{bmatrix} -\sin(x_p) & 0 & -\cos(x_p) \\ 0 & 0 & 0 \\ \cos(x_p) & 0 & -\sin(x_p) \end{bmatrix} \frac{\partial x_p}{\partial \omega_\mathrm{n}}$$

While the expression of the derivative of $\Re_x(y_p)$ with respect to ω_n is:

$$\frac{\partial \Re_x(y_p)}{\partial \omega_\mathrm{n}} = \begin{bmatrix} 0 & 0 & 0 \\ 0 & -\sin(y_p) & \cos(y_p) \\ 0 & -\cos(y_p) & -\sin(y_p) \end{bmatrix} \frac{\partial y_p}{\partial \omega_\mathrm{n}}$$

where:

$$\begin{cases} \dfrac{\partial x_p}{\partial \omega_1} = t\left[S_{x,n} \cos(\omega_n t) - C_{x,n} \sin(\omega_n t) \right] \\ \dfrac{\partial y_p}{\partial \omega_1} = t\left[S_{y,n} \cos(\omega_n t) - C_{y,n} \sin(\omega_n t) \right] \end{cases}$$

1.10. Derivative with respect to $\boldsymbol{\omega}_{\mathbf{CW}}$

The derivative of the body-fixed vector $\boldsymbol{R}$ with respect to the polar motion ω_{CW} frequency can be calculated by the formula:

$$\frac{\partial \boldsymbol{R}}{\partial \omega_{CW}} = \left[M_3 M_2 \frac{\partial M_1}{\partial \omega_{CW}}\right]^T \boldsymbol{r}$$

Where the only term differentiable with respect to $\mathrm{S}_{CW,y}$ is M_1, which can be expressed as:

$$\frac{\partial M_1}{\partial \omega_{CW}} = \frac{\partial\left[\Re_y(x_p)\Re_x(y_p)\right]}{\partial \omega_{CW}} = \frac{\partial \Re_y(x_p)}{\partial \omega_{CW}} \Re_x(y_p) + \Re_y(x_p) \frac{\partial \Re_x(y_p)}{\partial \omega_{CW}}$$

Where the expression of the derivative of $\Re_y(x_p)$ with respect to ω_{CW} is:

$$\frac{\partial \Re_y(x_p)}{\partial \omega_{CW}} = \begin{bmatrix} -\sin(x_p) & 0 & -\cos(x_p) \\ 0 & 0 & 0 \\ \cos(x_p) & 0 & -\sin(x_p) \end{bmatrix} \frac{\partial x_p}{\partial \omega_{CW}}$$

While the expression of the derivative of $\Re_x(y_p)$ with respect to ω_{CW} is:

$$\frac{\partial \Re_x(y_p)}{\partial \omega_{CW}} = \begin{bmatrix} 0 & 0 & 0 \\ 0 & -\sin(y_p) & \cos(y_p) \\ 0 & -\cos(y_p) & -\sin(y_p) \end{bmatrix} \frac{\partial y_p}{\partial \omega_{CW}}$$

Where:

$$\begin{cases} \dfrac{\partial x_p}{\partial \omega_{CW}} = t\left[S_{CW,x} \cos(\omega_{CW} t) - C_{CW,x} \sin(\omega_{CW} t)\right] \\ \dfrac{\partial y_p}{\partial \omega_{CW}} = t\left[S_{CW,y} \cos(\omega_{CW} t) - C_{CW,y} \sin(\omega_{CW} t)\right] \end{cases}$$

2. IERF - MORF parameters

The derivatives with respect to the IERF - MORF coordinate transformation are here reported.

2.1. Derivative with respect to ϕ_0

The derivative of the body-fixed vector $\boldsymbol{R}$ with respect to ϕ_0 angle can be calculated as it follows:

$$\frac{\partial \boldsymbol{R}}{\partial \phi_0} = \left[M_3 \frac{\partial M_2}{\partial \phi_0} M_1\right]^T \boldsymbol{r}$$

where the derivative of M_2 with respect to ϕ_0 can be expressed as:

$$\frac{\partial M_2}{\partial \phi_0} = \frac{\partial[\Re_z(-\psi)\Re_x(I)\Re_z(-\phi)]}{\partial \phi_0} = \Re_z(-\psi)\Re_x(I)\frac{\partial \Re_z(-\phi)}{\partial \phi_0}$$

and $\Re_z(-\phi)$ can be differentiated as:

$$\frac{\partial \Re_z(-\phi)}{\partial \phi_0} = \begin{bmatrix} \sin(-\phi) & -\cos(-\phi) & 0 \\ \cos(-\phi) & \sin(-\phi) & 0 \\ 0 & 0 & 0 \end{bmatrix}$$

2.2. Derivative with respect to I_0

The derivative of the body-fixed vector $\boldsymbol{R}$ with respect to I_0 angle can be calculated as it follows:

$$\frac{\partial \boldsymbol{R}}{\partial I_0} = \left[M_3 \frac{\partial M_2}{\partial I_0} M_1\right]^T \boldsymbol{r}$$

Where the derivative of M_2 with respect to I_0 can be expressed as:

$$\frac{\partial M_2}{\partial I_0} = \frac{\partial[\Re_z(-\psi)\Re_x(I)\Re_z(-\phi)]}{\partial I_0} = \Re_z(-\psi)\frac{\partial \Re_x(I)}{\partial I_0}\Re_z(-\phi)$$

and $\Re_x(I)$ can be differentiated as:

$$\frac{\partial \Re_x(I)}{\partial I_0} = \begin{bmatrix} 0 & 0 & 0 \\ 0 & -\sin(I) & \cos(I) \\ 0 & -\cos(I) & -\sin(I) \end{bmatrix}$$

2.3. Derivative with respect to ψ_0

The derivative of the body-fixed vector $\boldsymbol{R}$ with respect to ψ_0 angle can be calculated as it follows:

$$\frac{\partial \boldsymbol{R}}{\partial \psi_0} = \left[M_3 \frac{\partial M_2}{\partial \psi_0} M_1\right]^T \boldsymbol{r}$$

Where the derivative of M_2 with respect to ψ_0 can be expressed as:

$$\frac{\partial M_2}{\partial \psi_0} = \frac{\partial[\Re_z(-\psi)\Re_x(I)\Re_z(-\phi)]}{\partial \psi_0} = \frac{\partial \Re_z(-\psi)}{\partial \psi_0}\Re_x(I)\Re_z(-\phi)$$

and $\Re_z(-\psi)$ can be differentiated as:

$$\frac{\partial \Re_z(-\psi)}{\partial \psi_0} = \begin{bmatrix} \sin(-\psi) & -\cos(-\psi) & 0 \\ \cos(-\psi) & \sin(-\psi) & 0 \\ 0 & 0 & 0 \end{bmatrix}$$

2.4. Derivative with respect to $\dot{\phi}_0$

The derivative of the body-fixed vector $\boldsymbol{R}$ with respect to $\dot{\phi}_0$ angle can be calculated as it follows:

$$\frac{\partial \boldsymbol{R}}{\partial \dot{\phi}_0} = \left[M_3 \frac{\partial M_2}{\partial \dot{\phi}_0} M_1\right]^T \boldsymbol{r}$$

Where the derivative of M_2 with respect to $\dot{\phi}_0$ can be expressed as:

$$\frac{\partial M_2}{\partial \dot{\phi}_0} = \frac{\partial[\Re_z(-\psi)\Re_x(I)\Re_z(-\phi)]}{\partial \dot{\phi}_0} = \Re_z(-\psi)\Re_x(I)\frac{\partial \Re_z(-\phi)}{\partial \dot{\phi}_0}$$

and $\Re_z(-\phi)$ can be differentiated as:

$$\frac{\partial \Re_z(-\phi)}{\partial \dot{\phi}_0} = \begin{bmatrix} \sin(-\phi) & -\cos(-\phi) & 0 \\ \cos(-\phi) & \sin(-\phi) & 0 \\ 0 & 0 & 0 \end{bmatrix} t$$

2.5. Derivative with respect to $\dot{\mathbf{I}}_{\mathbf{0}}$

The derivative of the body-fixed vector $\boldsymbol{R}$ with respect to $\dot{I}_0$ angle can be calculated as it follows:

$$\frac{\partial \boldsymbol{R}}{\partial \dot{I}_0} = \left[M_3 \frac{\partial M_2}{\partial \dot{I}_0} M_1\right]^T \boldsymbol{r}$$

Where the derivative of M_2 with respect to $\dot{I}_0$ can be expressed as:

$$\frac{\partial M_2}{\partial \dot{I}_0} = \frac{\partial[\Re_z(-\psi)\Re_x(I)\Re_z(-\phi)]}{\partial \dot{I}_0} = \Re_z(-\psi)\frac{\partial \Re_x(I)}{\partial \dot{I}_0}\Re_z(-\phi)$$

and $\Re_x(I)$ can be differentiated as:

$$\frac{\partial \Re_x(I)}{\partial \dot{I}_0} = \begin{bmatrix} 0 & 0 & 0 \\ 0 & -\sin(I) & \cos(I) \\ 0 & -\cos(I) & -\sin(I) \end{bmatrix} t$$

2.6. Derivative with respect to $\dot{\psi}_0$

The derivative of the body-fixed vector ***R*** with respect to $\dot{\psi}_0$ angle can be calculated as it follows:

$$\frac{\partial \boldsymbol{R}}{\partial \dot{\psi}_0} = \left[M_3 \frac{\partial M_2}{\partial \dot{\psi}_0} M_1 \right]^T \boldsymbol{r}$$

Where the derivative of M_2 with respect to ψ_0 can be expressed as:

$$\frac{\partial M_2}{\partial \dot{\psi}_0} = \frac{\partial [\Re_z(-\psi)\Re_x(I)\Re_z(-\phi)]}{\partial \dot{\psi}_0} = \frac{\partial \Re_z(-\psi)}{\partial \dot{\psi}_0} \Re_x(I)\Re_z(-\phi)$$

and $\Re_z(-\psi)$ can be differentiated as:

$$\frac{\partial \Re_z(-\psi)}{\partial \dot{\psi}_0} = \begin{bmatrix} \sin(-\psi) & -\cos(-\psi) & 0 \\ \cos(-\psi) & \sin(-\psi) & 0 \\ 0 & 0 & 0 \end{bmatrix} \mathrm{t}$$

2.7. Derivative with respect to $C_{\phi,n}$

The derivative of the body-fixed vector ***R*** with respect to $C_{\phi,n}$ angle can be calculated as it follows:

$$\frac{\partial \boldsymbol{R}}{\partial C_{\phi,n}} = \left[M_3 \frac{\partial M_2}{\partial C_{\phi,n}} M_1 \right]^T \boldsymbol{r}$$

Where the derivative of M_2 with respect to $C_{\phi,n}$ can be expressed as:

$$\frac{\partial M_2}{\partial C_{\phi,n}} = \frac{\partial [\Re_z(-\psi)\Re_x(I)\Re_z(-\phi)]}{\partial C_{\phi,n}} = \Re_z(-\psi)\Re_x(I) \frac{\partial \Re_z(-\phi)}{\partial C_{\phi,n}}$$

and $\Re_z(-\phi)$ can be differentiated as:

$$\frac{\partial \Re_z(-\phi)}{\partial C_{\phi,n}} = \begin{bmatrix} \sin(-\phi) & -\cos(-\phi) & 0 \\ \cos(-\phi) & \sin(-\phi) & 0 \\ 0 & 0 & 0 \end{bmatrix} \cos(\omega_{\phi,n} t)$$

2.8. Derivative with respect to $C_{I,n}$

The derivative of the body-fixed vector ***R*** with respect to $C_{I,n}$ angle can be calculated as it follows:

$$\frac{\partial \boldsymbol{R}}{\partial C_{I,n}} = \left[M_3 \frac{\partial M_2}{\partial C_{I,n}} M_1 \right]^T \boldsymbol{r}$$

Where the derivative of M_2 with respect to $\dot{I}_0$ can be expressed as:

$$\frac{\partial M_2}{\partial C_{I,n}} = \frac{\partial[\Re_z(-\psi)\Re_x(I)\Re_z(-\phi)]}{\partial C_{I,n}} = \Re_z(-\psi)\frac{\partial \Re_x(I)}{\partial C_{I,n}}\Re_z(-\phi)$$

and $\Re_x(I)$ can be differentiated as:

$$\frac{\partial \Re_x(I)}{\partial C_{I,n}} = \begin{bmatrix} 0 & 0 & 0 \\ 0 & -\sin(I) & \cos(I) \\ 0 & -\cos(I) & -\sin(I) \end{bmatrix} \cos(\omega_{nut,n} t)$$

2.9. Derivative with respect to $\mathrm{C}_{\psi,\mathrm{n}}$

The derivative of the body-fixed vector $\boldsymbol{R}$ with respect to $C_{\psi,n}$ angle can be calculated as it follows:

$$\frac{\partial \boldsymbol{R}}{\partial C_{\psi,n}} = \left[M_3 \frac{\partial M_2}{\partial C_{\psi,n}} M_1\right]^T \boldsymbol{r}$$

Where the derivative of M_2 with respect to ψ_0 can be expressed as:

$$\frac{\partial M_2}{\partial C_{\psi,n}} = \frac{\partial[\Re_z(-\psi)\Re_x(I)\Re_z(-\phi)]}{\partial C_{\psi,n}} = \frac{\partial \Re_z(-\psi)}{\partial C_{\psi,n}}\Re_x(I)\Re_z(-\phi)$$

and $\Re_z(-\psi)$ can be differentiated as:

$$\frac{\partial \Re_z(-\psi)}{\partial C_{\psi,n}} = \begin{bmatrix} \sin(-\psi) & -\cos(-\psi) & 0 \\ \cos(-\psi) & \sin(-\psi) & 0 \\ 0 & 0 & 0 \end{bmatrix} \cos(\omega_{nut,n} t)$$

2.10. Derivative with respect to $\mathbf{S}_{\boldsymbol{\phi},\mathbf{n}}$

The derivative of the body-fixed vector $\boldsymbol{R}$ with respect to $S_{\phi,n}$ angle can be calculated as it follows:

$$\frac{\partial \boldsymbol{R}}{\partial S_{\phi,n}} = \left[M_3 \frac{\partial M_2}{\partial S_{\phi,n}} M_1\right]^T \boldsymbol{r}$$

Where the derivative of M_2 with respect to $C_{\phi,n}$ can be expressed as:

$$\frac{\partial M_2}{\partial S_{\phi,n}} = \frac{\partial[\Re_z(-\psi)\Re_x(I)\Re_z(-\phi)]}{\partial S_{\phi,n}} = \Re_z(-\psi)\Re_x(I)\frac{\partial \Re_z(-\phi)}{\partial S_{\phi,n}}$$

and $\Re_z(-\phi)$ can be differentiated as:

$$\frac{\partial \Re_z(-\phi)}{\partial S_{\phi,n}} = \begin{bmatrix} \sin(-\phi) & -\cos(-\phi) & 0 \\ \cos(-\phi) & \sin(-\phi) & 0 \\ 0 & 0 & 0 \end{bmatrix} \sin(\omega_{\phi,n} t)$$

2.11. Derivative with respect to $\mathbf{S_{I,n}}$

The derivative of the body-fixed vector $\boldsymbol{R}$ with respect to $S_{I,n}$ angle can be calculated as it follows:

$$\frac{\partial \boldsymbol{R}}{\partial C_{I,n}} = \left[M_3 \frac{\partial M_2}{\partial C_{I,n}} M_1\right]^T \boldsymbol{r}$$

Where the derivative of M_2 with respect to $S_{I,n}$ can be expressed as:

$$\frac{\partial M_2}{\partial S_{I,n}} = \frac{\partial[\Re_z(-\psi)\Re_x(I)\Re_z(-\phi)]}{\partial S_{I,n}} = \Re_z(-\psi)\frac{\partial \Re_x(I)}{\partial S_{I,n}}\Re_z(-\phi)$$

and $\Re_x(I)$ can be differentiated as:

$$\frac{\partial \Re_x(I)}{\partial S_{I,n}} = \begin{bmatrix} 0 & 0 & 0 \\ 0 & -\sin(I) & \cos(I) \\ 0 & -\cos(I) & -\sin(I) \end{bmatrix} \sin\left(\omega_{nut,n} t\right)$$

2.12. Derivative with respect to $\mathbf{S_{\psi,n}}$

The derivative of the body-fixed vector $\boldsymbol{R}$ with respect to $S_{\psi,n}$ angle can be calculated as it follows:

$$\frac{\partial \boldsymbol{R}}{\partial C_{\psi,n}} = \left[M_3 \frac{\partial M_2}{\partial C_{\psi,n}} M_1\right]^T \boldsymbol{r}$$

Where the derivative of M_2 with respect to $S_{\psi,n}$ can be expressed as:

$$\frac{\partial M_2}{\partial S_{\psi,n}} = \frac{\partial[\Re_z(-\psi)\Re_x(I)\Re_z(-\phi)]}{\partial S_{\psi,n}} = \frac{\partial \Re_z(-\psi)}{\partial S_{\psi,n}}\Re_x(I)\Re_z(-\phi)$$

and $\Re_z(-\psi)$ can be differentiated as:

$$\frac{\partial \Re_z(-\psi)}{\partial S_{\psi,n}} = \begin{bmatrix} \sin(-\psi) & -\cos(-\psi) & 0 \\ \cos(-\psi) & \sin(-\psi) & 0 \\ 0 & 0 & 0 \end{bmatrix} \sin\left(\omega_{nut,n} t\right)$$

2.13. Derivative with respect to $\boldsymbol{\omega_\phi}$

The derivative of the body-fixed vector $\boldsymbol{R}$ with respect to ω_ϕ angle can be calculated as it follows:

$$\frac{\partial \boldsymbol{R}}{\partial \omega_\phi} = \left[M_3 \frac{\partial M_2}{\partial \omega_\phi} M_1\right]^T \boldsymbol{r}$$

Where the derivative of M_2 with respect to ω_ϕ can be expressed as:

$$\frac{\partial M_2}{\partial \omega_\phi} = \frac{\partial[\mathfrak{R}_z(-\psi)\mathfrak{R}_x(I)\mathfrak{R}_z(-\phi)]}{\partial \omega_\phi} = \mathfrak{R}_z(-\psi)\mathfrak{R}_x(I)\frac{\partial \mathfrak{R}_z(-\phi)}{\partial \omega_\phi}$$

and $\mathfrak{R}_z(-\phi)$ can be differentiated as:

$$\frac{\partial \mathfrak{R}_z(-\phi)}{\partial \omega_\phi} = -\frac{\partial \mathfrak{R}_z(-\phi)}{\partial \phi}\frac{\partial \phi}{\partial \omega_\phi} =$$

$$= -\frac{\partial \mathfrak{R}_z(-\phi)}{\partial \phi}\, t\left[\sum_{n=1}^{N} n\left(S_{\phi,n}\cos\left(n\omega_\phi t\right) - C_{\phi,n}\sin\left(n\omega_\phi t\right)\right)\right]$$

2.14. Derivative with respect to $\boldsymbol{\omega}_{\mathbf{nut}}$

The derivative of the body-fixed vector ***R*** with respect to ω_{nut} frequency can be calculated as it follows:

$$\frac{\partial \boldsymbol{R}}{\partial \omega_{nut}} = \left[M_3\frac{\partial M_2}{\partial \omega_{nut}}M_1\right]^T \boldsymbol{r}$$

Where the derivative of M_2 with respect to ω_{nut} can be expressed as:

$$\frac{\partial M_2}{\partial \omega_{nut}} = \frac{\partial \mathfrak{R}_z(-\psi)}{\partial \omega_{nut}}\frac{\partial \mathfrak{R}_x(I)}{\partial \omega_{nut}}\mathfrak{R}_z(-\phi)$$

While $\mathfrak{R}_z(-\psi)$ can be differentiated as:

$$\frac{\partial \mathfrak{R}_z(-\psi)}{\partial \omega_{nut}} = -\frac{\partial \mathfrak{R}_z(-\psi)}{\partial \psi}\frac{\partial \psi}{\partial \omega_{nut}} =$$

$$= -\frac{\partial \mathfrak{R}_z(-\psi)}{\partial \psi}\, t\left[\sum_{n=1}^{N} n\left(S_{\psi,n}\, cos(n\omega_{nut}t) - C_{\psi,n} sin\,(n\omega_{nut}t)\right)\right]$$

and $\mathfrak{R}_x(I)$ can be differentiated as:

$$\frac{\partial \mathfrak{R}_x(I)}{\partial \omega_{nut}} = \frac{\partial \mathfrak{R}_x(I)}{\partial I}\frac{\partial I}{\partial \omega_{nut}} =$$

$$= \frac{\partial \mathfrak{R}_x(I)}{\partial I}\, t\left[\sum_{n=1}^{N} n\left(S_{I,n}\, cos(n\omega_{nut}t) - C_{I,n} sin\,(n\omega_{nut}t)\right)\right]$$

3. MORF – EMEJ2000 parameters

The derivatives with respect to the MORF – EMEJ2000 coordinate transformation are here reported.

3.1. Derivative with respect to N

The derivative of the body-fixed vector $\boldsymbol{R}$ with respect to the N angle can be calculated by the formula:

$$\frac{\partial \boldsymbol{R}}{\partial N} = \left[\frac{\partial M_3}{\partial N} M_2 M_1\right]^T \boldsymbol{r}$$

Where the only term differentiable with respect to y_p is M_1, which can be expressed as:

$$\frac{\partial M_3}{\partial N} = \frac{\partial[\Re_z(-N)\Re_x(-J)]}{\partial N} = \frac{\partial \Re_z(-N)}{\partial N} \Re_x(-J)$$

Where the expression of the derivative of $\Re_z(-N)$ with respect to N is:

$$\frac{\partial \Re_z(-N)}{\partial N} = \begin{bmatrix} \sin(-N) & -\cos(-N) & 0 \\ \cos(-N) & \sin(-N) & 0 \\ 0 & 0 & 0 \end{bmatrix}$$

3.2. Derivative with respect to J

The derivative of the body-fixed vector $\boldsymbol{R}$ with respect to the J angle can be calculated by the formula:

$$\frac{\partial \boldsymbol{R}}{\partial J} = \left[\frac{\partial M_3}{\partial J} M_2 M_1\right]^T \boldsymbol{r}$$

Where the only term differentiable with respect to y_p is M_1, which can be expressed as:

$$\frac{\partial M_3}{\partial J} = \frac{\partial[\Re_z(-N)\Re_x(-J)]}{\partial J} = \Re_z(-N) \frac{\partial \Re_x(-J)}{\partial J}$$

Where the expression of the derivative of $\Re_x(-J)$ with respect to J is:

$$\frac{\partial \Re_x(-J)}{\partial J} = \begin{bmatrix} 0 & 0 & 0 \\ 0 & \sin(-J) & -\cos(-J) \\ 0 & \cos(-J) & \sin(-J) \end{bmatrix}$$

Partial Derivatives of the Moon Extended Model

The partial derivatives for the Moon Extended model are here reported.

4. Lunar mean motion parameters

In this paragraph are computed the derivatives of the body-fixed TERF vector ***R*** with respect to the parameters describing the lunar mean motion.

4.1. Derivative with respect to $\boldsymbol{\phi_0}$

The derivative of the body-fixed vector ***R*** with respect to the ϕ_0 angle can be calculated by the formula:

$$\frac{\partial \boldsymbol{R}}{\partial \phi_0} = \left[M_3 \frac{\partial M_2}{\partial \phi_0}\right]^T \boldsymbol{r}$$

Where:

$$\frac{\partial M_2}{\partial \phi_0} = \frac{\partial[\Re_z(-\psi)\Re_x(\theta)\Re_z(-\phi)]}{\partial \phi_0} = \Re_z(-\psi)\Re_x(\theta)\frac{\partial \Re_z(-\phi)}{\partial \phi_0}$$

and where:

$$\frac{\partial \Re_z(-\phi)}{\partial \phi_0} = \begin{bmatrix} \sin(-\phi) & -\cos(-\phi) & 0 \\ \cos(-\phi) & \sin(-\phi) & 0 \\ 0 & 0 & 0 \end{bmatrix}$$

4.2. Derivative with respect to $\mathbf{I_0}$

The derivative of the body-fixed vector ***R*** with respect to the I_0 angle can be calculated by the formula:

$$\frac{\partial \boldsymbol{R}}{\partial I_0} = \left[M_3 \frac{\partial M_2}{\partial I_0}\right]^T \boldsymbol{r}$$

Where:

$$\frac{\partial M_2}{\partial I_0} = \frac{\partial[\Re_z(-\psi)\Re_x(\theta)\Re_z(-\phi)]}{\partial I_0} = \Re_z(-\psi)\frac{\partial \Re_x(\theta)}{\partial I_0}\Re_z(-\phi)$$

and where:

$$\frac{\partial \Re_x(\theta)}{\partial I_0} = \begin{bmatrix} 0 & 0 & 0 \\ 0 & -\sin(\theta) & \cos(\theta) \\ 0 & -\cos(\theta) & -\sin(\theta) \end{bmatrix}$$

4.3. Derivative with respect to $\boldsymbol{\psi_0}$

The derivative of the body-fixed vector $\boldsymbol{R}$ with respect to the ψ_0 angle can be calculated by the formula:

$$\frac{\partial \boldsymbol{R}}{\partial \psi_0} = \left[M_3 \frac{\partial M_2}{\partial \psi_0}\right]^T \boldsymbol{r}$$

Where:

$$\frac{\partial M_2}{\partial \psi_0} = \frac{\partial[\mathfrak{R}_z(-\psi)\mathfrak{R}_x(\theta)\mathfrak{R}_z(-\phi)]}{\partial \psi_0} = \frac{\partial \mathfrak{R}_z(-\psi)}{\partial \psi_0}\mathfrak{R}_x(\theta)\mathfrak{R}_z(-\phi)$$

and where:

$$\frac{\partial \mathfrak{R}_z(-\psi)}{\partial \psi_0} = \begin{bmatrix} \sin(-\psi) & -\cos(-\psi) & 0 \\ \cos(-\psi) & \sin(-\psi) & 0 \\ 0 & 0 & 0 \end{bmatrix}$$

4.4. Derivative with respect to $\boldsymbol{\dot{\phi}_0}$

The derivative of the body-fixed vector $\boldsymbol{R}$ with respect to the $\dot{\phi}_0$ angular velocity can be calculated by the formula:

$$\frac{\partial \boldsymbol{R}}{\partial \dot{\phi}_0} = \left[M_3 \frac{\partial M_2}{\partial \dot{\phi}_0}\right]^T \boldsymbol{r}$$

Where:

$$\frac{\partial M_2}{\partial \dot{\phi}_0} = \frac{\partial[\mathfrak{R}_z(-\psi)\mathfrak{R}_x(\theta)\mathfrak{R}_z(-\phi)]}{\partial \dot{\phi}_0} = \mathfrak{R}_z(-\psi)\mathfrak{R}_x(\theta)\frac{\partial \mathfrak{R}_z(-\phi)}{\partial \dot{\phi}_0}$$

And where:

$$\frac{\partial \mathfrak{R}_z(-\phi)}{\partial \dot{\phi}_0} = \begin{bmatrix} \sin(-\phi) & -\cos(-\phi) & 0 \\ \cos(-\phi) & \sin(-\phi) & 0 \\ 0 & 0 & 0 \end{bmatrix} t$$

4.5. Derivative with respect to $\boldsymbol{\dot{I}_0}$

The derivative of the body-fixed vector $\boldsymbol{R}$ with respect to the $\dot{I}_0$ angular velocity can be calculated by the formula:

$$\frac{\partial \boldsymbol{R}}{\partial \dot{I}_0} = \left[M_3 \frac{\partial M_2}{\partial \dot{I}_0}\right]^T \boldsymbol{r}$$

Where:

$$\frac{\partial M_2}{\partial \dot{I}_0} = \frac{\partial[\mathfrak{R}_z(-\psi)\mathfrak{R}_x(\theta)\mathfrak{R}_z(-\phi)]}{\partial \dot{I}_0} = \mathfrak{R}_z(-\psi)\frac{\partial \mathfrak{R}_x(\theta)}{\partial \dot{I}_0}\mathfrak{R}_z(-\phi)$$

and where:

$$\frac{\partial \mathfrak{R}_x(\theta)}{\partial \dot{I}_0} = \begin{bmatrix} 0 & 0 & 0 \\ 0 & -\sin(\theta) & \cos(\theta) \\ 0 & -\cos(\theta) & -\sin(\theta) \end{bmatrix} t$$

4.6. Derivative with respect to $\dot{\boldsymbol{\psi}}_{\mathbf{0}}$

The derivative of the body-fixed vector ***R*** with respect to the $\dot{\psi}_0$ angular velocity can be calculated by the formula:

$$\frac{\partial \boldsymbol{R}}{\partial \dot{\psi}_0} = \left[M_3 \frac{\partial M_2}{\partial \dot{\psi}_0}\right]^T \boldsymbol{r}$$

Where:

$$\frac{\partial M_2}{\partial \dot{\psi}_0} = \frac{\partial[\mathfrak{R}_z(-\psi)\mathfrak{R}_x(\theta)\mathfrak{R}_z(-\phi)]}{\partial \dot{\psi}_0} = \frac{\partial \mathfrak{R}_z(-\psi)}{\partial \dot{\psi}_0}\mathfrak{R}_x(\theta)\mathfrak{R}_z(-\phi)$$

and where:

$$\frac{\partial \mathfrak{R}_z(-\psi)}{\partial \dot{\psi}_0} = \begin{bmatrix} \sin(-\psi) & -\cos(-\psi) & 0 \\ \cos(-\psi) & \sin(-\psi) & 0 \\ 0 & 0 & 0 \end{bmatrix} t$$

4.7. Derivative with respect to $\boldsymbol{\sigma}_{\mathbf{i}}$

The derivative of the body-fixed vector ***R*** with respect to the σ_i nutation coefficients (with $i = 1,2,3$) can be calculated by the formula:

$$\frac{\partial \boldsymbol{R}}{\partial \sigma_i} = \left[M_3 \frac{\partial M_2}{\partial \sigma_i}\right]^T \boldsymbol{r}$$

Where:

$$\frac{\partial M_2}{\partial \sigma_i} = \frac{\partial[\mathfrak{R}_z(-\psi)\mathfrak{R}_x(\theta)\mathfrak{R}_z(-\phi)]}{\partial \sigma_i}$$
$$= \frac{\partial \mathfrak{R}_z(-\psi)}{\partial \sigma_i}\mathfrak{R}_x(\theta)\mathfrak{R}_z(-\phi) + \mathfrak{R}_z(-\psi)\mathfrak{R}_x(\theta)\frac{\partial \mathfrak{R}_z(-\phi)}{\partial \sigma_i}$$

and where:

$$\frac{\partial \mathfrak{R}_z(-\phi)}{\partial \sigma_i} = \begin{bmatrix} \sin(-\phi) & -\cos(-\phi) & 0 \\ \cos(-\phi) & \sin(-\phi) & 0 \\ 0 & 0 & 0 \end{bmatrix} \frac{\partial \phi}{\partial \sigma_i}$$

$$\frac{\partial \Re_z(-\psi)}{\partial \sigma_i} = \begin{bmatrix} \sin(-\psi) & -\cos(-\psi) & 0 \\ \cos(-\psi) & \sin(-\psi) & 0 \\ 0 & 0 & 0 \end{bmatrix} \frac{\partial \psi}{\partial \sigma_i}$$

Where the derivatives of ϕ and ψ with respect to σ_i can be expressed as:

$$\begin{cases} \dfrac{\partial \phi}{\partial \sigma_1} = -\sin(M_m) \\ \dfrac{\partial \phi}{\partial \sigma_2} = -\sin(M_m + 2\omega_m) \\ \dfrac{\partial \phi}{\partial \sigma_3} = -\sin(2M_m + 2\omega_m) \end{cases}$$

and:

$$\begin{cases} \dfrac{\partial \psi}{\partial \sigma_1} = \sin(M_m) \\ \dfrac{\partial \psi}{\partial \sigma_2} = \sin(M_m + 2\omega_m) \\ \dfrac{\partial \psi}{\partial \sigma_3} = \sin(2M_m + 2\omega_m) \end{cases}$$

4.8. Derivative with respect to τ_i

The derivative of the body-fixed vector $\boldsymbol{R}$ with respect to the τ_i nutation coefficients (with $i = 1,2,3$) can be calculated by the formula:

$$\frac{\partial \boldsymbol{R}}{\partial \tau_i} = \left[M_3 \frac{\partial M_2}{\partial \tau_i} \right]^T \boldsymbol{r}$$

Where:

$$\frac{\partial M_2}{\partial \tau_i} = \frac{\partial [\Re_z(-\psi)\Re_x(\theta)\Re_z(-\phi)]}{\partial \tau_i} = \Re_z(-\psi)\Re_x(\theta)\frac{\partial \Re_z(-\phi)}{\partial \tau_i}$$

and where:

$$\frac{\partial \Re_z(-\phi)}{\partial \tau_i} = \begin{bmatrix} \sin(-\phi) & -\cos(-\phi) & 0 \\ \cos(-\phi) & \sin(-\phi) & 0 \\ 0 & 0 & 0 \end{bmatrix} \frac{\partial \phi}{\partial \tau_i}$$

Where the derivatives of ϕ with respect to τ_i can be expressed as:

$$\begin{cases} \dfrac{\partial \phi}{\partial \tau_1} = \sin(M_s) \\ \dfrac{\partial \phi}{\partial \tau_2} = \sin(M_m) \\ \dfrac{\partial \phi}{\partial \tau_3} = \sin(2\omega_m) \end{cases}$$

4.9. Derivative with respect to ρ_i

The derivative of the body-fixed vector $\boldsymbol{R}$ with respect to the ρ_i nutation coefficients (with $i = 1,2,3$) can be calculated by the formula:

$$\frac{\partial \boldsymbol{R}}{\partial \rho_i} = \left[M_3 \frac{\partial M_2}{\partial \rho_i}\right]^T \boldsymbol{r}$$

where:

$$\frac{\partial M_2}{\partial \rho_i} = \frac{\partial[\Re_z(-\psi)\Re_x(\theta)\Re_z(-\phi)]}{\partial \rho_i} = \Re_z(-\psi)\frac{\partial \Re_x(\theta)}{\partial \tau_i}\Re_z(-\phi)$$

and where:

$$\frac{\partial \Re_x(\theta)}{\partial \rho_i} = \begin{bmatrix} 0 & 0 & 0 \\ 0 & -\sin(\theta) & \cos(\theta) \\ 0 & -\cos(\theta) & -\sin(\theta) \end{bmatrix} \frac{\partial \theta}{\partial \rho_i}$$

the derivatives of θ with respect to ρ_i can be expressed as:

$$\begin{cases} \dfrac{\partial \theta}{\partial \rho_1} = \cos(M_m) \\ \dfrac{\partial \theta}{\partial \rho_2} = \cos(M_m + 2\omega_m) \\ \dfrac{\partial \theta}{\partial \rho_3} = \cos(2M_m + 2\omega_m) \end{cases}$$